Surface and sub-surface dynamics of long-lived mesoscale eddies in the Mediterranean Sea under atmospheric forcing

Alexandre Barboni

INSTITUT POLYTECHNIQUE DE PARIS

NNT : 2023IPPAX103

Thèse de doctorat

Evolution de surface et de subsurface des tourbillons de méso-échelle sous l'influence du forçage atmosphérique : cas d'étude en Méditerranée

Thèse de doctorat de l'Institut Polytechnique de Paris
préparée à Ecole Polytechnique

École doctorale n°626 Institut Polytechnique de Paris (ED IPParis)
Spécialité de doctorat: Mécanique

Thèse présentée et soutenue à Paris, le 09 / 10 /2023, par

ALEXANDRE BARBONI

Composition du Jury :

Sabrina Speich Professeure, Ecole Normale Supérieure de Paris (Laboratoire de Météorologie Dynamique)	Présidente
Lionel Renault Directeur de recherche, Laboratoire d'Etudes en Géophysique et Océanographie Spatiales	Rapporteur
Yves Morel Directeur de recherche, Laboratoire d'Etudes en Géophysique et Océanographie Spatiales	Rapporteur
Anne Petrenko Maîtresse de conférence, Universite d'Aix Marseille (Institut Méditerranéen d'Océanographie)	Examinatrice
Johannes Karstensen Chercheur Senior, GEOMAR Helmholtz Center for Ocean Research	Examinateur
Alexandre Stegner Professeur chargé de cours, Ecole Polytechnique (Laboratoire de Météorologie Dynamique)	Directeur de thèse
Franck Dumas Ingénieur de recherche, Service Hydrographique et Océanographique de la Marine	Directeur de thèse
Xavier Carton Professeur, Université de Bretagne Occidentale (Laboratoire d'Océanographie Physique et Spatiale)	Invité

Remerciements

Au commencement d'une thèse, l'aboutissement d'un manuscrit paraît comme un objectif très élevé, un pic lointain et presque inatteignable. Pourtant chemin faisant, gravissant lentement des piles d'articles bibliographiques et des montagnes de code, des prises se découvrent dans ce qui semblait être un mur, et progressivement on s'élève de la brumeuse incompréhension des phénomènes physiques. Des crevasses apparaissent souvent, mais d'indéfectibles compagnons de cordées - virtuels ou réels - vous accompagnent tout du long. Grâce à eux beaucoup de torrents impétueux ont été franchis. Sans ordre ni d'importance ni chronologique, un immense merci à Marion, Laura, Jean, Adrien, Alice& Nicolas, Louise, Noémie, Doug, Evangelos, Manon, Alexandre, Matthieu, Rémi, et tant d'autres. Merci aussi à Raphaël et toute ma famille. Pour le soutien de toutes et tous, leur assurage sans faille et tant de bons moments échangés au coin du feu - voire sous l'igloo.

Malgré toute la technologie disponible, du GPS à ChatGPT, une boussole reste essentielle pour garder un cap. Merci donc à mes directeurs de thèse Alexandre, Franck et Xavier de m'avoir guidé toutes ces années. Le plus dur aura certainement été d'arriver à me supporter avec mes incessants changements de directions et multiples détours. D'autres viennent aussi vous guider en cours de route, merci à Anne et Lionel pour leur soutien et conseils quand le brouillard empêchait parfois de se réperer. Merci enfin à Yves et Johannes pour leurs questions intéressantes et constructives lors de la soutenance. Par ailleurs on ne part pas de rien en commençant une thèse : il n'y a pas d'élève sans professeur. Je remercierai donc aussi tous les profs qui se sont succédés et dont j'ai essayé de suivre les enseignements, avec plus ou moins de succès. Tenter une liste exhaustive conduirait à des oublis, et serait avouons-le un peu rébarbartif. À la place, puisque l'occasion est trop rarement donnée de parler des résultats négatifs, je citerai plutôt quelques échecs : merci à Mme Brulard (CE1, 1ère fois au coin), Mme Chambon (6ème, 1er zéro sur 20), et M. Barbet-Massin (PC*, 1ère catastrophe expérimentale en inondant une classe d'huile de tournesol). Une thèse a ceci de particulier qu'on peut parfois être le guide pour d'autres. Grâce à la confiance d'un certain nombre de profs (Sabrina, Riwal, Xavier, Alexandre) j'ai eu la chance de donner énormément de cours et TD durant ces trois années. Éclairer le chemin d'autres que soi-même est un métier et une expérience unique. Un grand merci à plusieurs de mes élèves qui ont accepté de me suivre sur des sentiers parfois tortueux : Imad, Oussama, Solange et Florian.

Il faut aussi se rendre compte d'un certain nombre de directions qui ont été prises, d'embranchements auxquels certains chemins ont été choisis, et dont j'aimerais en raconter deux. Le 3 septembre 2015 était un jour de rentrée à l'ENS Paris, avec des conférences présentant les départements de l'école. Arrivant par la sélection Physique, je comptais sans trop tergiverser continuer en Physique. Et puis une professeure de Géosciences est venue nous présenter son département, dont l'océanographie physique, et même plus particulièrement ses observations de tourbillons - oui déjà ! - embarquée dans l'Océan Austral. Ce jour-là j'ai choisi les sciences de la Terre[1], pour finir 8 ans plus tard une thèse en océanographie. Merci à Sabrina de m'avoir fait découvrir cette science, et les tourbillons par la même occasion. Le 8 mars 2020 était également un autre embranchement dans un contexte particulier. Ce matin-là un avion est parti pour Haïfa sans moi, ayant décidé de rester en France faire mon stage de M2. Malgré le fait que je n'ai finalement jamais rencontré ma directrice de stage en personne, ce stage a été très enrichissant, et s'est poursuivi en doctorat. Tous n'ont pas eu le chance de pouvoir être encadré ainsi cette année-là. Merci donc à Ayah et Alexandre pour leur patience, et à toute la famille de Courson pour leur accueil chaleureux durant le confinement.

Il y a pour finir des étoiles plus lointaines qui nous guident, que l'on garde en tête et dont on réalise souvent trop tard l'inspiration qu'elles ont insufflée. J'aimerais ainsi clôre par une pensée pour ceux dont j'aurais aimé qu'ils eussent pu lire ce manuscrit. À mes grands-parents et mon grand-oncle.

Arrivé au sommet, le panorama derrière soi laisse donc découvrir tout ce chemin parcouru. Et au-devant d'autres vallées, cols et crêtes apparaissent, peu ou pas explorées. Ce qui importe n'est donc pas le sommet, mais les compagnons de route et le voyage qui continue.

[1] L'aternative aurait été d'étudier la Physique statistique avec des Smarties. Calorique mais peu gastronomique. On y aurait perdu au change car tout le monde sait qu'on mange mieux sur les navires de la flotte océanographique.

Note

Cette thèse contient plusieurs travaux qui ne sont pas de mon seul fait, outre mes directeurs de thèse. Le présent manuscrit les rassemble afin de donner une vision claire et logique des outils et méthodes développés en commun, notamment les améliorations à l'atlas de tourbillons DYNED. Citons entre autres Solange Coadou-Chaventon, Evangelos Moschos, Briac Le Vu et Florian Barge. Lorsqu'elles ne sont pas intégralement de ma main, les figures présentes dans ce manuscrit sont systématiquement citées.

Abstract

Mesoscale eddies are ubiquitous turbulent structures in the oceans, in thermal wind balance with a signature in density. Anticyclones with negative vorticity are associated with a negative density anomaly translating in a sea surface height (SSH) elevation, and conversely for cyclones. Statistical studies really began with eddy automated detections based on gridded altimetry products. The first quantitative studies were done in a composite approach: many observations are collocated with eddy contours and gathered into a single mean eddy picture. This approach combined with remote-sensing and Argo profiling floats provided eddy average signature in sea surface temperature (SST), salinity, chlorophyll but also air-sea fluxes. Previous studies did not significantly investigate eddy temporal evolution, apart from trajectory statistics. Eddies interact with heat and momentum air-sea fluxes interact over both short and long timescale, but their evolution remains unknown. We then investigate the mesoscale evolution submitted to atmospheric interactions, in both surface and at depth. Mediterranean eddies provide an ideal case study with extensive in situ measurements and occurrence of long-lived anticyclones. In a first part, we define a Lagrangian method tracking eddies in altimetric data at 1/8°. Eddy observation are collocated with in situ vertical profiles to measure eddy subsurface physical properties, and an outside-eddy reference background is defined to retrieve the eddy-induced anomalies. In a second part, evolution of eddy SST anomalies reveals a strong seasonal signal. Anticyclonic cold and cyclonic warm surface signatures shift from very rare in winter to predominant in early summer. This seasonal oscillation also recovered tracking individual structures. Collocated vertical profiles reveals this summer shift to occur only in near-surface. Hence an eddy-modulated vertical mixing is hypothesized to drive this evolution, with increased mixing in anticyclones. Getting to the mixed layer depth (MLD) in a third part, anticyclones are observed to enhance winter mixed layer deepening (up to 350m anomaly) and significantly delay spring restratification (up to 2 months). Eddy MLD anomalies do not scale with relationship from previous composite studies, and are rather impacted by the subsurface density profile. In a fourth part, we assess the accuracy of eddy evolution in a high resolution numerical experiment with the CROCO model. Eddy seasonal variations in both SST and MLD are retrieved. Increased mixing in anticyclone is confirmed and found to be sensitive to grid resolution. Near-inertial waves triggered by high frequency winds propagate more into the anticyclonic negative relative vorticity and enhancing mixing, in a remarkable example of scales interaction. Last, remaining interactions are discussed, in particular the role of Ekman pumping, atmospheric retroactions and importance of salinity. This study highlights the rich evolution occurring in mesoscale eddies with atmospheric interactions, blurred in composite approach but observable using Lagrangian tracking, and not yet properly retrieved nor studied in global models.

Résumé

Les tourbillons méso-échelle sont des structures turbulentes omniprésentes dans l'océan, en équilibre thermique avec une signature en densité. Les anticyclones ont une vorticité négative associée à une anomalie de densité négative, et inversement pour les cyclones. Des descriptions quantitatives n'ont réellement commencé qu'avec les détections automatiques de tourbillons à partir sur des produits altimétriques maillés. Les premières études ont été réalisées avec une approche composite : de nombreuses observations colocalisées avec les contours de tourbillons dessinent une image moyenne. Cette approche combinée à la télédétection et aux profileurs Argo a permis de dévoiler la signature moyenne des tourbillons en température de surface de la mer (SST), en salinité, en chlorophylle mais aussi sur les flux air-mer. Ces études antérieures n'ont pas étudié de manière significative l'évolution temporelle des tourbillons, en dehors des statistiques de trajectoire. Les tourbillons interagissent avec l'atmosphère, à la fois en chaleur et en quantité de mouvement, aux courtes et aux longues échelles de temps, mais leur évolution demeure pourtant méconnue. Nous étudions ici l'évolution de structures méso-échelle sous l'effet des interactions air-mer, à la fois en surface et en profondeur. Les tourbillons méditerranéens constituent un cas d'étude idéal, avec une couverture dense en mesures in situ et la présence d'anticyclones à longue durée de vie. Dans une première partie, nous définissons la méthode de suivi lagrangien des tourbillons grâce à l'altimétrie au 1/8°. Les observations de tourbillons sont colocalisées avec des profils verticaux in situ pour mesurer les propriétés physiques, et un profil extérieur de référence est défini afin de mesurer les anomalies induites. Dans une deuxième partie, nous analysons l'évolution des anomalies de SST des tourbillon qui révèle un fort signal saisonnier. Les signatures de surface anticycloniques froides et cycloniques chaudes passant de très rares en hiver à prédominantes au début de l'été, ce qui est également vrai pour une structure individuelle. La colocalisation avec les profils verticaux révèlent que ce changement saisonnier ne se produit que proche de la surface, d'où l'hypothèse d'une modulation du mélange vertical par les tourbillons à l'origine de cette évolution saisonnière, avec un mélange accru dans les anticyclones. Une troisième partie étudie ensuite l'influence des tourbillons sur la couche de mélange (MLD). Les observations dans les anticyclones mettent en évidence un approfondissement considérablement de la couche de mélange hivernale (jusqu'à 350m plus profond) et une restratification estivale fortement retardée (jusqu'à 2 mois). Les anomalies de profondeur de couche de mélange ne correspondent pas aux relations des études composites antérieures, et sont plutôt influencées par l'interaction avec le profil de densité en subsurface. Dans une quatrième partie, nous simulons à haute résolution l'évolution des tourbillons avec le modèle numérique CROCO, retrouvant les variations saisonnières des tourbillons dans la SST et la couche de mélange. L'hypothèse d'un mélange accru dans les anticyclones est confirmée. Les ondes quasi-inertielles excitées par le forçage haute-fréquence se propagent davantage dans l'anticyclone et y augmentent le mélange, produisant un exemple remarquable d'interaction d'échelles. Enfin d'autres interactions sont discutées, en particulier le pompage d'Ekman, les rétroactions atmosphériques et le rôle de la salinité. Cette étude met en évidence la complexité de l'évolution des tourbillons de méso-échelle avec des interactions air-mer. Cette dynamique est gommée dans une vision composite mais s'observe par un suivi lagrangien, et elle reste peu étudiée dans les modèles globaux.

Contents

Chapter 1

Introduction

1.1 A history of eddy observation in oceanography

1.1.1 In situ oceanographic surveys

Before satellite observation, oceanic structures could only be surveyed through in situ measurements, with vertical profiles and currentmeters. Using steamers opportunity measurements across the North Atlantic, Church (1932) already identified eddies detachments from the Gulf Stream as warm core rings. We have to wait until the end of the Second World War to have observations of a strong correlation between temperature spatial gradients (and assumed density, but at that time most measurements were only provided through bathythermographs) and surface currents, in one of the first description of the Gulf Stream variability by Fuglister and Worthington (1951) (reproduced in Fig.1.1a). Numerous surveys on these ocean density lenses were programmed in the 60's and 70's. One can list Soviet navy POLYGON experiments in 1967 in the Arabian sea (Stockman et al., 1969) and in 1970 in the Tropical Northern Atlantic (Brekhovskikh et al., 1971), the American *Mid-Ocean Dynamics Experiment* (MODE Group, 1978), the joint US-Soviet POLYMODE experiment, the French-British *Tourbillon* experiment in the Gulf of Biscay in 1979 (Tourbillon Group, 1983), and at the end of the 80's some significant review were already available, e.g. McWilliams (1979), Monin and Zhikharev (1990), Koshlyakov and Belokopytov (2020). These first eddy oceanographic surveys already confirmed at their time ubiquity of oceanic eddies, with velocities in balanced flows around density anomalies over wavelengths about 200km (in the mid-latitude North Atlantic, hence radius four times smaller about 50km), characterizing the mesoscale. They also showed the baroclinic nature of oceanic eddies, with surface and bottom currents being largely uncorrelated. Eddies were already understood as contributing for a significant part of the ocean kinetic energy budget and to have temporal scale evolution ranging from few weeks to months (Richardson et al., 1989). But these surveys also brushed a zoology of various other dynamical structures. Analysis of ocean fronts at finer scale also revealed smaller dynamical scales in the upper ocean, largely unbalanced with density gradients (Pollard and Regier, 1992; Rudnick and Ferrari, 1999), what can then be labeled as "submesoscale". Observations from the POLYMODE experiment also revealed smaller scale features to be not uncommon at depth with no surface signature, referred to as "submesoscale coherent vortices" (McWilliams, 1985).

New oceanographic instruments offered new ways to observe eddies, such as mooring. The long term Bermuda Atlantic Time series (BATS) allowed similar in situ eddy measurements of density anomalies correlated with sea surface height variations (Siegel et al., 1999). McGillicuddy et al. (1999) identified a distinct type of eddy constituted by a very homogeneous core with isopycnals displacement above and below the eddy core. These homogeneous density lenses are referred to as "mode-water eddies". McGillicuddy et al. (1999, 2007) hypothesized they play a significant role in biological production through nutrient input by isopycnal displacement, the "eddy-upwelling" theory. Nutrients uptake and biological production appeared however in more recent studies to be mostly driven by submesoscale (Lévy et al., 2001, 2018). The deployment of long term mooring sites in the Labrador Sea also allowed to make repeated observation of eddies (Lilly and Rhines, 2002). Lilly et al. (2003) provided a method for objective eddy detections from a mooring site. Their method looked at mooring hodographs to identify rotating structures, assuming a slowly varying drift. They also distinguish between "apparent eddies" and "apparent non-eddies" by ensuring there is a distinct temperature and salinity anomaly in the first case, of which 33 events were recorded from 1994 to 1999 (21 cases for "non-eddies"). This highlights the double nature of mesoscale eddies signing in the velocity field as

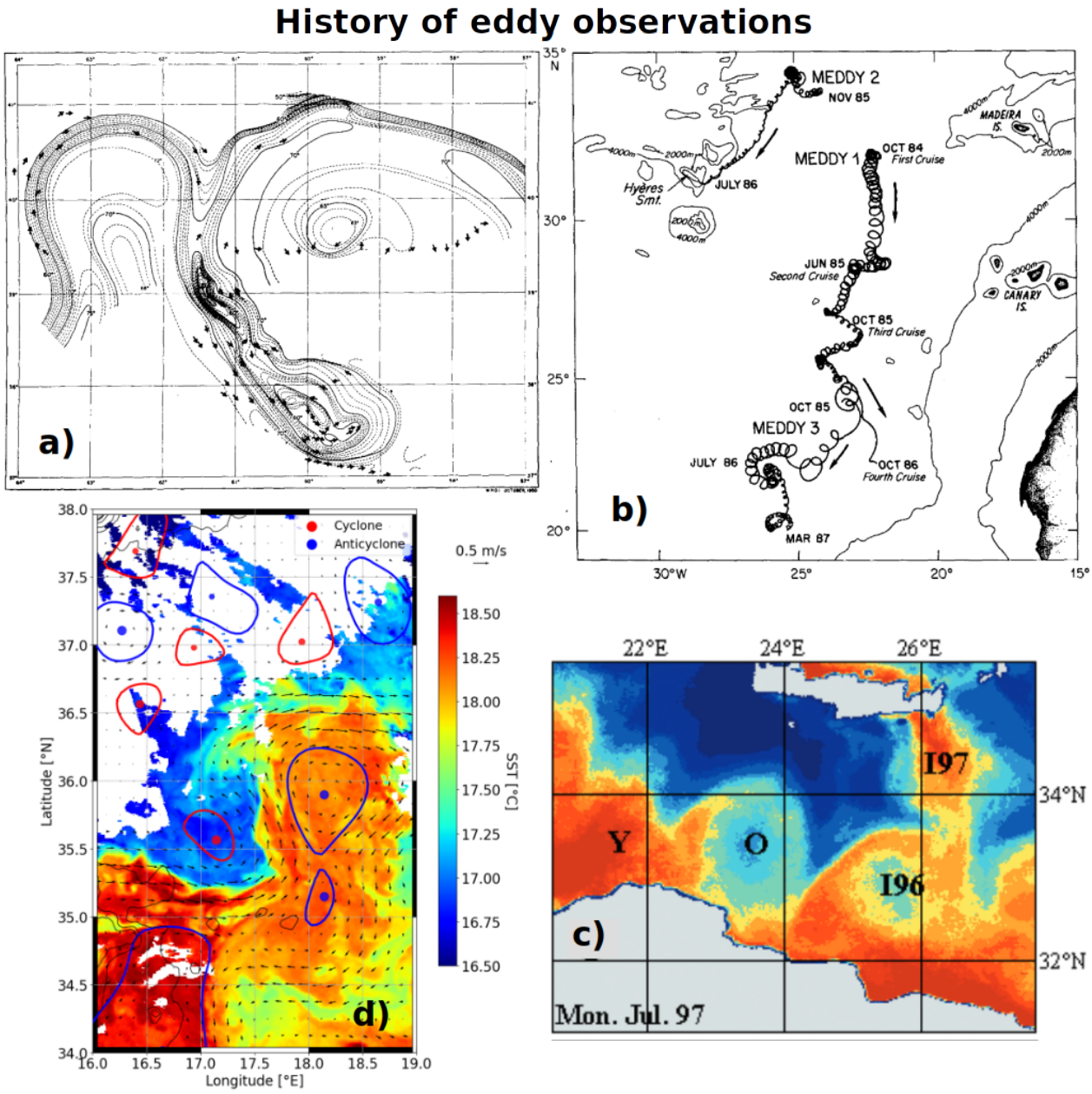

Figure 1.1: (a) Superposition of surface current velocities with 200m isotherms (in °F) showing the detachment of a cold core Gulf Stream ring, reproduced from Fuglister and Worthington (1951). (b) SOFAR floats trapped in Meddies revealing their pathway and rotation from Lagrangian trajectories, reproduced from Richardson et al. (1989). (c) Swirling filaments shaping hand-labeled anticyclones in sea surface temperature from Advanced Very High Resolution Radiometer weekly composite, reproduced from Hamad et al. (2006). (d) Automated eddy detection in the Ionian Sea on 2021-01-07 with AMEDA algorithm (contours) applied on AVISO 1/8°SSH (arrows) with Ultra-High Resolution SST (1/120°, colors, Nardelli et al. (2013)).

a swirling structure, but also driven by a physical anomaly at depth on temperature and salinity. Lilly et al. (2003) made an interesting distinction between "convective lenses" and "Irminger rings". Their origins were deduced from watermasses properties at their core: the first ones are intrathermocline lenses assumed to be formed by winter heat loss and deep convection at the center of the Labrador Sea (13 occurrences), and can be identified by a very homogenized core, then falling into the mode-water eddies definition. The second ones (12 occurrences) are formed by detachment of the Irminger coastal current. They reported for both eddy types the occurrence of composite core anticyclones vertically aligned, with less stratified layers separated by stronger stratification inside the eddy. They suggested these vertical structures to be formed by vertical alignment of previously formed mono-core structures, but could not assert it because the full eddy evolution was not measured. McGillicuddy (2015) theorized another mechanism than heat loss for mode-water eddies as a result of isopycnal doming or thinning from wind interaction, but in situ observations were still lacking.

In situ measurements indeed provided in-depth vision of mesoscale structures, but in most cases does not allow to study evolution because instruments only measure an instantaneous snapshot. Temporal evolution at depth requires numerous in situ campaigns, which was still attempted in some early studies. An early example dates back from Nilsson and Cresswell (1980) in a Tasman sea with repeated XBT transects revealing a seasonal evolution of an East Australian Current anticyclone. A remarkable Eastern Mediterranean example is Brenner (1993), studying from April 1988 to October 1990 the evolution of an anticyclone located south of Cyprus (see Mediterranean eddy climatology in Sect.1.5) locating its center through extensive CTD casts and computing the kinetic and available potential energy over time. More recently the increasingly cheaper cost of glider deployment allowed frequent surveys targeting eddy structure. In the same Cyprus eddy, Hayes et al. (2011) measured repeated sections from 2009 to 2011. Another anticyclone studied in the literature is the Loop Current Eddy in the Gulf of Mexico, which evolution on the vertical structure between 2 seasons was surveyed by Meunier et al. (2018). A last recurrent anticyclonic eddy further North to mention is the Lofoten Basin eddy, sampled through numerous glider surveys by Bosse et al. (2019).

1.1.2 Eddies from drifting floats

Eddying structures should advect particles around their core to form orbital trajectories. As early as the 80's this method was used to track Mediterranean eddies ("Meddies"). Meddies were discovered offshore from Bahamas island (McDowell and Rossby, 1978). These isolated anticyclonic lenses tend to spread salty Mediterranean waters at depth around 1000m in the Atlantic interior. Their observational need led to the development of the first eddy Lagrangian tracking, using SOFAR ballasting floats with 1000m parking depth. This technique revealed Meddies pathways, drifting speed and even record merging events or interaction with seamounts (Richardson et al., 1989, 2000). Several of these Meddies trajectories with SOFAR floats are reproduced from Richardson et al. (1989) in Fig.1.1b.

Later in the 90's, the large drifter deployment in part of the World Ocean Circulation Experiment (WOCE) (Sybrandy, 1991) provided a large cover of the global ocean with Lagrangian drifting trajectories. Veneziani et al. (2004) and Griffa et al. (2008) showed that most trajectories could be fitted with a simple Lagrangian stochastic model, and looping drifters identified with a finite rotation speed. Lumpkin (2016) updated the method to provide a global database of looping trajectories completing at least two orbits. This method ensures a geometrical reality of an eddy with a coherent rotating core, but it is however greatly limited by the drifter coverage, and provides only a surface current estimation.

This second limit was partly resolved with development of the Argo program. Argo profiling floats were developed at the end the 90's to "provide an enhanced real-time capability for measurement of temperature and salinity" (Argo Steering Team, 1998). Standard floats have a temperature, salinity and pressure sensors, staying at a parking depth of usually 1000m and measuring vertical profiles from 2000m to the surface every 10 days (Roemmich and Argo Steering Team, 2009). Although originally deployed for climatological studies, Argo floats trajectories provide useful estimation of Lagrangian pathways at depth, with small errors due to its vertical displacement (Park et al., 2005) and collected for instance in the ANDRO dataset (Ollitrault and Rannou, 2013). Looping Argo floats can then describe an eddy at depth. Better than surface drifters, they can also provide temperature and density section of the structure, as computed by L'Hégaret et al. (2013) (Gulf of Oman) or Nencioli et al. (2018) (Agulhas ring). This method was however often used in combination with remote-sensing to provide a in situ validation of a rotating eddy. To our knowledge Argo floats were never used alone to define an eddy from Lagrangian trajectories because of the long time step between two

profiles (usually 10 days).

1.1.3 Mesoscale through remote-sensing

As in any part of oceanography, large progress was achieved with the availability of remote-sensing observation, first of all sea surface temperature (SST). Eddies could be identified as swirling structure shaping circular temperature fronts in surface. This method identifying eddies in SST was possible in powerful eddying regions or with strong meridional gradients, where these turbulent structures produce visible stirring. This is the case in Western boundaries current extension regions, such as the Gulf Stream rings (Richardson, 1980), the Agulhas current retroflexion (Olson and Evans, 1986), or the Kuroshio extension (Yasuda et al., 1992). It confirmed the ubiquitous presence of eddies throughout the world ocean. Due to smaller deformation radius in the Mediterranean Sea (see Fig.1.2 later), this method of eddy tracking only in SST proved to be very useful (e.g. Philippe and Harang (1982) or Matteoda and Glenn (1996) for the Eastern Basin). SST was primarily used until the mid-2000's in the Mediterranean Sea by Millot and Taupier-Letage (2005) and Hamad et al. (2006) to identify eddies accumulation areas. An example of such SST eddy tracking is reproduced in Fig.1.1c.

The availability of altimetric products since the launch of ERS1 in July 1991 and TOPEX/Poseidon (T/P) in August 1992 opened a new area to study ocean currents, and most particularly for eddies. Altimetric data indeed provide an almost global measurement coverage free from cloud effect. Eddies were first seen in an Eulerian point of view as current variability (Wilkin and Morrow, 1994; Stammer, 1997) (see Sect.1.2.3). Later the improvement of sea surface height (SSH) mapping in gridded maps every 10 days (Le Traon et al., 1998), then every day (Dibarboure et al., 2011) allowed to follow eddies as propagating waves of Sea Level Anomaly (SLA) (Chaigneau and Pizarro, 2005; Amitai et al., 2010). The study of mesoscale eddies radically changed with the development of detection and tracking algorithms. They allow to study eddies as coherent oceanic structures to be followed in time, what we will later describe as the "Lagrangian" approach. First merely tracking SLA extrema (Fang and Morrow, 2003), these algorithms soon became more complex in identifying effectively rotating structures in SSH. First physical algorithms relied on the Okubo-Weiss criterion to detect regions dominated by vorticity (Isern-Fontanet et al., 2003; Penven et al., 2005), but then numerous other geometrical or hybrid (geometrical and physical) methods were proposed. A review of algorithms available in the literature is proposed in Sect.1.2.5. An example of automated eddy detection in the Ionian Sea using AMEDA algorithm applied on AVISO 1/8°SSH is shown in Fig.1.1d, together with geostrophic velocities (see Eq.1.5) and SST.

The primary physical measurement used for most early eddy detection algorithm was SLA (Fang and Morrow, 2003; Morrow et al., 2004; Chaigneau et al., 2009; Chelton et al., 2011b; Mason et al., 2014; Faghmous et al., 2015). Typical error on SSH is about 2cm since the late 90's (Le Traon et al., 1998; Pujol et al., 2016), but uncertainty on the mean sea level, i.e. the Mean Dynamic Topography (MDT), required more than another decade to study current variability on Absolute Dynamic Topography (ADT) (Rio et al., 2014). Recent comparison confirmed that eddy detections are more reliable on ADT than SLA alone, recurrent eddies providing a mean SSH bias giving spurious detections (Pegliasco et al., 2021). Nowadays eddy atlases start to be available in delayed and near-real-time, providing eddy trajectories at global scale (Pegliasco et al., 2022).

The Argo floats array was not designed to be eddy-resolving, with only about 3000 floats worldwide and 100 profiles expected on average every 10°square of ocean (Roemmich and Argo Steering Team, 2009). Nonetheless the collocation between Argo profiles and eddies detected from remote-sensing greatly improved our ability to observe them. A pioneering example is Chaigneau et al. (2011) with collocated Argo floats in the Peru-Chile upwelling system. They composed an eddy mean picture by reporting Argo profiles as a function of normalized distance to the eddy center. This so-called composite method could also reveal eddy influence with other physical or environmental variable, in particular air-sea interactions (Chelton et al., 2011a; Frenger et al., 2013; Gaube et al., 2014; Dufois et al., 2016). However the eddy evolution received little attention, nor their atmospheric retroactions. The context of a mean water transport through Meddies lead to early attempt of eddy Lagrangian tracking, as presented above. Only in recent years a similar issue emerged with the Indian ocean watermasses tranport into the Atlantic, known as "Agulhas leakage". This issue lead to the development of a proper Lagrangian approach combining Argo profiles and remote-sensing to study and track eddies in time (Laxenaire et al., 2018, 2019). These composite and Lagrangian methods are further detailed in Sect.1.3.

1.2 What is a mesoscale eddy? Theoretical and practical definitions

As presented in the above section, eddies were studied since at least the end of Second World War, with various platforms and above all through various observed variables: temperature, density, velocities or trajectories, in surface or at depth. These different variables entail different definitions of mesoscale eddies, with different assumptions depending on the object of interest.

1.2.1 Hydrological definition

As introduced above, several early oceanographic surveys already showed that current variability is often linked with a perturbation of the density field. Considering a background density stratification $\rho_{back}(z)$, a density anomaly $\sigma(x, y, z)$ of sufficiently large scale is in geostrophic equilibrium: the induced pressure gradients is countered by the Coriolis force. The induced velocities can then be described as a "balanced flow", and the 3D flow structure is given by the thermal wind balance. Its zonal (northward) component being noted u and the meridional (eastward) noted v, with Coriolis parameter f and gravitational acceleration $g = 9.81 m.s^{-2}$:

$$\rho = \rho_{back} + \sigma \tag{1.1}$$

$$\begin{cases} u(z) = \int_{ref}^{z} \frac{g}{f\rho_0} \partial_x \sigma(\tilde{z}) d\tilde{z} \\ v(z) = -\int_{ref}^{z} \frac{g}{f\rho_0} \partial_y \sigma(\tilde{z}) d\tilde{z} \end{cases} \tag{1.2}$$

The Coriolis parameter (or planetary vorticity) f is related to the latitude λ and Earth rotation period T_e: $f = 4\pi sin(\lambda)/T_e$. f going to zero at the Equator leads to the geostrophic equilibrium being only valid away from the Equator (in practice it is often considered $|\lambda| > 5°$). A density anomaly in thermal wind balance then provides a first hydrological definition of a mesoscale eddy. Equations 1.2 show that a negative density anomaly will create a clockwise rotating structure - called an anticyclone - a positive one a counter-clockwise rotating structure - a cyclone - in the Northern Hemisphere (positive f). Direction of rotation is opposite in the Southern Hemisphere but a negative density anomaly remains an anticyclone by definition. Spatial scales associated with these density anomalies are related to a deformation of the mean stratification, defined with the Brunt-Vaisala frequency (BVF) $N(z)$:

$$N(z) = \sqrt{-\frac{g}{\rho}\frac{\partial \rho}{\partial z}} \tag{1.3}$$

Following equation(5.204) in Vallis (2006), considering wave motion in a quasi-geostrophic system with Boussinescq approximation and streamfunction Ψ, we obtained for its vertical shape the following equation :

$$\partial_z \left(\frac{f^2}{N(z)^2} \partial_z \Psi \right) = -\frac{1}{R^2} \Psi \tag{1.4}$$

The largest solution R with boundary conditions $\Psi(z = 0, H) = 0$ is the first baroclinic deformation radius (R_d hereafter). R_d is the mesoscale, the characteristic horizontal scale of baroclinic quasi-geostrophic motion. In other words, R_d is the scale at which stratification can support baroclinic density fronts in geostrophic equilibrium. It is then a spatial scale intrinsic of the ocean, and eddy real scale L can be larger or smaller than R_d. The Burger number R_d^2/L^2 then defines the non-dimensional eddy size. Mesoscale should be distinguished from two other important spatial scales, which are larger wind-driven gyres at the basin scale (Stommel, 1948) ($L \sim 1000 km$) and submesoscale structures smaller than the deformation radius (McWilliams, 1985) ($L \sim 1 km$).

A map of the first baroclinic deformation radius is shown in Fig.1.2 for the Mediterranean Sea, computed as integration of the ordinary differential equation Eq.1.4 (referred to as ODE method). It should be noticed that R_d computation is usually done with the Wentzel-Kramers-Brillouin (WKB) approximation, which

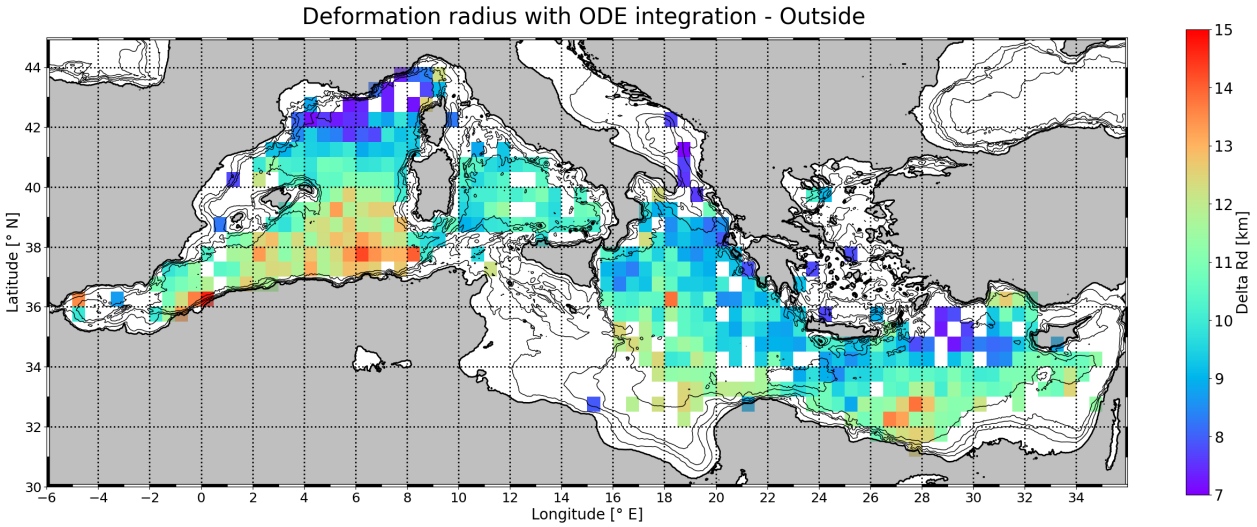

Figure 1.2: Rossby deformation radius map based on outside-eddy vertical profiles (collocation method in Sect.2.3) with ordered differential equation integration (Eq. 1.4).

translates in considering $N(z)$ as a constant in Eq.1.4 (Chelton et al., 1998). Additionally in Fig.1.2, vertical data for $N(z)$ come only from profiles outside-eddy due to avoid the mean effect of eddies on the stratification (further discussed in Appendix A). The deformation radius depends on latitude but is roughly about 50 to $100km$ in the global ocean (Chelton et al., 1998). It should then be highlighted that due to weaker mean stratification, R_d is a lot smaller in the Mediterranean Sea, only about 11km. Spatial scales discussed in this study has to be rescaled accordingly to be compared with other regions.

On the other hand to fulfil the geostrophic equilibrium the eddy temporal scale (called orbital period L/V_{max}) has to be large compared to the Earth rotation, defined by the inertial period $2\pi/f$. The ratio of these two temporal scales is the Rossby number (discarding 2π) $Ro = V_{max}/Lf$, quantifying the eddy non-dimensional strength. Laboratory and numerical experiments showed that anticyclone remain stable when being larger than R_d (low Burger number) (Perret et al., 2006; Dong et al., 2007). Studies on cyclone-anticyclone asymmetry further showed that anticyclones are more resistant to external shear (Arai and Yamagata, 1994; Graves et al., 2006).

This hydrological definition is conceptually interesting to study eddy evolution, because it relies on an eddy description through its watermasses. However measuring eddy physical properties continuously or at least repeatedly is very difficult with ship campaigns. Apart from those specific campaigns previously introduced (Nilsson and Cresswell, 1980; Brenner, 1993; Meunier et al., 2018; Bosse et al., 2019), in-situ studies offer only snapshots of dynamical structures evolving over few weeks. They additionally focus on specific recurrent structures easy to sample, often powerful anticyclone. This hydrological definition must then be adapted to more permanent observation platforms, which is offered by satellite remote-sensing.

1.2.2 Geometrical definition

The hydrological definition presented in the above section relies on the geostrophic equilibrium (Eq.1.2) to describe the flow velocities. On the opposite, an eddy can be defined as a rotating flow structure, trapping water parcels in its core (Haller, 2005). This definition takes into account the true Lagrangian pathways of water parcels. We will refer to this second definition as a "geometrical" - or kinematic - definition, to distinguish it from the eddy Lagrangian tracking (introduced later in Sect.1.3), and in consistence with geometrical eddy detection algorithms (see Sect.1.2.5).

This definition can very easily be applied with in situ instruments recording drifting trajectories. As previously introduced (Sect.1.1.2), this could be done for Meddies with SOFAR floats (Richardson et al., 1989) (see Fig.1.1), or even computing a looping trajectories database describing eddies (Lumpkin, 2016) with buoys from the WOCE program. Other new oceanographic measurement techniques allow to apply this

geometrical definition through instruments mounted on a ship or anchored. Fixed moorings allow to observe an eddy signature, in both density field and with hodographs from currentmeters, but assuming an almost constant drifting speed (Lilly and Rhines, 2002; Stramma et al., 2014). Vessel-mounted acoustic Doppler currentmeter profilers (ADCP) allows to measure the true and instantaneous speed section of a swirling eddy, without slow drift assumption (Castelão and Johns, 2011). Repeated sections in different directions can also show some elliptical deviation from a circular shape.

Despite relying on in situ velocity measurement (and density profile if adding Argo profiles) and being more accurate to describe oceanic flows, the geometrical definition is difficult to maintain in operational conditions. Looping Argo floats or surface drifters only measure an eddy for a few orbital periods, with some exceptions for SOFAR drifters maintained trapped in Meddies for months. Measuring an eddy temporal evolution then involves to use continuously available data, which is offered by satellite remote-sensing.

1.2.3 An Eulerian approach from Eddy kinetic energy

Due to their signature on density and thanks to the isostatic equilibrium, mesoscale have a signature in sea surface height. An anticyclonic negative density anomaly will then sign as a high in SSH and conversely a cyclone as a low. With the availability of altimetry detection, eddy velocities can then be estimated from SLA h':

$$u' = -\frac{g}{f}\partial_y h' \quad ; \quad v' = \frac{g}{f}\partial_x h' \tag{1.5}$$

A more statistical description of eddy activity can be estimated through the Eddy Kinetic Energy (EKE, see Mediterranean map later in Fig.1.7). This approach allows to compute statistics on gridded fields, and is therefore often referred to as "Eulerian", but it does not allow to track individual structures:

$$EKE = \frac{1}{2}(\overline{u'^2} + \overline{v'^2}) \tag{1.6}$$

In the Mediterranean Sea, the first eddy studies were based on EKE estimation with sea level standard deviation (Iudicone et al., 1998; Ayoub et al., 1998; Larnicol et al., 2002; Amitai et al., 2010). Some collocation with SST could be studied on a case by case basis, comparing directly SSH measured at the satellite nadir and SST (Iudicone et al., 1998). Mapping error and resolution were at that time limiting factors with more than 1°between successive tracks and a SSH root-mean-square error about 3cm (Le Traon et al., 1998) while SSH deviation in the Mediterranean Sea was measured to range between 1 and 8 cm by Iudicone et al. (1998).

1.2.4 β drift and non-linearity criterion

Another way to consider mesoscale eddies is to see them as circular Rossby waves. They then experience westward drift due to meridional variations of the Coriolis parameter, the β-effect. This β-drift was theorized by Rossby (1948) for atmospheric vortices, then by Nof (1981) for baroclinic ocean vortices assuming they are circular and steady, and later generalized by Cushman-Roisin et al. (1990). They showed the drift to be westwards and scaling as :

$$v_\beta = \beta R_d^2 \quad \text{where} \quad \beta = \partial_y f = \frac{4\pi cos(\lambda)}{T_e R_e} \tag{1.7}$$

For the Mediterranean Sea at mid-latitude ($\lambda \approx 35°$) and Earth radius $R_e = 6371km$, $\beta \approx 2 \times 10^{-11} m^{-1}.s^{-1}$, a median value. The β-drift is nonetheless very weak due to the small deformation radius: $v_\beta \approx 0.5 km.d^{-1}$. For large open basins this westward drift is significant (Chelton et al., 1998), and eddies are indeed observed to flow mostly westwards (Chelton et al., 2007). For intense eddies with Rossby number reaching values of order unity, a meridional drift correction has to be added. A correction computed by Killworth (1983) and confirmed in observations by (Morrow et al., 2004): intense cyclones move also polewards and anticyclones equatorwards.

Translation in time of what is physically detected as an eddy raised the question whether water parcels remained trapped in the eddy core. A simple criterion theorized by Flierl (1981) is that if the eddy rotational speed is higher than the eddy drifting speed, then water parcels can be trapped in a so-called "non-linear" Rossby wave. This criterion is more difficult to satisfy close to the Equator, where the deformation radius gets very large. In this region, β-drift is faster than rotational speed, leading to "linear" Rossby waves. Observing

that eddy drifting speed follows approximately the phase speed of baroclinic Rossby waves, Chelton et al. (2007) then defined a non-linearity parameter with eddy maximal rotational speed V_{max}:

$$\gamma = \frac{V_{max}}{v_\beta} \tag{1.8}$$

This non-linearity criterion allows us to conciliate the hydrological and geometrical definitions of an eddy: A mesoscale eddy is then defined by two criteria: it has a density anomaly σ in thermal wind balance (Eq.1.2), and it satisfies the non-linearity criterion ($\gamma > 1$). The first condition ensures that it has a geostrophic signature in sea surface height (SSH), allowing to detect it through remote-sensing altimetry. The second condition ensures that it is a distinct hydrological structure, allowing to consider it as an individual structure. The non-linearity criterion γ alone is of course not sufficient to consider that a SSH contour is indeed a transport barrier. Beron-Vera et al. (2013) showed that defining an eddy only on SSH contours leads to a strong underestimation of eddy transport trough trapped water parcels, compared to a geometrical contour based on least sheared streamline. Nonetheless this non-linear hydrological definition was routinely applied for eddy detection and tracking, and proved to be quite robust for eddy transport across ocean basins: e.g. Meddies in the North Atlantic with SOFAR floats (Robinson, 1983), or Agulhas rings in the South Atlantic (Laxenaire et al., 2020). As our focus is the eddy temporal evolution, we will keep this definition and apply it from a Lagrangian perspective to automatic eddy detections.

1.2.5 Eddy automated algorithms and atlases: towards a Lagrangian approach

Eddy detection

To study eddy individual structures, early studies simply looked at temporal propagation of sea level anomalies without eddy automatic detections (Chaigneau and Pizarro, 2005). But in the beginning of the 2000's several studies attempted to provide automated detections of individual eddies based on the altimetric field. Three different types of eddy detection algorithm should be distinguished, whether they rely 1) on a physical property of the flow, 2) on a geometrical property, or 3) hybrid. Fang and Morrow (2003) proposed a detection based on peaks larger than $\pm 10cm$- in gridded SLA fields. They used merged Topex/Poseidon and ERS2 satellite altimetric data every 10 days, and focused on intense warm-core anticyclones detached from the Leeuwin current. This gives SLA maxima between 20 and 70cm they had to track manually from one time step to another. They also observed a high correlation between steric height integrated from CTD casts and satellite SLA added to hydrological climatology, confirming the link between sea level and density anomaly at depth. Chaigneau and Pizarro (2005) used a similar method in the Southeastern Pacific with $\pm 6cm$ threshold on SLA, and confirmed eddy characteristics (rotation period and velocity) with looping drifting buoys. They noticed an overall good agreement, despite slight underestimation of swirling speed from altimetry.

Okubo-Weiss methods SSH mapping was not very efficient until the 2010's, then other studies proposed a physical approach based on the Okubo-Weiss parameter (Okubo, 1970; Weiss, 1991):

$$W = s_n^2 + s_s^2 - \omega^2 \tag{1.9}$$

Where $s_n = \partial_x u - \partial_y v$ and $s_s = \partial_x v + \partial_y u$ are the normal and shear components of the strain, $\omega = \partial_x v - \partial_y u$ the relative vorticity. The Okubo-Weiss parameter then gives information of the relative dominance of strain compared to vorticity. McWilliams (1984) proposed to classify the flow into three regions between elliptic ($W < -W_0$), hyperbolic ($W > W_0$) and background regions ($|W| < W_0$). W_0 is a threshold to be determined, and it then defines an eddy as a connected region dominated by vorticity and hence negative W. Isern-Fontanet et al. (2006) proposed an eddy detection method with threshold $W_0 = 0.2\,\sigma_W$, where σ_W is W spatial deviation. They produced with this method the first automated detections and trajectories in the Mediterranean Sea. It was also successfully applied in the global ocean by Morrow et al. (2004) and then Chelton et al. (2007) but with a constant W_0 parameter. Penven et al. (2005) resolved this issue on W_0 threshold by smoothing with a Hanning filter and selecting W minima. Kurian et al. (2011) also improved the method by discarding "banana shape" eddies, introducing a shape parameter as a ratio of the eddy contour over the best fitted circle.

Winding-angle method The main problem with the Okubo-Weiss parameter is that it based on flow derivative and is then quite sensitive to altimetry errors, still on the order of $3cm$ for AVISO product. This leads to an overestimated number of eddy observation (Chaigneau et al., 2008). The threshold determination W_0 remained a problem to determine eddy edge, i.e. where to end the eddy extent (Souza et al., 2011). To resolve these problems of the Okubo-Weiss criterion, the geometric "winding-angle" method was developed by Sadarjoen and Post (2000). Chaigneau et al. (2008) applied it to altimetric maps in the Peru-Chile upwelling system and proved this method to be more accurate than the Okubo-Weiss criterion. They detected eddy centers as SLA extrema (the method is then hybrid as it starts from a physical variable) and computed streamlines by releasing particles in the geostrophic flow. Computational cost of this method was improved in Chaigneau et al. (2009) by looking at surrounding SLA contours instead of streamlines, as it is parallel to SLA in the geostrophic approximation. Laxenaire et al. (2018) later adapted Chaigneau et al. (2009) hybrid method for the TOEddies algorithm.

SLA hybrid method Chelton et al. (2011b) used a SLA-only approach to detect eddies, but the method still relies somehow on a threshold on SLA. This method was also adapted in other successive algorithms. Mason et al. (2014) and Faghmous et al. (2015) improved it by considering only eddies having a single SLA extrema within a closed SLA contour, avoiding spurious detections. Proposing a more objective eddy detection method without sensitivity to chosen parameters, Mkhinini et al. (2014) extended Nencioli's method to introduce a new physical index based on a locally integrated quantity: the local normalized angular momentum (LNAM). The normalization makes it independent from the vortex intensity, giving a net distinction between elliptical and hyperbolic flow points and removing the threshold problem. Contours are also searched as surrounding closed SSH, making also a hybrid method.

Other altimetric methods Several other methods were proposed to overcome Okubo-Weiss limitations. Some of them are physical: Doglioli et al. (2007) method is based on wavelet analysis decomposing the vorticity field to find coherent structures. d'Ovidio et al. (2009) proposed to introduce information from the temporal variability through an eddy identification based on Lyapunov exponent. Halo et al. (2014) combined Okubo-Weiss and SLA approaches by keeping only eddies detected in both methods, achieving similar results on both models and remote-sensing SSH despite different resolution. Last, one should list the recent development of numerous neural networks algorithms using primarly altimetry (Lguensat et al., 2018; Franz et al., 2018; Duo et al., 2019).

Geometrical methods Other methods are based purely on the flow geometry, consistent with the geometrical definition of an eddy (see Sect.1.2.2) proposed by Nencioli et al. (2010), looking for center of rotation in velocity field. Haller and Beron-Vera (2012) proposed another geometrical method (called "geodesic" method) totally based on an eddy ability to trap water parcels. This method looks for flow transport barriers in least sheared streamlines. Last, one can also list among geometrical eddy detection using sea surface temperature. This approach was recently refreshed in artificial intelligence methods to provide automated detections (Moschos et al., 2023; Liu and Li, 2023). SST is considered as a quasi passive tracer, enabling to detect transport barriers and then consider an eddy through its geometrical definition.

Doglioli et al. (2007) wavelet method, Chaigneau et al. (2009) improved "winding-angle" method and Chelton et al. (2007) Okubo-Weiss method (with constant W_0 threshold) were compared in Souza et al. (2011). Okubo-Weiss and wavelet methods appeared to be less efficient in regions of high SLA variance, and Okubo-Weiss method underestimates eddy diameter. Geometric "winding-angle" approach appeared to be the most efficient in terms of computational cost. Nonetheless it still relies on some threshold choices.

Except some recent deep learning algorithms using only SST, most algorithms are based on SSH, whether they primarily have a geometrical, physical or hybrid use of the SSH, and they measure geostrophic speed based on SSH gradient. This eddy velocity associated with maximal SSH gradient is often considered as the characteristic speed V_{max}. However due to the Gaussian interpolation scheme in time and space to reconstruct altimetric maps (Le Traon et al., 1998), SSH gradients are somehow smoothed and hence geostrophic velocities and EKE underestimated. This effect is even more pronounced in the Mediterranean Sea due to the small deformation radius (Amores et al., 2018; Stegner et al., 2021). Additionally for intense eddies with

finite Rossby number, the geostrophic approximation becomes inaccurate. Centrifugal acceleration of the rotating eddy has to be taken into account to correct azimuthal geostrophic velocity V_g in a cyclo-geostrophic equilibrium velocity V_c (Penven et al., 2014):

$$V_c + \frac{V_c^2}{fR_{max}} = V_g \tag{1.10}$$

In the Mediterranean Sea, Ioannou et al. (2019) showed the cyclo-geostrophic correction to be as high as $0.5\,m.s^{-1}$ in specific areas, such as the Ierapetra eddy or Western Alborán gyre. Despite these uncertainties on the velocity field, from early Okubo-Weiss methods to hybrid algorithms, eddy detection algorithms proved over the past decade to be nonetheless relatively efficient to detect structures. To access information on eddy evolution, we then need to track eddies in time through successive detections.

Temporal tracking

Linking observations trough different time steps allows to reconstruct an eddy trajectory. It then enables to define a Lagrangian approach of an eddy, in a similar way to water parcel. But eddy tracking is a second challenge for eddy algorithms, the first studies addressing this issue relied on handmade attribution (Morrow et al., 2004; Hamad et al., 2006), which was then subjective. Various algorithms were proposed to resolve it. Isern-Fontanet et al. (2006) only had access to altimetric maps every $\Delta t = 10d$, and their tracking method only implied for each eddy to look for the next available observation closer than $c_{max}\Delta t$, with $c_{max} = 10km.d^{-1}$. They considered an eddy merged (or split) if two distinct eddies get closer (further away) than $20km$ at the next time step. Looking for the closest most likely next attribution in time was also the method used for more recent eddy atlases (Chelton et al., 2011b; Faghmous et al., 2015). Chelton et al. (2011b) however modify the method to take into account the westwards drift, looking for next observation in an elliptical region more elongated westwards.

Several tracking algorithm rely instead on a cost function minimization. Penven et al. (2005) proposed a cost function between two possible observations i and j of the same eddy at different time steps, based on distance (ΔX), vorticity ($\Delta\omega$) and radius (ΔR) changes:

$$X_{i,j} = \sqrt{\left(\frac{\Delta X}{X_0}\right)^2 + \left(\frac{\Delta R}{R_0}\right)^2 + \left(\frac{\Delta\omega}{\omega_0}\right)^2} \tag{1.11}$$

It however has to rely on some characteristic scales: X_0, ω_0 and R_0. In the Peru-Chile upwelling system, Penven et al. (2005) chose $X_0 = 100km$, $\omega_0 = 10^{-6}s^{-1}$ and $R_0 = 50km$, but these parameters have to be tuned for each studied regions, e.g. Souza et al. (2011) in the South Atlantic or Raj et al. (2016) in the Lofoten Basin. Chaigneau et al. (2008) tracking method is a modification from Eq.1.11 but considering a fourth term for EKE variation, with same scales as Penven et al. (2005) and choosing an EKE characteristic scale $EKE_0 = 100cm^2.s^{-2}$. At last Pegliasco et al. (2015) and Laxenaire et al. (2018) proposed a simpler method to track eddies by looking at overlapping areas from one time step to another. They also both analyzed merging and splitting events when more than one allocation at next time step was possible, determining the main track by a cost function.

Tracking efficiency strongly relies on detection efficiency. Souza et al. (2011) compared eddy detection algorithms but applied for all the same tracking method from Penven et al. (2005). It revealed that Okubo-Weiss and wavelet decomposition methods strongly underestimate eddy lifetime and drifting speed, because some detections are often missed, leading to fragmented tracks. This "missing eddy" problem, notably due to large error between satellite tracks, lead to various solutions: Mkhinini et al. (2014) and Chelton et al. (2011b) proposed to simply extend the research circle to look for the eddy next apparition. Le Vu et al. (2018) consider instead an additional term in the tracking cost function, allowing to lose an eddy for several days (see Sect.2.2). They also improved detection of merging and splitting events, defined as outcome of an eddy interaction. They defined such interaction as two distinct LNAM maxima sharing a closed SSH contour for several time steps.

Over the past decade, the improved performance in mesoscale eddy detection and tracking, together with the availability of daily AVISO SSH product, enables the development of global or regional eddy atlases. The pioneering eddy atlas was produced by Chelton et al. (2007), with improved method in Chelton et al.

(2011b). These atlases provided global statistics on eddy behavior, notably on the non-linearity criterion and westward drift(see Sect.1.2.4). Some eddy atlases are now available at the global scale on an operational basis, such as the META3 atlas based on Mason et al. (2014) Py-Eddy-Tracker algorithm (Pegliasco et al., 2022). Using the LNAM-based method from Le Vu et al. (2018), the DYNED Atlas provides similar eddy detections for the Mediterranean Sea, and is presented with more details in Sect.2.2. The development of these eddy atlases with centers, contours and trajectories paved the way to study eddy temporal evolution. However the correlation between eddy tracking in time, its evolution in a Lagrangian way, and other physical variables has been very little investigated so far.

1.3 Eddy composite versus Lagrangian tracking

The availability of reliable eddy detections allowed numerous possible collocation with other measurements, both in situ and remote-sensing. Most of the previous studies focused on a composite approach: numerous measurements are collocated with eddy detection and normalized by the radius, giving an average eddy signature. Hausmann and Czaja (2012) then estimated the average SST anomaly for cyclones and anticyclones in the Gulf Stream region, confirming that anticyclones (cyclones) are predominantly warm (cold) at the surface. Other physical properties were remotely measured at scale smaller or comparable to the mesoscale, such as chlorophyll from SeaWIFS, surface wind from QuickSCAT, or sea surface salinity (SSS) from SMOS or SMAP missions. Chelton et al. (2011a) and Gaube et al. (2014) looked at the average imprint of mesoscale eddies on chlorophyll. Using wind stress from QuickSCAT sensor, Gaube et al. (2015) produced an eddy Ekman pumping estimate. In another interesting study, Delcroix et al. (2019) tracked eddy-induced salinity anomalies in the Equatorial Pacific. Changes in eddy-induced SSS anomaly pattern, with the help of salinity vertical structure from collocated Argo floats, lead them to diagnose a salt transport mostly driven by horizontal advection in the Central Equatorial Pacific and by vertical advection in the Eastern Equatorial Pacific.

To study the eddy vertical structure, Chaigneau et al. (2011) adapted the composite method to collocate eddy detections with in situ data, and in particular Argo floats. Chaigneau et al. (2011) showed the average vertical anomalies of cyclones and anticyclones in the Peru-Chile upwelling system. They could then derived the vertical velocity profile from the thermal wind balance. Given that eddy velocity profile slows down at depth, they extended the non-linearity parameter at depth and were then able to measure the depth above which water can be trapped in the eddy core. With this method they could estimate the cross-shore heat and volume transport associated to individual eddies. Interestingly the main error source they discussed was the Argo float deviation while moving vertically (estimated to be smaller than 5km), but they did not estimate the uncertainty of the eddy contour position although acknowledging it might be larger. This method was extended to various regions of the world ocean, such as the Kuroshio extension (Sun et al., 2017), the Arabian Sea (de Marez et al., 2019) or the South China Sea (Zhang et al., 2016). A novelty in Sun et al. (2017) was to look at seasonal variability making seasonal composite, giving a first insight of the eddy seasonal cycle. It revealed an eddy-modulation of the mixed layer depth (MLD) cycle, anticyclones deepening the mixed layer, and cyclones making it shallower. This was confirmed in a global composite picture by Gaube et al. (2019), also proposing a scaling law as a function of the eddy SLA.

Interestingly, no regional study using the composite method was attempted at the scale of the Mediterranean Sea, likely because of the great variability of structure encountered in terms of dynamics and water-masses. Eddy studies in the Mediterranean Sea has been so far mostly a collection of specific local campaigns. An interesting comparison is the BOUM campaign in 2008, where 3 different anticyclones (an Algerian anticyclone, a Ionian anticyclone and a Cyprus eddy) were sampled and compared (Moutin and Prieur, 2012). Before the beginning of this thesis and already using the DYNED Atlas (see Sect.2.2), Stegner et al. (2019) provided a figure on the depth of Mediterranean anticyclones and cyclones, confirming that maximal density anomalies get deeper eastwards in the basin.

The drawback of the composite method lies in its temporal and spatial averaging. The spatial distribution of different mesoscale structures is reduced in a simple mean picture. Everett et al. (2012) produced a more statistical description of eddies in the Tasman Sea, revealing that the commonly accepted warm (cold) surface signature for anticyclone (cyclone) is not universal. Warm-core cyclones and cold-core anticyclones, referred to as "inverse" SST signatures in the literature gained lots of attention over the past four years. Trott et al. (2019); Sun et al. (2019) and Ni et al. (2021) revealed that they are very common features in various regions

of the world ocean. Sun et al. (2019) first showed that there is a seasonal cycle, inverse SST being always more predominant in summer. Several mechanisms were proposed to explain this variability and discussed in our study (see Sect.5 and Sect.6), from lateral exchanges (Itoh and Yasuda, 2010a; Sun et al., 2022), differential effect of heat and salinity fluxes (He et al., 2020), and eddy-induced Ekman pumping due to wind work interaction with surface currents - the so-called current feedback - (McGillicuddy, 2015; Ni et al., 2023).

Averaging in a composite also prevents to investigate any temporal evolution. Recently, some Lagrangian tracking methods were developed to fill this gap. The main idea is to follow an eddy over several time steps from its first to its last detection, to study its temporal evolution. In the context of Indian ocean leakage into the Atlantic, Laxenaire et al. (2019, 2020) developed a Lagrangian method to track heat and salt anomalies transported by Agulhas rings. With collocated Argo profiles, they also measured a seasonal evolution in the upper thermocline due to spring restratification and a westwards subduction of the anticyclonic density anomalies. In the Mediterranean Sea, some other studies attempted to adopt a similar viewpoint. In the Gulf of Lion, the LATEX program surveyed for 5 years the formation and fate of coastal eddies formed with wind curl interaction, combining ship surveys and remote-sensing tracking Petrenko et al. (2017). Pessini et al. (2018) studied Algerian eddies characteristics per bin (dividing the Algerian basin in 9 bins) as a function of their origin region. Lagrangian tracking is then a very promising tool to study eddy temporal evolution, but so far no investigation of the physical processes underlying this evolution was attempted.

1.4 Eddy interaction with atmosphere

Interactions between ocean mesoscale eddies and the atmosphere have been theorized and observed almost since the beginning of eddy observations. With a buoyancy anomaly and swirling velocity, eddies can interact both on heat and momentum fluxes but also through the wind stress curl.

Wind curl Eddy rotating structure submitted to uniform wind arises as a circular case of the Ekman transport phenomenon, the so-called "Ekman pumping". Stern (1965) already described how a rotating cyclone can experience surface downwelling due to positive surface current vorticity. Conversely an anticyclone should experience upwelling. In oceanic basins, the large wind stress curl at scales about 5×10^3km between mid-latitudes westerlies and tropical easterlies drives convergence and hence downwelling in the subtropical gyres (Stommel, 1948). Ekman pumping in mesoscale eddies was detailed in Gaube et al. (2015) and estimated in composite eddies using remote-sensing wind stress observations. They revealed the vertical velocity pattern to be either mono-polar or bipolar, depending on the relative strength of the wind speed compared to the eddy velocity. They also observed the additional pumping caused by flux divergence above eddies due to SST anomaly to be secondary.

Conversely if the wind stress curl happens to be at the ocean mesoscale, it can also force eddy generation. This mechanism was first proposed by Patzert (1969) as a formation mechanism for the eddies in the lee of Hawaii. Several occurrence of eddies formed by channeled orographic jets were observed in diverse regions, such as Southern California (Caldeira and Marchesiello, 2002), Western Mexican coast (McCreary et al., 1989), or in the lee of islands: Madeira (Caldeira et al., 2014) and Gran Canaria (Barton et al., 2000). The rough topography of the Mediterranean coast gives several examples of wind forced gyres in anticyclone-cyclone pairs. The most studied structures being the Ierapetra anticyclone (Horton et al., 1994; Ioannou et al., 2020a) and cyclonic Rhodes gyre, but also the Bonifacio anticyclone and the Southwestern Corsican cyclone (Moen, 1984; Ciuffardi et al., 2016). These wind-forced dipoles often develop a strong cyclone-anticyclone asymmetry with only the anticyclone remaining stable, as shown in both observation and model by Ioannou et al. (2020a) and Kersale et al. (2013).

Wind stress The eddy velocity field can also directly influence the wind stress drag, the eddy side opposing the wind experiencing higher wind stress than the other. Dewar and Flierl (1987) showed this differential effect to trigger a bipolar Ekman pumping (one of the Ekman pumping contributions studied by Gaube et al. (2015)), and also to lead to faster eddy decay. This current feedback (CFB) mechanism was shown to play a significant role in air-sea momentum exchanges, acting as an eddy killing mechanism by decreasing the EKE, but also reflecting part of the eddy energy to the atmosphere. The differential stress on the wind itself acts as producing a wind curl of opposite sign, then dampening the eddy by Ekman pumping described above

(Renault et al., 2016b). Even if they track eddies to measure their decay, Renault et al. (2016b) were still in a composite approach.

Thermal feedback The thermal feedback of eddy SST patterns on heat fluxes focused also numerous studies. Chelton et al. (2004) showed a strong correlation between wind divergence and curl and both crosswind and downwind SST in energetic eddying regions. In the Agulhas retroflexion region, O'Neill et al. (2005) also noticed this effect to be twice higher during winter. Frenger et al. (2013) completed the picture with eddy composite over the Southern ocean, showing enhanced surface winds, wind divergence, precipitations and rainfalls above anticyclones (respectively reduced above cyclones). Collocating remote-sensing turbulent heat flux measurements above eddies also showed significant impact of the mesoscale. In the Agulhas and Brazil-Malvinas Confluence regions, Villas Bôas et al. (2015) measured the eddies to account for up to 20% of heat flux variations. Cyclones (anticyclones) tend to increase turbulent heat flux above their core. However most of these studies focused on very energetic eddies with strong and marked signature on SST. They do not go into analyzed temporal variations, and rely on a static vision of cold-core cyclone (warm-core anticyclone).

Individual eddy evolution Few studies were done however on the influence of atmospheric forcing on the long-term temporal evolution of an individual mesoscale eddy. Among numerical studies, Renault et al. (2016b) studied current feedback tracking individual structures. They show that eddy decay faster, but did not detailed the variability for different structures. A more detailed study can be found in Braby et al. (2020), where the impact on current feedback is investigated between altimetry and numerical simulation in the Agulhas region. This comparison is performed not only on Eulerian variables, such as EKE or Mean Kinetic Energy (MKE), but also on eddies Lagrangian variables: eddy life time, radius, SSH amplitude and maximal speed, retrieved through Halo et al. (2014) algorithm. However while adding current feedback in the model, they did not notice a significant reduction of the model deviation to observed eddies, except for anticyclones amplitude and maximal speed. For wind curl impact, Ioannou et al. (2020b) studied the generation process of the specific Ierapetra anticyclone in a 3D model over several years to assess the bottom and coastal dissipation effect.

Some examples of mesoscale individual evolution can also be found from in situ observation studies. An important study by Meunier et al. (2018) showed the vertical structure of the Loop current eddy to evolve at 4 months intervals between two gliders transects because of diapycnal transformation driven by heat and freshwater fluxes. Studying the Lofoten Basin eddy, Bosse et al. (2019) suggested an anticyclonic subsurface anomaly being maintained through successive merging from smaller anticyclones detached from the coast. But merging processes is likely eased by winter cooling reducing the stratification barrier. Such mechanism was a numerically proven by de Marez et al. (2021) for another long-lived subsurface anticyclone, the Rockwall Trough eddy.

Despite numerous studies documenting air-sea fluxes interacting with mesoscale, very few studies assessed the impacts of these interactions on mesoscale evolution. Eddies are then mostly understood as a heterogeneous field forcing the atmosphere rather than truly having coupled interactions, even though seasonal variability at mesoscale is attested in both surface (Sun et al., 2019) and subsurface (Sun et al., 2017; Gaube et al., 2019). As shown by glider surveys (Meunier et al., 2018; Bosse et al., 2019), an observational challenge is to maintain in situ measurement at depth for several months while following the mesoscale structure, which is then not possible with a usual mooring. The Mediterranean Sea then appears as a promising case study for mesoscale eddy evolution because of the extensive data coverage and various eddying structures well described by the literature.

1.5 The Mediterranean Sea and its eddy climatology

With important maritime traffic, numerous coastal countries and important economic activities, the Mediterranean Sea has always been an important case study for oceanography. It is then not surprising that it offers a very dense in situ data coverage allowing to study mesoscale in details. We aim to describe in the present section a brief vision of the Mediterranean Sea general circulation, its atmospheric forcing and eddy climatology. The oceanographic surveys in the 60's already shaped the circulation of the Mediterranean Sea as being overall anti-estuarine (Ovchinnikov, 1966) and greatly shaped by the rough topography of the Mediterranean

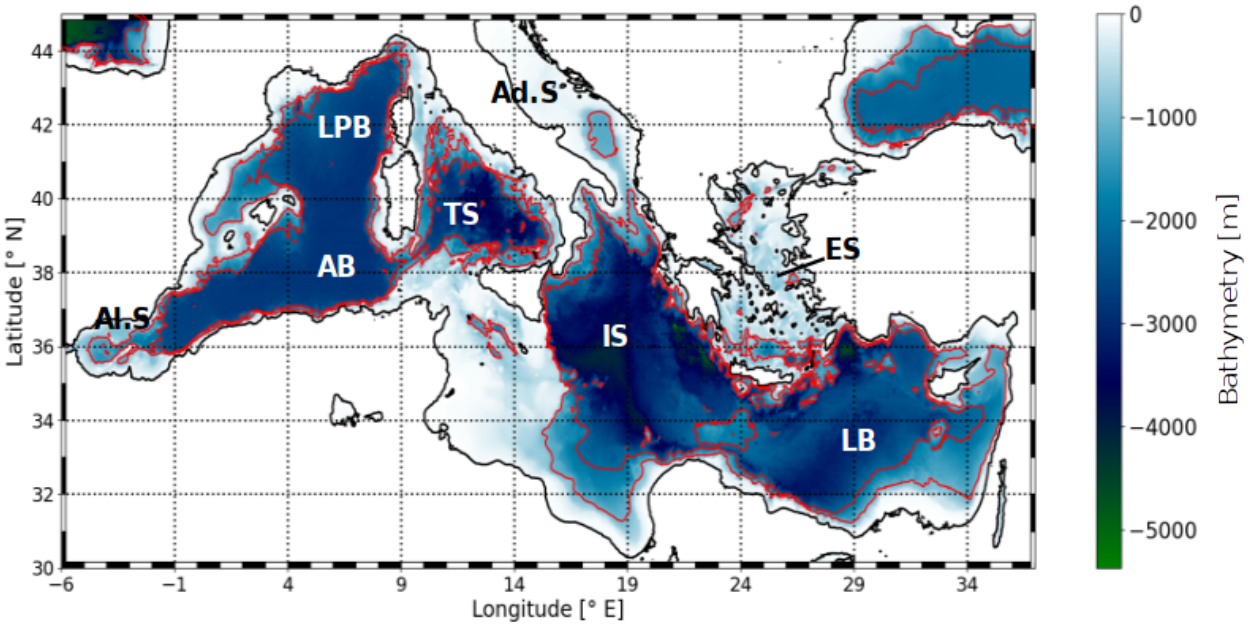

Figure 1.3: Bathymetric map of the Mediterranean Sea, data from ETOPO1 (Smith and Sandwell, 1997). 0m isobath is black line, 500 and 1000m isobaths in red lines. Al.S refers to Alborán Sea, AB: Algerian Basin, LPB: Liguro-Provencal Basin, TS; Tyrrhenian Sea, Ad.S: Adriatic Sea, IS: Ionian Sea, ES: Aegean Sea, LB: Levantine Basin.

Basin, shown in Fig.1.3.

The classical divide is the Western Basin from Gibraltar to the Straits of Sicily and Messina and eastwards the Eastern Basin. The eastern part is further divided in the Ionian Sea from Sicily to Crete and the Levantine Basin from Crete to the Levantine coast. The main regional circulation is an entrance of Atlantic surface waters through the Gibraltar strait, following the Southern coast in the Algerian current. This flow is partly deflected in the Tyrrhenian Sea in the Northern Ligurian current, shaping the border of the cyclonic gyres in the Gulf of Lion and Ligurian sea. Due to the influence of Mistral wind blows (Schott et al., 1988) and the preconditioning of cyclonic activity (Grignon et al., 2010), deep convection regularly occurs in this gyre. Part of the Atlantic waters flow continues in the Eastern Basin following the Southern Mediterranean coast in the Libyo-Egyptian current progressively transformed into saltier and denser waters. It reaches the Rhodes cyclonic gyre south of Rhodes island, where it convects in winter at depth to form the salty Levantine intermediate waters (LIW), the LIW flowing westwards following the Northern coast. Watermasses transformed in the Mediterranean sea eventually flow out at the Gibraltar Strait below 200m and spread in the Atlantic Ocean at mid-depth. This surface circulation, established at the beginning of the 2000's thanks to SST measurement (Millot and Taupier-Letage, 2005), is also clearly visible in the MDT map shown in Fig.1.4. The lighter Atlantic waters flow signs in an enhanced MDT vein along the Southern coast, the cyclonic Rhodes gyre and Ligurian Sea being the areas at lowest MDT.

The atmospheric forcing in the Mediterranean Sea is specific, first for the freshwater fluxes because it is an evaporation basin with very marked seasonal cycle (Peixoto et al., 1982). Precipitation has seasonal variation about $0.7\,m.y^{-1}$ and an annual mean about 0.33 to 0.47 $m.y^{-1}$ following Pettenuzzo et al. (2010) (ERA40 data from 1958 to 2001). Evaporation has similar or even larger seasonal amplitude anti-correlated in time, with annual average about $-1.0\,m.y^{-1}$. Total freshwater flux is the addition of evaporation, precipitation and river contributions. River discharge being significantly weaker (about $0.1m.y^{-1}$ see details in Jordà et al. (2017)), consequently the total net freshwater fluxes is always negative for the Mediterranean Sea: about $-0.5\,m.y^{-1}$ (Mariotti et al., 2002) to $-0.9 \pm 0.2\,m.y^{-1}$ from 2005 to 2010 in Jordà et al. (2017). Freshwater fluxes retrieved from ARPEGE operational weather forecast model (Courtier et al., 1991) are shown in Fig.1.5a for the spatial distribution (2012-2019 average) and in Fig.1.6a for the temporal variability (spatial average). A consequence of this negative freshwater budget is the overall heat loss by evaporation, compensated by a net influx at Gibraltar Strait. Mediterranean annually averaged total heat flux shows a

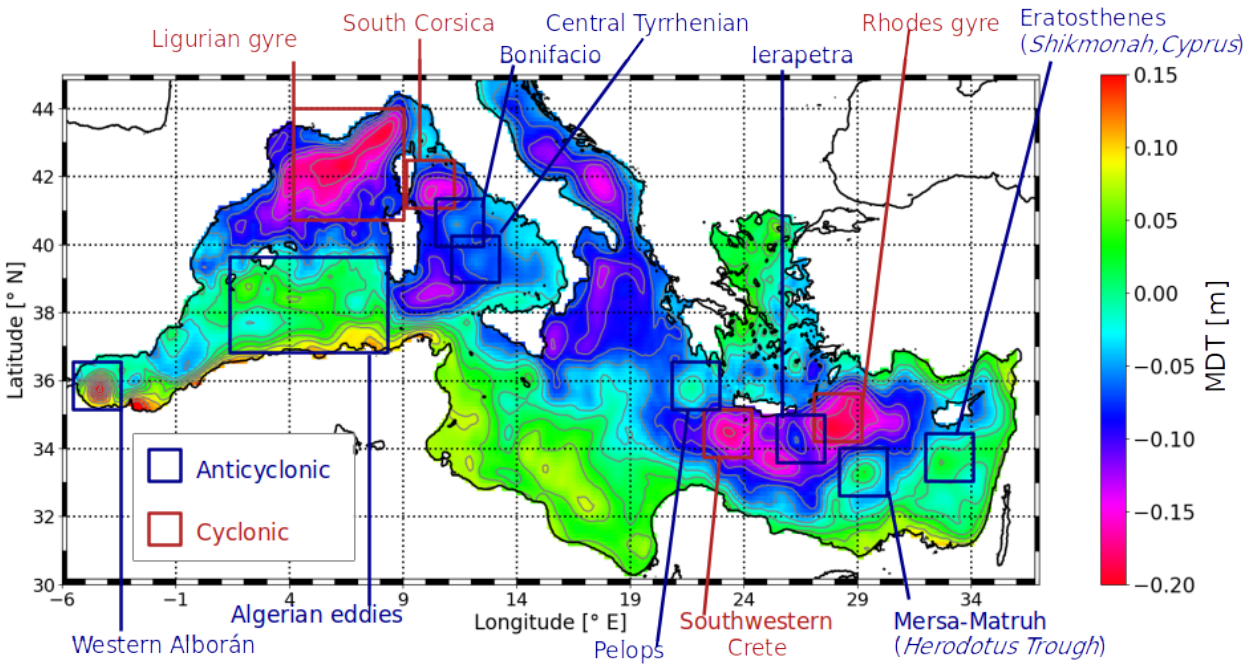

Figure 1.4: Mean dynamic topography (MDT) from 2000 to 2018, gray lines are 2cm isolines. Insets remind main cyclonic (red) and anticyclonic (blue) structures identified in the literature. Alternative names are put in parentheses when necessary.

net loss, ranging between $-7\,W.m^{-2}$ (Pettenuzzo et al., 2010) to $-3 \pm 8\,W.m^{-2}$ (Jordà et al., 2017). Secondly the wind forcing is also specific because of its marked temporal and spatial variability. The rough topography of the Mediterranean coastline shapes strong wind speed gradients and curl, with blocking island effect (Kotroni et al., 2001) (see wind speed in Fig.1.5c). This results in the creation of several wind-forced anticyclone-cyclone pairs (introduced earlier in Sect. 1.4). Temporal variability is also marked and wind blows are noticeably powerful even in summer, in particular in the Eastern Basin due to Etesian winds (Kotroni et al., 2001) (see wind speed time series in Fig.1.6c).

In the Mediterranean Sea we have to wait until the beginning of the 80's to have eddy surveys similar to the MODE experiment in the Atlantic Ocean, such as the Marine Climate experiment (1979-1985) and Physical Oceanography of the Eastern Mediterranean (POEM, 1985-1989) studies in the Eastern Basin (Robinson et al., 1991). These Mediterranean campaigns were at first mostly focused on the regional circulation, on surface and intermediate waters pathways. Most of the early eddy literature focused on recurrent cruises, often understanding eddies as standing meanders (Robinson et al., 1987, 1991). The persistence and recurrence of several anticyclones in the Eastern Basin enabled some studies to look at their temporal variability tracking eddies (mostly anticyclones) as warm spots in SST (Matteoda and Glenn, 1996; Hamad et al., 2006). Later with altimetry other numerous studies adopted an Eulerian point of view (Iudicone et al., 1998; Ayoub et al., 1998; Larnicol et al., 2002; Pujol and Larnicol, 2005; Amitai et al., 2010), or temporal average of surface drifters trajectories (Poulain and Zambianchi, 2007; Menna et al., 2012). A challenge in the Mediterranean Sea is a small Rossby deformation radius from 8 to 15 km (see Sect.1.2.1 and Fig.1.2 above) compared to other open ocean basins (Chelton et al., 1998). Consequently the β-drift is very weak and virtually all eddies satisfy the non-linearity criterion (see Sect.1.2.4, Mkhinini et al. (2014)). Some eddy displacement intensification near the coast reaching $1 - 3\,km.d^{-1}$ can be observed due to mirror effect (Sutyrin et al., 2009). Altimetry map has been available at 1/8 °resolution for about two decades (Pujol and Larnicol, 2005), but the small deformation radius makes eddy detection from altimetry still challenging (Stegner et al., 2021), involving less reliable cyclonic detections. Several studies were nonetheless dedicated to eddy detection and tracking in the Mediterranean Sea, among the pioneering studies from Isern-Fontanet et al. (2003, 2006), Mkhinini et al. (2014) or Le Vu et al. (2018).

This extensive oceanographic literature already described well mesoscale structures across the basin. In the Western basin, the most notable eddies are instability detachments of the Algerian current forming Alge-

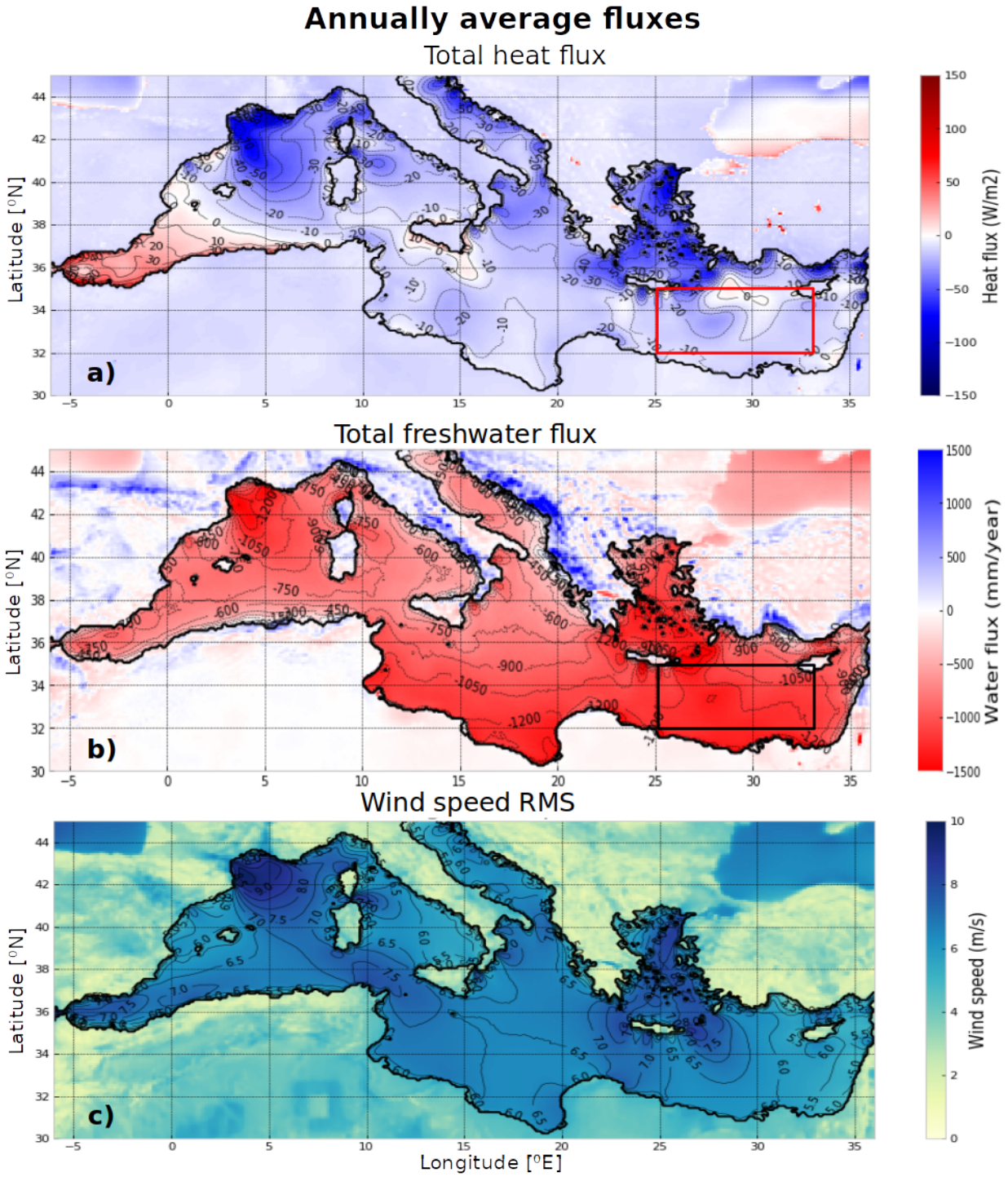

Figure 1.5: 2012-2019 average (a) net heat flux, (b) freshwater flux, and (c) wind speed (root mean square) over the Mediterranean Sea from ARPEGE weather forecast operational output. The rectangle in the Levantine Basin indicates the area where regional time series in Fig.1.6 is extracted.

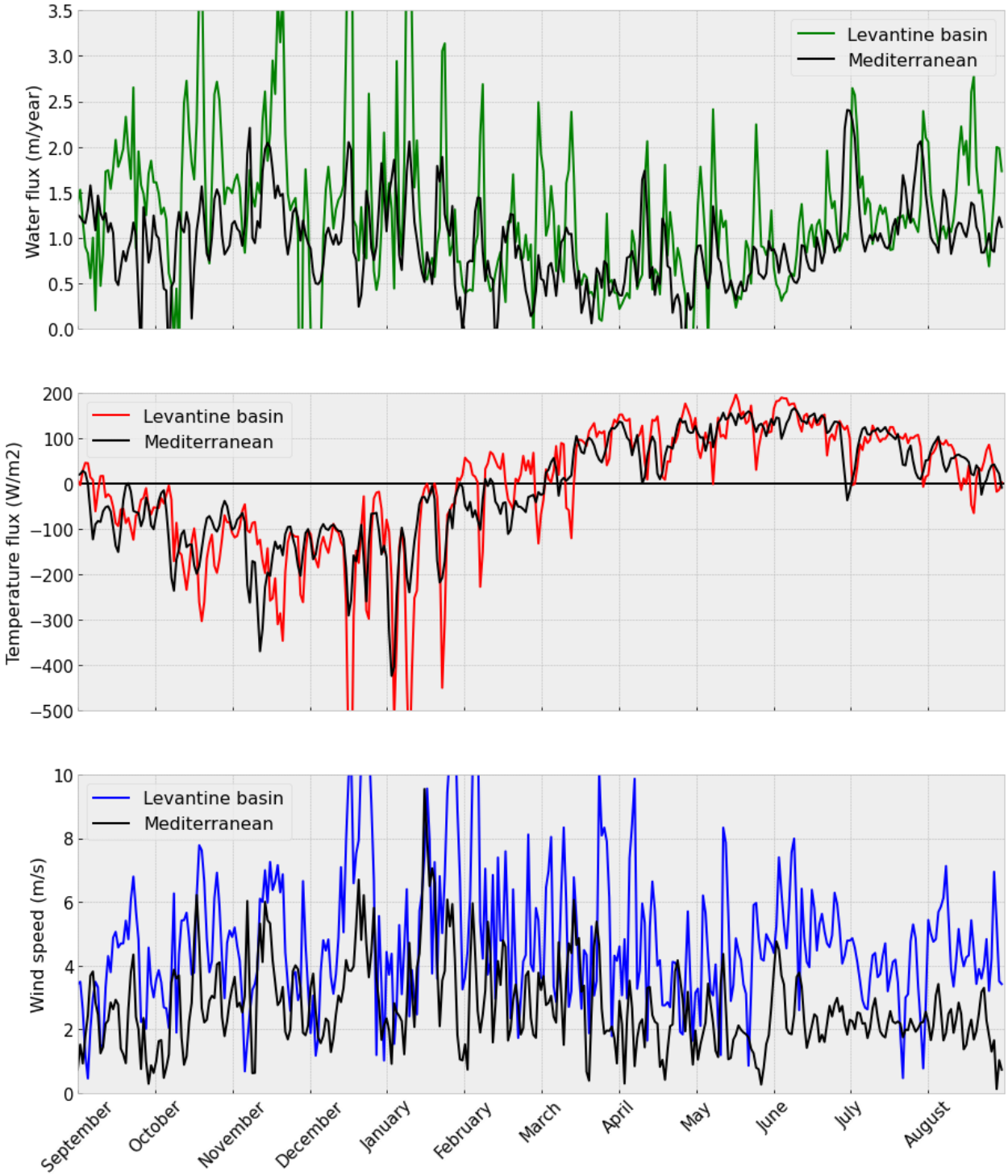

Figure 1.6: (a) Freshwater, (b) heat fluxes and (c) wind speed (root mean square) daily average over the Mediterranean Sea from ARPEGE weather forecast operational output from September 2015 to September 2016. Colored lines are averages over the Levantine Basin (rectangle in Fig.1.5).

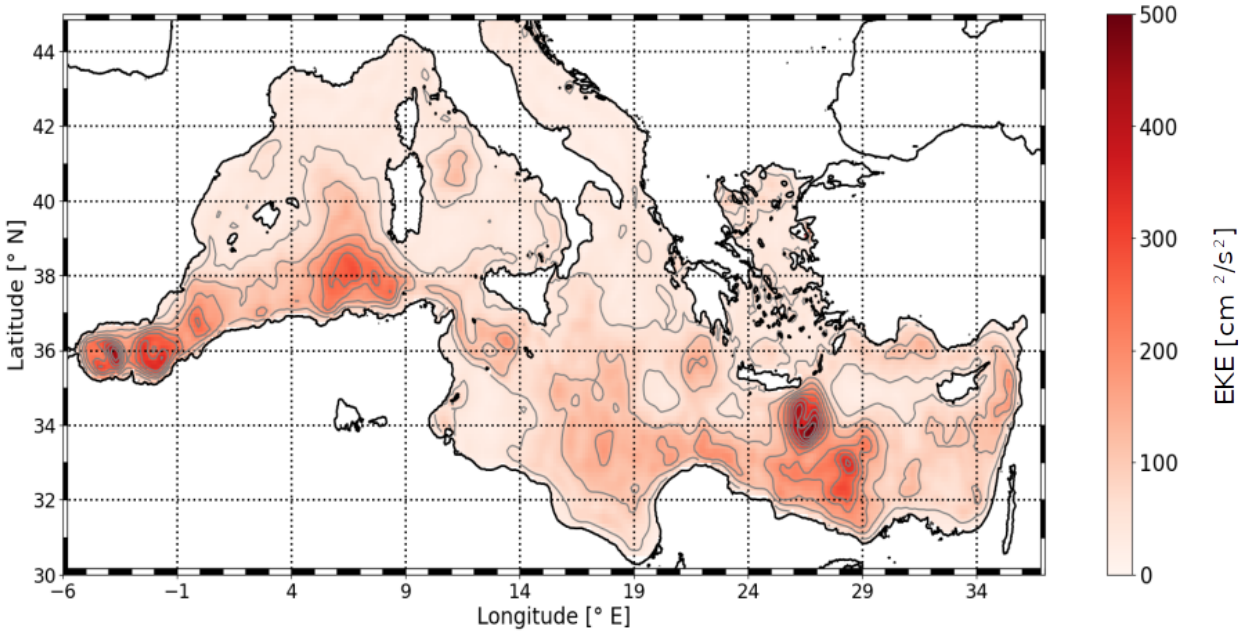

Figure 1.7: Eddy kinetic energy (EKE) from 2000 to 2015 using altimetry in geostrophic approximation, gray lines are $50cm^2.s^{-2}$ isolines.

rian anticyclones, drifting northwards up to the Balearic front - southern limit of the Ligurian gyre - and then westwards (Puillat et al., 2002). In the Eastern Basin recurrent anticyclonic structures Northwest of the Nile delta - *Mersa-Matruh* anticyclone - and South of Cyprus island - *Eratosthenes* anticyclone - (Robinson et al., 1991; Malanotte-Rizzoli et al., 1997). These structures were identified as areas of anticyclones accumulation in the Levantine Basin for numerous eddies are formed as instabilities of the coastal current (Hamad et al., 2006). The rough topography of the Mediterranean coasts can create strong wind stress curls and hence anticyclone-cyclone dipoles (see Sect. 1.4). Several Mediterranean eddies are formed through this process. In the Gulf of Lion this mechanism and the evolution of the anticyclone formed on the shelf was reviewed by Petrenko et al. (2017). In the Tyrrhenian Sea one can list the Bonifacio anticyclone and South Corsican gyre (Philippe and Harang, 1982; Moen, 1984; Artale et al., 1994). In the Eastern Basin, at the outcome of Antikythera strait there are the Pelops anticyclone and Southwestern Cretean gyre (Horton et al., 1994; Matteoda and Glenn, 1996). At the outcome of the Kasos strait there is the recurrent Ierapetra eddy, very powerful structure formed each year at the end of summer, with its cyclonic counter-part the Rhodes gyre (Theocharis et al., 1993). Bonifacio, Algerian, Pelops, Ierapetra and Mersa-Matruh anticyclones all sign in EKE as regions of active eddying field (Fig.1.7), but they also produce a mean signal on the mean dynamic topography. Main structures identified in the literature are reported on the MDT map in Fig.1.4. In the central Ionian Sea and Levantine Basin, a turbulent jet also flows eastwards in surface due to the velocity contribution of numerous eddies, called the Middle-Mediterranean Jet (MMJ) which existence is debated (Millot and Taupier-Letage, 2005; Millot and Gerin, 2010). Not clearly visible in SSH or SST instantaneous view, it was ultimately identified through SLA propagation by Amitai et al. (2010). Several sub-basins are distinct: the Adriatic Sea, separated by the Otrante strait, and the Aegean Sea, separated by the Kos and Antikythera straits. These sub-basins host a dynamical mesoscale activity, but mostly shaped by topography, notably the large cyclonic gyre in the South Adriatic pit. Evidence of atmospheric interactions are numerous, but uncertainty with altimetric product and too strong topographic control make these structures out of the scope of our study. Some last powerful anticyclonic structures to list are the Alborán eddies just East of Gibraltar Strait, also contributing to higher EKE. But they are mostly under direct control of the Atlantic waters inflow (Vazquez-Cuervo et al., 1996) and are then very particular cases out of the scope of our study.

In the present introduction, we detailed how a compromise between hydrological and geometrical definitions of an eddy can be met considering non-linear mesoscale structures signing in SSH (in the sense of Eq.1.8). This would result in approximations for water transport trapped in eddy core (Beron-Vera et al., 2013) and close to the equatorial band (Chelton et al., 2011b), but we will consider it as accurate for our study. This definition is also extremely practical and easy to adapt to automatically detect and track eddies through

remote-sensing altimetry. As detailed above, numerous studies documented a mesoscale eddy influence on air-sea interactions in both individual cases and at global scale (Chelton et al., 2011a; Frenger et al., 2013). Composite studies were important to shape a first picture of eddies, but studies from Sun et al. (2017) for the mixed layer depth and Sun et al. (2019) for the eddy-induced SST signatures revealed both the contributions and limits of this method. They indeed clearly showed that mesoscale eddies experience variability at the seasonal scale or shorter. Despite numerous researches at global or regional scale considering eddy statistical description, very few studies tackle the subject of eddies evolution after their formation. Imprint of mesoscale eddies on ocean physical, biological and chemical properties but also fluxes was diagnosed, but always assuming a stationary eddy field and the retroaction on eddy themselves has not yet been addressed. Several studies from both remote-sensing and in situ measurements observed eddy variability in ocean-atmosphere interactions, in particular at the seasonal time scale. But only few studies in very specific in situ cases (the Loop Current eddy for Meunier et al. (2018), the Lofoten eddy for Bosse et al. (2019), an Agulhas ring for Laxenaire et al. (2019)) attempted to accurately describe mesoscale eddies individual evolution over the vertical and their interaction with atmosphere. No study of the surface and subsurface evolution of mesoscale structures submitted to atmosphere forcing was then attempted so far, and it will then be the focus of our study. The Mediterranean Sea is a small but eddy-rich basin, presenting an ocean-like circulation, with numerous and extensive oceanographic surveys. Various mesoscale structures are described in the literature throughout the Mediterranean Basin, which makes it an ideal site to study mesoscale evolution. In a first chapter we will present the DYNED Atlas, gathering eddy tracks in the Mediterranean Sea over 20 years and the collocation method with in situ data to accurately measure eddy-induced anomalies. In a second chapter we assess the seasonal variability of eddy-induced SST anomalies and briefly present a new driving mechanism through eddy-modulated vertical mixing. In a third chapter we describe in detail the evolution of mixed layer inside Mediterranean anticyclones compared to the outside-eddy background and assess the interaction between mixed layer depth anomaly and eddy vertical structure. In a fourth chapter we confirm the eddy-modulated vertical mixing hypothesis in numerical simulations. We additionally investigate the role of high frequency wind forcing and SST retroaction on air-sea fluxes in shaping eddy SST signatures. Last, in a fifth chapter we discuss the remaining mechanisms, in particular other proposed drivers for inverse eddy SST signatures.

Chapter 2

Eddy Lagrangian observation in surface and subsurface

2.1 AMEDA eddy observation from altimetry

Eddy detections are provided through the Angular Momentum Eddy Detection and Tracking Algorithm (AMEDA). AMEDA is a mixed velocity-altimetry approach, relying on using primarily streamlines from a velocity field and identifying possible eddy centers computed as maxima of local normalized angular momentum (Le Vu et al., 2018). It was successfully used in several regions of the world ocean in altimetric data (Aroucha et al., 2020; Ayouche et al., 2021; Barboni et al., 2021), high-frequency radar data (Liu et al., 2020) or numerical simulations (de Marez et al., 2021).

In each eddy single observation (one eddy observed one day), AMEDA detects a center and two contours. The "maximal speed" contour is the enclosed streamline with maximal speed V_{max}, i.e. in the geostrophic approximation, the contour of maximal SSH gradient. It is assumed to be the limit of the eddy core region where water parcels are trapped. The "end" contour is the outermost closed SSH contour surrounding the eddy center and the maximal speed contour; it is assumed to be the area of the eddy footprint, larger than just its core but still influenced by the eddy shear (Le Vu et al., 2018). Example of eddy detections in the Levantine Basin with both contours are shown with 2 days timestep in Fig.2.1, using SSH near-real-time (NRT) product (Pujol, 2021). These detections were used for the BHO *Beautemps-Beaupré* transect in spring 2021 surveying the Mersa-Matruh anticyclone (see Table 1 in Barboni et al. (2023a), MM6 event). The maximal speed radius R_{max} is defined as the radius of the circle having the same area A_{max} than the maximal speed contour:

$$R_{max} = \sqrt{\frac{A_{max}}{\pi}} \tag{2.1}$$

Eddy occurrence in the Mediterranean Sea is shown for anticyclones and cyclones in Fig.2.2. Eddy detections are performed using AMEDA applied on AVISO (Archiving, Validation and Interpretation of Satellite Oceanographic data) delayed-time ADT at 1/8 °from 2000 to 2019. Occurrence is computed as time percentage spend by each (1/8°x 1/8°) pixel inside the maximal speed radius of an eddy of the given polarity. The first important result is the striking location difference between anticyclonic and cyclonic occurrences in particular in the Eastern Basin. Eddy occurence hotspots are indeed observed for each polarity but clearly separate. Some well-known structures already described in the literature can be observed (see Sect.1.5): Algerian anticyclones offshore Algerian coast, Bonifacio and Central Tyrrhenian anticyclone in the Tyrrhenian Sea. In the Eastern Basin, the Pelops anticyclone has a marked signature south of the Peloponnese peninsula, Ierapetra anticyclone South-East of the Crete island, Mersa-Matruh anticyclone North-West of the Nile delta, Eratosthenes anticyclone (also called Cyprus or Shikmonah) South of Cyprus. Regions of intense cyclonic activity also coincide with known structures, such as the Ligurian and Adriatic seas, Cretean gyre South-West of Crete and Rhodes gyre East of Rhodes island. At the global scale, heterogeneous eddy repartition was recently also highlighted in the global META3.1 Atlas (Pegliasco et al., 2022), with very different probability of occurrence in coastal areas.

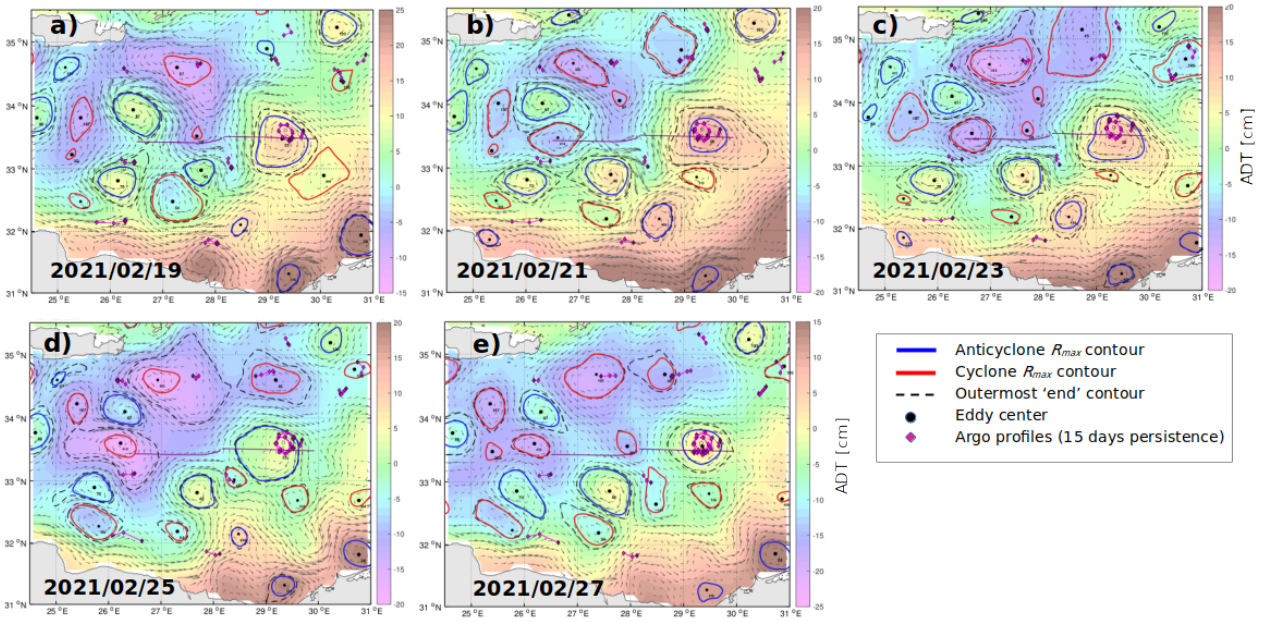

Figure 2.1: AMEDA eddy detections using AVISO NRT product at day+6 during the BHO *Beautemps-Beaupré* transect (purple thin line), with maximal speed (continuous line) and SSH end contours (dashed line). This survey aimed to sample the Mersa-Matruh anticyclone ($\sim 33°30'N; 29°30'E$). Argo floats are in pink diamonds with past positions over 15 days. Courtesy of Briac Le Vu (LMD/Amphitrite).

The other noticeable feature is the difference between this eddy occurrence map, which can be considered as an average Lagrangian vision, and the average Eulerian vision represented in the mean EKE (see Fig.1.7). An interesting example is the Ierapetra anticyclone with Rossby number reaching 0.25 (Ioannou et al., 2017), giving a marked signature in both mean EKE and MDT as introduced earlier. It is however not significantly present in eddy occurrence time, reaching maximum 30% in a small hotspot. Neighboring Mersa-Matruh and Eratosthenes anticyclones have a larger footprint (actually reaching 50% of the time, but colorbar was reduced to spot other structures). Even smaller anticyclones of the Tyrrhenian Sea have a more marked occurrence, which is consistent with observations from repeated XBT transects (Ciuffardi et al., 2016). The Ierapetra anticyclone is indeed a very strong structure at it is formation site but often drifts away and slowly decays to less significant Rossby number (about 0.1). It sometimes stays at the same location and can be re-intensified by Etesians winds the next summer (Ioannou et al., 2017). Amitai et al. (2010) also showed in an Eulerian view that the Ierapetra eddy was clearly the first mode of variability in the Levantine Basin, despite Mersa-Matruh and Eratosthenes anticyclones being significant on average. This particular example shows that EKE might not be the most appropriate metric, as it focuses on the most variable and intense structure.

2.2 Tracking eddies in the Mediterranean Sea: the DYNED Atlas

To study eddy temporal evolution, we then need to accurately link eddy observations in time, gathering them in eddy tracks. AMEDA tracking is similar to Penven et al. (2005) method (Eq.1.11): a cost function ϵ between 2 observations i and j minimize change in position d_{ij}, size δR_m and strength δRo. Compared to previous studies with similar approaches, a fourth term is added to take into account the possibility to miss a detection at each successive time step. Due to altimetric tracks scarcity in the Mediterranean Sea compared to the deformation radius (Amores et al., 2018), an eddy can indeed be temporarily lost for several days dt_{ij}, $T_c = 10$ days at most. T_c defines the eddy correlation time, and distance changes are then reported to distance at maximal correlation time $D_{ij}(T_c)$ (Eq.12 from Le Vu et al. (2018)):

$$\epsilon_{ij} = \sqrt{\left(\frac{d_{ij}}{D_{ij}(T_c)}\right)^2 + \left(\frac{\delta R_m}{R_{m,i} + R_{m,j}}\right)^2 + \left(\frac{\delta Ro}{Ro_i + Ro_j}\right)^2 + \left(\frac{dt_{ij}}{2T_c}\right)^2} \tag{2.2}$$

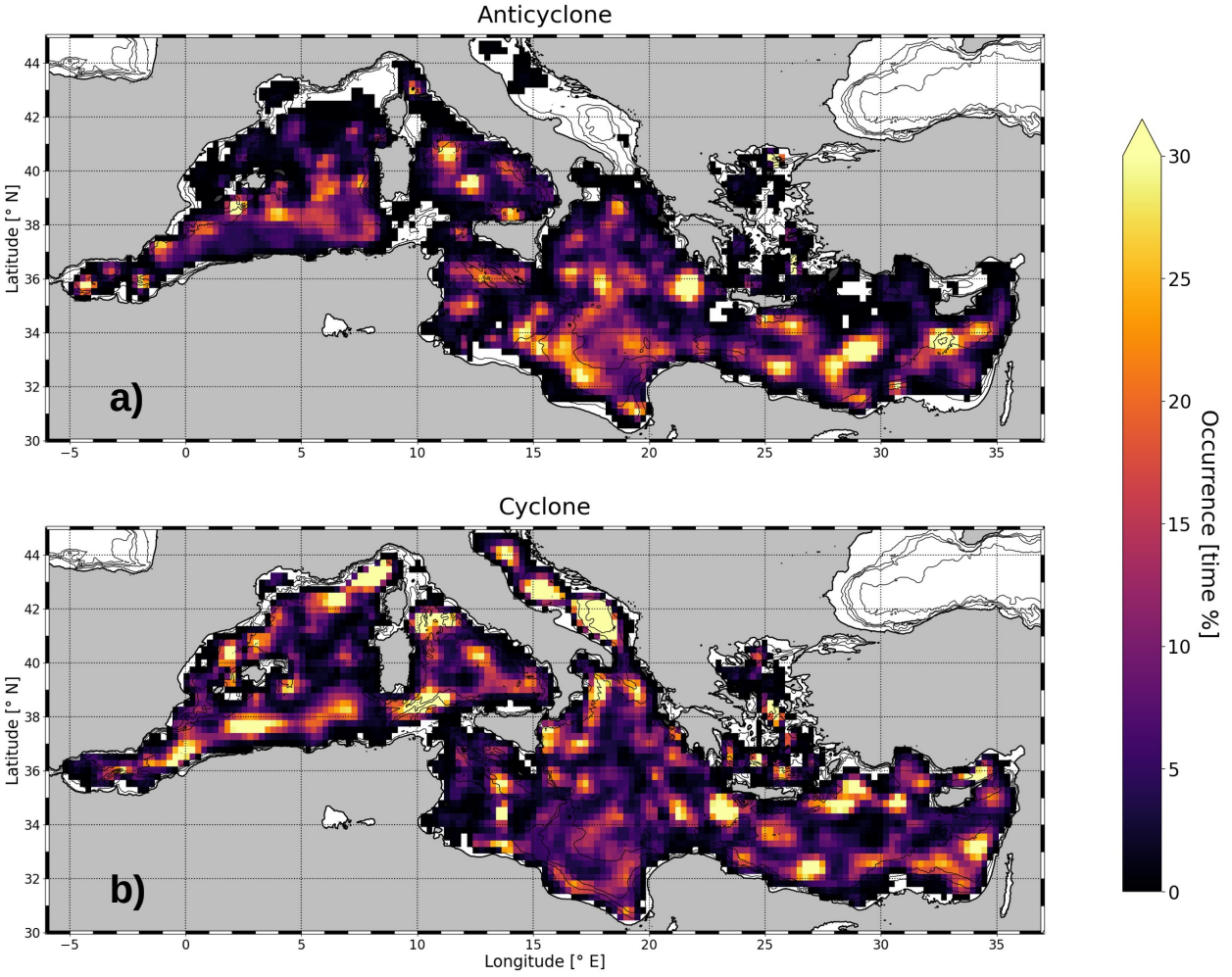

Figure 2.2: Time occurrence of (a) anticyclonic and (b) cyclonic eddies, defined as the time percentage spent inside an eddy maximal speed radius observation. Eddies observations are AMEDA output applied on AVISO delayed-time 1/8 °SSH from 2000 to 2019.

In practice, an eddy next observation can then be looked for up to 10 days ahead. Eddy tracks shorter than two orbital periods are also discarded as they are not considered as reliable detections. Last, a key AMEDA feature is to detect eddy merging and splitting events as output of eddy interactions, detected as a time period when two eddies of the same polarity share a closed velocity contour (Le Vu et al., 2018). Fig.2.3 shows as example the temporal evolution of a Pelops anticyclone formed in autumn 2013 and drifting across the Ionian Sea. Multiple splitting events were recorded (Fig.2.3a), with smaller detached anticyclone drifting away from the main tracked structure (Fig.2.3c).

The eddy tracks collection in the whole Mediterranean Sea constitutes the DYNED Atlas database (Stegner et al., 2020), and is available online for the years 2000 to 2019 at: `https://www1.lmd.polytechnique.fr/dyned/`. From 2000 to 2019, AMEDA is applied on AVISO SSH delayed-time product at a resolution of 1/8°with daily output. To allow comparison with most recent oceanographic surveys in the Levantine Basin (see Table 1 in Barboni et al. (2023a)), the DYNED Atlas is extended in 2020 and 2021, using AVISO near-real-time SSH (Pujol, 2021) at the same spatial and temporal resolution, using day+6 product (delivered 6 days after observation date). From 2000 to 2021, a total of 7038 (respectively 8890) anticyclonic (cyclonic) eddy tracks were retrieved. The asymmetry in eddy numbers is driven by a lifetime difference, anticyclones living noticeably longer in the Mediterranean. Figure 2.4 shows the difference in cumulative lifetime for eddies between 2000 and 2018, i.e. the fraction of eddy tracked living more than a given time, on a logarithmic scale. Anticyclones live significantly longer: 105 anticyclones (out of 5770) compared with 70 cyclones (out of 7159) are found to live longer than 400 days. In the Levantine Basin the asymmetry is even more marked: 39 anticyclones (out of 1210) compared with 17 cyclones (out of 1630) live longer than 400 days. Long-lived anticyclones are common in this area, the 0.5% living longer than 3 years (1095 days) actually represents 18 tracks. This asymmetry is expected for theoretical reasons, cyclones being less stable when greater than the deformation radius and more subject to external shear (Arai and Yamagata, 1994; Graves et al., 2006). Despite the higher resolution of the 1/8 °SSH product ($\sim 12km$), it is still on the order of average Mediterranean deformation radius (Fig.1.2), not allowing to accurately detect eddies below 20 to 30km radius (Amores et al., 2018). Anticyclone-cyclone size asymmetry leads to an observational bias, and observing simulation system experiments confirmed that small eddy detections below 20 km are not reliable, hence anticyclonic detections are more reliable (Stegner et al., 2021). It is then difficult to distinguish whether cyclone tracks are shorter because they have indeed shorter lifetime or whether their detections are less reliable. Considering the results from Stegner et al. (2021), we will assume that anticyclone detections and tracks are correct, but will assume some uncertainty for in situ data collocation.

2.3 In situ vertical profiles collocation with eddies

A climatological database is created collecting in-situ vertical profiles from the Coriolis Reanalysis (CORA) dataset. CORA delayed-time (DT) (Szekely et al., 2019) profiles are recovered from 2000 to 2019, and Copernicus near-real-time (NRT) (Copernicus, 2021) profiles are recovered from 2020 to 2021, using the **history** release. Over the 2000-2019 period, some profiles were available only in NRT mode, and were kept after careful check. In both DT and NRT dataset we gathered in situ data coming from XBT, CTD, glider and profiling floats, which means selecting files with respective data codes **XB, CT, GL, PF**. A first selection was done collecting only profiles reaching 400m deep, having a first valid value above 50m and more than 40 measurements in-between. When available, "ADJUSTED" properties are collected, and successive quality checks are processed, described in Appendix A of Barboni et al. (2023a). Density is computed on temperature and salinity profiles using the Thermodynamic Equation of Seawater 2010 (McDougall et al., 2009) implemented in the `gsw` Python package `https://teos-10.github.io/GSW-Python/` (Delahoyde and Hyland, 2017).

Figure 2.5a shows the profiles spatial distribution. Oversampling of some areas is obvious, such as the Gulf of Lion, offshore Crete and south of Cyprus, whereas some other areas are very poorly sampled, in particular the southern part of the Ionian Sea. This heterogeneous sampling of the Mediterranean Sea was already discussed in previous in-situ studies (d'Ortenzio et al., 2005b; Houpert et al., 2015). Figure 2.5b is the histogram of available data from 2000 to 2022, distinguishing profiles coming from DT and NRT datasets. Measurement frequency considerably increased after 2010 due to more frequent floats deployments of the Argo program, whereas most of the data prior to 2010 are XBT transects and sparse glider missions.

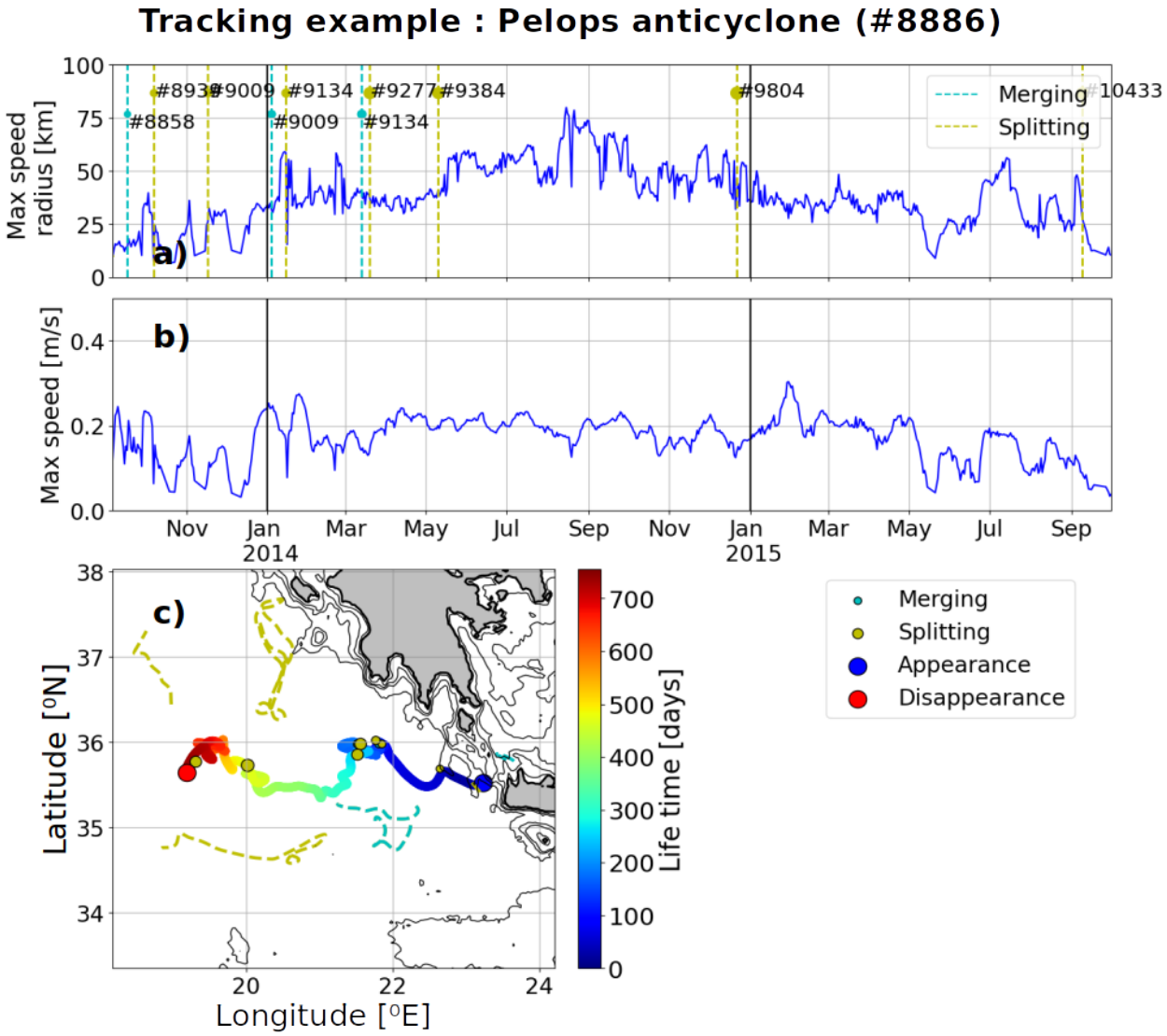

Figure 2.3: Example of AMEDA tracking for the Pelops anticyclone formed in autumn 2013. (a) Radius R_{max} time series, with splitting (yellow dots) and merging events (cyan dots), numbers refer to DYNED Atlas tracks numbers. (b) Maximal speed V_{max} time series. (c) Map of the Ionian Sea with the anticyclone trajectory, with split (respectively merged) eddy trajectories in yellow (cyan) dashed line. Thin black lines are 100, 500, 1000 and 2000m isobaths from ETOPO1 bathymetry (Smith and Sandwell, 1997).

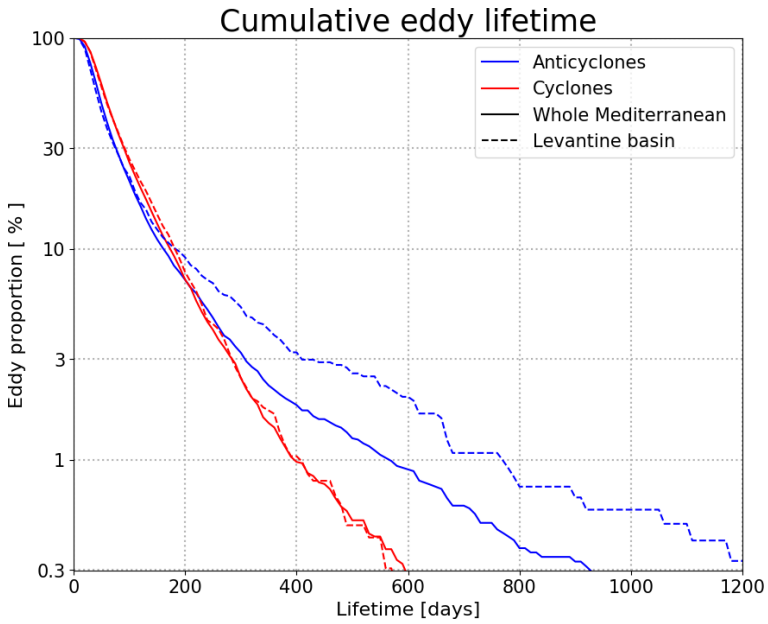

Figure 2.4: Cumulative eddy lifetime as a percentage on a logarithmic scale, separated for cyclones and anticyclones and for the Levantine Basin and the whole Mediterranean Sea.

To study eddy vertical evolution, profiles have to be collocated with eddy detections. However, eddy contours provided by AMEDA suffer errors and variations in time due to SSH product inaccuracy. As shown in Fig.2.1, the Mersa-Matruh anticyclone sampled with two Argo floats ($\sim 33°30'N; 29°30'E$) has great contour distortions and changes size over few days. On the opposite, Argo floats Lagrangian trajectories consistently loop inside the structure with negligible radial distortion over 2 weeks. Note that for this particular survey, floats were ARVOR floats programmed to sample at a rate of 1 profile per day, and with parking depth at 300m to stay trapped inside the anticyclone velocity core.

To compensate those eddy contours inaccuracies, an eddy tag is defined. The position of a cast profile is compared to eddy observation at ± 2 days. If persistence shows that the profile stays inside the maximal speed contour of an eddy at ± 2 days, it is labeled as "inside-eddy". On the other hand a profile is labeled as "outside-eddy" only if it stays outside any SSH end contour at ± 2 days. Consequently, profiles not meeting these criteria, i.e. changing from inside an eddy to outside, are labeled as "ambiguous". From 2000 to 2021, out of 157 053 profiles retrieved in the Mediterranean Sea, 104 787 are labeled outside-eddy (tag 0), 7939 are inside anticyclones (tag -2), 14 919 are inside cyclones (tag +2) and the remaining 29 410 one are labeled as ambiguous (tag ± 1). Illustration of the collocation method is given in Fig.2 in Barboni et al. (2023a). As shown in Fig.2.5a, in situ sampling is very heterogeneous. The cyclonic gyre in the Gulf of Lion was frequently surveyed with gliders (Coppola et al., 2019), while the southern side of the Mediterranean Sea (Southern Ionian Sea and the Algerian coast) was poorly sampled. Despite cyclones having twice less eddy observations in the DYNED Atlas, this leads to twice more profiles collocated inside cyclones than inside anticyclone.

A collocation example is shown in Fig.2.6 for a Biogeochemistry (BGC) Argo float in the Ionian Sea. This figure is a courtesy from Vincent Taillandier (LOV), as part of prospective study on Pelops anticyclones influence on Levantine Intermediate waters in the PROTEION project. The eddy tag (Fig.2.6b and 2.6d) temporal evolution shows this profiling float being detected several time inside both anticyclonic (blue) and cyclonic (red) structures. Comparison with vertical profile time series reveals that almost all isopycnals thickening and deepening events (Fig.2.6e) coincide with anticyclonic collocation (August 2015, September 2016, July 2017, January and April 2018). Conversely almost all isopycnal shoaling events are detected inside cyclones (March 2016, December 2016 to March 2017 and February 2018). The only unexplained event is the 29.1 $kg.m^{-3}$ isopycnal reaching 600m in March 2017. The collocation method presented above then showed to be quite robust to identify eddy signature on the vertical structure, even for a single Argo float.

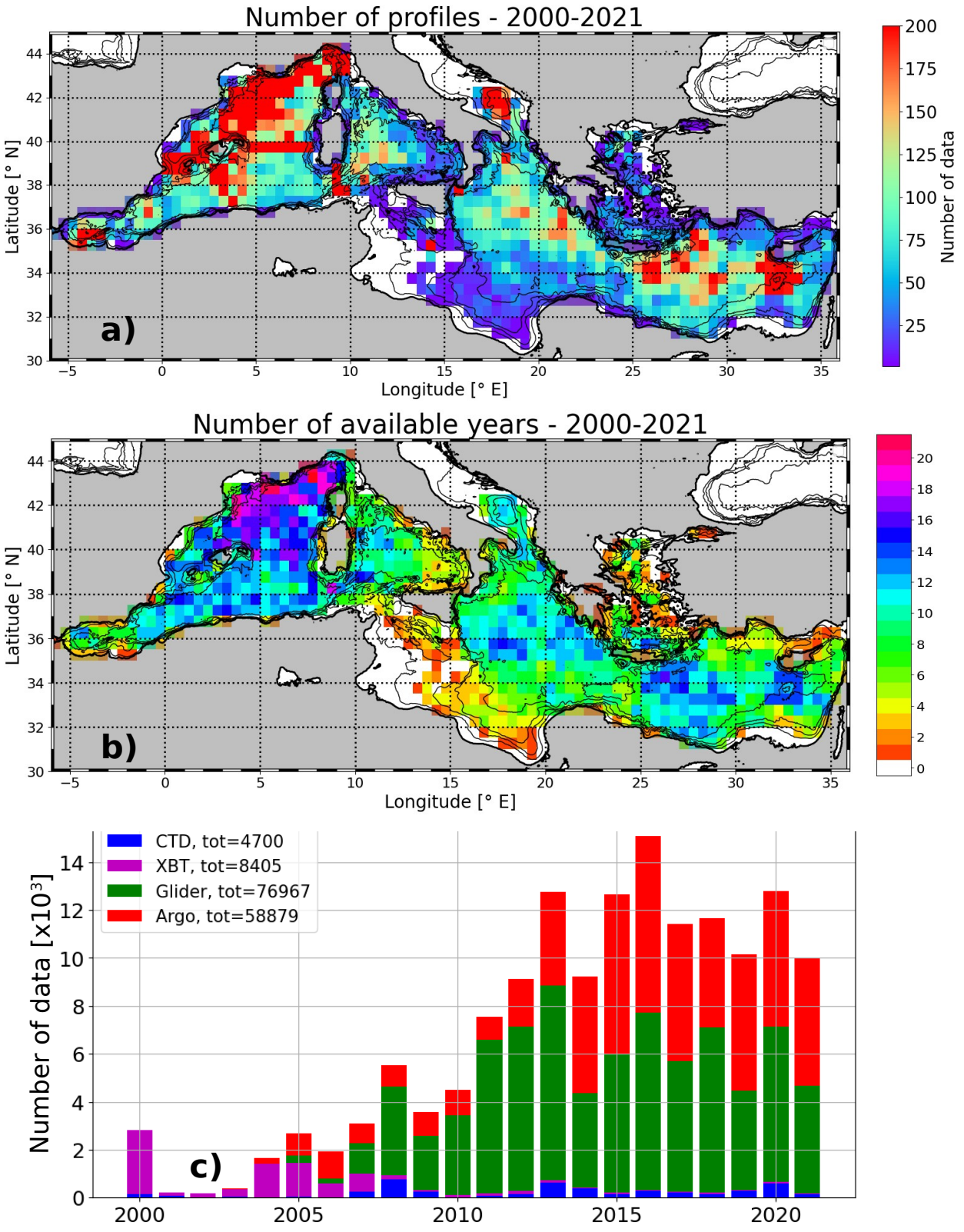

Figure 2.5: (a) Number of available measurements per 0.5°bins; (b) number of years with available measurements per 0.5°bins; (c) yearly histogram of in situ profiles distinguishing different data types.

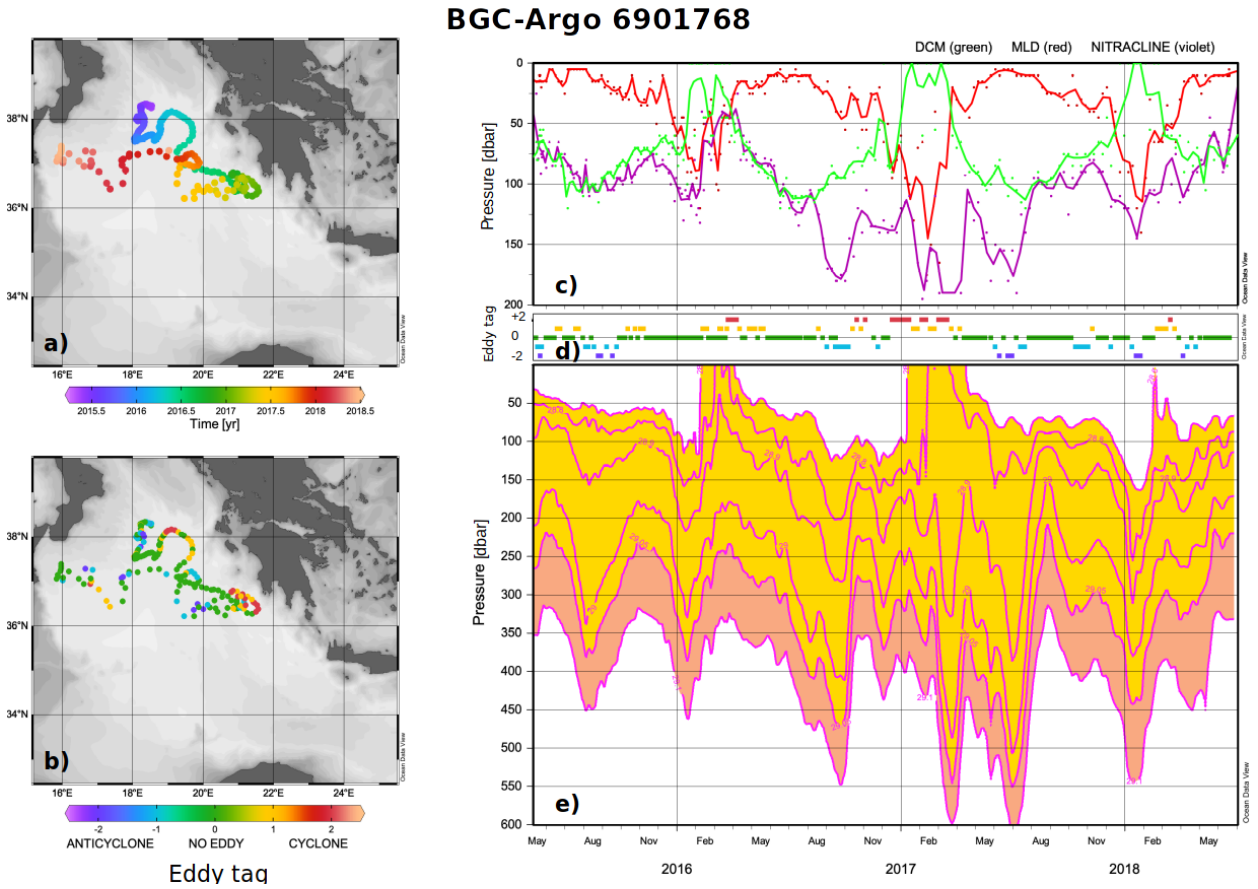

Figure 2.6: Argo float collocation example in the Ionian Sea with BGC-Argo 6901768. (a) Timeline evolution. (b) Eddy tag positions ranging from -2 (inside-anticyclone, blue) to 0 (outside-eddy, green) then +2 (inside-cyclone,red). (c) Deep chlorophyll maximum (DCM, green), mixed layer depth (MLD, red) and nitracline (purple) time series. (d) Eddy tag time series with same color code as in panel (b). (e) Potential density σ isopycnals time series, with only $\sigma = 28.6, 28.8, 28.9, 29.0, 29.05$ and $29.1\, kg.m^{-3}$. This figure is a courtesy from Vincent Taillandier (LOV).

2.4 Eddy anomaly compared to an outside-eddy background

In situ vertical profiles having been collocated with eddies, we can compute the eddy-induced anomaly X' for a given property X by comparing it to a reference state X_{back}:

$$X' = X - X_{back} \tag{2.3}$$

Once resolved the collocation issue (which profiles are outside, which ones are inside), the main issue is to define X_{back}. The first studies on eddy vertical structure used climatological database, for instance CARS with monthly fields for Chaigneau et al. (2011). Castelao (2014) improved the method in the North Atlantic by computing for each Argo profile a climatological background composed by all profiles within 100 km radius and separated by less than 30 days from the cast date of profile, including profiles from any year. This method enables to remove spurious variability in the upper layers due to seasonal cycle. It was successfully generalized by Pegliasco et al. (2015) for major eastern boundaries upwelling systems with a 200 km radius. However this method assumes that averaging in time and space, even locally, is enough to entirely remove the eddy-induced signature to have a clean reference state. The eddy mean effect on climatology is then entirely neglected. A striking illustration is Chaigneau et al. (2011) who already considered an "outside-eddy" profile category. They revealed a weak but still not negligible temperature and salinity anomalies outside-eddy compared to the CARS climatology. This accounted for up to $-2 \times 10^{-3} kg.m^{-3}$ at 200m, then about 15% of the average density anomalies inside eddies.

This assumption of eddy anomalies vanishing in temporal and spatial average actually relies on the vision of eddies as transient structure, cyclones and anticyclones compensating each other on long time scales. Three main arguments should be opposed. At first cyclones and anticyclones occurrence distributions are not homogeneous, as presented earlier in Fig.2.2. Secondly, cyclones and anticyclones can only partly compensate each other as their density anomalies usually do not have the same depth. A clear example can once again be found in Chaigneau et al. (2011) in the Southeastern Pacific, anticyclones being predominantly subsurface-intensified and cyclones surface-intensified. Consequently anticyclones and cyclones both contribute to a negative density anomaly in the upper 200m in the considered region. This consideration is less a problem in energetic regions with cyclones and anticyclones having very similar depth extension. See for instance the Gulf Stream region in Castelao (2014) and Kuroshio extension region in Sun et al. (2017). A last and third argument to list is that climatology assumes that data sampling is not totally heterogeneous. This assumption is likely true in the North Atlantic or Pacific oceans but should be reconsidered in the Mediterranean Sea. As discussed earlier in Sect.2.3 and shown in Fig.2.5a, most of the available profiles are concentrated on the northern side of the Mediterranean hosting mostly cyclonic gyres, while the southern part is poorly sampled.

Discarding the profiles inside eddies from a climatological background would have tremendous consequences on the climatology itself, likely more important in the Mediterranean Sea than elsewhere because of the heterogeneous eddy repartition between semi-enclosed basins. This climatological eddy-induced effect is not the core of our study, but we provide a discussion for interested reader in Appendix A. We will only stress here that computing a classical climatology encompassing all profiles whether they are inside- or outside-eddy induces a mean bias compared to an "outside-eddy" climatology. Due to the strong remanence of several anticyclonic structures in the Mediterranean Sea, this bias could be estimated in temperature to be up to $+0.5°C$ even at 500m depth locally in the Eastern Basin. The bias on salinity could be locally down to $-0.2PSU$ in the Tyrrhenian and Ionian Sea mostly in the upper 200m, up to $+0.2PSU$ in the Eastern Basin (see Fig.A.1). The effect on mixed layer depth is however less pronounced (see Fig.A.3), likely because submesoscale instabilities explain more proportion of the MLD variability.

Considering all the drawbacks of computing an eddy anomaly compared to an averaged climatological state, we first followed Laxenaire et al. (2019) approach computing a reference state using only profiles identified as "outside-eddy". Their background defined per eddy gathers profiles within a 2.5°x 2.5°box and cast within $\Delta day = \pm 30$ days of the eddy observation but independently of the year. Using this method Laxenaire et al. (2019) quantitatively measured the stratification evolution inside an Agulhas ring compared to the background stratification throughout the South Atlantic. Adapting this background method to the Mediterranean Sea, the DYNED Atlas originally computed for each profile a background composed by all "outside-eddy" profiles within $D_c = 150km$ of the considered profile and with cast date separated by less than $\Delta day = \pm 30$ days independently of the year.

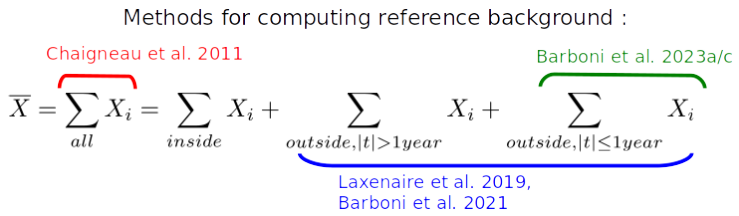

Figure 2.7: Various methods to compute background reference state X_{back} used in Eq.2.3.

Applying the Lagrangian tracking method to reconstitute the eddy network in the Southeastern Levantine Basin revealed the Eratosthenes anticyclonic attractor structure, a study published in Barboni et al. (2021) and included in Appendix B. Although not entirely centered on our subject, this study is a good example of the advantages of using both a Lagrangian tracking method on the temporal dimension, and an outside-eddy background on the vertical dimension. It is also an interesting example on anticyclone temporal evolution through successive merging events, an issue that is not addressed in this study. Also note that the DYNED Atlas in situ database originally only included Argo floats, to which additional profiles were added to study the Levantine Basin (see 2.3 in Barboni et al. (2021) for details).

2.5 Background interannual variability

A limit of the original DYNED Atlas background method as previously presented in Sect.2.4 and specific to the Mediterranean Sea is a marked interannual variability. The occurrence of Mediterranean transient events affecting intermediate waters production (Malanotte-Rizzoli et al., 1999; Schroeder et al., 2006), strong interannual warming trend (Mariotti, 2010) in particular in the Eastern Basin (Ozer et al., 2017), and overall faster climate change effects (Giorgi and Lionello, 2008; Pastor et al., 2020) led to more uncertainty regarding an interannual background. Moreover the vertical in situ sampling is sparse but also heterogeneous in time (see Fig.2.5c), with often less than 1000 profiles per year from 2000-2005 and more than 5000 per year since 2010 thanks to the massive glider and Argo floats deployments. Consequently using a reference background compiling outside-eddy profiles from any year will over-represent the ocean state in the best-sampled years, which might be a strong issue in the case of strong interannual variability.

A more representative background is then computed using only outside-eddy profiles less than $\Delta year = \pm 1y$ apart, keeping $D_c = 150km$ and $\Delta day = \pm 30days$. For instance, considering a profile cast on 15 February 2018, this new background will encompass all outside-eddy profiles cast within 150km between 15 January and 15 March in 2017, 2018 or 2019. This is eventually the method retained to compute the background for compute our eddy-induced anomalies in Sect.4. Note that these D_c and Δday parameters have to be tuned to the spatio-temporal variability of the studied object. MLD having more temporal variability than eddy temperature anomaly, background MLD in Sect.4 is computed with $D_c = 250km$ and $\Delta day = \pm 10$ days. But the major conceptual change between Laxenaire et al. (2019) and Barboni et al. (2023a) is to reduce interannual variability. The differences between the various background methods are summarized in figure 2.7 below, and the in situ database collocated with remote-sensing eddies and eddy-induced anomalies was made publicly available on SEANOE with reference: Barboni et al. (2023c).

An example of the Lagrangian eddy tracking together with collocated in situ vertical profiles is shown in Fig.2.8, for the same Pelops anticyclone which track was previously shown in Fig.2.3. MLD is computed as in Houpert et al. (2015) with a 0.1° difference threshold from 10m depth temperature. It is shown in Fig.2.8b with the background MLD for comparison. Background MLD is defined as median MLD among the background profiles, its spread as the difference between the 20^{th} and 80^{th} percentiles. Using MLD standard deviation to have an estimate of MLD spread is inappropriate, as the deviation is of the same order than the mean MLD (Houpert et al., 2015). This would lead to an upper bound of background MLD sometimes above surface. This issue is further discussed in Appendix A. Inside-eddy stratification (Fig.2.8c). It shows a clear seasonal evolution with stratification in spring in the upper layer, followed by the winter mixed layer deepening and letting an homogenized layer in the upper 250m. A strong MLD anomaly can be measured between maximal MLD reaching 250m inside-eddy, and not deeper than 100m in the background. This winter

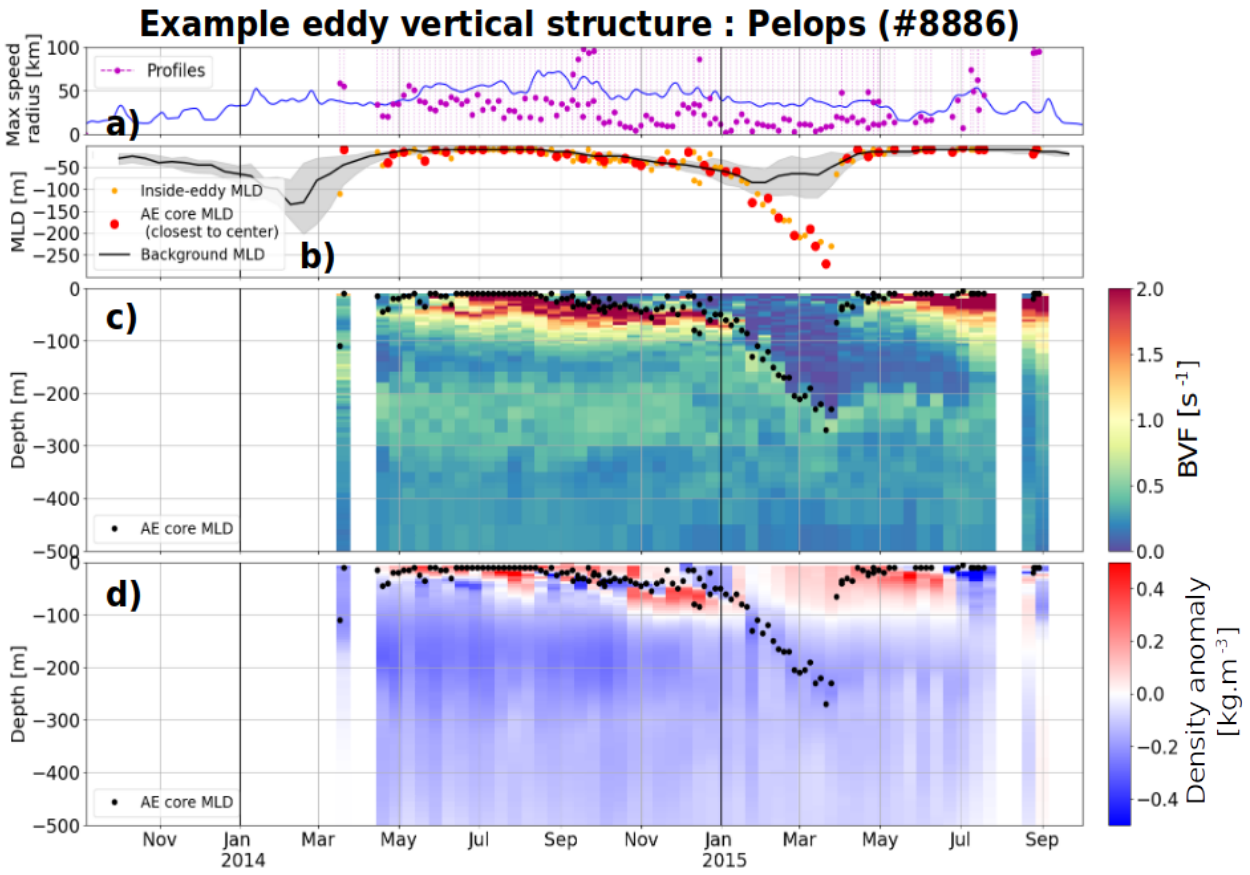

Figure 2.8: Example of inside-eddy vertical structure, for the Pelops anticyclone shown in Fig.2.3. (a) Maximal speed radius, showing profiles collocation as pink dots. Pink dots displacements show their distance to the eddy center. (b) MLD inside-eddy (orange dots), inside-eddy closest to eddy center per 10 days (red dots) and background MLD (black line), with its spread in gray shades. (c) Inside-eddy stratification with Brunt-Vaisala frequency (BVF, Eq.1.3) with scale factor 100, inside-eddy MLD being reminded as black dots. (d) Density anomaly using for background only profiles outside eddies with $\Delta year = \pm 1y$, $D_c = 150km$, $\Delta day = \pm 30d$.

mixed layer deepening event is later analyzed in Barboni et al. (2023a) as event PEL1. Density anomaly (Fig.2.8d) shows that this Pelops anticyclone has a negative density anomaly about $-0.2\,kg.m^{-3}$, mostly between 100 and 300m but extending also at least to 500m. Such isopycnals displacements are consistent with anticyclone encountered in the Ionian Sea (see Fig.2.6e). The eddy is clearly in subsurface as density anomaly gets positive in the upper 50m following Assassi et al. (2016). The subsurface anticyclonic density anomaly gets connected with surface in winter 2014-2015 and is recapped by stratification in summer 2015.

A specificity of the Eastern Mediterranean Sea is the persistence of long-lived anticyclones attracting and merging with smaller anticyclones. Barboni et al. (2021) studied the particular case of the Eratosthenes anticyclones. Even though it is not always the same eddy occupying the central place of anticyclonic attractor, there is always one anticyclone present. By defining what was referred to as "order 0" anticyclones and gathering collocated profiles inside these order 0 anticyclones, we were able in this study to show the annually averaged vertical properties of this attractor with interannual variability from 2000 to 2018. Background definition would then be at stake when considering such long time series, and we aim here to show the effect of heterogeneous sampling in time. Figure 11 from Barboni et al. (2021) is reproduced here in Fig.2.9 with an update until 2021, and using background with $\Delta year = \pm 1y$. Other recurrent structures (e.g. Mersa-Matruh or Pelops) could also be studied, but the Eratosthenes anticyclones have the opportunity of a very extensive data coverage, with in situ measurements available 20 years out of 22.

Background sensitivity is then evaluated on the vertically integrated anomalies in Fig.2.10, comparing the all-years background (red dots, Laxenaire et al. (2019)'s method), background with $\Delta year = \pm 1y$ (yellow dots), and the classical all-profiles background not separating outside- and inside-eddy profiles (black dots,

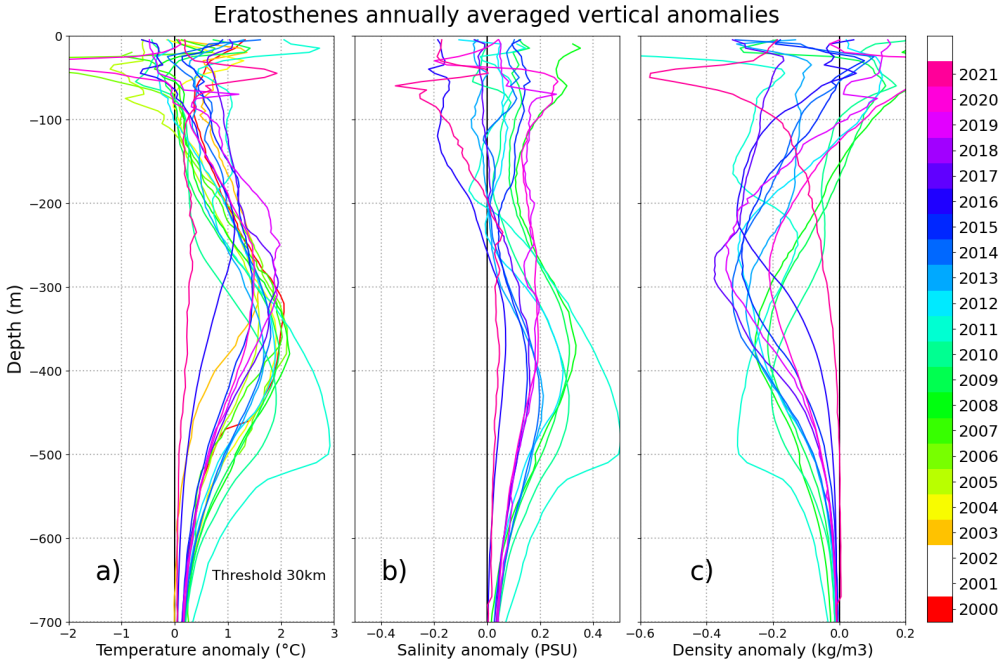

Figure 2.9: Annually averaged anomalies using profiles collocated inside Eratosthenes order 0 anticyclones defined as in Barboni et al. (2021), for (a) temperature, (b) salinity, (c) density. Only profiles closer than 30km to the center are used. Anomalies are computed using a background with only outside-eddy profiles with $\Delta year = \pm 1y$, $D_c = 150km$,$\Delta day = \pm 30d$.

Chaigneau et al. (2011)'s method with $D_c = 150km$). Yellow dots in Fig.2.10 then correspond to the vertical integration of Fig.2.9. Only anomalies between 100 and 900m depth are considered to avoid seasonal variations in the upper column. Heat content is computed from temperature anomaly T' using a mean density $\rho_0 = 1026\, kg.m^{-3}$ and heat capacity $c_p = 4185 J.kg^{-1}$:

$$H = \int_{100}^{900} \rho_0 c_p T' dz \tag{2.4}$$

As expected, a significant cold and constant bias is observed using the all-profiles background ($-0.56 GJ.m^{-2}$ compared to all-year background, $-0.68 GJ.m^{-2}$ compared to ± 1 year background, see Fig.2.10a). This bias also affects salt and density anomalies (fresher and denser bias) but this is more difficult to assess as the 2000-2010 decade gathers mostly XBT with no density information. This confirms that not separating inside- and outside-eddy profiles leads to artificially measure a warmer background due to the eddy mean warm anomaly, and decrease the observed heat content. Secondly, using an all-years background leads to under-estimate anomalies when fewer in situ data are available. In the Eratosthenes case in 2003 to 2005, the anticyclone heat anomaly is $1 GJ.m^2$ warmer using a ± 1 year background compared to the all-years one. More recent years after 2010 being warmer and more sampled, eddy-induced anomalies in the later decade are then artificially decreased. In the case of Eratosthenes anticyclones, the years 2009 to 2015 have very weak disagreements between the all-years and ± 1 year background, likely because extensive glider surveys were conducted between 2009 and 2012 (Hayes et al., 2011).

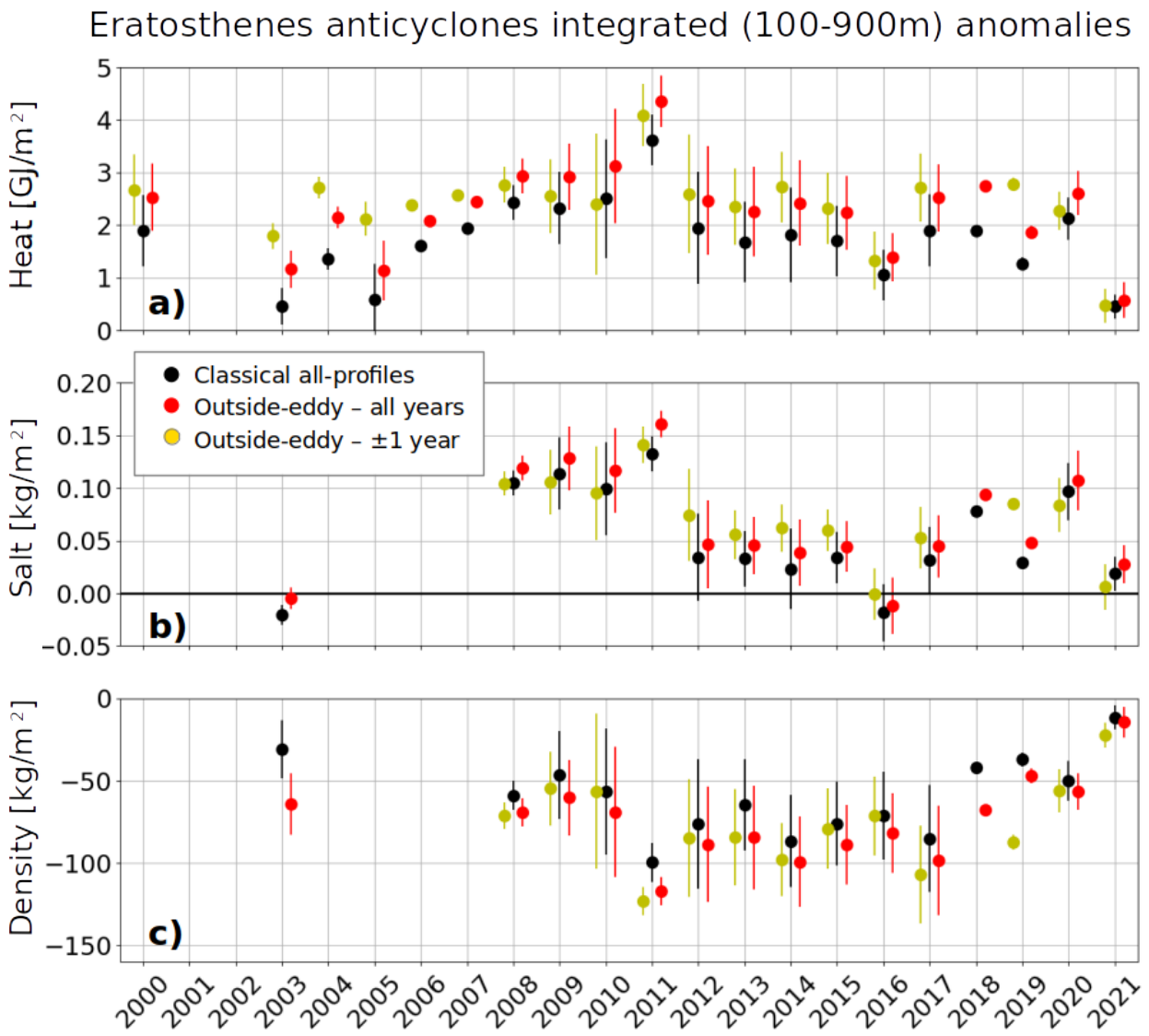

Figure 2.10: Vertical integration of annual averaged anomalies for (a) heat, (b) salt and (c) density. Anomalies computed related to three different backgrounds are compared: All-profiles (Chaigneau et al. (2011)'s method with $D_c = 150km$, black dots), outside-eddy profiles from all years (Laxenaire et al. (2019)'s method, red dots) and outside-eddy profiles with $\Delta year = \pm 1y$ (yellow dots). To enhance readability yellow dots are displaced 2 months earlier, red dots 2 months later.

Chapter 3

Seasonal evolution of eddy-induced surface signature

Lagrangian tracking method detailed above (Sect.2) can be applied to SST measurements to study the eddy-induced SST anomalies and track them in time. This work was done in the whole Mediterranean basin using Ultra-High resolution (1/120 °) SST product collocated with eddy detection from the DYNED Atlas. It allows to study the occurrence of warm-core cyclones and cold-core anticyclones, referred to as "inverse" eddy SST signatures. These inverse signatures were known since a long time: Hamad et al. (2006) already mentioned them in Mediterranean anticyclones (see an example reproduced in Fig.1.1c). They were recently showcased by an increasing number of studies revealing a important fraction of inverse eddy SST signatures in any region of the world ocean (Sun et al., 2019; Ni et al., 2021). Several mechanisms were proposed, but none was ascertained. Here we describe an observed strong seasonal shift of SST signatures in the Mediterranean Sea, and an eddy-modulated vertical mixing model is proposed as explanatory mechanism.

This work in collaboration with Evangelos Moschos (*LMD/Amphitrite*) was published in *Remote Sensing* and is included below. The SST observations are from Evangelos Moschos, and the vertical mixing model and simulations are from myself.

3.1 Moschos et al. (2022). Why do inverse eddy surface temperature anomalies emerge? The case of the Mediterranean Sea. *Remote Sensing*

remote sensing

MDPI

Article

Why Do Inverse Eddy Surface Temperature Anomalies Emerge? The Case of the Mediterranean Sea

Evangelos Moschos *, Alexandre Barboni and Alexandre Stegner

Laboratoire de Météorologie Dynamique, CNRS-IPSL, Ecole Polytechnique, 91128 Palaiseau, France
* Correspondence: evangelos.moschos@polytechnique.edu

Abstract: It is widely accepted that the signature of anticyclonic (cyclonic) eddies on the sea surface temperature corresponds to a warm (cold) core anomaly. Nevertheless, this statement has been put to question by recent regional studies showing the existence of inverse eddy SST anomalies: Cold Core anticyclones and, respectively, Warm Core cyclones. This study shows that the emergence of these inverse anomalies is a seasonal phenomenon that affects the life cycle of mesoscale eddies in the Mediterranean Sea. We use remote sensing observations and in situ data to analyse the eddy-induced SST anomaly over a 3-year period (2016–2018). We build an eddy core SST anomaly index to quantify the amount of Cold Core anticyclones and Warm Core cyclones all over the year and especially during the spring re-stratification period. We find that 70% of eddy anomalies are inverse in May and June both for cyclones and anticyclones. Regular temperature anomalies could reach 1.5 °C, while inverse ones are only present in the first 50 m of the oceanic layer and hardly exceed 1 °C. In order to understand the underlying dynamical processes, we construct a simple vertical column model to study the impact of the seasonal air–sea fluxes on the surface stratification inside and outside eddies. It is only by taking into account a differential diapycnal eddy mixing—increased in anticyclones and reduced in cyclones—that we reproduce correctly, in agreement with the observations, the surface temperature inversion in the eddy core. This simplified model suggests that vertical mixing modulation by mesoscale eddies might be the key mechanism that leads to the eddy–SSTA seasonal inversion in the ocean.

Keywords: ocean mesoscale eddies; sea surface temperature; vertical mixing

Citation: Moschos, E.; Barboni, A.; Stegner, A. Why Do Inverse Eddy Surface Temperature Anomalies Emerge? The Case of the Mediterranean Sea. *Remote Sens.* **2022**, *14*, 3807. https://doi.org/10.3390/rs14153807

Academic Editors: Angelo Perilli and Mariona Claret

Received: 29 June 2022
Accepted: 5 August 2022
Published: 7 August 2022

1. Introduction

Mesoscale eddies are coherent structures with typical radii of the order of tens up to a hundred kilometres and timescales on the order of a month. These eddies can be sometimes long-lived, surviving several months or even years. Significant advances in the resolution of both satellite altimetry measurements [1] and high-resolution oceanic numerical models [2] have revealed the predominance of these mesoscale eddies in the global oceanic circulation. They are able to trap and transport heat, salt, pollutants and various biogeochemical components from their regions of formation to remote areas [3,4]. Eddies are formed through shear and meander instability of boundary currents [5], baroclinic instability [6], the effect of wind on the sea surface [7] and other mechanisms. Their dynamics can impact significantly the biological productivity at the ocean surface [8–10], modify the depth of the mixed layer [11], influence clouds and rainfall within their vicinity [12], amplify locally the vertical motions [13], attract pelagic species [14–16] or concentrate and transport microplastics [17]. Long-lived mesoscale eddies are ubiquitous in the global ocean and play a major role in its circulation differentiating from mean patterns. In the Mediterranean Sea, the domain of this study, mesoscale eddies have been identified, tracked and analysed, both on their surface and subsurface structure in many studies [7,18–24].

The use of infrared images, which measure the Sea Surface Temperature (SST), has allowed the detection of many oceanic eddies and a better understanding of regional circulations [18,25,26]. These detections were performed visually by expert oceanographers.

However, due to the scarcity of in situ observations, it was not until the intensive development of satellite altimetry and the development of automatic vortex detection algorithms on Sea Surface Height (SSH) [1] that a statistical link between Eddy-induced Sea Surface Temperature Anomalies (eddy-SSTA) and SSH anomalies was established.

Several studies working on SST composites of eddies detected on the SSH associate Warm Core eddies (positive eddy-SSTA) with anticyclones and Cold Core eddies (negative eddy-SSTA) with cyclones [12,27,28]. However, through the individual analysis of eddies, various regional studies have shown the existence of inverse temperature anomalies, i.e., anticyclones (respectively cyclones) with a Cold (Warm) core anomaly. In a study of Mediterranean circulation using SST data, Ref. [18] performed observations of some Cold Core anticyclones on the summer period in the Eastern Mediterranean sea. In the Tasman Sea, Ref. [29] observed the existence of an important fraction (70%) of inverse anomalies. In the southwestern Atlantic Ocean, [30] found cyclones with a warm eddy-SSTA, which are explained through their (warm) region of formation. In the Arabian Sea, Ref. [31] showed the existence of inverse anomalies while searching for a link between the SST and Mixed Layer Depth (MLD) anomaly. In the North Pacific Ocean, Ref. [32] performed similar observations of inverse anomalies and also showed a seasonal variability in the regional eddy temperature anomaly distribution, noting that these inverse anomalies appear for shorter times than the regular ones. In the same fashion, Ref. [33] analysed the inverse eddy-SSTA in the South China Sea and noted a slight dependence on both seasonal effects and eddy amplitude. The last two studies both link inverse anomalies with the summer re-stratification at the ocean surface. Furthermore, Ref. [34] build an index based on the SST anomaly of an eddy to distinguish between surface and subsurface structure.

The presence of Cold Core anticyclonic and Warm Core cyclonic eddies on a global scale has also been documented by two recent studies. Through a Deep Learning eddy identification method, Ref. [33] detected and classified eddies and their surface temperature anomaly. An important fraction of inverse anomalies is revealed around the globe, reaching up to 40%. The authors also showcase the seasonal variation of this fraction as well as an inter-annual trend of diminishing inverse anomalies. In the same manner, [35] showcases that inverse anomaly eddies have lower absolute eddy-SSTA values than their regular counterparts. Exhibiting strong seasonal variation, inverse anomalies cover according to this paper 15% of anticyclones (10% cyclones) in the summer period. Finally, the authors show a correlation of this seasonal variation of eddy SST anomalies with the mixed layer modulation, along with the inversion of wind-stress and heat-flux patterns over these eddies. It should be noted that the percentages of inverse anomalies differs significantly between the aforementioned studies (regional and global) based on the method used to quantify them.

However, correlation does not imply causation, and even if some of the aforementioned articles create a strong observational link, regionally or globally, between the mixed layer modulation and the inversion of eddy-SSTA, none of them demonstrates an underlying mechanism for this phenomenon.

The goal of this work is to perform a comprehensive study on the formation of inverse sea surface temperature anomaly of mesoscale eddies and propose an underlying physical mechanism. As a case study, observations in the Mediterranean Sea are examined, although our results can be expanded to other regions of the globe. Here, we attempt to answer four questions:

- *How does the eddy-SSTA distribution vary seasonally?* We first define an eddy core surface temperature anomaly index to quantify the intensity of the eddy-SSTA for a large number of anticyclonic and cyclonic eddies in the Mediterranean Sea. This index allows us to perform a statistical analysis of the seasonal variations of the temperature anomaly inside coherent eddies and study its correlation with the evolution of the MLD.
- *How does the SST signature and anomaly of an individual mesoscale structure evolve?* We investigate a few long-lived eddies to follow the temporal evolution of their SST

anomaly with respect to their dynamical parameters and the seasonal stratification of the ocean surface.

- *Is the surface temperature anomaly linked with the subsurface structure ?* We quantify more precisely the evolution of the surface stratification inside and outside these selected eddies using ARGO profiles to estimate the eddy vertical temperature structure and compare it with the surface temperature anomaly.
- *Why do inverse SST anomalies emerge?* We propose a mechanism based on differential vertical mixing between the eddy core and its periphery under atmospheric fluxes, which is illustrated with idealised single-column numerical simulations. The relevance of this physical model to explain the inverse emergence of inverse eddy-SSTA and its agreement with the remote-sensing and in situ observations are discussed in the conclusion.

2. Materials and Methods

2.1. Satellite and In Situ Data

This study focuses on the mesoscale oceanic eddies of the Mediterranean Sea, during the three-year period 2016–2018. To perform our analysis, we combine satellite and in situ data to characterise both the ocean surface and the subsurface stratification. The infrared satellite imagery provides the SST maps which are the core data of this study. We use the DYNED-Atlas database to obtain the dynamical parameters and the contours of mesoscale eddies detected on standard satellite altimetry products. The three-dimensional structures of the studied eddies as well as the surface stratification and the MLD were derived from the in situ Argo floats measurements.

2.1.1. Satellite Data

Daily, high-resolution (1/120°) super-collated SST maps of the Mediterranean Sea are received from the Copernicus—Marine Environment Monitoring Service (CMEMS), Ultra High Resolution L3S SST Dataset (https://doi.org/10.48670/moi-00171, accessed on 28 June 2022), produced by the CNR—Italy and distributed by CMEMS. The process of supercollation uses SST measurements derived from multiple sensors, representative of nighttime SST values [36]. Sea Surface Height (SSH) and geostrophic velocity fields, used for the detections of eddies in this study, are L4 AVISO/CMEMS altimetric products at 1/8° resolution retrieved from the CMEMS L4 Sea Level dataset. (https://doi.org/10.48670/moi-00141, accessed on 28 June 2022)

2.1.2. Eddy Contours, Centers and Tracks

The dynamical evolution of eddies and their individual tracks are retrieved from the DYNED-Atlas database for the three year period 2016–2018. The DYNED-Atlas (https://www1.lmd.polytechnique.fr/dyned/, accessed on 28 June 2022) project containing eddy tracks and their physical properties is publicly accessible. The tracking of these eddies is performed by the AMEDA eddy detection algorithm [37] applied on daily geostrophic velocity fields derived from the AVISO/CMEMS SSH maps. A cyclostrophic correction is applied on these geostrophic velocities to accurately quantify eddy dynamical properties [38]. Unlike standard eddy detection and tracking algorithms, the main advantage of the AMEDA algorithm is that it detects the merging and the splitting events and allows thus for a dynamical tracking of eddies [37].

The identification of potential eddy centers by AMEDA is performed by computing the Local Normalised Angular Momentum (LNAM) [21] of the geostrophic velocity field. Only eddy centers with at least one closed contour of the stream function of the velocity field are retained. A radial profile of the velocity for each detected eddy center is calculated by computing the average velocity and radius at each closed streamline around it:

$$\langle V \rangle = \frac{1}{L_p} \oint \vec{V}\, d\vec{l} \tag{1}$$

where V is the local geostrophic velocity field and L_p is the streamline perimeter. The maximum velocity, obtained through Equation (1), will be hereby noted as V_{max} and the radius corresponding to the characteristic contour. The radius R_{max} of the characteristic contour is obtained by considering a circular contour of an equivalent area A:

$$\langle R \rangle = \sqrt{\frac{A}{\pi}} \tag{2}$$

The eddy centers and their characteristic radius R_{max} are important parameters used to retrieve SST patches for each eddy detection.

2.1.3. Argo Floats

Hydrographic profiles of Argo floats are received through the CORIOLIS program database (http://www.coriolis.eu.org/, accessed on 28 June 2022). Potential temperature and salinity profiles are received from Argo floats through which the potential density profiles are derived. A co-localisation is performed between the position of Argo floats and the detected eddies of the DYNED-Atlas database. Argo profiles are marked as inside an eddy if their distance r from any eddy center is $r < R_{max}$ and outside an eddy if the above condition is false for every eddy detection of the same day.

To calculate the MLD of each Argo observation, we use its potential density profile and search for the maximum depth at which a threshold of $\delta\rho = 0.03$ kg/m^3 is reached [39].

2.2. A Method to Quantify Eddy-Induced SST Anomalies

Mesoscale eddies often have a visible signature on SST images, with a temperature difference between the waters in the eddy core and the waters in its periphery. This difference is defined as the eddy-induced surface temperature anomaly (eddy-SSTA) of an eddy, and it can be quantified through our proposed methods.

A procedure to retrieve a large dataset of SST image patches containing eddy signatures is proposed, following [40,41]. The Eddy-Core Surface Temperature Anomaly Index (δT), a simple and heuristic method for quantifying the eddy-induced temperature anomaly represented in each image, is then defined. The proposed methodology, applied here to observations in the Mediterranean Sea, is generic enough to provide results in every oceanic domain.

2.2.1. Eddy SST Patches Dataset

A thorough statistical analysis of eddy-induced SST anomalies requires a large dataset of SST image patches in the Mediterranean Sea. The characteristic contours (highest mean velocity) of the mesoscale eddies contained in the DYNED-Atlas are used to crop patches from SST maps, which are centred on the detected eddies. These contours can either represent Anticyclonic Eddies (AE) or Cyclonic Eddies (CE) rotating clockwise and anti-clockwise, respectively, in the northern hemisphere. For each eddy, a square patch of size ($5R_{max} \times 5R_{max}$) is cropped and centred on the contour barycenter. Cloud coverage creates missing values on satellite SST images and can corrupt the signature of the cropped image patches. Thus, only patches with less than 50% of cloudy pixels are retained.

The eddy SST signatures can be distinguished either as Warm Core or Cold Core anomalies, as discussed earlier. Four such cases are depicted in Figure 1 in which both positive and negative SSH anomalies can correspond to a Warm or a Cold SST anomaly. The characteristic contours of each eddy (in black) are superimposed on the Absolute Dynamic Topography (ADT), derived from the SSH, and the corresponding SST patch.

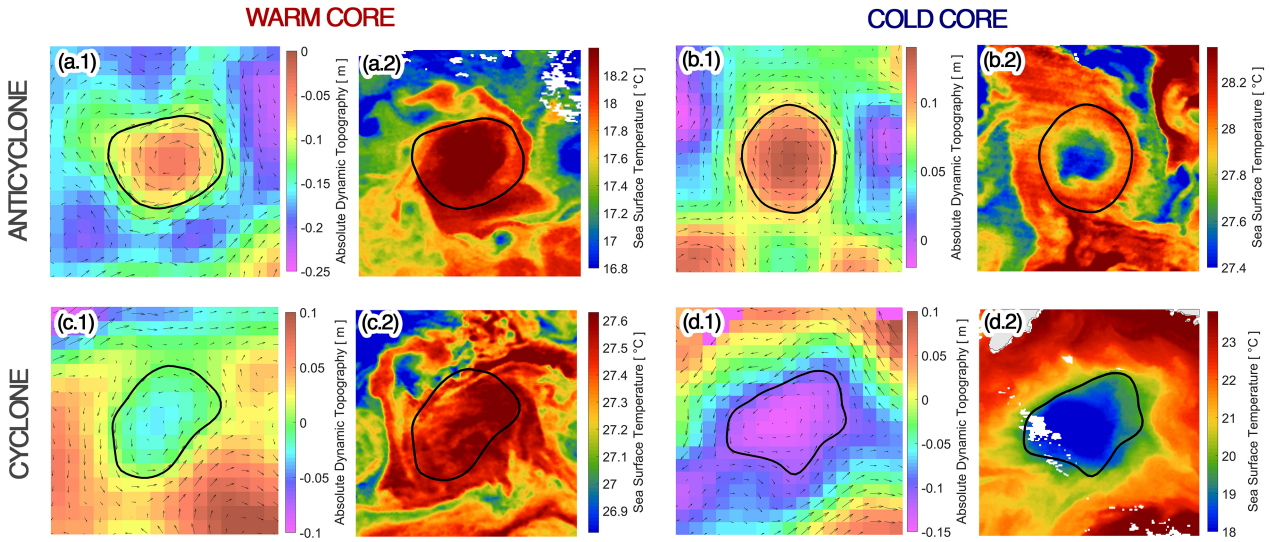

Figure 1. Samples of eddy-induced SST anomalies for a (**a**) Warm Core Anticyclone, (**b**) Cold Core Anticyclone, (**c**) Warm Core Cyclone, (**d**) Cold Core Cyclone. On the leftmost panels numbered with (**1**), the velocity vectors and the characteristic contour, computed by the AMEDA algorithm (black line), are superimposed on the Absolute Dynamic Topography. On the rightmost panels numbered with (**2**), the characteristic contour (black line) is superimposed on the patches of Sea Surface Temperature field centred on the detected eddy. Image patches are of side $5R_{max}$, which are chosen in order to include the temperature of waters.

2.2.2. The Eddy-Core Surface Temperature Anomaly Index [δT]

The Eddy-Core Surface Temperature Anomaly Index (hereby δT) is a simple and heuristic metric of the temperature difference between the core (centre) of the eddy and its periphery. We define the core of the eddy as the region enclosed by the maximum velocity contour [37]. The value of δT is calculated as the difference between the mean of the temperature values inside a *core-mean frame* and a *periphery-mean frame* in a given patch, with units in °C. These two square frames, which share a common centre, have sides of R_{max} and $5R_{max}$, respectively. For the calculation of the mean value in the periphery-mean frame, the values contained in the core-mean frame are ignored. A positive δT value denotes a larger core-mean temperature than its periphery-mean temperature and thus a Warm Core Eddy, while a negative δT denotes, respectively, a Cold Core Eddy. The calculation of the δT variable by use of the core-mean and periphery-mean frames is shown in Figure 2. Examples (a) and (b) show the two centred anomalies, which are shown also in Figure 1a.2,b.2. The δT values are 0.75 °C for the Warm Core example (a) and -0.27 °C for the Cold Core example (b).

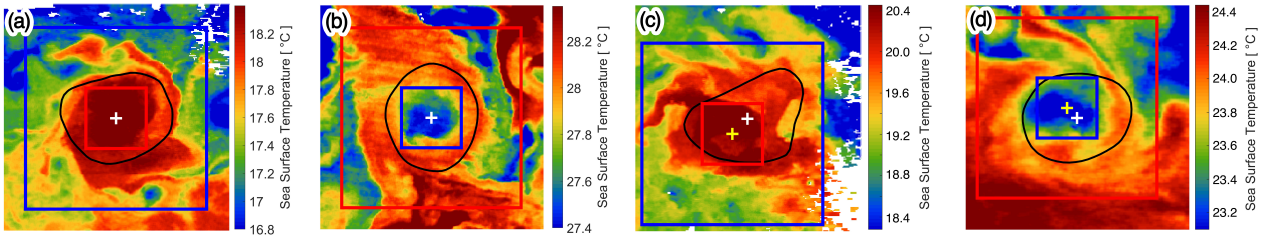

Figure 2. Examples of the eddy-core surface temperature anomaly computation and offset method. Snapshots represent Sea Surface Temperature in degrees. Black lines are superimposed altimetric detection contours. Small squares represent the core-mean and large ones represent the periphery-mean frames. Core-periphery values are coloured red-blue or blue-red based on the sign of δT. Examples (**a**–**d**) illustrate the correction by offset: A white cross marks the centre of the image. A yellow cross marks the center of the core-mean and periphery-mean frames, if it differs from the centre of the image. Examples (**a**,**b**) are centred while (**c**,**d**) are offset.

However, the barycenter of the velocity contour can differ from the centre of the eddy SST anomaly core, due to bias or errors of altimetric maps [42,43]. Therefore, an offset of both frames is considered in order to locate the exact position of the maximum eddy-SSTA and correct the index value.

This correction is computed as follows: First, the value of δT is calculated through squares centred on the image, as described above. The sign of the eddy-induced SST anomaly is thus defined. Then, if δT is positive (negative), the warmest (coldest) core-mean value is searched for by offsetting the core-mean frame in all directions with a stride of $\frac{1}{9}R$ and a maximum offset of $\frac{2}{3}R$. Finally, the periphery-mean frame is centred along the shifted core-mean frame, and the corrected δT value is computed. In the rest of this manuscript, δT represents the final values calculated by applying the offset correction.

Examples of off-centred eddy detections are shown in Figure 2c,d. The core and periphery have been shifted in order to maximise the eddy-core surface temperature anomaly index. The geometric centre of the image is shown with a white cross, while the shifted centre of the core-mean frame is shown with a yellow cross. The δT values are 0.68 °C corrected to 0.86 °C by offseting for the Warm Core example (c) and -0.46 °C corrected to -0.55 °C by offseting for the Cold Core example (d).

Nevertheless, even with this correction, a significant amount of noisy and/or corrupted SST signatures remain. This could be due to the combination of erroneous eddy detections on gridded AVISO/CMEMS altimetry products, large-scale air–sea interactions that mask the mesoscale eddy signature or the presence of clouds [41].

In order to exclude these images with unclear SST signatures, two thresholds are considered. The Cloud Coverage threshold, described above, is used to retain only images that have a Cloud Coverage Percentage (CCP) lower than 50%. The CCP is defined as the percentage of pixels covered by clouds on a given area. This criterion is applied twice: on the whole image patch (CCP_{patch}) as well as the core-mean frame (CCP_{frame}). The threshold is chosen so that the eddy SST signature is not corrupted, which could produce errors in the calculated δT value [41].

An illustration of the application of the Cloud Coverage threshold is provided in Figure 3a–d, where snapshots of the SST signature of the same eddy (Ierapetra) are provided at different days of December 2016 along with core-mean and periphery-mean frames. Example (a) on 19/12 shows a patch with an overly clear eddy signature ($CCP_{patch} = 8\%$, $CCP_{frame} = 0\%$) retained in the dataset. Example (b) on 20/12 shows a patch with an eddy signature covered by clouds ($CCP_{patch} = 40\%$, $CCP_{frame} = 48\%$), which however does not surpass the 50% threshold and is retained in the dataset. Examples (c) on 29/12 ($CCP_{patch} = 48\%$, $CCP_{frame} = 90\%$) and (d) on 30/12 ($CCP_{patch} = 72\%$, $CCP_{frame} = 76\%$) show patches exceeding the Cloud Coverage threshold and therefore filtered from the dataset.

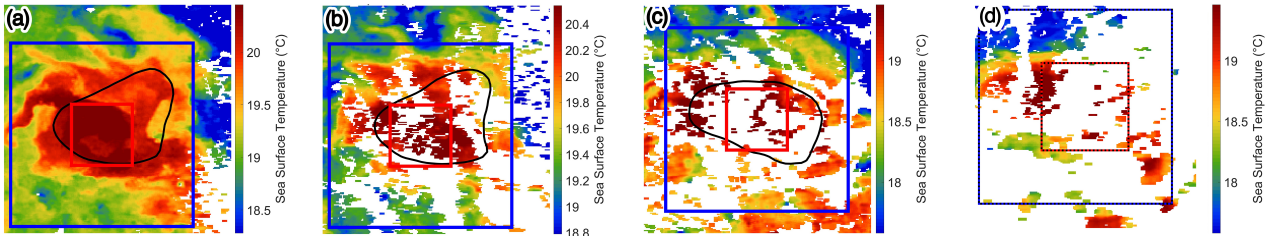

Figure 3. Examples with different Cloud Coverage. Snapshots represent Sea Surface Temperature in degrees. Contours and squares are the same as Figure 2. Snapshots of the same eddy (Ierapetra) on different days of December 2016 (**a**) 19/12, (**b**) 20/12, (**c**) 29/12, and (**d**) 30/12. Cloud coverage percentage is increasingly high. Examples (**a**,**b**) are retained, while (**c**,**d**) are not retained

Finally, a filter on weak δT values is also applied. We have noticed by visual inspection that unclear SST signatures often induce a weak value of the δT. Hence, to filter out these noisy images, we retain only SST patches if $|\delta T| > 0.1$.

3. Results

3.1. Seasonal Variability of the Eddy-Induced Temperature Anomaly

The seasonal variability of the eddy-induced temperature anomaly, and more generally the signature of eddies on the SST, is analysed in this section through two different perspectives: first, a statistical analysis is carried out on the δT values calculated on every retained eddy detection. Furthermore, the change of the surface temperature anomaly is examined over the lifetime of several long-lived eddies in the Mediterranean Sea while particularly focusing on the subsurface structure of one of them.

3.1.1. Statistical Analysis

Composite averages are often employed in the bibliography to represent the SST anomaly of mesoscale eddies [12,27,28]. This averaging leads frequently to the association of a Warm Core anomaly to anticyclonic eddies and a Cold Core anomaly to cyclonic eddies.

To examine these average temperature anomalies, we calculate here the composites of all eddy SST patches retained after first performing a normalisation per patch. To receive the Normalised SST Anomaly, we subtract from each pixel the mean value of all the SST values of the entire patch and divide the result by the standard deviation of all the SST values of the entire patch. In Figure 4, composites of Anticyclonic and Cyclonic Normalised SST Anomaly are plotted for all eddies and those observed on the Winter (December–January–February) and Summer (May–June–July) period. These two oceanic seasons are chosen on the three-month period when the mean value of the MLD, computed outside the detected eddies, reaches its largest or smallest value .

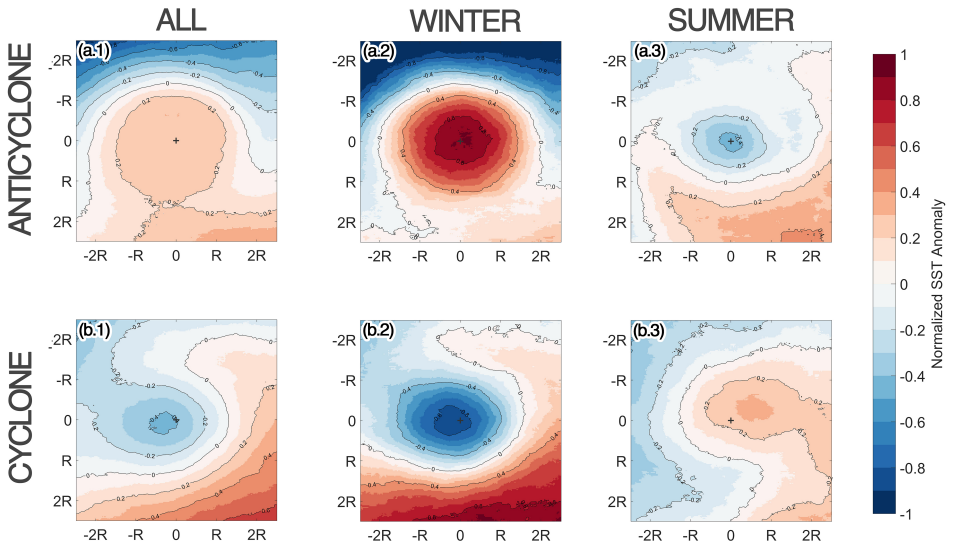

Figure 4. Composite averages of normalised SST anomaly for (**a**) Anticyclonic and (**b**) Cyclonic eddies for (**1**) all, (**2**) winter (DJF), and (**3**) summer (MJJ) observations. Each value in an eddy SST patch is normalised by subtracting the mean value and dividing by the standard deviation of all values. Composites are retained by averaging between patches.

From the composites of Figure 4, it can be seen that the average SST anomaly of all anticyclonic (cyclonic) observations indeed corresponds to a Warm (Cold) Core structure, or else the regular eddy anomaly. Nevertheless, a strong seasonal variation of this average anomaly is revealed by plotting the winter and summer composites. In winter, the regular anomaly is even more pronounced with double to triple normalised anomaly values. However, summer composites show an inverse average anomaly, i.e., Cold Core Anticyclones and Warm Core Cyclones on average, while also having weaker normalised anomaly values. The latter is coherent with the findings of other studies, showing that the SST signatures on the vicinity of eddies on summer tend to be more spatially uniform [35,44].

While composites suffice to portray the seasonal inversion of eddy temperature anomalies, averaging out patch values does not retain the variance in eddy anomalies on the SST. To quantify the latter, we perform a statistical analysis of the δT index values computed for all the patches retained.

The histograms of the δT index are shown in Figure 5, separately for anticyclonic and cyclonic eddies, in winter (DJF) and summer (MJJ). On the histograms, red bins represent Warm Core observations, while blue bins represent Cold Core observations. Grey bins represent observations where $|\delta T| < 0.1$. These bins correspond to outlier values linked with the noise on the SST data as well as errors on the sensors observation and our method. A threshold of $|\delta T| > 0.1$ is fixed to filter out these observations in the analysis/figures that follow.

If we consider a year-long statistical distribution, AE are predominantly Warm Core and CE are predominantly Cold Core; in other words, AE and CE, exhibit on average an *regular* anomaly on the SST. However, the distribution of δT values in the histograms of Figure 5 suggest that the eddy-core temperature anomaly exhibits strong seasonal variation, altering between Warm Core and Cold Core anomaly regimes. Specifically, during winter, the regular anomalies are preponderant: 93% of AE observations correspond to Warm Core eddy, while 92% of CE observations are Cold Core. However, during summer, Cold Core AE and Warm Core CE observations become dominant with, respectively, 69% and 66% of the observations. It is due to this seasonal inversion of the regular anomaly that we name the Cold Core AE and Warm Core CE as *inverse* SST anomaly.

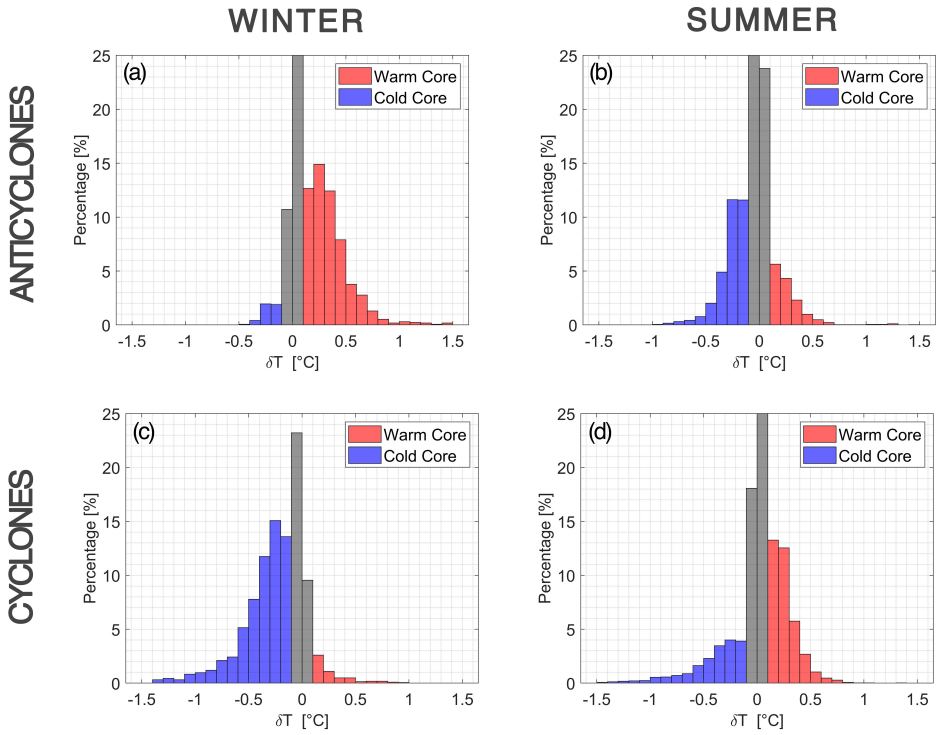

Figure 5. Seasonal histograms of δT values. (**a**) AE in the winter mixing period (DJF), (**b**) AE in the summer restratification period (MJJ), (**c**) CE in the winter mixing period (DJF) and (**d**) CE in the summer restratification period (MJJ). Red bins represent positive δT Warm Core observations, while blue bins represent negative δT Cold Core observations. Grey bins represent observations where $|\delta T| < 0.1$.

The seasonal cycle of the eddy-SSTA of both AE and CE, in the Mediterranean Sea, coincides with the seasonal variation of the MLD. This is portrayed in Figure 6, where the monthly variation of the percentage of inverse eddy core anomalies is plotted along with the monthly variation of the MLD. The later is calculated as the mean of all Argo profiles that are located outside eddies. The winter mixing period (DJF), when the mean MLD is at its largest extent, coincides with the period when eddy anomaly are dominantly regular, with only 5–15% of inverse anomalies (i.e., 95–85% regular anomalies) for both AE and CE. Conversely, the end of the spring re-stratification period (MJJ) when the mean MLD is at its shallowest coincides with the period where most eddies have an inverse anomaly, reaching a peak of 70% of Cold Core AE and Warm Core CE observations for the months of May and June.

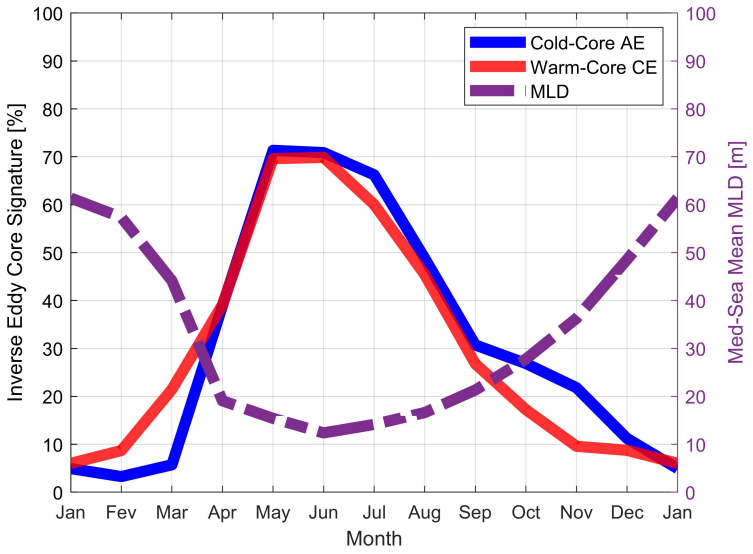

Figure 6. Seasonal variation of the mean MLD with inverse eddy anomaly percentage. For each month, the mean percentage of Cold Core AE observations is plotted with a blue line, the mean percentage of Warm Core CE observations is plotted with a red line, and the mean MLD of all Argo profiles located outside eddies with a dashed purple line.

The seasonal variation of the core anomalies and their summer inversion, seen on Figures 4–6, is also analysed spatially. In Figure 7, we plot the δT values of all anticyclonic/cyclonic eddy detections in the Mediterranean Sea for one winter (DJF) and one summer (MJJ) season. The predominance of regular anomalies (Warm Core AE, Cold Core CE) in winter (panels a and c) and inverse anomalies (Cold Core AE, Warm Core CE) in summer (panels b and d) is spatially homogeneous over the Mediterranean Sea. Regular temperature anomalies reach higher absolute values, as can be seen by the intense red dots (i.e., Warm Core anticyclones on panels a and b) and blue dots (Cold Core cyclones on panels c and d). The inverse anomalies have lower absolute values, as portrayed in the histograms of Figure 5. Finally, Figure 7 also portrays a spatial homogeneity, with the emergence of inverse eddy anomalies on summer happening all over the Mediterranean Sea.

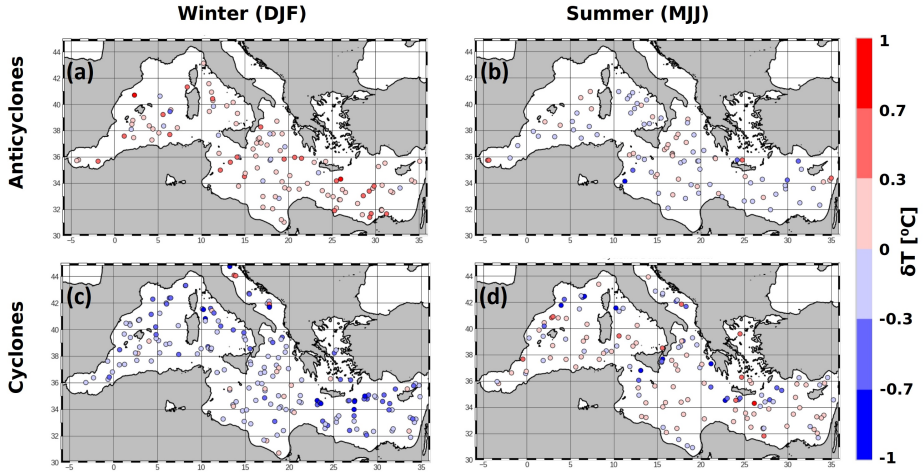

Figure 7. Spatial variation of δT values in the Mediterranean Sea for (**a**) Anticyclones in winter, (**b**) Anticyclones in summer, (**c**) Cyclones in winter, and (**d**) Cyclones in summer. Red (Blue) dots correspond to warm (cold) anomalies. The colour intensity depicts the absolute value of the anomaly.

3.1.2. Individual Eddy Analysis

To better investigate how the seasonal evolution of the surface stratification inside mesoscale eddies impacts their surface temperature signature, we track four long-lived eddies and follow the temporal evolution of their dynamical parameters, the surrounding MLD and their surface SST anomaly. One of them, an Ierapetra Anticyclone, formed south of the island of Crete, was sampled for over a year by Argo floats trapped inside its core. Three more eddies are considered: a Cyprus anticyclone located among and around the Eratosthenes seamount, an Algeria Anticyclone drifting along the Algerian coast and an elongated cyclone located in the Ligurian sea. The timeline of the Ierapetra eddy is shown in Figure 8, while those of the Algeria, Cyprus and Liguria eddies are shown, respectively, in Figures A1–A3 of the Appendix A.

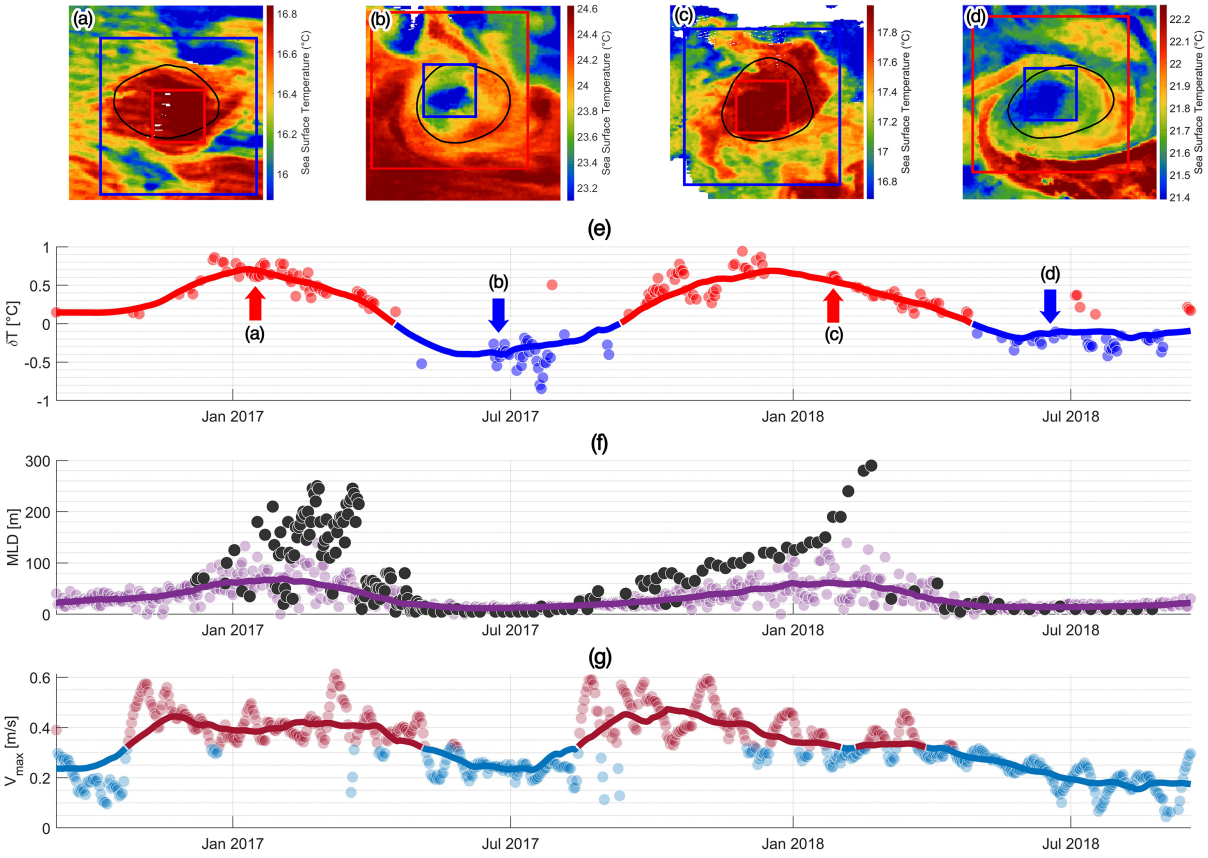

Figure 8. Timeline of the Ierapetra anticyclone with DYNED ID #11099. Four characteristic SST patches are shown in panels (**a**–**d**) which correspond to different regimes of the evolution of the eddy SST anomaly. In panel (**e**), the δT index values are plotted for every retained observation with red (blue) dots for positive (negative) values. The Monthly Mean Average of these values is plotted with a red (blue) line showing the regime change between a Warm Core and a Cold Core eddy. On panel (**f**), the depth of the mixed layer (MLD) is plotted with pink dots for values outside the eddy and black dots inside the Ierapetra eddy. A Monthly Mean Average of the MLD evolution outside the eddy is plotted with a pink line. On panel (**g**), the surface maximal velocities (V_{max}) for each timestep in the DYNED-Atlas eddy track are plotted with dots and their Monthly Mean Average is plotted with a line. Velocities are plotted with magenta (cyan) when they are higher (lower) than the mean velocity in the eddy lifetime.

For each of these four eddies, we create an *Eddy Timeline* that contains the δT index, the evolution of the MLD in the eddy area, the eddy intensity and a few characteristic snapshots of the eddy SST signature. Moreover, to highlight the seasonal variations, a Monthly Mean Average is calculated for each parameter. The daily values of the Core Temperature Anomaly Index (δT) are plotted when the cloud coverage is not too high and the temperature anomaly is not too small (i.e., $|\delta T| > 0.1$). The calculated (δT) (dots) as well as the corresponding Monthly Mean Average (line) are coloured in red (blue), when their value is positive (negative), denoting a warm (cold) core regime.

To construct the MLD time series (pink dots), we use all the Argo profiles that were measured outside eddy contours in a surrounding area, which are defined as a rectangular box of one degree of latitude and longitude and centred on the eddy. More than one MLD observation might exist for a certain day, causing a spread of values, especially for the winter mixing period. When in situ measurements are available inside the eddy contour, the MLD is plotted with black dots. The variations of the eddy intensity, quantified here by V_{max}, are plotted during the same period. In order to highlight the seasonal variations, we use distinct colours for the velocity above (magenta) and below (cyan) the mean velocity value averaged over the whole period.

Our analysis is focused on the evolution of an Ierapetra Anticyclone from September 2016 to September 2018. According to Figure 8, this anticyclone changes regimes twice from a regular to an inverse anomaly. The inverse Sea Surface Temperature anomaly begins in spring, when the re-stratification sets in, and continues until fall.

As can be seen in panel (f) of Figure 8, in winter months, while the eddy is in a Warm Core regime in panel (e), the MLD is two or three times deeper inside the Ierapetra anticyclone than in its surroundings, reaching 300 m of depth while being shallower than 120 m in its surroundings. The Warm Core surface anomaly of the eddy (panels (a) and (c)) can be linked therefore with its subsurface heat content. On the other hand, during the spring re-stratification period and a Cold Core regime, the MLD is rather shallow, not exceeding a few tens of meters both inside and outside the anticyclone. The Cold Core surface anomaly (panels (b) and (d)) is disconnected from the warm subsurface heat content. It should also be noted that it is during the winter months, when the MLD is deeper in the eddy core, that the anticyclone passes an intensification phase shown in the evolution of the surface velocity V_{max}.

Similar regime transitions from a regular to an inverse sea surface temperature anomaly are visualised in Appendix A of this article for two other anticyclones in Figures A1 and A2 as well as a cyclone in Figure A3. For all these eddies, the inverse Sea Surface Temperature anomaly is directly correlated to a small MLD in the area surrounding the eddy. This indicates a strong surface stratification on the same period, leading to a disconnection of the inverse surface anomaly with the subsurface heat content.

To investigate if the change in the surface core temperature anomaly is linked with the subsurface anomaly of the Ierapetra anticyclone, two profiles from an ARGO float released inside the core of the eddy are examined. From a series of observations, the profiles are chosen on two dates where the SST signature of the eddy is not corrupted by clouds and the in situ profile samples well the eddy core. In winter, a regular Warm Core observation on 26 February 2017 can be seen in panel (a.2) of Figure 9, corresponding to panel (a) of Figure 8. In summer, on 26 June 2017, we retain an inverse Cold Core observation of the same eddy that can be seen in panel (b.2) of Figure 9, corresponding to panel (b) of Figure 8. On these panels, a white star corresponds to the location of the eddy-sampling ARGO float. On panels (a.1) and (b.1) of Figure 8, the location of the eddy-sampling floats are shown with a star in a wider map, where we also plot the region (dashed rectangle) where we search for background sampling ARGO floats. We consider a $\pm$ 1 week period from the observation date and search for ARGO profiles in that region that fall outside of eddies. The temperature measurements of these background outside-eddy profiles is plotted with dashed grey lines on panels (c) and (d) of Figure 8 while their mean is plotted with a thick black line. The eddy-sampling profile is plotted on panels (c) and (d) of Figure 8,

corresponding to the winter and summer periods, respectively. When the eddy-sampling profile is warmer (cooler) than the mean outside-eddy profile, it is plotted with a thick red (blue) line.

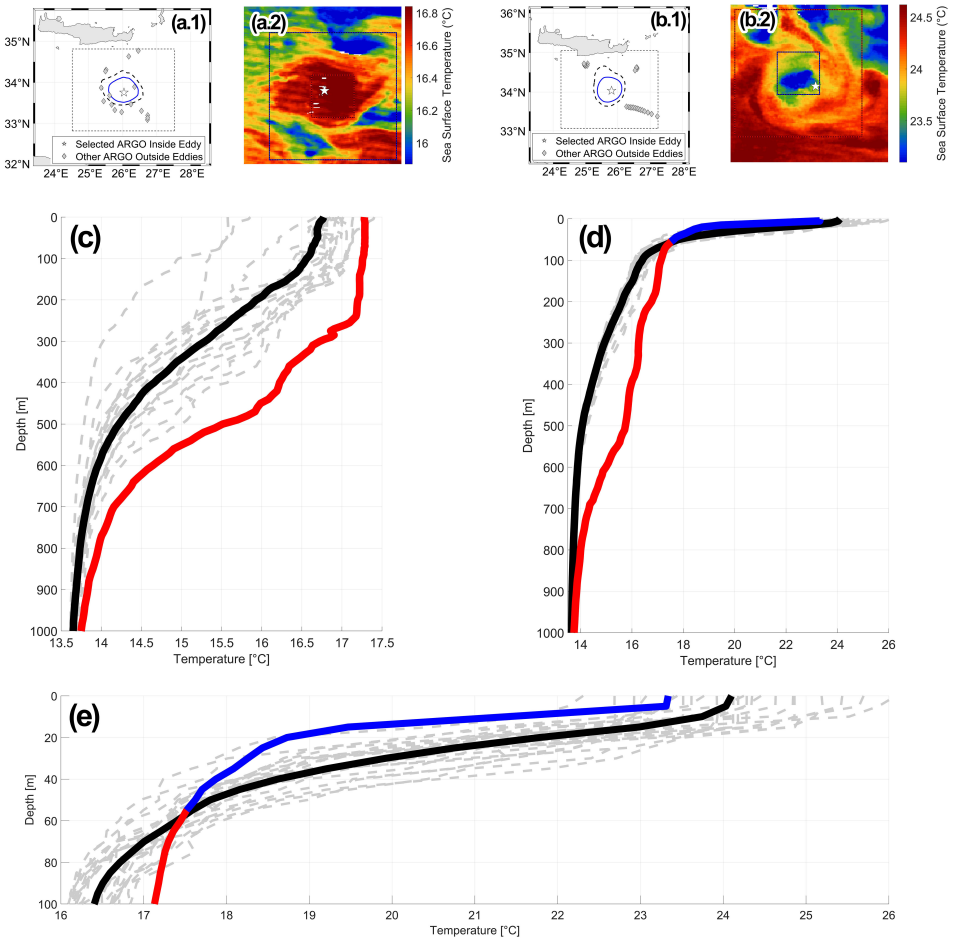

Figure 9. Seasonal evolution of the vertical structure of the Ierapetra eddy. Panels (**a**,**c**) correspond to a Warm Core SST observation of the eddy on 26/02/2017. Panels (**b**–**e**) correspond to a Cold Core SST observation on 26/07/2017. Maps (**a.1**,**a.2**) show the maximum velocity contour and outermost contour of the eddy, the eddy-sampling ARGO profile with a star and the outside-eddy profiles with diamonds, which are retained in a region outlined by the dashed rectangle. Patches (**b.1**,**b.2**) show the SST anomaly of the eddy along with the location of the eddy-sampling profile, which is plotted with a star. Vertical plots (**c**–**e**) show the outside-eddy profiles plotted with dashed gray lines and their mean outside-eddy profile with a thick black line. The eddy-sampling profile is plotted with a thick red (blue) line when it is warmer (colder) than the mean outside-eddy profile. Profile (**c**) shows the winter regular surface anomaly, with a warm structure, profile (**d**) shows the summer inverse surface anomaly with a cold surface and a warm subsurface structure, while panel (**e**) zooms into the 100 first meters of (**d**) to portray the SST inversion.

Due to the deep winter mixed layer, the Warm Core SST anomaly extends down to 250 m (Figure 9c). On this winter profile, the core of the anticyclone is always warmer that its surrounding down to 1000 m. An inversion of the eddy-SSTA is visible on the summer profile (Figure 9d). However, this Cold Core temperature anomaly does not extend below a few tens of meters (Figure 9e). Below the strong summer stratification, at −100 m for instance, the core temperature of the anticyclone is warmer than its surrounding waters

whose temperature is portrayed by the mean outside-eddy profile (black line in Figure 9d). The subsurface temperature anomaly reaches a positive value of +1 °C at 500 m, which is coherent with other observations of long-lived anticyclonic eddies in the region [24,45]. Hence, these unique in situ measurements indicate that the inverse eddy-SSTA remains confined to a few dozen meters below the ocean surface and does not correspond to the deep subsurface heat content of the anticyclone.

3.2. A Mechanism of SST Anomaly Inversion: Single Column Simulations

The analysis from the perspective of the regime change of individual eddies between Warm and Cold Core portrays that the winter mixed layer varies significantly inside long-lived mesoscale eddies, particularly in the core of anticyclones. However, is this MLD difference between the core of the eddy and its vicinity sufficient enough to explain the inverse eddy-SSTA that occurs during the spring re-stratification?

To answer this question and investigate other hypotheses, we use a simplified 1D model of the vertical advection–diffusion of heat in a stratified water column inside and outside mesoscale eddies. The seasonal forcing of the atmosphere is simulated with a sinusoidal surface temperature flux as $Q = Q_0 sin(2\pi t/365.25)$ ($Q_0 > 0$, positive for ocean heat gain), so that the simulation starts with a temperature flux increasing from zero (corresponding to spring). A value of $Q_0 = 150$ W/m^2 is chosen as an accurate Mediterranean average of total surface heat flux seasonal cycle, following [46], with a negative (positive) maximum heat flux approximately in December (July). As salinity effects are neglected, the temperature flux is equivalent to the buoyancy flux.

An equal surface heat flux is applied for different temperature profiles corresponding to water columns inside a cyclone, anticyclone and a profile outside an eddy, respectively. The simulation starts on the end of the winter period when the MLD is at its deepest. The initial profiles are described analytically in Equation (3), whose parameters are chosen so that the simulated profiles represent average temperature profiles in the Mediterranean sea. These stand for a homogeneous MLD of $Z_{MLD} = 50$ m at $T_0 = 16$ °C for a cyclone core, 200 m at 18 °C for an anticyclone core and 100 m at 17 °C for the outside-eddy profile. Below the mixed layer, we introduce an exponential decrease (typical thickness $Z_T = 150$ m) to a deep ocean value of $T_b = 13.5$ °C. The $T(z)$ profiles are plotted on panels (b) and (d) of Figure 10, with a blue, red and black line for the anticyclone, cyclone and outside-eddy profiles, respectively.

$$\begin{aligned} T(z) &= T_0 && ; \text{if} z > Z_{MLD} \\ T(z) &= T_b + (T_0 - T_b) exp\left(\frac{z - Z_{MLD}}{Z_T}\right) && ; \text{if} z < Z_{MLD} \end{aligned} \tag{3}$$

Vertical profiles are forced by the surface heat flux, and in a one-dimensional space, the temperature temporal evolution follows a simple diffusion equation:

$$\frac{\partial T}{\partial t} = \frac{\partial}{\partial z}\left(A(z)\frac{\partial T}{\partial z}\right) \tag{4}$$

We assume a steady turbulent mixing coefficient $A(z)$ which depends only on depth. This vertical mixing profile is set by the Equation (5), starting from a surface value A_0 down to a deep ocean value A_{back} with a Gaussian vertical shape, with $Z_T = 150$ m. The static instability (i.e., $\partial_z T < 0$) is inhibited by simply boosting the mixing coefficient $A(z)$ to 1 m^2/s.

$$A(z) = A_{back} + A_0 e^{-(z/Z_T)^2} \tag{5}$$

We first assume that the vertical mixing profile remains the same in the cyclone, the anticyclone and the outside-eddy. The surface value A_0 of 10^{-4} m^{2}s^{-1} is chosen as a typical value for turbulent mixing in the upper ocean, while in the deep ocean, the mixing is

reduced by two orders of magnitude down to $A_{back} = 1.0 \times 10^{-6}$ m^{2}s^{-1}, which is the water kinematic viscosity.

The uniform vertical mixing profile, common for both three water columns, is plotted in panel (a) of Figure 10, while the response of the three water columns (anticyclone, cyclone, outside-eddy) is plotted in panel (b). The simulation starts from a deep-MLD profile at the end of the winter mixing period (dashed line). During spring re-stratification, the positive surface is transferred downwards at the same rate for all water columns. As a consequence, the surface temperature difference between the three winter profiles is also maintained in summer (continuous line). This effect is also observed in panel (b) of Figure 11 where the seasonal evolution of the SST of the three water columns is plotted on a 18-month period. The anticyclonic (cyclonic) profile is constantly warmer (colder) than the outside-eddy profile. A two-month lag between the surface flux of Figure 11 panel (a) and the SST of panel (b) is explained through the delay needed for the water column to integrate the radiative forcing.

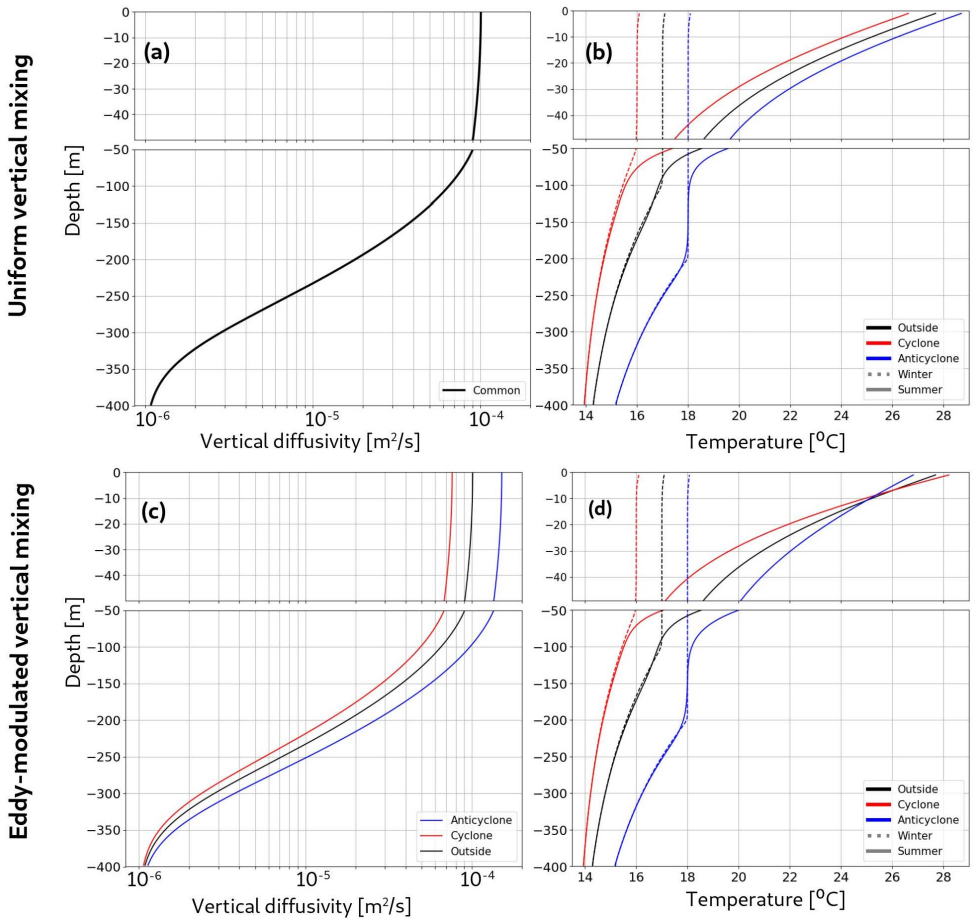

Figure 10. One-dimensional (1D) single column experiments: vertical structure. With a uniform vertical mixing: (**a**) vertical diffusivity $A(z)$ from Equation (5) and (**b**) temperature profiles in winter (dashed line) and summer (continuous line), corresponding time of the year being reported on Figure 11b . Initial winter profiles are set in Equation (3). With eddy-modulated vertical mixing: (**c**) vertical diffusivity and (**d**) temperature profiles.

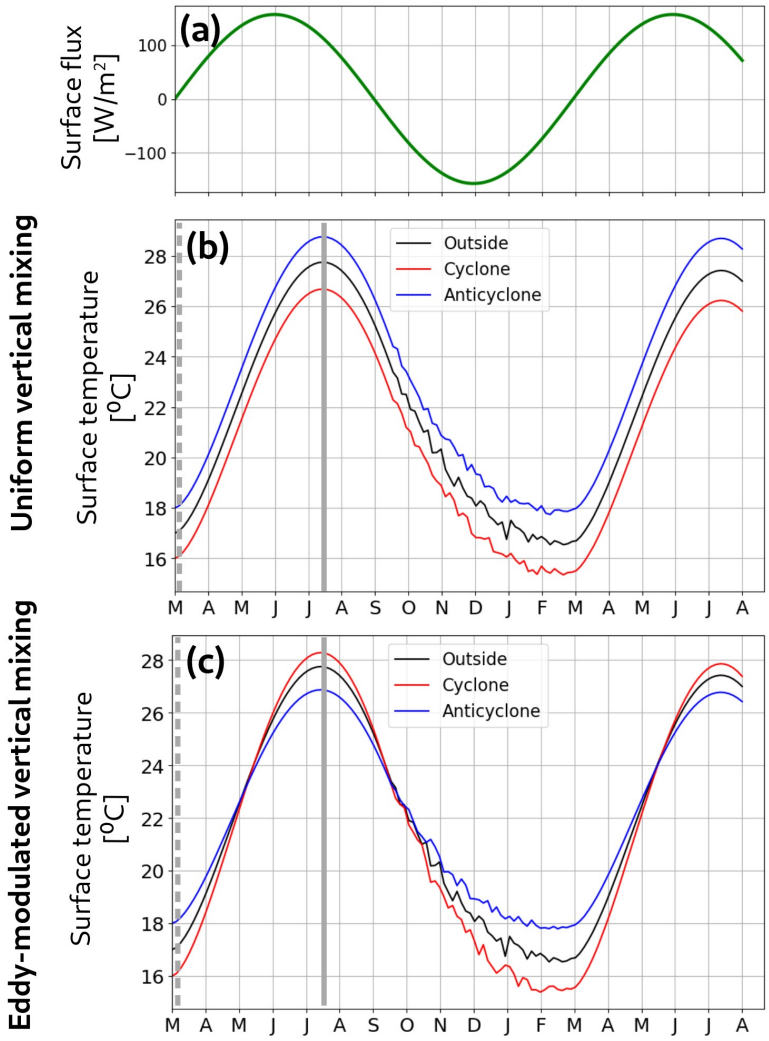

Figure 11. One-dimensional (1D) single column experiments: surface temperature. (**a**) Surface heat flux forcing the simulation, (**b**) Surface temperature evolution for anticyclone, cyclone and outside-eddy profiles with a uniform vertical mixing and (**c**) same as (**b**) but with an eddy-modulated vertical mixing, as shown in Figure 10c.

The initial differences of temperature profiles and winter MLD are not sufficient to reproduce observed eddy-SSTA inversion, suggesting that an additional physical process is missing. To explore such a mechanism, we assume that the vertical mixing coefficient is, on the one hand, enhanced in the core of anticyclonic eddies and, on the other hand, reduced in the core of cyclonic eddies. To test this hypothesis, we perform another set of heat vertical diffusion experiments with the same vertical profiles (Equation (3)) and diffusion process (Equations (4) and (5)) but with a varying surface vertical diffusivity value. A_0 stays outside-eddy at $1.0 \times 10^{-4}\,\mathrm{m^2 s^{-1}}$ but is divided by a factor of 2 to $5.0 \times 10^{-5}\,\mathrm{m^2 s^{-1}}$ in the cyclone profile and multiplied by 2 to $2.0 \times 10^{-4}\,\mathrm{m^2 s^{-1}}$ in the anticyclone one. These eddy-modulated vertical mixing profiles are plotted in panel (c) of Figure 10 with a blue/red/black colour representing the anticyclone/cyclone/outside-eddy profile.

Through the seasonal evolution results of the eddy-modulated vertical mixing model, as shown in panel (d) of Figure 10, it is observed that heat penetrates deeper in the vertical structure of the anticyclone, resulting in a less stratified profile in summer (blue continuous line). Vice versa, the heat reaches a shallower depth of the cyclone, resulting in a more stratified summer profile (red continuous line). The vertical diffusivity difference is strong

enough that the anticyclone (respectively cyclone) profile becomes cooler (warmer) than the outside-eddy profile, resulting in an isotherm crossing similar to what was observed in the Ierapetra anticyclone, which is seen at panel (e) of Figure 9.

The evolution of surface temperature given by the eddy modulated vertical mixing model, shown in panel (c) of Figure 11 for more than a year and a half, reproduces the same SST anomaly summer inversion in cyclones and anticyclones. The column representative of an AE (CE) core is indeed warmer (colder) in winter at the surface than a column representative of an outside-eddy profile stratification while turning colder (warmer) in summer, implying that an inverse SST anomaly has emerged.

These simplified 1D model simulations show that despite initial differences in vertical stratification or MLD, a differential mixing coefficient between the core and the periphery of oceanic eddies is needed to explain the inverse sea surface temperature anomalies which emerge during the spring re-stratification period.

4. Discussion

The emergence of inverse eddy SST anomalies during the summer season, in the global ocean as well as in regional seas, has been well documented by recent studies [30–33,35]. Some of them also link this inversion of the eddy surface anomaly with the spring re-stratification of the ocean surface. This study confirms that such seasonal correlation is also valid for the Mediterranean Sea (Figure 6). Nevertheless, we showcase here that the difference in the MLD alone is a necessary but not sufficient condition for the emergence of an inverse eddy SST anomaly. We consider the hypothesis that eddies modulate the diapycnal mixing in their interior, creating a vertical spacing (tightening) of isopycnals in anticyclones (cyclones). Our 1D single column modelling experiment (Figures 10 and 11) shows that a modulation of vertical mixing $A(z)$ inside eddies is needed to reproduce the inversion of the eddy-induced SST anomalies during summer. The origin of this vertical mixing modulation might stem from 3D dynamical processes that cannot be reproduced explicitly in the 1D vertical model.

Some hypotheses exist in the bibliography, and several papers studied the trapping of Near-Inertial Oscillations (NIO) in anticyclones either through a theoretical formulation [47,48] or through modelling experiments [49–51] and observations [52]. Enhanced turbulent mixing at depth was also reported when NIO were trapped inside anticyclones [53,54]. Nevertheless, we are not aware of a theoretical study that provides a direct link between the trapping of NIO and enhanced vertical mixing in the thermocline layer. The opposite trend for cyclones is still under discussion. However, due to the Coriolis effect $f_{eff} = f + \zeta$, which is higher for positive vorticity area ($\zeta > 0$), the spectrum of NIO is expected to be reduced in the core of cyclonic eddies [47,48]. This impact of NIO within the eddies is a very plausible explanation of the differential vertical mixing and the observed eddy-SSTA asymmetry between cyclone and anticyclones. Nevertheless, other mechanisms could also be responsible for inverse eddy SST anomalies such as nonlinear wind-induced Ekman pumping.

Motivated by the impact of eddies on biological productivity, several studies investigate the self-induced Ekman pumping in the core of mesoscale cyclones and anticyclones. Local currents induced by coherent eddies generate a curl to the surface stress from the relative motion between surface air and water, even if the wind stress is uniform. Hence, a uniform wind applied to an anticyclonic eddy can lead to a divergence and upwelling in its core [9,28,55]. A local upwelling could therefore induce a Cold Core anomaly for anticyclones. However, such a mechanism depends directly on the eddy intensity, and we did not find on the data of this study any correlation between the amplitude of the temperature anomaly in the core of the eddy and its intensity. Nevertheless, to investigate in more details the impacts of the wind-induced Ekman pumping on the emergence of inverse eddy SST anomalies, a full 3D numerical simulation will be performed in a future work.

5. Summary and Conclusions

The emergence of inverse eddy SST anomalies in the Mediterranean Sea is a seasonal phenomenon that affects all mesoscale eddies. Remote sensing and in situ observations were used to detect and quantify the eddy-induced SST anomaly over a 2-year period (2016–2018). We build an eddy core SST anomaly index to quantify the amount of Cold Core Anticyclones and Warm Core Cyclones all over the year and especially during the spring re-stratification period. We find that these inverse eddy anomalies could reach a peak of 70% in May and June. This seasonal cycle coincides with the seasonal variation of the MLD both through a statistical analysis, on a basin scale, and through an individual analysis for long-lived eddies. By tracking these eddies, we find that some of them alternate several times, from one season to another, between a Warm Core and a Cold Core SST anomaly. However, the inverse eddy anomalies are constrained to the upper layer of the ocean. For instance, co-localising ARGO profiles in Cold Core anticyclonic eddies reveals that their cold temperature anomaly inversion is limited to the first 50 m of the ocean, while a warm subsurface anomaly persists deeper.

We propose a simple dynamical mechanism, based on a differential mixing between the eddy core and its surroundings, that leads to reproducing Cold Core (Warm Core) anticyclones (cyclones) during the spring re-stratification period. To do so, we construct a simple vertical column model to compute the impact of the seasonal air–sea flux on the vertical stratification inside and outside eddies. We start off by a winter stratification setup with a deep mixed layer and investigate how the spring re-stratification of the ocean surface differs between the eddy core and its surrounding. By considering only the MLD difference, we were not able to reproduce the inverse eddy-SSTA that are observed during the spring re-stratification period in satellite data. It is only by taking into account a differential diapycnal eddy mixing—increased in anticyclones and diminished in cyclones—that we reproduce correctly the surface temperature inversion in the eddy core with respect to an outside-eddy profile. This simplified model suggests that vertical mixing modulation by mesoscale eddies might be the key mechanism that leads to the eddy-SSTA seasonal inversion in the ocean. Even if our study focuses on the Mediterranean Sea, the mechanism proposed here is, a priori, independent of the oceanic region.

Several theoretical studies on near inertial oscillations and corresponding in situ observations could explain the modulation of the vertical mixing induced by oceanic eddies and the cyclone/anticyclone asymmetry. However, full 3-dimensional modelling is necessary to further investigate these dynamical modes in combination with the wind-induced Ekman pumping inside the eddy core. Such high-resolution simulations are beyond the scope of this study and will be the perspectives of a future work.

Lastly, this study showcases that a detailed analysis of remote sensing observations of the complex eddy signature at the ocean surface could reveal its subsurface structure in the first tens of metres. This would provide valuable information on the vertical extension of the mixing layer or the bio-geochemical activity in the euphotic layer.

Author Contributions: Conceptualization, E.M., A.B. and A.S.; methodology, E.M, A.B. and A.S.; software, E.M. and A.B.; validation, A.S.; formal analysis, E.M., A.B. and A.S.; investigation, E.M., A.B. and A.S.; resources, A.S.; data curation, E.M. and A.B.; writing—original draft preparation, E.M. and A.B.; writing—review and editing, A.S.; visualization, E.M. and A.B.; supervision, A.S.; project administration, A.S.; funding acquisition, A.S. All authors have read and agreed to the published version of the manuscript.

Funding: This research received no external funding.

Data Availability Statement: This study has been conducted using E.U. Copernicus Marine Service Information; https://doi.org/10.48670/moi-00141, https://doi.org/10.48670/moi-00171. The DYNED-Atlas of eddy tracks in the Mediterranean Sea is publicly available: https://www1.lmd.polytechnique.fr/dyned/.

Conflicts of Interest: The authors declare no conflict of interest.

Appendix A. Eddy Timelines

We provide three additional eddy timelines of long-lived eddies: an Algeria anticyclone (Figure A1), a Cyprus (Eratosthenes) anticyclone (Figure A2) and a Liguria cyclone (Figure A3). The reader is referred to Figure 8 (timeline of the Ierapetra long-lived eddy) in the main corpus of the text for a detailed description of the timelines as individual eddy analysis of the sea surface temperature anomaly evolution.

We note several particularities compared with the Ierapetra anticyclone: The Algeria anticyclone in the western Mediterranean shows the same swift between Cold Core anomaly (summer) to Warm Core anomaly (winter) while having a smaller local MLD than the Ierapetra eddy. The Cyprus anticyclone in the eastern Mediterranean shows a persistent inverse Cold Core anomaly ranging from May to December, while the regular Warm Core anomaly appears only for a few winter months. Finally, the Liguria cyclone shows that the shift between regular and inverse anomalies can also emerge for long-lived cyclones, corresponding also with the MLD seasonal cycle.

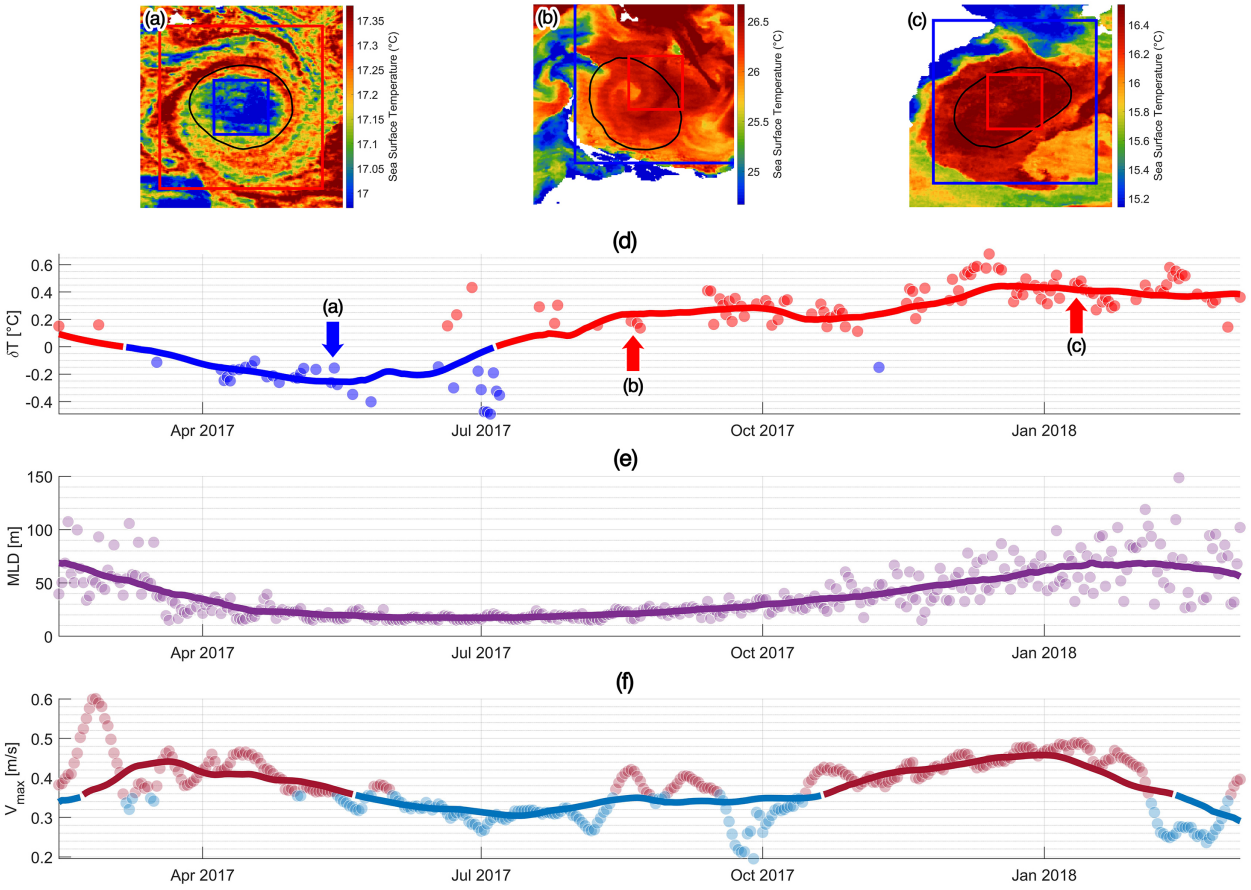

Figure A1. Timeline of the Algeria anticyclone with DYNED ID #11411. Panels (**a**–**c**) show four characteristic SST patches corresponding with the δT evolution in panel (**d**). Panel (**e**) shows the evolution of the MLD outside the eddy. Panel (**f**) shows the evolution of the maximal velocity. Lines represent the Monthly Mean Average of each variable. For more information, the reader is referred to Figure 8.

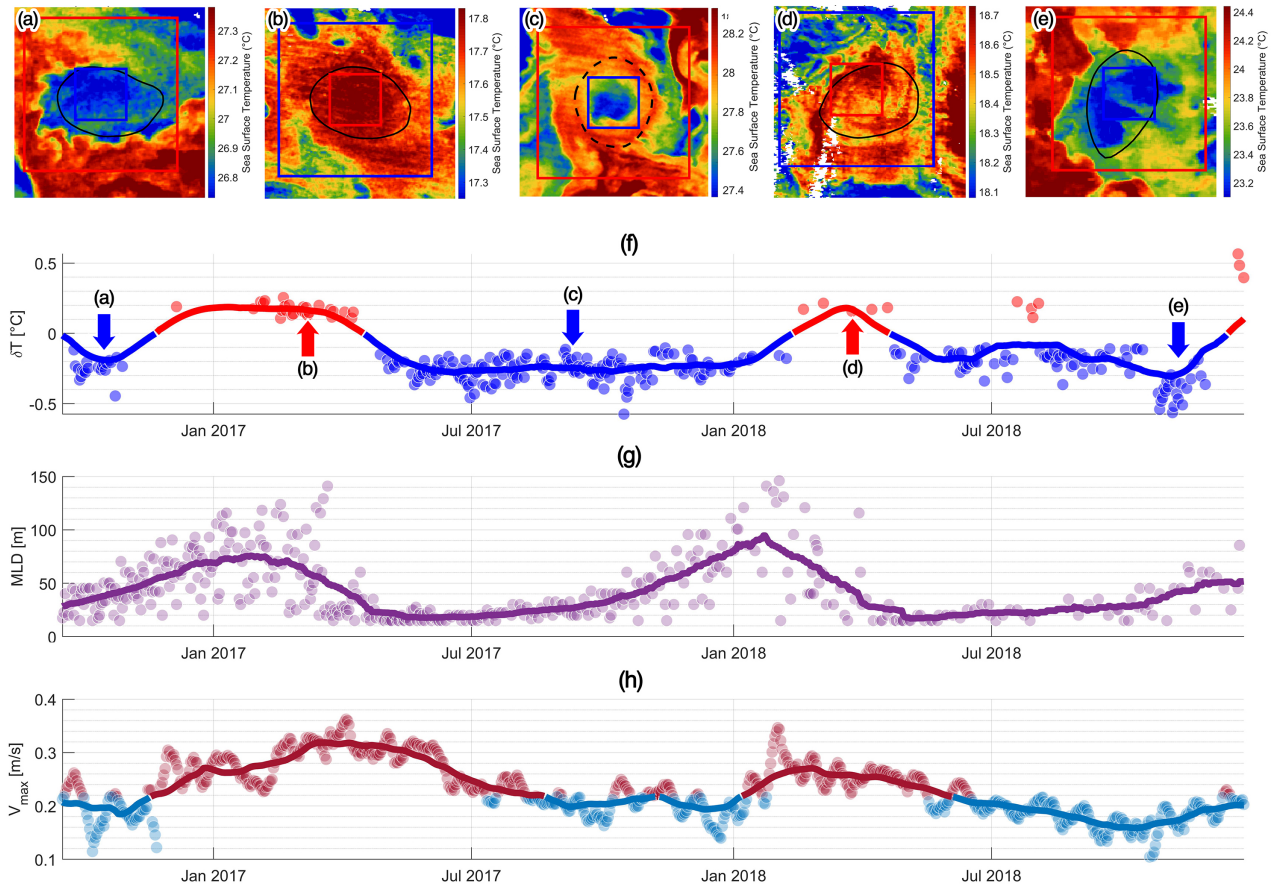

Figure A2. Timeline of the Cyprus (Eratosthenes) anticyclone with DYNED ID #10754. Panels (**a**–**e**) show four characteristic SST patches corresponding with the δT evolution in panel (**f**). Panel (**g**) shows the evolution of the MLD outside the eddy. Panel (**h**) shows the evolution of the maximal velocity. Lines represent the Monthly Mean Average of each variable. For more information, the reader is referred to Figure 8.

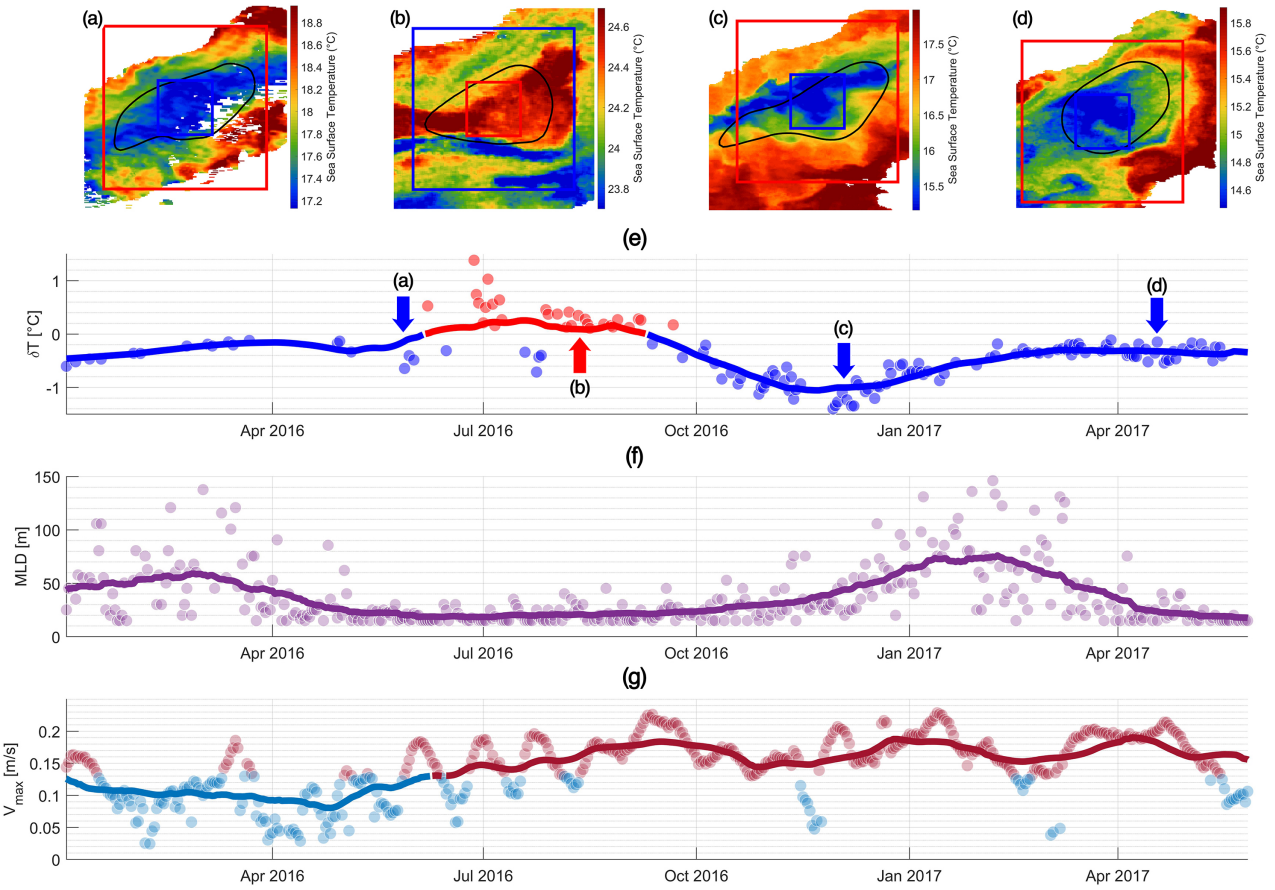

Figure A3. Timeline of the Liguria cyclone with DYNED ID #9784. Panels (**a**–**d**) show four characteristic SST patches corresponding with the δT evolution in panel (**e**). Panel (**f**) shows the evolution of the MLD outside the eddy. Panel (**g**) shows the evolution of the maximal velocity. Lines represent the Monthly Mean Average of each variable. For more information, the reader is referred to Figure 8.

References

1. Chelton, D.B.; Schlax, M.G.; Samelson, R.M. Global observations of nonlinear mesoscale eddies. *Prog. Oceanogr.* **2011**, *91*, 167–216. [CrossRef]
2. Su, Z.; Wang, J.; Klein, P.; Thompson, A.F.; Menemenlis, D. Ocean submesoscales as a key component of the global heat budget. *Nat. Commun.* **2018**, *9*, 775. [CrossRef] [PubMed]
3. Zhang, Z.; Wang, W.; Qiu, B. Oceanic mass transport by mesoscale eddies. *Science* **2014**, *345*, 322–324. [CrossRef] [PubMed]
4. Laxenaire, R.; Speich, S.; Blanke, B.; Chaigneau, A.; Pegliasco, C.; Stegner, A. Anticyclonic eddies connecting the western boundaries of Indian and Atlantic Oceans. *J. Geophys. Res. Ocean.* **2018**, *123*, 7651–7677. [CrossRef]
5. Ji, J.; Dong, C.; Zhang, B.; Liu, Y.; Zou, B.; King, G.P.; Xu, G.; Chen, D. Oceanic eddy characteristics and generation mechanisms in the Kuroshio Extension region. *J. Geophys. Res. Ocean.* **2018**, *123*, 8548–8567. [CrossRef]
6. Badin, G.; Williams, R.; Holt, J.; Fernand, L. Are mesoscale eddies in shelf seas formed by baroclinic instability of tidal fronts? *J. Geophys. Res. Ocean.* **2009**, *114*, C10021. [CrossRef]
7. Ioannou, A.; Stegner, A.; Le Vu, B.; Taupier-Letage, I.; Speich, S. Dynamical evolution of intense Ierapetra eddies on a 22 year long period. *J. Geophys. Res. Ocean.* **2017**, *122*, 9276–9298. [CrossRef]
8. Gaube, P.; Chelton, D.B.; Strutton, P.G.; Behrenfeld, M.J. Satellite observations of chlorophyll, phytoplankton biomass, and Ekman pumping in nonlinear mesoscale eddies. *J. Geophys. Res. Ocean.* **2013**, *118*, 6349–6370. [CrossRef]
9. McGillicuddy, D.J., Jr. Mechanisms of physical-biological-biogeochemical interaction at the oceanic mesoscale. *Annu. Rev. Mar. Sci.* **2016**, *8*, 125–159. [CrossRef]
10. Lévy, M.; Franks, P.J.; Smith, K.S. The role of submesoscale currents in structuring marine ecosystems. *Nat. Commun.* **2018**, *9*, 4758. [CrossRef]

11. Gaube, P.; J. McGillicuddy, D., Jr.; Moulin, A.J. Mesoscale eddies modulate mixed layer depth globally. *Geophys. Res. Lett.* **2019**, *46*, 1505–1512. [CrossRef]
12. Frenger, I.; Gruber, N.; Knutti, R.; Münnich, M. Imprint of Southern Ocean eddies on winds, clouds and rainfall. *Nat. Geosci.* **2013**, *6*, 608–612. [CrossRef]
13. Klein, P.; Lapeyre, G. The oceanic vertical pump induced by mesoscale and submesoscale turbulence. *Annu. Rev. Mar. Sci.* **2009**, *1*, 351–375. [CrossRef]
14. Baudena, A.; Ser-Giacomi, E.; D'Onofrio, D.; Capet, X.; Cotté, C.; Cherel, Y.; D'Ovidio, F. Fine-scale structures as spots of increased fish concentration in the open ocean. *Sci. Rep.* **2021**, *11*, 15805. [CrossRef]
15. Abrahms, B.; Scales, K.L.; Hazen, E.L.; Bograd, S.J.; Schick, R.S.; Robinson, P.W.; Costa, D.P. Mesoscale activity facilitates energy gain in a top predator. *Proc. R. Soc. B* **2018**, *285*, 20181101. [CrossRef]
16. Gómez, G.S.D.; Nagai, T.; Yokawa, K. Mesoscale warm-core eddies drive interannual modulations of swordfish catch in the Kuroshio Extension System. *Front. Mar. Sci.* **2020**, *7*, 680. [CrossRef]
17. Brach, L.; Deixonne, P.; Bernard, M.F.; Durand, E.; Desjean, M.C.; Perez, E.; van Sebille, E.; Ter Halle, A. Anticyclonic eddies increase accumulation of microplastic in the North Atlantic subtropical gyre. *Mar. Pollut. Bull.* **2018**, *126*, 191–196. [CrossRef]
18. Hamad, N.; Millot, C.; Taupier-Letage, I. The surface circulation in the eastern basin of the Mediterranean Sea. *Sci. Mar.* **2006**, *70*, 457–503.
19. Amitai, Y.; Lehahn, Y.; Lazar, A.; Heifetz, E. Surface circulation of the eastern Mediterranean Levantine basin: Insights from analyzing 14 years of satellite altimetry data. *J. Geophys. Res. Ocean.* **2010**, *115*, C10058. [CrossRef]
20. Menna, M.; Poulain, P.M.; Zodiatis, G.; Gertman, I. On the surface circulation of the Levantine sub-basin derived from Lagrangian drifters and satellite altimetry data. *Deep. Sea Res. Part I Oceanogr. Res. Pap.* **2012**, *65*, 46–58. [CrossRef]
21. Mkhinini, N.; Coimbra, A.L.S.; Stegner, A.; Arsouze, T.; Taupier-Letage, I.; Béranger, K. Long-lived mesoscale eddies in the eastern Mediterranean Sea: Analysis of 20 years of AVISO geostrophic velocities. *J. Geophys. Res. Ocean.* **2014**, *119*, 8603–8626. [CrossRef]
22. Escudier, R.; Renault, L.; Pascual, A.; Brasseur, P.; Chelton, D.; Beuvier, J. Eddy properties in the Western Mediterranean Sea from satellite altimetry and a numerical simulation. *J. Geophys. Res. Ocean.* **2016**, *121*, 3990–4006. [CrossRef]
23. Pessini, F.; Olita, A.; Cotroneo, Y.; Perilli, A. Mesoscale eddies in the Algerian Basin: Do they differ as a function of their formation site? *Ocean. Sci.* **2018**, *14*, 669–688. [CrossRef]
24. Barboni, A.; Lazar, A.; Stegner, A.; Moschos, E. Lagrangian eddy tracking reveals the Eratosthenes anticyclonic attractor in the eastern Levantine basin. *Ocean. Sci. Discuss.* **2021**,*17*, 1231–1250. [CrossRef]
25. Millot, C. Some features of the Algerian Current. *J. Geophys. Res. Ocean.* **1985**, *90*, 7169–7176. [CrossRef]
26. Auer, S.J. Five-year climatological survey of the Gulf Stream system and its associated rings. *J. Geophys. Res. Ocean.* **1987**, *92*, 11709–11726. [CrossRef]
27. Hausmann, U.; Czaja, A. The observed signature of mesoscale eddies in sea surface temperature and the associated heat transport. *Deep. Sea Res. Part Oceanogr. Res. Pap.* **2012**, *70*, 60–72. [CrossRef]
28. Gaube, P.; Chelton, D.B.; Samelson, R.M.; Schlax, M.G.; O'Neill, L.W. Satellite observations of mesoscale eddy-induced Ekman pumping. *J. Phys. Oceanogr.* **2015**, *45*, 104–132. [CrossRef]
29. Everett, J.; Baird, M.; Oke, P.; Suthers, I. An avenue of eddies: Quantifying the biophysical properties of mesoscale eddies in the Tasman Sea. *Geophys. Res. Lett.* **2012**, *39*, L16608. [CrossRef]
30. Leyba, I.M.; Saraceno, M.; Solman, S.A. Air-sea heat fluxes associated to mesoscale eddies in the Southwestern Atlantic Ocean and their dependence on different regional conditions. *Clim. Dyn.* **2017**, *49*, 2491–2501. [CrossRef]
31. Trott, C.B.; Subrahmanyam, B.; Chaigneau, A.; Roman-Stork, H.L. Eddy-induced temperature and salinity variability in the Arabian Sea. *Geophys. Res. Lett.* **2019**, *46*, 2734–2742. [CrossRef]
32. Sun, W.; Dong, C.; Tan, W.; He, Y. Statistical Characteristics of Cyclonic Warm-Core Eddies and Anticyclonic Cold-Core Eddies in the North Pacific Based on Remote Sensing Data. *Remote Sens.* **2019**, *11*, 208. [CrossRef]
33. Liu, Y.; Yu, L.; Chen, G. Characterization of Sea Surface Temperature and Air-Sea Heat Flux Anomalies Associated With Mesoscale Eddies in the South China Sea. *J. Geophys. Res. Ocean.* **2020**, *125*, e2019JC015470. [CrossRef]
34. Assassi, C.; Morel, Y.; Vandermeirsch, F.; Chaigneau, A.; Pegliasco, C.; Morrow, R.; Colas, F.; Fleury, S.; Carton, X.; Klein, P.; et al. An index to distinguish surface-and subsurface-intensified vortices from surface observations. *J. Phys. Oceanogr.* **2016**, *46*, 2529–2552. [CrossRef]
35. Ni, Q.; Zhai, X.; Jiang, X.; Chen, D. Abundant cold anticyclonic eddies and warm cyclonic eddies in the global ocean. *J. Phys. Oceanogr.* **2021**, *51*, 2793–2806. [CrossRef]
36. Nardelli, B.B.; Tronconi, C.; Pisano, A.; Santoleri, R. High and Ultra-High resolution processing of satellite Sea Surface Temperature data over Southern European Seas in the framework of MyOcean project. *Remote Sens. Environ.* **2013**, *129*, 1–16. [CrossRef]
37. Le Vu, B.; Stegner, A.; Arsouze, T. Angular Momentum Eddy Detection and tracking Algorithm (AMEDA) and its application to coastal eddy formation. *J. Atmos. Ocean. Technol.* **2018**, *35*, 739–762. [CrossRef]
38. Ioannou, A.; Stegner, A.; Tuel, A.; Levu, B.; Dumas, F.; Speich, S. Cyclostrophic corrections of AVISO/DUACS surface velocities and its application to mesoscale eddies in the Mediterranean Sea. *J. Geophys. Res. Ocean.* **2019**, *124*, 8913–8932. [CrossRef]
39. de Boyer Montégut, C.; Madec, G.; Fischer, A.S.; Lazar, A.; Iudicone, D. Mixed layer depth over the global ocean: An examination of profile data and a profile-based climatology. *J. Geophys. Res. Ocean.* **2004**, *109*, C12003. [CrossRef]

40. Moschos, E.; Schwander, O.; Stegner, A.; Gallinari, P. DEEP-SST-EDDIES: A Deep Learning framework to detect oceanic eddies in Sea Surface Temperature images. In Proceedings of the ICASSP 2020-2020 IEEE International Conference on Acoustics, Speech and Signal Processing (ICASSP), Barcelona, Spain, 4–8 May 2020; pp. 4307–4311.
41. Moschos, E.; Stegner, A.; Schwander, O.; Gallinari, P. Classification of Eddy Sea Surface Temperature Signatures under Cloud Coverage. *IEEE J. Sel. Top. Appl. Earth Obs. Remote. Sens.* **2020**, *13*, 3437–3447. [CrossRef]
42. Amores, A.; Jordà, G.; Arsouze, T.; Le Sommer, J. Up to what extent can we characterize ocean eddies using present-day gridded altimetric products? *J. Geophys. Res. Ocean.* **2018**, *123*, 7220–7236. [CrossRef]
43. Stegner, A.; Le Vu, B.; Dumas, F.; Ghannami, M.A.; Nicolle, A.; Durand, C.; Faugere, Y. Cyclone-Anticyclone Asymmetry of Eddy Detection on Gridded Altimetry Product in the Mediterranean Sea. *J. Geophys. Res. Ocean.* **2021**, *126*, e2021JC017475. [CrossRef]
44. Liu, Y.; Weisberg, R.H.; Hu, C.; Kovach, C.; Riethmüller, R. Evolution of the Loop Current system during the Deepwater Horizon oil spill event as observed with drifters and satellites. *Monit. Model. Deep. Horiz. Oil Spill Rec.-Break. Enterp. Geophys. Monogr. Ser* **2011**, *195*, 91–101.
45. Moutin, T.; Prieur, L. Influence of anticyclonic eddies on the Biogeochemistry from the Oligotrophic to the Ultraoligotrophic Mediterranean (BOUM cruise). *Biogeosciences* **2012**, *9*, 3827–3855. [CrossRef]
46. Pettenuzzo, D.; Large, W.; Pinardi, N. On the corrections of ERA-40 surface flux products consistent with the Mediterranean heat and water budgets and the connection between basin surface total heat flux and NAO. *J. Geophys. Res. Ocean.* **2010**, *115*, C06022. [CrossRef]
47. Kunze, E. Near-inertial wave propagation in geostrophic shear. *J. Phys. Oceanogr.* **1985**, *15*, 544–565. [CrossRef]
48. Young, W.; Jelloul, M.B. Propagation of near-inertial oscillations through a geostrophic flow. *J. Mar. Res.* **1997**, *55*, 735–766. [CrossRef]
49. Klein, P.; Smith, S.L. Horizontal dispersion of near-inertial oscillations in a turbulent mesoscale eddy field. *J. Mar. Res.* **2001**, *59*, 697–723. [CrossRef]
50. Danioux, E.; Vanneste, J.; Bühler, O. On the concentration of near-inertial waves in anticyclones. *J. Fluid Mech.* **2015**, *773*, R2. [CrossRef]
51. Lelong, M.P.; Cuypers, Y.; Bouruet-Aubertot, P. Near-inertial energy propagation inside a Mediterranean anticyclonic eddy. *J. Phys. Oceanogr.* **2020**, *50*, 2271–2288. [CrossRef]
52. Elipot, S.; Lumpkin, R.; Prieto, G. Modification of inertial oscillations by the mesoscale eddy field. *J. Geophys. Res. Ocean.* **2010**, *115*, C09010. [CrossRef]
53. Whalen, C.B.; MacKinnon, J.A.; Talley, L.D. Large-scale impacts of the mesoscale environment on mixing from wind-driven internal waves. *Nat. Geosci.* **2018**, *11*, 842–847. [CrossRef]
54. Martínez-Marrero, A.; Barceló-Llull, B.; Pallàs-Sanz, E.; Aguiar-González, B.; Estrada-Allis, S.N.; Gordo, C.; Grisolía, D.; Rodríguez-Santana, A.; Arístegui, J. Near-inertial wave trapping near the base of an anticyclonic mesoscale eddy under normal atmospheric conditions. *J. Geophys. Res. Ocean.* **2019**, *124*, 8455–8467. [CrossRef]
55. Ledwell, J.R.; McGillicuddy, D.J., Jr.; Anderson, L.A. Nutrient flux into an intense deep chlorophyll layer in a mode-water eddy. *Deep. Sea Res. Part II Top. Stud. Oceanogr.* **2008**, *55*, 1139–1160. [CrossRef]

Chapter 4

Eddy-induced mixed layer and interaction with subsurface anomalies

The mixed layer is the uppermost layer of the ocean, defined as the homogeneous layer extending from the surface to the first stratified layer. In practice the surface is often replaced by 10m in order to avoid the thin stratification in the last meter due to diurnal cycle (de Boyer Montégut et al., 2004). The mixed layer is then the ocean layer in contact with the atmosphere and driving air-ocean interactions. To have a first estimation of the eddy-induced effect on the mixed layer depth (MLD), the collocated in situ database presented in Sect.2.3 is used to compute the MLD, and anomalies are presented separetely for cyclones and anticyclones in Fig.4.1. The MLD is computed as the depth where the temperature at 10m is exceeded by a threshold $\Delta T = \pm 0.1°C$, following Houpert et al. (2015). To compare MLD anomalies induced by eddies, a background MLD is defined for each vertical profile as the median MLD among profiles constituting the reference background defined in Sect.2.5, with convention positive anomalies for deeper MLD. Winter MLD anomalies reveal extremely large values for both cyclones and anticyclones, winter being defined here at first from DeJanuary to March. As indicated in Fig.4.1b, anticyclonic MLD anomalies are largely positive, reaching $+200m$, and the largest observed values coincide with strong and recurrent anticyclonic structures already presented above and in Fig.2.2. On the opposite, winter eddy-induced MLD anomalies in cyclones are weaker (note the different colorbar range) and mostly negative despite some variability. We recover the composite vision from Sun et al. (2017) and Gaube et al. (2019) of anticyclones deepening the winter MLD and cyclones shallowing it, with a marked cyclone-anticyclone asymmetry similarly to eddy lifetime (Fig.2.4). The observed variability in cyclonic MLD anomalies could be due to different factors. The first is obviously as detailed in Sect.2.1 that cyclonic detections are a lot less reliable, then a significant part of profiles collocated inside cyclones are actually not inside the mesoscale structure but most likely in a patch of smaller cyclonic submesoscale structures (Stegner et al., 2021). A second effect is geometric: as cyclones tend to shoal isopycnals, MLD is shallower; but if the stratification is entirely mixed then deep convection conditions are met and then MLD values get very large. This deep convection preconditioning in cyclonic gyres has been extensively studied in the literature (Legg and Marshall, 1998). The cyclonic gyres in the Gulf of Lion (MEDOC Group, 1970; Send et al., 1995; Margirier et al., 2020) and the Southern Adriatic sea (Gačić et al., 2002) regularly host deep convection events explaining the large positive MLD anomalies labeled as inside cyclones.

Figure 4.1 should then be considered as the climatological vision of eddy-induced MLD anomalies, to be compared with classical MLD climatologies not labeling eddies (d'Ortenzio et al., 2005a; Houpert et al., 2015). But using the Lagrangian tracking from the DYNED Atlas, we can further investigate what is the detailed MLD temporal evolution inside each anticyclone, and link it to its vertical structure. This study published in *Ocean Science* journal (Barboni et al., 2023a) is included below and was conducted together with Solange Coadou-Chaventon (LMD, at that time WAPE Master 2 student). Following MLD evolution at short temporal scale on the order of the week led to reconsider the MLD method (gradient method instead of threshold method) and the background definition (see Sect.2.5). Details are given in Sect.3.2 of the study below, but the main difference is that profiles constituting the background are at a maximal distance of $D_c = 250km$ and $\Delta day = \pm 10d$, compared to $D_c = 150km$ and $\Delta day = \pm 10d$ in Sect.2.5. Δy is kept to $\pm 1y$ and threshold number to compute background to 10. These changes allow to study more accurately the MLD evolving on shorter timescales while keeping enough profiles to define a background. Sensitivity of the

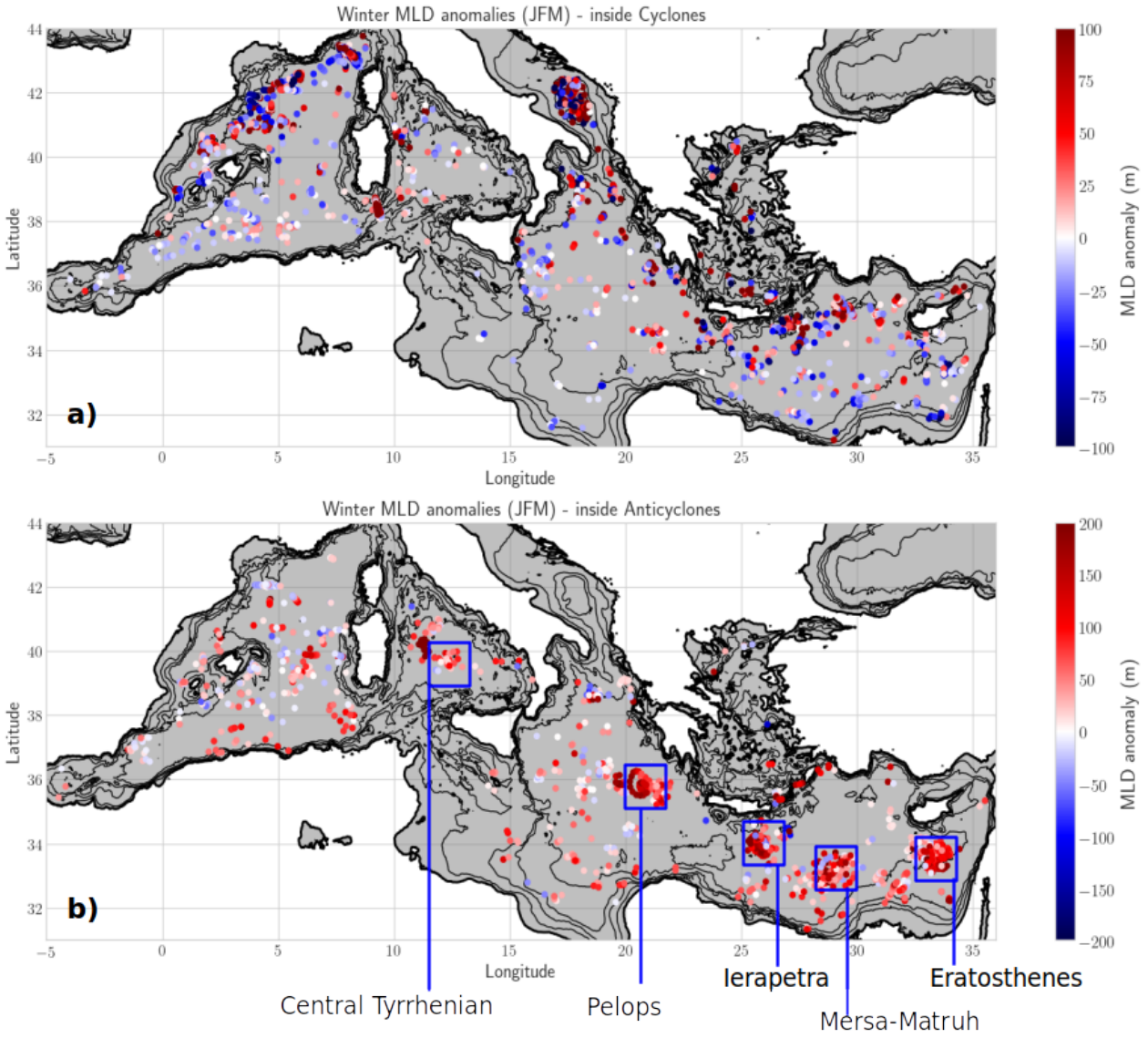

Figure 4.1: MLD anomalies from January to March shown as dots, for (a) cyclones and (b) anticyclones (2008-2021). Colorbar are scaled differently due to cyclone-anticyclone asymmetry in MLD anomalies. Main anticyclonic structures are reminded in blue squares.

Δday and Δy parameters is discussed in Appendix A of Barboni et al. (2023a).

4.1 Barboni et al. (2023a). How subsurface and double-core anticyclones intensify the winter mixed-layer deepening in the Mediterranean Sea. *Ocean Science*.

Ocean Sci., 19, 229–250, 2023
https://doi.org/10.5194/os-19-229-2023

Ocean Science Open Access EGU

How subsurface and double-core anticyclones intensify the winter mixed-layer deepening in the Mediterranean Sea

Alexandre Barboni[1,2,3], **Solange Coadou-Chaventon**[1], **Alexandre Stegner**[1], **Briac Le Vu**[1], **and Franck Dumas**[2,3]

[1]Laboratoire de Météorologie Dynamique/IPSL, École Polytechnique, Institut Polytechnique de Paris, ENS, Université PSL, Sorbonne Université, CNRS, Palaiseau, France
[2]Département de Recherche en Océanographie Physique, Service Hydrographique et Océanographique de la Marine (SHOM), Brest, France
[3]Laboratoire d'Océanographie Physique et Spatiale, UBO, Ifremer, IRD, Plouzané, France

Correspondence: Alexandre Barboni (alexandre.barboni@lmd.ipsl.fr) and Solange Coadou-Chaventon (solange.coadou-chaventon@lmd.ipsl.fr)

Received: 14 July 2022 – Discussion started: 3 August 2022
Revised: 16 December 2022 – Accepted: 24 January 2023 – Published: 7 March 2023

Abstract. The mixed layer is the uppermost layer of the ocean, connecting the atmosphere to the subsurface ocean through atmospheric fluxes. It is subject to pronounced seasonal variations: it deepens in winter due to buoyancy loss and shallows in spring while heat flux increases and restratifies the water column. A mixed-layer depth (MLD) modulation over this seasonal cycle has been observed within mesoscale eddies. Taking advantage of the numerous Argo floats deployed and trapped within large Mediterranean anticyclones over the last decades, we reveal for the first time this modulation at a 10 d temporal scale, free of the smoothing effect of composite approaches. The analysis of 16 continuous MLD time series inside 13 long-lived anticyclones at a fine temporal scale brings to light the importance of the eddy pre-existing vertical structure in setting the MLD modulation by mesoscale eddies. Extreme MLD anomalies of up to 330 m are observed when the winter mixed layer connects with a pre-existing subsurface anticyclonic core, greatly accelerating mixed-layer deepening. The winter MLD sometimes does not achieve such connection but homogenizes another subsurface layer, then forming a multi-core anticyclone with spring restratification. An MLD restratification delay is always observed, reaching more than 2 months in 3 out the 16 MLD time series. The water column starts to restratify outside anticyclones, while the mixed layer keeps deepening and cooling at the eddy core for a longer time. These new elements provide new keys for understanding anticyclone vertical-structure formation and evolution.

1 Introduction

The mixed layer corresponds to the ocean surface layer over which water properties are kept uniform through active mixing. It connects the atmosphere to the subsurface ocean through air–sea fluxes of heat, fresh water or other chemical components such as carbon (Takahashi et al., 2009; Large and Yeager, 2012). The mixed-layer depth (MLD) controls how deep the mixing acts, bringing water properties from below to the surface and the other way around. This depth is subject to pronounced seasonal variations, the mixed layer deepening with winter heat loss, while spring surface heating restratifies the column and the mixed layer gets shallower. Due to its importance for both ocean physics and biogeochemistry, global MLD climatologies were computed (de Boyer Montégut et al., 2004; Holte et al., 2017). Several MLD climatologies were also computed for the Mediterranean Sea (D'Ortenzio et al., 2005; Houpert et al., 2015), showing specific dynamics in winter convective regions such as the Gulf of Lion, the Aegean and the Adriatic seas, or the Rhodes gyre, with biological impacts on plankton bloom (D'Ortenzio and Ribera d'Alcalà, 2009; Lavigne et al., 2013). However large spread in MLD was also observed in regions hosting intense anticyclones such as the Algerian, Ionian and Levantine basins (Houpert et al., 2015), highlighting the need to take into account the local impact of mesoscale eddies.

Recent development of automatic eddy-tracking algorithms and eddy atlases (at a global scale, see for example Chelton et al., 2011, and Pegliasco et al., 2022; in the Mediterranean, see Stegner and Le Vu, 2019), combined with an increase of in situ measurements thanks to the development of autonomous platforms (Le Traon, 2013), recently allowed the influence of mesoscale oceanic eddies on the MLD to be studied. It is now well known that anticyclonic (respectively cyclonic) eddies tend to deepen (shoal) the MLD (Dufois et al., 2016; Hausmann et al., 2017; Gaube et al., 2019). Eddies actually amplify the MLD seasonal cycle, the deepest MLD anomaly being reached during winter (Hausmann et al., 2017; Gaube et al., 2019). A first mechanism was proposed by Williams (1988), the eddy modulation of the MLD being related to their induced sea surface temperature anomaly (SSTA). Indeed, as shown by Hausmann and Czaja (2012), anticyclonic (cyclonic) eddies are usually associated with positive (negative) SSTAs, and this is at least true in winter in the Mediterranean Sea (Moschos et al., 2022). It leads to stronger (weaker) heat loss during the winter and the triggering of enhanced (reduced) ocean convection and therefore deeper (shallower) MLD. In addition, Hausmann et al. (2017) and Gaube et al. (2019) found out that, for the Southern Ocean and global ocean respectively, the eddy MLD anomaly, computed from eddy composites, scales with the eddy sea surface height (SSH) amplitude. Gaube et al. (2019) proposed the same linear trend at the global scale ± 1 m MLD anomaly for each 1 cm SSH for both cyclones and anticyclones. Physical drivers controlling the eddy-induced MLD are supported by other studies showing an eddy modulation of air–sea exchanges. Villas Bôas et al. (2015) found that ocean heat loss was enhanced (respectively reduced) in anticyclones (cyclones) in energetic regions of the South Atlantic Ocean, once again scaling with eddy amplitude, for both sensible and latent heat flux. Frenger et al. (2013) showed enhanced rainfall and cloud cover above anticyclones in the Southern Ocean as a consequence of enhanced turbulent heat fluxes but suggested a scaling with the eddy SSTA. Such a relation should remain coherent, as Hausmann and Czaja (2012) also found anticyclonic warm (cyclonic cold) eddy SSTAs to scale with the eddy amplitude in the Gulf Stream region. Altogether, eddy MLD anomalies are expected to be easily inferred provided that background measurements outside eddies are available, a promising link for remote sensing application.

However, all these studies were at a coarse monthly temporal resolution, whereas the mixed layer is driven by air–ocean fluxes and thus is expected to react at a timescale close to the inertial period (D'Asaro, 1985; Lévy et al., 2012). If several studies showed the MLD and upper-ocean stratification to vary over timescales of a week at regional scales (Lacour et al., 2019 in the North Atlantic or D'Ortenzio et al. (2021) in the Rhodes gyre), no studies are yet available on the temporal evolution of eddy MLD anomalies. A second limit in previous studies is the use of composite datasets that smooth out the non-linearities induced by eddies. If the composite analysis can provide a first-order trend, this is likely not sufficient to quantify accurately the various impacts of the wide diversity of individual eddies varying in size and intensity. A third but linked limit – explicitly pointed out by Villas Bôas et al. (2015) and Hausmann et al. (2017) – is their focus on surface-intensified eddies with the most coherent surface signature. Indeed, the relation between eddy SSTAs and SSH amplitude strongly relies on the hypothesis of a surface-intensified structure, and Assassi et al. (2016) showed that it should not be the case for subsurface anticyclones. Subsurface eddies are of a mesoscale structure where the density anomaly (compared to the outside-eddy density profile) is overlaid by an anomaly of opposite sign. For instance, a subsurface anticyclone has a lighter core at depth overlaid by a negative density anomaly near the surface. Following the thermal-wind equation, the depth of the maximal geostrophic speed is below the surface. The isopycnals and isotherms doming above a subsurface anticyclone core could greatly impact the upper-layer stratification and subsequently the inside-eddy mixed-layer dynamics. In the South China Sea and still using the composite method, He et al. (2018) found the anticyclones to be predominantly subsurface eddies. They also observed a linear trend between the subsurface temperature anomaly and SSH on an annual average and an eddy-induced MLD anomaly, but based on monthly climatology, and did not find a relationship with MLD. A more detailed comparison with more observational data and, in particular, a better temporal resolution is then lacking.

The Mediterranean Sea is an interesting region to study eddy influence on MLD. At first, due to repeated oceanographic campaigns, the density of in situ measurements is relatively high, and in particular, several campaigns specifically targeted long-lived mesoscale anticyclones in both western and eastern basins. Without aiming for exhaustiveness, one can list the following in particular: EGYPT (Taupier-Letage et al., 2010), BOUM (Moutin and Prieur, 2012), "Eye of the Levantine" (Hayes et al., 2011), PROTEVS (Garreau et al., 2018) and PERLE (Ioannou et al., 2019). Additionally, several Argo profiling floats were launched inside eddies and remained trapped for a long time (Ioannou et al., 2020), altogether allowing one to accurately follow particular eddies and to go beyond the averaged composite vision in the Mediterranean Sea. Moreover, data from these programmes were often only analysed in the scope of the campaigns, and an eddy study with a larger statistical focus is still lacking. A second relevance for Mediterranean eddies is the variety of mesoscale structures in terms of dynamics, from intense Algerian and Ierapetra anticyclones needing cyclogeostrophic corrections (Ioannou et al., 2019) to subsurface eddies with strong density anomalies but weak SSH signatures (Hayes et al., 2011). Moutin and Prieur (2012) also showed the vertical structure, in temperature and salinity, of mesoscale eddies to be very different from one basin to another. Barboni et al. (2021) showed the marked subsurface difference be-

tween a new anticyclone detached from the coast compared to an offshore structure having been tracked for more than a year. All these structures should provide different examples of eddy–MLD interactions.

In the Mediterranean Sea, there is additionally a strong asymmetry between cyclones and anticyclones, remarkable in terms of lifetime difference (Mkhinini et al., 2014). The deformation radius in the Mediterranean Sea is indeed about 8 to 12 km (Kurkin et al., 2020), and cyclones are less stable when greater than the deformation radius and more subject to external shear (Arai and Yamagata, 1994; Graves et al., 2006). This leads to cyclones being predominantly below the effective resolution of SSH products by about 20 km (Stegner et al., 2021). As a consequence, anticyclones are coherent larger vortices, while cyclones in the Mediterranean Sea, as detected by altimetry, are instead cyclonic gyres bounded by topography or hydrographic fronts such as the Ligurian, southwestern Crete or Rhodes gyre (Stegner et al., 2021). MLD evolution inside these cyclonic gyres was already surveyed because of their importance for biological production, in particular with the development of BGC-Argo (D'Ortenzio et al., 2021; Taillandier et al., 2022). Apart from specific campaigns, Mediterranean anticyclones remain poorly analysed despite being more coherent, and statistical comparison based on vertical profiles is lacking, with the noticeable exception of the Biogeochemistry from the Oligotrophic to the Ultraoligotrophic Mediterranean (BOUM) campaign surveying three anticyclones across the Mediterranean in 2008 (Moutin and Prieur, 2012).

This paper aims to study the temporal evolution of the mixed layer inside a wide diversity of long-lived anticyclones in the Mediterranean Sea compared to the evolution of the background MLD. The goal is to quantify more precisely the local impacts of individual eddies on the winter mixed-layer deepening. The paper is organized as follows. Section 2 describes the eddy detection and tracking algorithm and the in situ profile database. Section 3 details the methodology used to compute the MLD and to colocalize profiles and eddies in order to quantify accurately the MLD anomalies induced by individual eddies. In Sect. 4, we analyse the MLD evolution at anticyclone cores, provide statistical analysis over the variety of structures surveyed and discuss the impact of complex vertical eddy structures on winter mixed-layer deepening. Finally, in Sect. 5, we discuss the possible physical drivers and implications of these MLD anomalies.

2 Data

2.1 Anticyclone detections: the DYNED-Atlas

Eddy detections are provided through the angular momentum eddy detection and tracking algorithm (AMEDA). AMEDA is a mixed velocity–altimetry approach; it relies on using primarily streamlines from a velocity field and identifying possible eddy centres computed as maxima of local normalized angular momentum (Le Vu et al., 2018). It was successfully used in several regions of the world ocean using altimetric data (Aroucha et al., 2020; Ayouche et al., 2021; Barboni et al., 2021), high-frequency radar data (Liu et al., 2020) or numerical simulations (de Marez et al., 2021). From 1 January 2000 to 31 December 2019, AMEDA was applied on the Archiving, Validation and Interpretation of Satellite Oceanographic data (AVISO) sea surface height (SSH) delayed-time product at a resolution of $1/8°$ with daily output. From 1 January 2020 to 31 December 2021, AMEDA was applied on the AVISO SSH near-real-time day + 6 product (Pujol, 2021) at the same spatial and temporal resolutions. In each eddy single observation (one eddy observed one day), AMEDA gives a centre and two contours. The "maximal speed" contour is the enclosed streamline with maximal speed (i.e. in the geostrophic approximation, with maximal SSH gradient); it is assumed to be the limit of the eddy core region where water parcels are trapped. The "end" contour is the outermost closed SSH contour surrounding the eddy centre and the maximal speed contour; it is assumed to be the area of the eddy footprint, larger than just its core but still influenced by the eddy shear (Le Vu et al., 2018). AMEDA gathers eddy observations in eddy tracks, allowing the same structure to be followed in time and space, sometimes over several months. The eddy track collection in the whole Mediterranean Sea constitutes the DYNED-Atlas database (Stegner and Le Vu, 2019), which is available online (for the years 2000 to 2019) at https://www1.lmd.polytechnique.fr/dyned/, last access: 21 February 2023. From 2000 to 2021, a total of 7038 (respectively 8890) anticyclonic (cyclonic) eddy tracks were retrieved. The asymmetry in eddy numbers is driven by a lifetime difference, with anticyclones living noticeably longer, an asymmetry even more marked in the Levantine Basin (Barboni et al., 2021).

2.2 In situ profiles

A climatological database is created collecting in situ profiles from the Coriolis Ocean Dataset for Reanalysis (CORA). Delayed-time (CORA-DT; Szekely et al., 2019b) profiles are recovered from 2000 to 2019 (113 486 profiles), and near-real-time (Copernicus-NRT; Copernicus, 2021) profiles are recovered from 2020 to 2021, included using the "history" release (22 821 profiles). These datasets are multi-platform, gathering in situ vertical measurements from conductivity–temperature–depth (CTD) casts, expendable bathythermograph (XBT) measurements (mostly before 2008), Argo floats (mostly after 2005, with a strong increase after 2012) and gliders (mostly after 2008), enabling an average of 10 000 profiles available per year from 2011 onwards. In addition, some profiles prior to 2020 have not yet been released in CORA-DT but are available in Copernicus-NRT. This happens in particular when the salinity sensor of an Argo float has abnormal values but the temperature is still

correct (by visual inspection and correct quality flag). As the MLD computation can be performed on a temperature profile alone, profiles were also retrieved in NRT mode after careful checking, as described in Appendix A. This provides an extra 20 746 profiles from 2000 to 2019. Spotted duplicates between CORA-DT and Copernicus-NRT are retrieved only from CORA-DT. The complete database then accounts for 157 053 profiles in total, with the following platform distribution: 8596 CTDs, 11375 XBTs, 60 019 Argo, 76 967 glider profiles and 96 unspecified and is available at https://doi.org/10.17882/93077 (Barboni et al., 2023).

3 Methods

3.1 MLD computation

The global analysis conducted by de Boyer Montégut et al. (2004) led to MLD being detected by threshold values of $0.03\,\mathrm{kg\,m^{-3}}$ for density and 0.2 °C for temperature, based on a reference depth of 10 m to avoid diurnal heating at the surface. In the Mediterranean Sea, D'Ortenzio et al. (2005) used this methodology for a 0.5°-resolution MLD climatology. Houpert et al. (2015) updated it with 8 supplementary years of data but opted for a 0.1 °C temperature threshold. This more restrictive criterion enables the reduction of the difference between the MLD computed on temperature profiles and the one computed on density profiles. Gradient methods look in a similar way for critical gradients as an indicator of the mixed-layer base. Typical gradient threshold values in use are $2.5\times10^{-2}\,\mathrm{°C\,m^{-1}}$ for temperature profiles and range from 5×10^{-4} to $5\times10^{-2}\,\mathrm{kg\,m^{-4}}$ for potential density profiles (Dong et al., 2008). Mixed gradient and threshold methods were also developed (Holte and Talley, 2009). Here, we aim to capture as accurately as possible the MLD evolution, which can vary on timescales shorter than a month. More specifically, we observed in several cases that the threshold method (with criteria $\Delta\sigma = 0.03\,\mathrm{kg\,m^{-3}}$ and $\Delta T = 0.1\,°\mathrm{C}$) can miss the mixed layer and return the main thermocline instead (see Fig. 1a). The main thermocline is indeed characterized by a small jump in potential density (or in temperature) but a significant peak in the gradient profile, and it happens mostly in the spring, probably due to a start of restratification that quickly becomes mixed. To capture such small-scale restratification events, we built the following methodology, combining both threshold and gradient approaches. Using the thresholds $\Delta\sigma = 0.03\,\mathrm{kg\,m^{-3}}$ and $\Delta T = 0.1\,°\mathrm{C}$, we derive a first estimate of the MLD. If it is shallower than 20 m, we take it as our estimate of the MLD. Otherwise, we apply a three-point running average to remove small spikes and to compute the gradient using a second-order centred difference. From the subsurface (20 m) up to the first MLD estimate, we apply a gradient method with the given gradient thresholds: $|\partial_z\sigma| > 5\times10^{-4}\,\mathrm{kg\,m^{-4}}$ or $|\partial_z T| > 2.5\times10^{-3}\,\mathrm{°C\,m^{-1}}$. If the gradient fails to exceed the threshold within the given depth range, then the first MLD estimate is kept.

Threshold and gradient methods are limited by their dependence on the criterion values which can have strong influence on the MLD estimate. The relatively low gradient thresholds chosen here appeared to be necessary to catch the MLD in some of our profiles, as higher thresholds would return the main thermocline (see Fig. 1a). A sample of 400 randomly picked profiles collocated inside eddies was used for validation. We chose this validation dataset with profiles inside eddies because it is our main focus. Wrong detection on double-gradient profiles inside eddies was found to be quite large, sometimes exceeding 100 m. On these 400 profiles, 22 (5.5 %) of them were identified as double-gradient profiles, resulting in an overestimated MLD when derived with the threshold method. Moving to our methodology, this issue is now only encountered for two profiles (0.5 %). However, with the gradient method comes some issues for profiles with small residual spikes despite the applied smoothing. For two profiles, the gradient method returned wrong MLD detection where the threshold method was correct. However, the gradient method was found overall to be more accurate for estimating the MLD.

Moreover, the chosen thresholds should return similar estimates between an MLD obtained from a temperature profile ($\mathrm{MLD_T}$) and one obtained from a potential-density profile (MLD_σ). Potential density is a better estimate of the stability of a layer, and thus MLD_σ should give a more reliable value. However, salinity (and hence density) suffers from data holes, representing about 15 % in our dataset. Temperature profiles then offer a good alternative in evaluating the MLD, providing $\mathrm{MLD_T}$ gives a estimate to that of MLD_σ. An $\mathrm{MLD_T}$ and MLD_σ difference histogram is shown in Fig. 1b: the gradient method appears to reduce this difference slightly, with 64 % of the profiles leading to the same estimate and 94 % to less than a 30 m difference compared to 62 % and 93 % respectively for the threshold method. MLD is then computed on the density profile or, if no density is available, on the temperature profile.

3.2 Eddy colocalization and background estimate

In order to characterize the impact of anticyclonic eddies on the MLD seasonal evolution and spatial gradient, we need to accurately colocalize in situ profiles with eddy observations. However, due to altimetric product interpolation and disparate satellite tracks, SSH-based contours can vary a lot in size and position, making a single eddy observation less reliable in the Mediterranean Sea (Amores et al., 2019; Stegner et al., 2021). Therefore, we colocalize eddy observations and in situ profiles at ±2 d. Assuming a profile position fixed at cast date D, it is then labelled as "inside-eddy" if it remains inside the maximal speed contours of the same eddy at $D-2$, $D-1$, D, $D+1$ and $D+2$ (at least four contours out of five). This four-out-of-five threshold avoids the neglect of a collo-

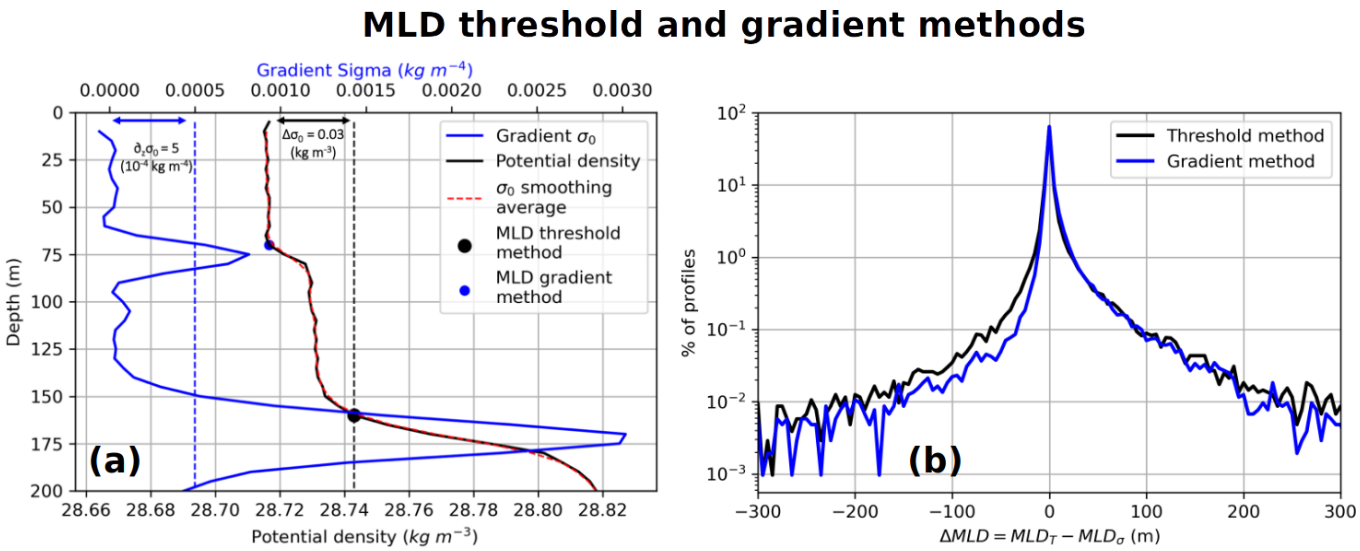

Figure 1. **(a)** MLD detection on one potential density profile with our gradient method (blue dot) and threshold method (black dot); **(b)** fraction of the profiles as a function of ΔMLD for the threshold (black line) and gradient (blue line) method.

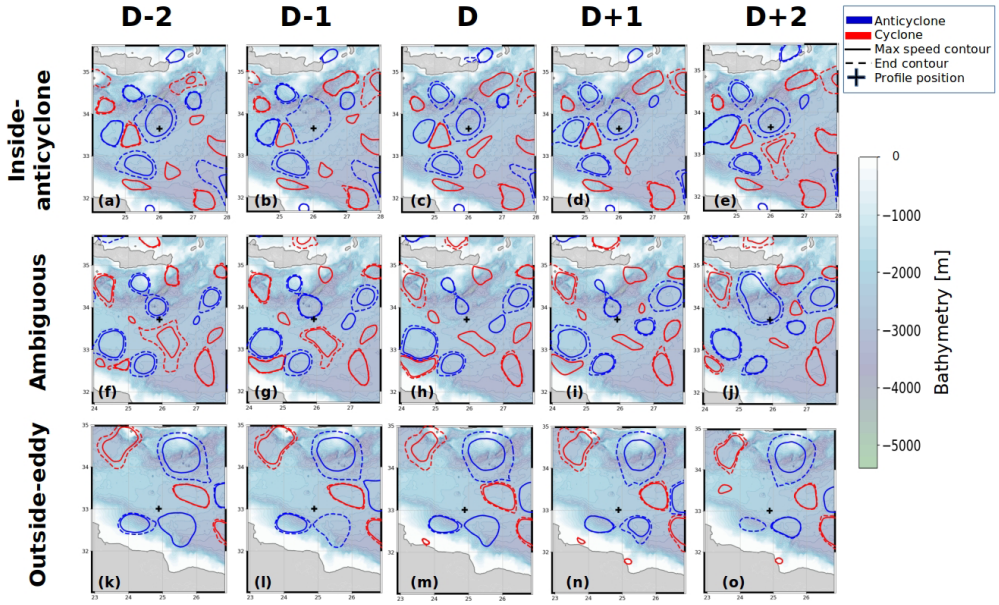

Figure 2. Profile colocalization with eddy contours for an "inside-anticyclone" profile **(a–e)**, an "ambiguous" profile **(f–j)** and an "outside-eddy" profile **(k–o)**. Profile cast position is assumed to be fixed and is compared to eddy contours at $D-2$, $D-1$, D, $D+1$ and $D+2$, D being the profile cast date.

cated profile when the eddy contour is not available for just one day (see Fig. 2b). For the same purpose, hereafter, the eddy centre and the distance of a profile to the eddy centre are averaged at ±2 d.

AMEDA also gives, for each observation, the last closed SSH contour (see Sect. 2.1), inside which there is still an impact by the eddy shear, but outside of the maximal speed contour, the water particles are not assumed to be trapped. The area between the maximal speed and last closed SSH contours is then considered to be an intermediate zone to be discarded. Consistently with the "inside-eddy" definition, we label as "outside-eddy" only the profiles that stay outside any eddy contours at ±2 d of its cast date. Any profile being neither "inside-" nor "outside-eddy" is considered to be ambiguous and is discarded. From 2000 to 2021, out of 157 053 profiles retrieved in the Mediterranean Sea, 104 787 are labelled "outside-eddy", 7939 are "inside-anticyclone" and 14 919 are "inside-cyclone"; the remaining 29 410 "ambiguous" profiles are removed from this analysis. This asymmetry between anticyclones and cyclones sampling is also

due to heterogeneous oceanographic surveys (Houpert et al., 2015), particularly the numerous glider missions in the Gulf of Lion, a cyclonic gyre with no large anticyclones (Millot and Taupier-Letage, 2005). Figure 2 illustrates the colocalization method detailed above with three examples: an "inside-anticyclone" profile (Fig. 2a–e), an "ambiguous" one (Fig. 2f–j) and an "outside-eddy" one (Fig. 2k–o). For this particular "inside-anticyclone" profile, the maximal speed contour was missing at day $D-1$ but was available for the other days, and the profile was indeed cast close to the eddy centre.

To follow the accurate evolution of the MLD inside anticyclones, we need a reference for comparison: an unperturbed, local and time-coincident ocean state without eddies, hereafter called "background". This outside-eddy background differs from a classical climatology used in previous studies (Gaube et al., 2019) by the removal of the eddy mean effect and by avoiding time averaging as much as possible. The background of an eddy, at a given time t and centre position $C(t)$, is then constituted by the mean of all profiles labelled as outside-eddy that are closer than 250 km to $C(t)$, cast within $\Delta\text{day} = \pm 10$ d of the same year or of the previous or the following year ($\Delta y = \pm 1$ year). For example, when computing the corresponding background of an eddy around 15 February 2018, the background encompasses profiles that are labelled as outside-eddy, are closer than 250 km, and are cast from 5 to 25 February 2017, 2018 and 2019. A threshold on the number of profiles is required: if fewer than 10 profiles meet the distance, time and outside-eddy requirements, then no background is computed. At last, we define the "background MLD" to be the median MLD of the profiles constituting the background. Computing the median is preferred to the mean, as the MLD distribution is not centred but skewed downwards. This computation is performed for each time step with a temporal resolution of 5 d. As shown in Appendix (Fig. A1), with the test case of the Ierapetra anticyclone taking place over 2 years (corresponding events "IER1–2" on Table 1 and Fig. 10), the background MLD is not highly sensitive to the choice of Δday and Δy. The background MLD evolution is indeed similar, with $\Delta\text{day} = 10$, 15 or 20 d and $\Delta y = 0, 1$ or 2 years. It is, however, important not to take all years, as interannual variability then starts to smooth the background MLD evolution. On the other hand, taking only profiles of the same year ($\Delta y = 0$) sometimes translates into not having enough profiles to have a background estimate (see Fig. A1a). We therefore chose $\Delta\text{day} = 10$ d and $\Delta y = 1$ year as day and year intervals in order to capture MLD variations that are as short as possible, which is crucial for parameters that vary quickly, such as the MLD. For the two earliest recorded events (Mersa Matruh 1 and 2 in 2006 and in 2008; see Table 1), Δy is set to 2 years because no background MLD was available otherwise. Choosing $\Delta y = 1$ allows one to have accurate eddy-induced anomalies without them being corrupted by interannual variability of temperature and salinity fields, which can be marked in the Mediterranean,

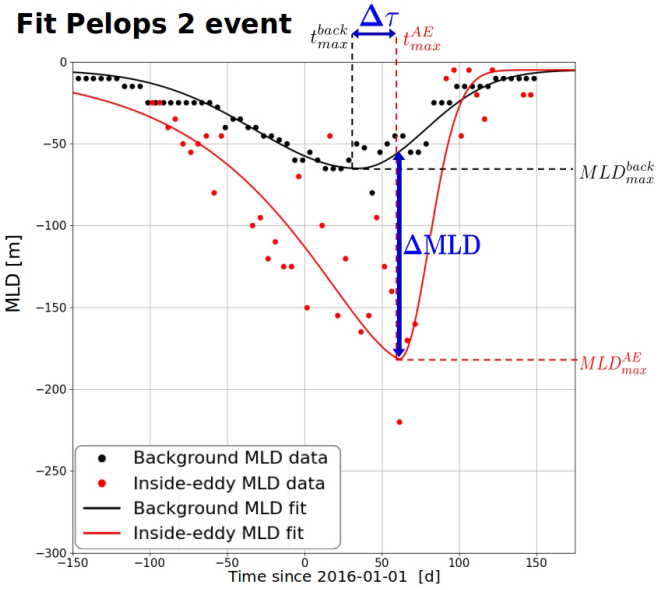

Figure 3. Detail of winter deepening event Pelops (PEL) 2 in 2016 (see Table 1 for details). Anticyclonic core MLD data are shown as red dots, and background MLDs are shown as black dots, with time steps of 5 d. MLD fit is shown as a red line for the anticyclonic core (see Eq. 2) and as a black line for background MLD (see Eq. 1).

particularly in the eastern basin (Ozer et al., 2017). A significant warming trend is also observed (Parras-Berrocal et al., 2020).

3.3 MLD evolution function fit

To describe more objectively the MLD seasonal evolution in the background, we performed a function fit using the Python optimization routine `scipy.optimize.curve_fit`. MLD data points are selected according to 5 d time steps. Background MLD is fitted by a skewed Gaussian, $t^{\text{back}}_{\text{max}}$ being the time when the deepest MLD ($\text{MLD}^{\text{back}}_{\text{max}}$) is reached; σ and τ are respectively the restratification and deepening timescales:

$$\begin{aligned} f(t) &= \text{MLD}^{\text{back}}_{\text{max}} \exp\left(-\frac{\left(t-t^{\text{back}}_{\text{max}}\right)^2}{2\tau^2}\right) \quad \text{if} \quad t < t^{\text{back}}_{\text{max}}, \\ f(t) &= \text{MLD}^{\text{back}}_{\text{max}} \exp\left(-\frac{\left(t-t^{\text{back}}_{\text{max}}\right)^2}{2\sigma^2}\right) \quad \text{otherwise.} \end{aligned} \tag{1}$$

This fit captures the background MLD evolution, somehow smooth, typically with a sharper restratification than deepening ($\tau < \sigma$). However, this is not sufficient for the anticyclonic core MLD evolution that can have more abrupt variations, then calling for a more complex fit with two deep-

ening timescales τ_1 and τ_2:

$$\begin{aligned} f(t) &= \left(\mathrm{MLD}^{\mathrm{AE}}_{\max} - B\right)\exp\left(\tfrac{t-t^{\mathrm{AE}}_{\max}}{\tau_1}\right), \\ &+ B\exp\left(\tfrac{t-t^{\mathrm{AE}}_{\max}}{\tau_2}\right) \quad \text{if} \quad t < t^{\mathrm{AE}}_{\max} \\ f(t) &= \mathrm{MLD}^{\mathrm{AE}}_{\max}\exp\left(-\tfrac{\left(t-t^{\mathrm{AE}}_{\max}\right)^2}{2\sigma^2}\right) \quad \text{otherwise.} \end{aligned} \tag{2}$$

To fit the MLD evolution accurately, and particularly to have the maximal depth reached, data are fitted with weights proportional to their depth. Because it is difficult to have long and continuous time series, data are often missing for the previous or next summers. To ensure physical behaviour, fit is forced back to 10 m on the edges, miming summer stratification. The MLD anomaly ($\mathrm{MLD}^{\mathrm{anom}}$) is defined as the difference between the fitted background and anticyclonic core MLD. $\mathrm{MLD}^{\mathrm{anom}}$ is a function of time but reaches its maximum (ΔMLD) at almost the same time as the absolute anticyclonic core MLD, as the latter has more amplitude than the background one. At last, an advantage of the `scipy.optimize.curve_fit` routine is that it provides the parameter covariance matrix and hence an error estimate, taking the square root of the covariance matrix diagonal (Bevington et al., 1993). It can happen that the covariance matrix has very large values – in this case, we used an upper uncertainty of ± 30 m for ΔMLD and ± 20 d for $t^{\mathrm{AE}}_{\max}$. A fit illustration is provided in Fig. 3 for the Pelops 2 event in 2016 (see Table 1), with the real MLD as dot data and the fits as continuous lines and with the background in black and the anticyclonic core in red. Using the fit routine, maximal MLD anomaly is then estimated as $\Delta\mathrm{MLD} = 127 \pm 13$ m for this event. One can also notice an absence of coincidence between the deepest inside-eddy and background MLDs. Following previous notation, we can then define a restratification delay of the anticyclonic core MLD, which is used throughout this study: $\Delta\tau = t^{\mathrm{AE}}_{\max} - t^{\mathrm{back}}_{\max}$. In the example shown in Fig. 3, $\Delta\tau = 26 \pm 11$ d.

4 Results

Several long-lived anticyclones are tracked for several months, recording up to 16 winter mixed-layer deepening events at their core. In order to investigate the relation between the MLD evolution and the vertical eddy structure, we plot together the time series of MLD and vertical temperature gradients inside the eddy core. Two different MLD temporal patterns are observed, depending on whether or not the current winter mixed layer reaches the subsurface anticyclone core. This core is constituted by a pre-existing homogeneous layer, and in the following, we define as "homogenized" a layer with a temperature gradient constantly below 2.5×10^{-3} °C m^{-1} in absolute value.

4.1 Winter deepening connecting pre-existing subsurface core

A very deep mixed layer can be observed in several anticyclones when the MLD erodes the inside-eddy stratification and abruptly connects with a subsurface homogenized core, an event hereafter called a "connecting" MLD. An example of this evolution is described below with a long-lived Eratosthenes anticyclone during winter 2008–2009. Its temporal evolution from August 2007 to April 2009 is shown in Fig. 4 and is listed hereafter and in Table 1 with the name "Eratosthenes (ERA) 1". This kind of anticyclone, also called "Cyprus eddy" or even "Shikmonah gyre", are large mesoscale structures with an almost stationary position south of the island of Cyprus in the Levantine Basin, extensively studied with several CTDs (Brenner, 1993; Krom et al., 1992; Moutin and Prieur, 2012), gliders and Argo float deployments (Hayes et al., 2011). The anticyclonic density anomaly is characterized, on average, by a deep (about 400 m) and extremely warm temperature anomaly (up to +2 °C at 400 m) (Moutin and Prieur, 2012; Barboni et al., 2021), sometimes with a strong salt anomaly (Hayes et al., 2011). Thus temperature profiles are considered to be a good estimate for the relative density and temperature gradient for stratification.

An Argo float remained trapped inside this anticyclone from mid-2008 to the death of this eddy in early 2009, allowing an MLD deepening event during winter 2008–2009 to be captured well. An inside-anticyclone profile is shown at the beginning (12 January 2009; Fig. 4c) and the end (1 March 2009; Fig. 4e) of the winter. First, one can notice that the anticyclone vertical structure in January 2009 is constituted by a subsurface homogenized layer from 100 to 300 m, which can be tracked from July 2008 on the stratification time series (Fig. 4b) and was likely formed by convection in the previous winter. The anticyclone core profile in Fig. 4c indeed has a marked temperature anomaly on the order of +2 °C at 450 m compared to the background, proving they indeed sample the eddy core. Some profiles with a very warm temperature at 400 m deep are misleadingly considered to be outside-eddy but do not corrupt the mean background (thick grey line). MLD is also deeper inside the Eratosthenes anticyclone: the anticyclonic core MLD is 90 m deep, while it is around 60 m in the background. The deeper homogenized core remains unmixed below a seasonal thermocline: +1 °C temperature jump at 100 m in Fig. 4c. Later, the winter cooling and subsequent MLD deepening eroded this stratification inside the anticyclone, as shown by the temperature gradient vanishing in the upper 100 m, and the winter MLD connected with the primitive core and mixed with it in February 2009 (Fig. 4b). Then on 1 March 2009 (Fig. 4e), the anticyclone core profile measured an MLD reaching 350 m.

Inside- and outside-eddy MLD temporal evolutions noticeably do not coincide: on MLD time series (Fig. 4a), background MLD shoaled from the end of January,

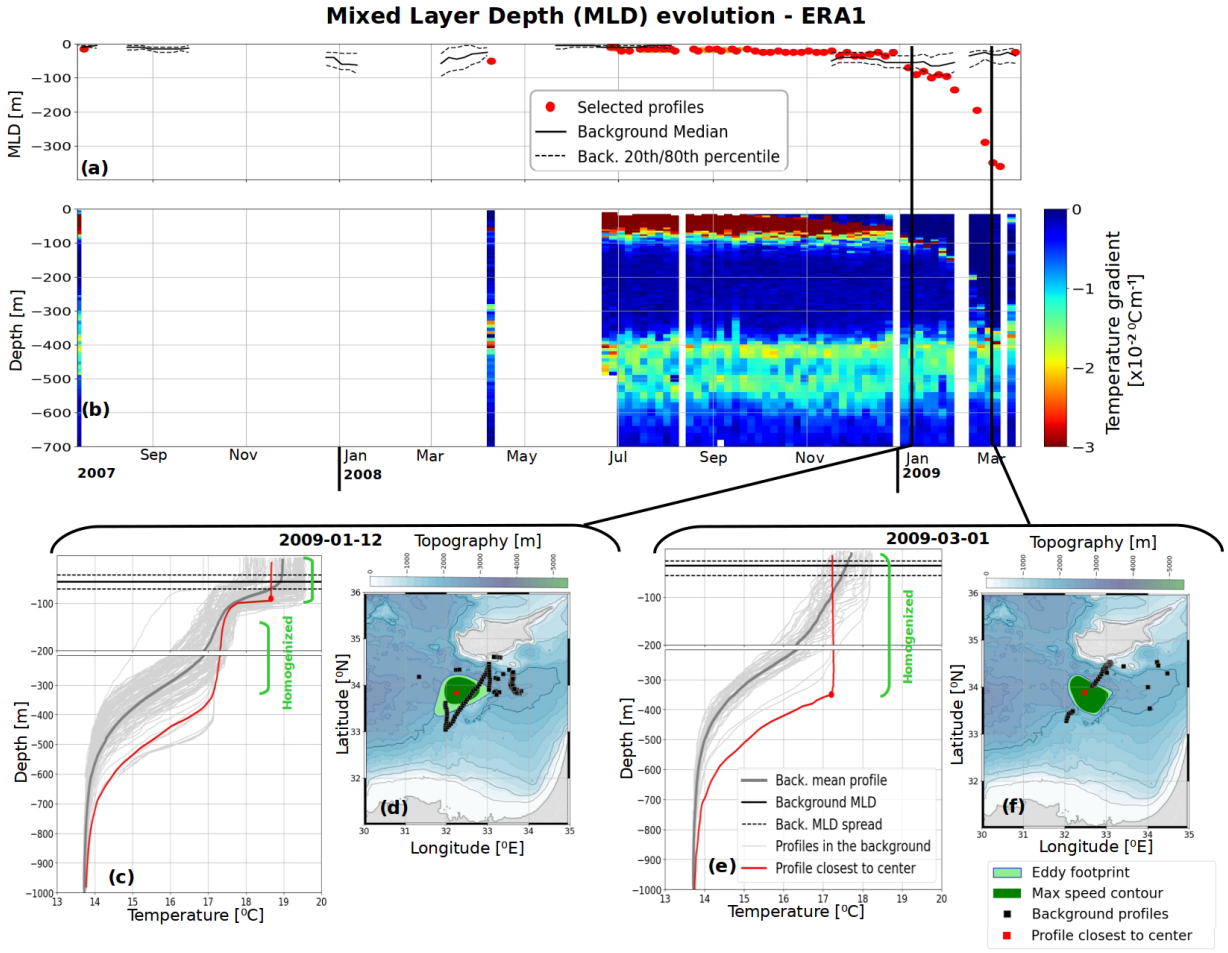

Figure 4. In-depth evolution of an Eratosthenes anticyclone, listed as "ERA1" in Table 1. **(a)** MLD evolution, with continuous black line for background MLD (and dashed line for associated spread between 20th and 80th percentiles) and red dots for the anticyclonic core MLD closest to eddy centre. **(b)** Time series of inside-eddy temperature gradient, blue showing homogeneous and red showing stratified layers; **(c)** (respectively **e**) shows vertical profiles around 12 January 2009 (1 March 2009) with background profiles in thin grey lines, background mean as thick grey line, inside-eddy profile as red line, a red dot highlighting anticyclonic core MLD and a green bar indicating homogenized layers (temperature gradient below $2.5 \times 10^{-3}\,^{\circ}\mathrm{C\,m^{-1}}$). Horizontal continuous and dashed black line refer back to background MLD and spread from panel **(a)**; **(d)** (respectively **f**) shows profiles' corresponding position on a map with same colour code together with the eddy maximal-speed contour (dark green shape) and eddy footprint (outermost closed SSH contour, light green shape). Bathymetric data are from ETOPO1 (Smith and Sandwell, 1997).

whereas inside-eddy MLD continued to deepen. Then on 1 March 2009, most background profiles started to restratify, with temperature gradients in the upper 100 m (thin grey lines in Fig. 4e), while anticyclonic core MLD rose back to about 20 m only in late March 2009 (Fig. 4a). This restratification, occurring at a different time outside- and inside-eddy, with a delay of about 2 months, leads to the noticeable situation measured on 1 March 2009: the inside-anticyclone profile is warmer than its environment at depth (100 to 350 m deep) but is homogenized in its upper part, whereas background profiles are stratified with positive temperature gradients. Such geometrical configuration leads to an anticyclone negative temperature (and hence positive density) anomaly from 50 m to the surface compared to the stratified outside-eddy profile. Such a positive density anomaly above the eddy core is then a clear signature of a subsurface anticyclone (Assassi et al., 2016).

Over the whole 2008–2009 winter, background MLD barely reached 60 m, whereas the anticyclonic core MLD went down to 350 m. This intense deepening at the anticyclone core is due to the pre-existing subsurface eddy, made of a well-mixed layer at a depth of a few hundred metres below the summer stratification. When the winter mixed layer deepens, it reconnects to this deep subsurface core and leads to a rapid and strong MLD increase in comparison to the eddy background. This MLD temporal pattern is characteristic of a "connecting" event, observed 10 times in our analysis and throughout the Mediterranean Sea (see Sect. 4.3).

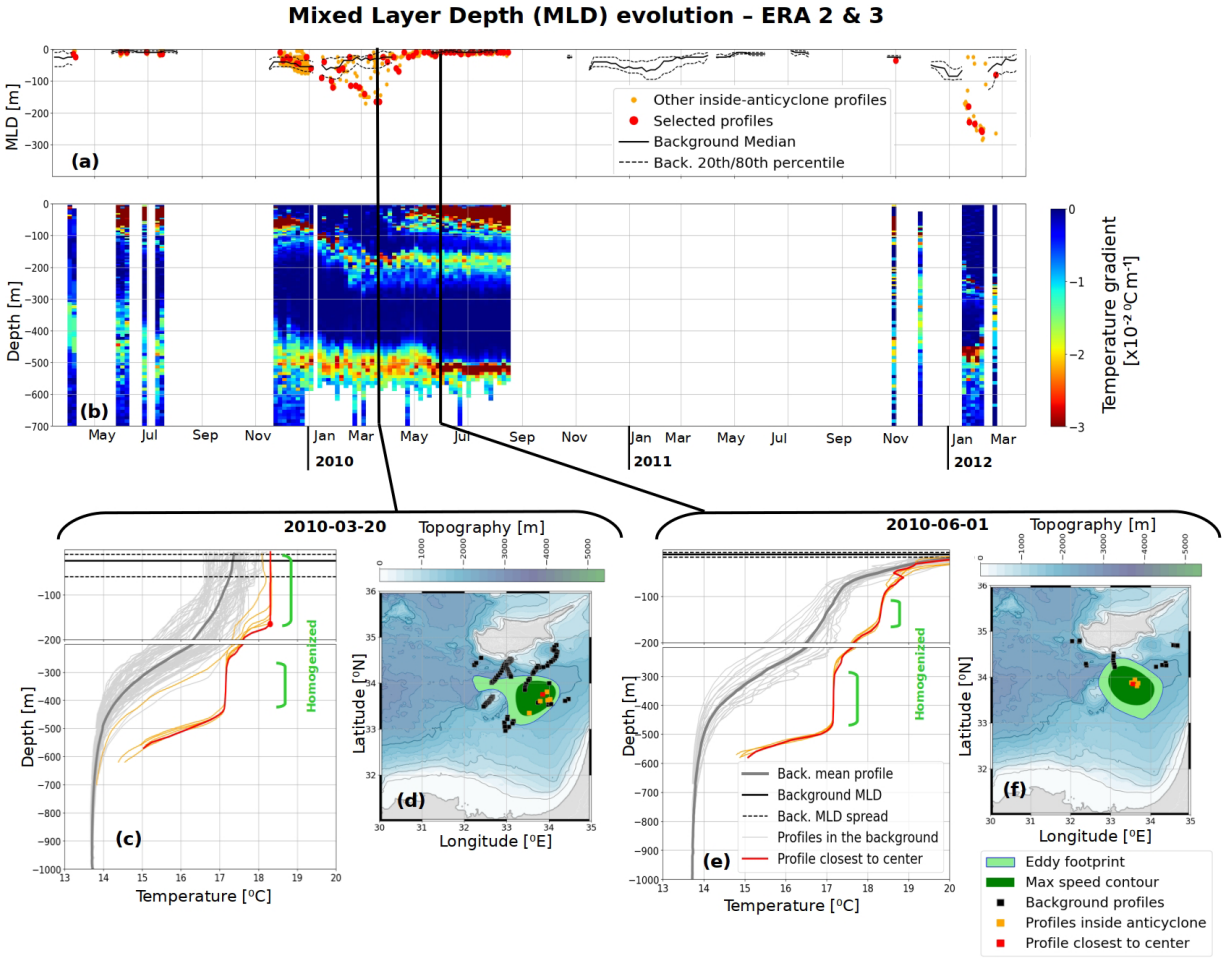

Figure 5. Same colour codes and legend as in Fig. 4. In panels **(a)**, **(c)** and **(e)**, orange lines and dots show additional inside-eddy profiles and corresponding MLD, but these are further away from the eddy centre than the selected one shown in red.

4.2 Winter deepening not connecting pre-existing subsurface core

Conversely, for some other anticyclones, it can clearly be seen that the subsurface temperature anomaly does not connect with the winter mixed layer and remains unperturbed and homogenized at depth. Such an event is hereafter called a "non-connecting" MLD. Figure 5 shows the evolution of another Eratosthenes anticyclone living from 2009 to early 2012, with two recorded anticyclonic core MLD deepenings in 2010 and 2012 (respectively listed in Table 1 as"ERA2" and "ERA3"), with same colour codes as in Fig. 4, with profiles on 20 March 2010 and 15 June 2010. As several profiles were located at the same time inside the anticyclone, they are shown with the orange line in Fig. 5c and e (respectively orange dot for MLD in Fig. 5a). The red line highlights only the profile with the closest distance to the eddy centre, assumed to be more representative of the eddy core.

Similarly to the "ERA1" event in 2009 described above, a thick and deep subsurface anomaly forms a primitive eddy core in late 2009 as a homogeneous layer from 250 to 400 m deep (green bar on Fig. 5c), reaching an anomaly of about +2.5 °C at 400 m. However, the anticyclonic-core MLD did not deepen below 150 m in the winter 2009–2010, only forming a second homogeneous layer above. This constitutes a second surface core, still separated from the primitive core by a temperature stratification, revealed by a temperature gradient continuous in time (Fig. 5b). On the vertical profile on 20 March 2010 (Fig. 5c), a temperature jump of about 1 °C remains between the two cores, forming a double-core anticyclone. In June 2010 (Fig. 5e), this second homogeneous layer is itself covered by the spring restratification, then forming what is also referred to as "thermostad" or "mode-water eddy" in the literature (Dugan et al., 1982). Thanks to the trapped Argo floats remaining near the eddy core for months, both cores could be tracked until August 2010 as separated in the subsurface.

Such "non-connecting" winter MLD inside anticyclone reveals the possibility of a persisting separation between a primitive subsurface anticyclone core and the new homoge-

neous layer formed by the current winter mixing, then constituting a double-core anticyclone. The example showed in Fig. 5 occurred on an Eratosthenes anticyclone, in the same region as the anticyclone in which a "connecting" MLD example was previously shown in Fig. 4. This MLD pattern is not limited to this example and was also observed five times in other regions, as detailed in the next section. Consequences of the formation of a double-core anticyclone are discussed in Sect. 5.2 hereafter, with another remarkable example in Fig. 10.

4.3 Inside-anticyclone MLD statistics

From 2000 to 2021, thanks to extensive Argo deployments sampling eddies, 16 winter MLD deepening events were accurately recorded with vertical profiles in 13 mesoscale eddies, 10 being "connecting" events and 6 being "non-connecting" ones. Several structures were surveyed over two winters (see Figs. 5 and 10). For each event, the fitting method detailed in Sect. 3.3 was applied, and parameters are reported in Table 1 together with eddy characteristics: eddy SSH amplitude, maximal speed $V_{\max}$ and maximal speed radius $R_{\max}$. Eddy measurements are estimated by the mean from November to March of the corresponding winter. Figure 6 shows the location of each structure, which actually corresponds to types of long-lived structures already identified in the literature (Millot and Taupier-Letage, 2005; Hamad et al., 2006; Budillon et al., 2009; Barboni et al., 2021); these are listed from west to east as follows: Central Tyrrhenian anticyclone (abbreviated TYR), Pelops (PEL), Ierapetra (IER), Mersa Matruh (MM) and Eratosthenes (ERA). Position is computed as the mean position during the corresponding winter, even though eddies do not drift a lot in the Mediterranean Sea (Mkhinini et al., 2014). Despite regional differences and limited data availability, both types can occur in each region and provide an observation database allowing statistical comparison. Inside-eddy maximal MLD time $t_{\max}^{\mathrm{AE}}$ and hence $\Delta\tau$ could not be computed for events MM4 and PEL3, as gaps in the time series do not allow one to accurately measure them. However, ΔMLD could always be computed, as in worst cases there are still inside-eddy profiles later in the year, allowing one to check that maximal MLD was indeed reached (in a similar way to Moutin and Prieur, 2012, for previous winter MLD retrieved in April). Both types of events entail interaction (or lack thereof) with a deep subsurface homogeneous layer (layer with temperature gradient below $2.5\times10^{-3}\,^{\circ}\mathrm{C\,m^{-1}}$ in absolute value), either a pre-existing one (see Figs. 4c, 5c and 10c) or a new one (see Figs. 5e and 10d). In all winter deepening events listed in Table 1, such homogeneous layers of least 50 m thick were indeed visible on vertical profiles. For Tyrrhenian Sea anticyclones (TYR1 and 2) with stronger salinity influence (Budillon et al., 2009), homogeneous layers with a density gradient below $5.0\times10^{-4}\,\mathrm{kg\,m^{-4}}$ were also visible. One can also notice that "non-connecting"' events are quite common, but double-core structures should be even more frequent. Indeed, a "connecting" event can occur inside a double-core structure and reconnect only the homogeneous core formed in the previous winter but not the deepest anomaly, as shown later in Fig. 10b–e. In other words, the proportion of "non-connecting" events in Table 1 and Fig. 6 should be considered as a lower bound for double-core structures, revealing their high occurrence.

Hausmann et al. (2017) and Gaube et al. (2019) proposed a linear relation between the anticyclonic core MLD anomaly and its SSH amplitude, using regional average and monthly climatology. We previously showed that MLD anomaly varying over very short timescales can produce sharp MLD gradients and anomalies reaching several hundreds metres, which is not captured by smoothed composites. The relation between MLD anomaly and eddy amplitude is tested in Fig. 7a, distinguishing "connecting" (red dots) and "non-connecting" (green dots) events, together with the relation of Gaube et al. (2019) in the dashed line (1 m MLD anomaly for 1 cm eddy amplitude). This proposed relation is obviously not verified, the deep MLD observed in Mediterranean anticyclones exceeding by far the relation. On the opposite end, the deepest MLD anomalies seem to be observed in the eddies with the weakest SSH signature. Although surprising at first sight, this trend might be explained by the fact that the deepest MLD can be observed when the mixed layer abruptly connects to an anticyclonic deep homogeneous core in the subsurface, hidden by a strong seasonal thermocline. This is particularly the case for "ERA1" shown in Fig. 4, which has an extreme ΔMLD deeper than 300 m but the lowest SSH signature in Table 1.

The relation between the MLD anomaly and the eddy Rossby and Burger numbers is also tested in Fig. 7b and c. Rossby number, defined as $Ro = V_{\max}/f R_{\max}$, where f is the Coriolis frequency, is a non-dimensional measurement of the eddy intensity. The Burger number, defined as $Bu = (R_{\mathrm{d}}/R_{\max})^2$, with R_{d} being the deformation radius (8 to 12 km in the Mediterranean Sea), is a non-dimensional eddy size. Similarly to eddy SSH amplitude, no clear relation can be retrieved; deep and shallow MLD anomalies appear for various eddy intensities and sizes and for both "connecting" and "non-connecting" events. One can only notice that "connecting" events pull MLD deeper in general and that these events are slightly more observed in large structures (small Bu). Remote sensing measurements are then hard to link with observed eddy-induced MLD anomalies. On the opposite end, the diversity of vertical structures shown in this study (Figs. 4, 5 and 10) suggests that eddy vertical structure might have more influence, and previously proposed linear relations seem to apply mostly for surface-intensified structures.

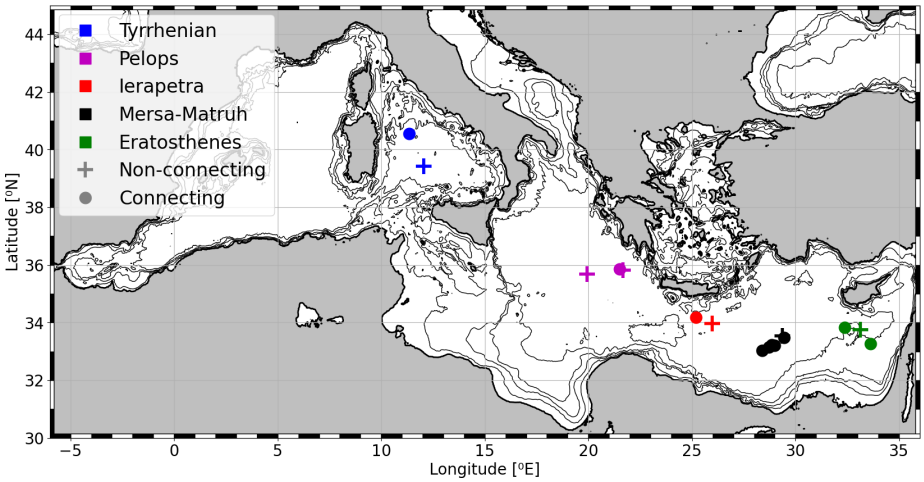

Figure 6. Map of well-sampled winter mixed-layer deepening events inside anticyclones listed in Table 1. Big dots show "connecting" events, while crosses show "non-connecting" ones. Colour depends on the region: Central Tyrrhenian (TYR), Pelops (PEL), Ierapetra (IER), Mersa Matruh (MM) and Eratosthenes (ERA, also called "Cyprus"). Isobaths shown on the maps are at 100, 500, 1000 and 1500 m depth; topographic data from ETOPO1 (Smith and Sandwell, 1997).

Table 1. Main characteristics of the 16 anticyclonic core mixed-layer deepening events studied; fitting method and uncertainties are detailed in Sect. 3.3. Eddy ID refers to track number in the DYNED-Atlas. Event types are "C" for "connecting" and "N" for "non-connecting". Year "2018" corresponds to winter 2017–2018. Regions codes, ordered from west to east, stand for central Tyrrhenian (TYR), Pelops (PEL), Ierapetra (IER), Mersa Matruh (MM) and Eratosthenes (ERA). ΔMLD, t^{AE}_{max} and $\Delta\tau$ are illustrated in Fig. 3. Note that sometimes two different winters are recorded in the same anticyclone (for example: "IER 1–2") and that one eddy tracking ("MM 6") stopped because the dataset finished in December 2021.

Event	Eddy ID	Type	Year	Position (° N; ° E)	ΔMLD (m)	t^{AE}_{max} (days since 1 January)	$\Delta\tau$ (d)	Amplitude (cm)	R_{max} (km)	V_{max} ($m\,s^{-1}$)	Eddy lifetime (d)
TYR1	11780	C	2018	40.6; 11.3	255 ± 15	50 ± 3	17 ± 4	5.5 ± 0.9	38.3 ± 4.3	0.24 ± 0.02	498
TYR2	12976	N	2020	39.4; 12.0	49 ± 4	28 ± 4	4 ± 5	7.2 ± 3.4	33.4 ± 2.6	0.18 ± 0.02	541
PEL1	8886	N	2015	35.7; 19.9	196 ± 7	79 ± 4	62 ± 5	4.2 ± 0.9	42.0 ± 8.7	0.19 ± 0.04	756
PEL2	10054	N	2016	35.8; 21.7	127 ± 13	61 ± 10	26 ± 11	6.3 ± 1.7	38.1 ± 8.7	0.31 ± 0.07	578
PEL3	11649	C	2019	35.9; 21.5	79 ± 23	–	–	7.8 ± 0.9	39.3 ± 6.6	0.36 ± 0.04	1010
IER1	11099	N	2017	34.0; 26.0	175 ± 41	67 ± 20	46 ± 20	7.7 ± 1.1	37.3 ± 4.3	0.41 ± 0.05	780
IER2	11099	C	2018	34.2; 25.2	211 ± 12	51 ± 4	16 ± 6	7.4 ± 1.6	40.9 ± 6.9	0.35 ± 0.07	780
MM1	3556	C	2006	33.1; 28.7	197 ± 30	40 ± 20	13 ± 20	9.3 ± 1.2	45.4 ± 7.5	0.41 ± 0.06	345
MM2	4125	C	2008	33.5; 29.4	325 ± 12	47 ± 2	36 ± 8	3.7 ± 0.7	37.7 ± 5.7	0.20 ± 0.04	790
MM3	7656	C	2015	33.2; 28.8	236 ± 7	38 ± 2	42 ± 5	8.6 ± 2.2	47.8 ± 9.3	0.35 ± 0.04	1229
MM4	11544	C	2018	33.2; 29.0	187 ± 30	–	–	11.4 ± 1.6	61.0 ± 10.0	0.38 ± 0.04	1045
MM5	11544	C	2019	33.0; 28.4	215 ± 30	29 ± 20	13 ± 20	8.7 ± 0.9	43.0 ± 4.6	0.41 ± 0.05	1045
MM6	14400	N	2021	33.5; 29.4	151 ± 12	80 ± 5	74 ± 7	3.1 ± 1.1	35.9 ± 7.0	0.18 ± 0.03	476+
ERA1	4914	C	2009	33.8; 32.4	338 ± 30	62 ± 5	39 ± 7	2.1 ± 1.0	34.9 ± 7.8	0.12 ± 0.04	616
ERA2	5906	N	2010	33.8; 33.1	136 ± 7	76 ± 4	67 ± 8	3.2 ± 2.0	40.1 ± 13.6	0.16 ± 0.08	1110
ERA3	5906	C	2012	33.3; 33.6	180 ± 30	37 ± 20	13 ± 20	4.6 ± 1.0	41.8 ± 5.8	0.22 ± 0.04	1110

4.4 Inside-anticyclone restratification delay

A new and important observation is that MLD inside anticyclones tends, on average, to clearly restratify later than the neighbouring background. It was shown for two individual events in Fig. 4 (ERA1, "connecting") and Fig. 5 (ERA2, "non-connecting"), but it is statistically robust in Table 1: average t^{back}_{max} is 22 d, and average t^{AE}_{max} is 49 d, meaning restratification usually begins in the second half of February in anticyclones, on average 1 month later than outside-eddy. Restratification delay $\Delta\tau$ can reach 2 months in some cases: 67 d for ERA2 or 74 d for MM6 (see Fig. 9b). Figure 8a

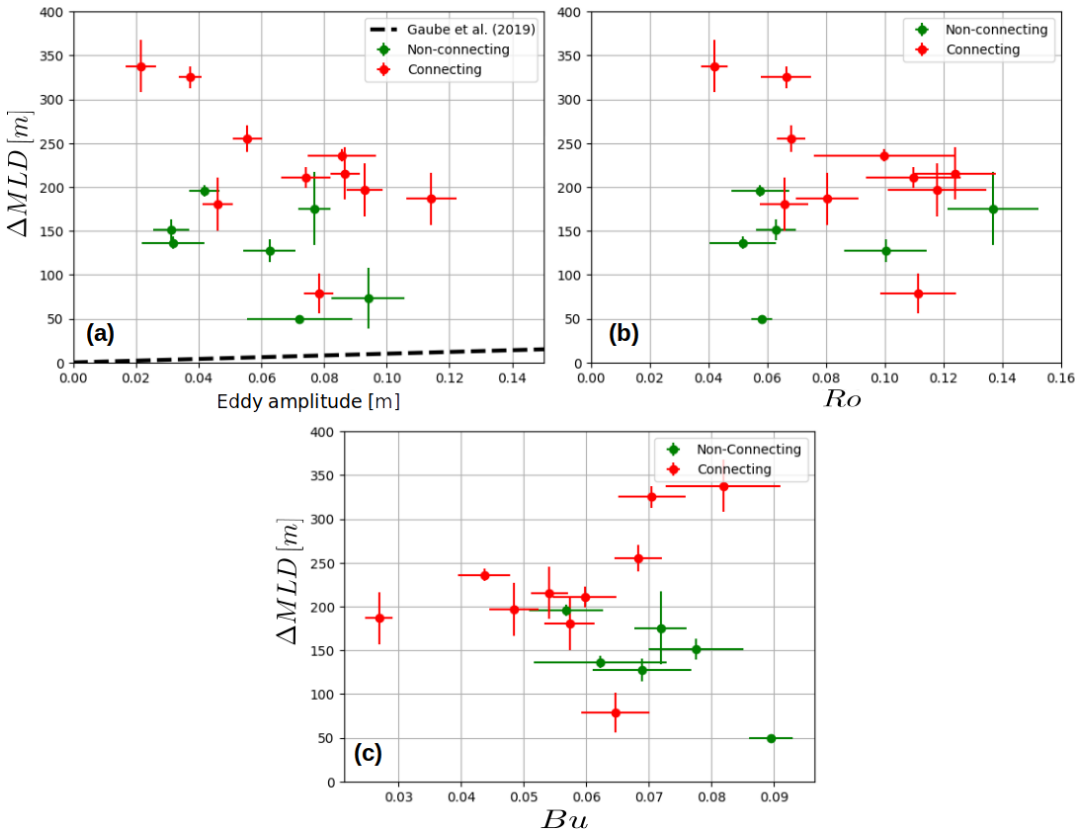

Figure 7. Relationship between maximal MLD anomaly (ΔMLD) and eddy parameters possibly measured through remote sensing: **(a)** eddy SSH amplitude, compared with proposed 1 m MLD for 1 cm SSH relation (Gaube et al., 2019); **(b)** Rossby number (eddy intensity); and **(c)** Burger number (non-dimensional eddy size).

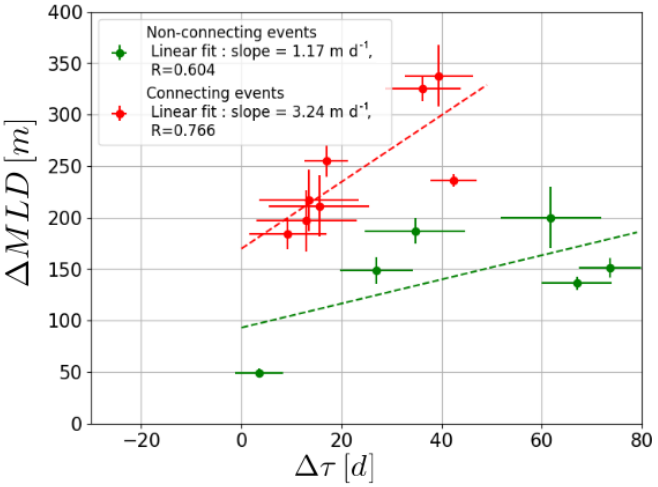

Figure 8. Scaling between the maximal MLD anomaly (ΔMLD) and restratification delay $\Delta\tau$ (see scheme in Fig. 3), distinguishing "connecting" (red) and "non-connecting" (green) events. Linear fit is applied separately, and correlation coefficient is put in the legend. Data and uncertainty are from Table 1.

shows the relation between $\Delta\tau$ and ΔMLD and reveals that no clear trend can be identified alone: deep MLD anomalies are observed when the anticyclone MLD restratified early (low $\Delta\tau$) or later (large $\Delta\tau$). However, when distinguishing "connecting" and "non-connecting" events, a linear trend appears separately: MLD anomalies go deeper as $\Delta\tau$ increases, and for similar $\Delta\tau$ values, "connecting" events go deeper. Linear fit is performed separately for both types, shown by the dashed line in Fig. 8: for each day of continued MLD deepening inside anticyclones, a "connecting" (respectively "non-connecting") MLD gets about 3 m deeper, with a correlation coefficient of 0.766 (1 m deeper, with a correlation coefficient of 0.604). This trend is logical, as a later restratification (large $\Delta\tau$) lets the MLD deepen longer and hence leads to larger ΔMLD.

In order to analyse the MLD evolution together with the mixed-layer cooling, Fig. 9 shows in the upper panels the MLD fits (see Sect. 3.3) and in the lower panels the corresponding mixed-layer temperature for the PEL2 and MM6 events. Both events are representative of the observed evolution where the temperature can be followed over the whole winter. Maximal background MLD is reached for PEL2 (respectively MM6) around 30 January 2016 (10 January 2021),

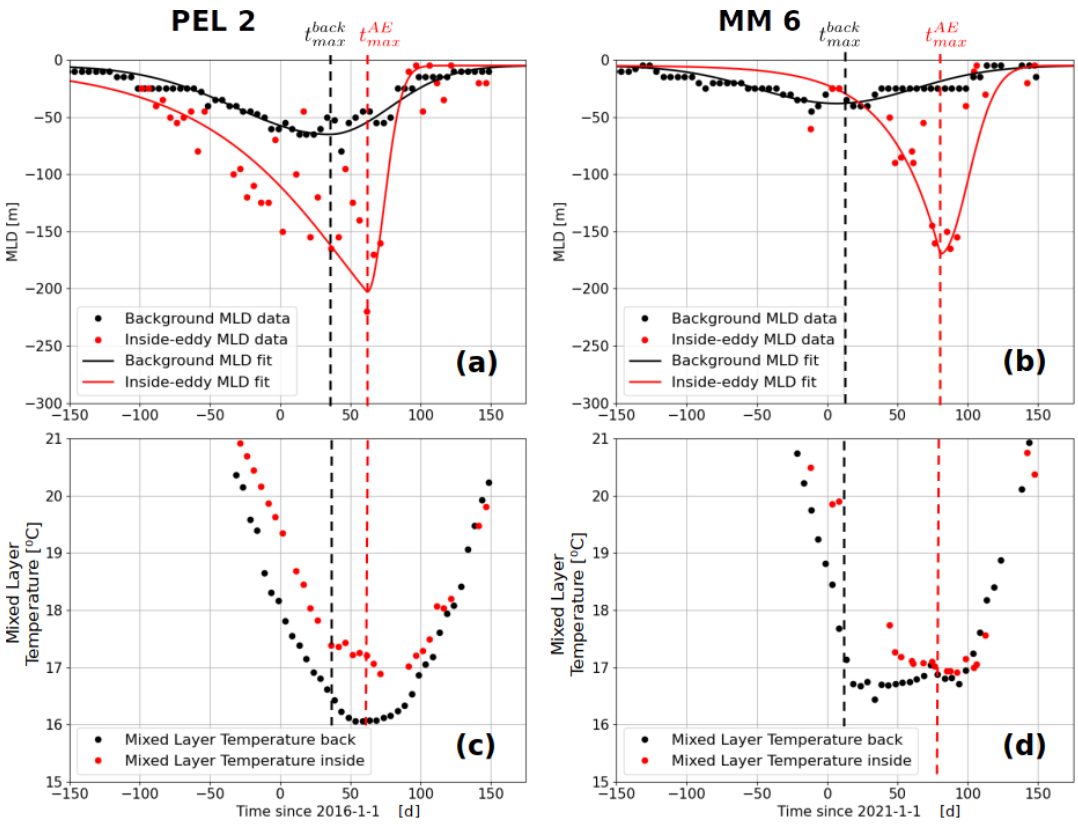

Figure 9. MLD data and fit for inside- and outside-eddy, illustrated for event PEL2 **(a)** and MM6 **(b)** (see Table 1). In the lower panel, corresponding mixed-layer temperature evolution for PEL2 **(c)** and MM6 **(d)** is shown. A dashed black (red) line marks the time of maximal background (inside-eddy) MLD.

marking the end of background mixed-layer cooling with a plateau temperature of about 16 °C, maintained for about 1.5 months (about 16.5 °C for about 3 months) before warming up. In early 2016 (2021), the anticyclone core is indeed about +1 °C warmer than its background, and it continues to cool for a while. The inside-eddy maximal MLD is reached around 1 March 2016 (20 March 2021) or +60 (+80) d in Fig. 9c (respectively Fig. 9d). A few weeks after, both background and anticyclonic core mixed layers started to warm again around 1 April (in both PEL2 and MM6), but background MLD started to restratify 1 month earlier in PEL2 (2 months earlier in MM6). Although it is hard to infer a mechanism from a few observations, it seems that the beginning of outside-eddy restratification does not mean that the mixed layer is warmed up again; rather, the outside-eddy mixed layer remains cold. The restratification delay seems to be the consequence of a maintained cooling of the initially warmer anticyclone core. Summer heating seems, on the other hand, to begin at the same time inside- and outside-eddy. Possible mechanisms driving this sustained mixing at the anticyclone core are discussed later in Sect. 5.3. An important observation is also that temperature difference between anticyclone core and the background is on the order of +1 °C while MLD deepens but almost vanishes (or even becomes slightly negative) when the mixed layer warms again. Although sparse, these in situ observation are in total agreement with the observed eddy SSTA switch (Moschos et al., 2022) from winter warm-core anticyclones to predominant cold-core anticyclones with spring restratification in the Mediterranean Sea.

5 Discussion on physical drivers and perspectives

5.1 MLD anomaly scaling

We clearly identified the distinction between "connecting" and "non-connecting" events as a more important driver than other eddy parameters such as eddy amplitude, surface intensity or size (see Figs. 7–8), and this might explain the difficulty in finding a general law for any eddy-induced MLD anomaly. Indeed, "connecting" deepening mixed layers seem limited by the bottom of the pre-existing subsurface homogeneous core to which they connect (example in Fig. 4e), whereas "non-connecting" ones by definition do not go deep enough, are then expected to be limited by the heat loss, and are likely also influenced by the eddy. The other important parameter is the restratification delay ($\Delta\tau$), measuring how long the anticyclone continues to deepen the MLD or not and

which eventually scales with the maximal MLD anomaly. From a remote sensing perspective, both parameters seem very hard to assess without in situ profiles inside the eddies. Examples shown in this study (Figs. 4, 5 and 10 below) showed the complexity induced by possible connection with previous subsurface anomalies and, more generally, the key role of the anticyclone vertical structure that was totally smoothed in previous composite studies. The relationship between eddy-induced MLD anomalies and satellite measurements are definitely more complex. However, as theorized by Assassi et al. (2016), detecting remotely information on the eddy vertical structure could be possible, particularly distinguishing the subsurface- or surface-intensified nature by comparing eddy signatures in SSH and SST. For instance, the ERA1 event in Fig. 4 is an almost textbook case of a subsurface anticyclone with isopycnals doming, leading to a cold eddy SSTA.

5.2 Double-core eddy formation

The high occurrence of "non-connecting" events (crosses in Fig. 6) is very interesting, as they show the formation of double-core anticyclones through winter deepening of the surface layer above a pre-existing density anomaly. Double-core eddies were often surveyed in the world ocean (Lilly et al., 2003; Belkin et al., 2020), including in the western Mediterranean Sea (Garreau et al., 2018). Despite various propositions (see e.g. Belkin et al., 2020, for a list), no clear formation mechanisms emerged. Several studies focused on the so-called "vertical alignment" of two eddies with different densities in experimental works (Nof and Dewar, 1994), observations (Lilly et al., 2003) or modelling (Trodahl et al., 2020). Interestingly, Lilly et al. (2003) observed well in the Labrador Sea that double-core anticyclones mostly consist of convective lenses formed in different winters, the heat flux interannual variability leading to different density anomalies, but they explained double-core structures with eddies formed separately and that later aligned. There were nonetheless previous observations of the generation of a second lighter core above a pre-existing anticyclone. Thanks to repeated XBT transects, Nilsson and Cresswell (1980) surveyed such phenomena in an anticyclone detached from the East Australian Current, caused by winter heat loss. Bosse et al. (2019) surveyed this in the Lofoten Basin eddy with winter convection but through glider sections spaced in time and then with a temporal resolution on the order of a month. More recently, Meunier et al. (2018) explained the formation of a double-core Loop Current eddy by winter diabatic processes. However, this case is different from the Mediterranean anticyclones, as the Loop Current eddy consists of an advection of a large structure of Caribbean waters into the Gulf of Mexico, experiencing different surface fluxes with more heat loss and precipitation than the area where they originate. These diabatic processes by surface winter mixing result in a fresher, shallower core above a saline core of subtropical under-waters. Moreover, Meunier et al. (2018) explained quantitatively the observed anomaly against the regional average of atmospheric fluxes, whereas in our study, the differential MLD evolution between the eddy core and the background (Figs. 4a and 5a) suggested flux variations at the scale of the eddy.

What drives the formation of double-core structures should be further investigated, but one could expect the interannual variability of heat fluxes to be the main driver. This was already suspected by Lilly et al. (2003), although for them it was for separate eddies, and by Moutin and Prieur (2012). A winter with strong heat loss is expected to deepen MLD a lot, including inside-eddy, and a subsequently warmer winter would not be able to deepen the MLD as much. This mechanism drives mode-water formation, and it was already shown in other regions, mostly the Atlantic Ocean, that eddies could modulate mode-water formation (Dugan et al., 1982; Chen et al., 2022). Such a hypothesis could also explain the high occurrence of "non-connecting" events in the Mediterranean Sea, this region being known for a high interannual variability of winter heat loss. Pettenuzzo et al. (2010) found maximal winter heat loss to vary by 20 % to 30 % (in terms of regional monthly average) and also found a plausible connection with the North Atlantic Oscillation (NAO). This interannual variability of the heat flux was already shown to influence deep convection in the northwestern Mediterranean Sea (L'Hévéder et al., 2013); thus, a higher occurrence of double-core anticyclones due to a stronger Mediterranean Sea stratification in a warming climate could be expected (Somot et al., 2006).

An important consequence in the formation of this lighter core in a "non-connecting" winter deepening is that the second core is separated from the surface by a thinner seasonal stratification. The next winter is then likely to connect again the new mixed layer with the upper core while possibly keeping the primitive deeper core untouched. Such an interaction from one winter to another was observed in the Ierapetra eddy and is presented in Fig. 10 (with the same colour code as in Figs. 4a–f and 5a–f). The Ierapetra eddy is a recurrent long-lived and intense anticyclone formed southeast of Crete (Theocharis et al., 1993; Lascaratos and Tsantilas, 1997; Ioannou et al., 2017) and recently surveyed by the PERLE 1 and 2 campaigns (Ioannou et al., 2019; Wimart-Rousseau, 2021). Similarly to Eratosthenes anticyclones previously shown, the density anomaly is mostly driven by a warm core, allowing the temperature profile to be used as a proxy for stratification (Ioannou et al., 2017). Figure 10 shows the Ierapetra anticyclone formed in autumn 2016. The first winter 2016–2017 turned out to be a "non-connecting" event ("IER1" in Table 1). Indeed, in March 2017, a pre-existing subsurface homogenized layer remained between 350 and 450 m, below the maximal anticyclonic core MLD of 220 m (Fig. 10c) and with about +2 °C temperature anomaly. From April to December 2017, summer heating restratified the upper layer and left below a second homogeneous layer

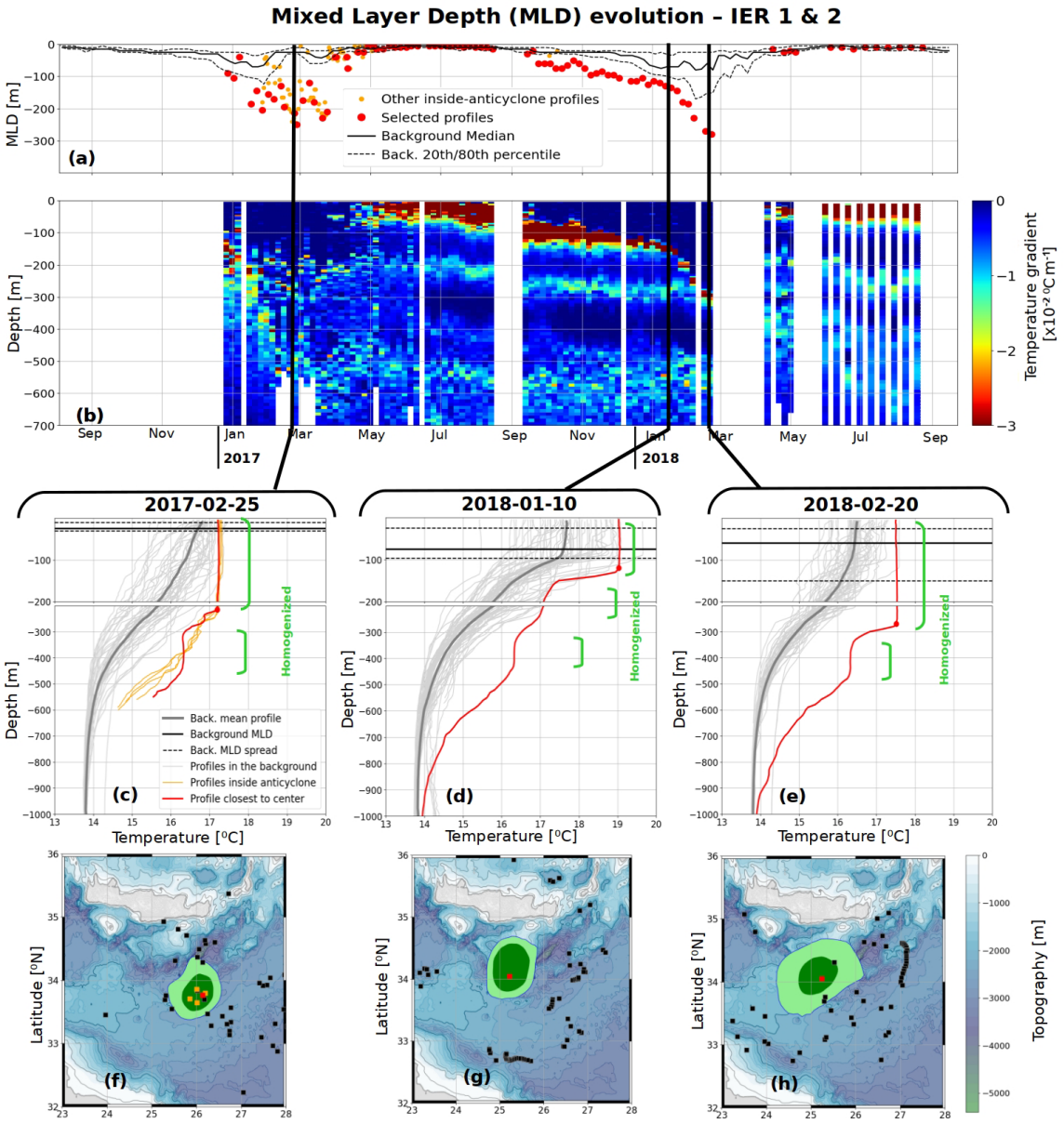

Figure 10. Same colour codes and legend as in Figs. 4 and 5 but for a Ierapetra anticyclone formed in 2016. Three vertical sections show respectively the mixing in early 2017 not reaching the deep subsurface core **(c)**, the winter in early 2018 with a double core, the shallow core from winter 2017–2018 and the deep core still untouched **(d)**, and at last the MLD deepening in March 2018 connecting the anomaly formed in March 2017 with the surface **(e)**.

between ∼ 100 and 200 m deep. The primitive core remained homogenized at depth and was separated by a temperature gradient throughout the summer (Fig. 10b). In January 2018 (Fig. 10d), the inside-eddy vertical profile showed the mixed-layer deepening at 120 m, which was already deeper than the background MLD, and the double-core structure was still retrieved. At last, at the end of February 2018 (Fig. 10e), the MLD completely eroded the seasonal stratification and connected the current MLD with the previous winter's subsurface core, then reaching about 280 m. The winter 2017–2018 is then a "connecting" event ("IER2" in Table 1). The time series is interrupted inside the anticyclone, but Argo floats are again colocalized in May 2018, and despite some variability, a temperature gradient continuously separated the two cores between 200 and 250 m (see Fig. 10b). IER2 was then a "connecting" event on a double-core structure. The primitive anticyclonic core was not mixed but remained homogenized at depth. These data bring to light a possible formation process of a double-core anticyclone through winter convection and also document for the first time the fate of the formed subsurface anomaly, which can be tracked up to the next winter when it gets mixed again.

5.3 Physical drivers

The observed importance of restratification delay $\Delta\tau$ should also have underlying physical mechanisms. Prolonged MLD deepening and cooling inside-eddy (see examples in Fig. 9) leads to the extreme MLD anomalies sometimes larger than 300 m and hence to marked MLD gradients that occur at the scale of the eddy radius or shorter. Indeed, Gaube et al. (2019) found anomalies on the order of the mesoscale (R_m), but in a composite vision, and for large eddies compared to the deformation radius (small Burger numbers), MLD gradients in eddies should occur on shorter scales (Meunier et al., 2018). Such marked MLD gradients should trigger mixed-layer instabilities leading to restratification (Boccaletti et al., 2007; Fox-Kemper et al., 2008), which calls for mechanisms sustaining the mixing inside-eddy during the restratification delay. It should be noted that a homogenized layer itself does not prove active mixing but still reveals the absence of restratification. Interestingly, we also noticed that, in several cases, Argo floats remained well in the anticyclone core during the MLD deepening phase but often left the eddy soon after, which may be a signature for mixed-layer instabilities impacting the eddy. The first mechanism explaining longer mixing in anticyclones could be an eddy modulation of air–sea fluxes by eddy-induced SSTA. Villas Bôas et al. (2015) observed such eddy modulation on air–sea sensible and latent heat fluxes but in regions of energetic surface-intensified eddies with very warm anticyclones (particularly the Agulhas current retroflexion). For subsurface anticyclones, the eddy-induced SSTA is, on the opposite end, expected to be weakened (see the example of the cold-core anticyclone shown in Fig. 4e and the study of Assassi et al., 2016), and this mechanism might then not be the most important. MLD deepening enhanced in anticyclones could be explained by other eddy retroactions besides the heat fluxes, a possible mechanism being the eddy-induced Ekman pumping (Stern, 1965; Gaube et al., 2015) or enhanced mixing in anticyclones due to near-inertial wave trapping (Kunze, 1985).

5.4 Impact on eddy dynamics

Connecting events also raise interesting questions on the consequence of such mixing of deeper subsurface anticyclone cores, particularly the role of inside-eddy convection in relation to the eddy dynamics itself. Studies in the literature mostly focused on winter convection inside cyclones because of the preconditioning with isopycnals doming at their centre (Legg et al., 1998; Legg and McWilliams, 2001). Such a phenomenon should also applied to subsurface anticyclones due to the surface isopycnals doming and subsequent stratification weakening (Assassi et al., 2016). The coincidence of observed multiple "connecting" winters in long-lived anticyclones like the Mersa Matruh and Eratosthenes structures suggests a possible mechanism regenerating these structures, which maybe explains the extremely marked cyclone–anticyclone lifetime asymmetry in the Levantine Basin (Mkhinini et al., 2014; Barboni et al., 2021). Interestingly, Brenner (1993) already proposed winter cooling as a possible mechanism explaining the sustained lifetime of the anticyclone surveyed south of Cyprus. The other structure calling for comparison is the Lofoten eddy in the Sea of Norway and the Rockwall Trough eddy offshore Ireland, two long-lived deep anticyclonic structures. Winter convection was observed inside the core of the Lofoten eddy and was once thought to help regenerate the structure (Ivanov and Korablev, 1995; Köhl, 2007; Bosse et al., 2019). Double-core formation was also observed in the Lofoten eddy (Bosse et al., 2019). Recent numerical studies showed that this regeneration was primarily driven by the merging of smaller structures (Köhl, 2007; Trodahl et al., 2020); however, de Marez et al. (2021) showed that wintertime convection eased this merging process by deepening of the eddy core. Merging of eddies detached from the coast towards an offshore anticyclonic attractor was also observed in the Levantine Basin (Barboni et al., 2021), which could provide another explanation for the long-lived Mediterranean anticyclones. Cyclone–anticyclone asymmetry might not have just one mechanism, as other arguments have already proposed. Anticyclones indeed have a larger radius and are more coherent.

5.5 Biological impacts inside anticyclones

"Connecting"' the winter mixed layer in the Eratosthenes anticyclone was already observed by Krom et al. (1992) with a biogeochemical focus in 1989 (there called the "Cyprus eddy"). They measured a February inside-anticyclone MLD of 450 m (compared to 200 m) at the eddy boundary, with later spring restratification in May. Their temperature profile clearly corresponded to a "connecting" event, with even deeper MLD than in our study. Also comparing nitrates, phosphates and chlorophyll, they showed that chlorophyll production was about 30 % more abundant at the eddy core while being relatively similar to the Levantine Basin average at its edge. The main nitracline was consistently measured below the winter mixed layer and also at the eddy core, then around 450 m. While spring phytoplankton bloom occurred at the surface, they observed a mixed homogeneous layer that remained aphotic between the euphotic zone (the upper 120 m) and this deep main nitracline (called the "decomposition zone" in Krom et al., 1992). Here, they observed instead that, from February 1989 to January 1990, there was an increase in both nitrates and phosphates. Consequently, in the eddy, a second nitracline formed at the bottom of the euphotic layer at approximately the same level as a summer deep-chlorophyll maximum. Similarly, in another Eratosthenes structure in July 2008, Moutin and Prieur (2012) also estimated the maximal mixed layer in the previous winter to have reached 396 m and left only a stratified thermocline below, another clear description of a "connecting" win-

ter mixing. Moutin and Prieur (2012) also observed in the eddy a main nitracline at roughly 400 m depth and a second one around 100 m together with a deep-chlorophyll maximum. The 100–400 m depth zone continued with low mineralization and high values of dissolved organic matter (DOC). From these observations, it seems that a "connecting" deep MLD induces a strong nutrient input to the euphotic layer but establishes in summer a homogenized aphotic subsurface layer with high DOC export at depth.

Neither of the two studies mentioned above observed the case of a "non-connecting" MLD, as frequently observed in our study and also in an Eratosthenes anticyclone (see Fig. 5). However, Moutin and Prieur (2012) discussed this possibility: if the winter MLD does not reach the main nitracline and/or phosphacline, it would keep the upper layer away from the deep nutriment source. The whole system would then evolve towards an ultra-oligotrophic system because of nutrients being very weakly injected to the euphotic layer. This is expected to be the case particularly when a primitive subsurface core does not connect to the surface for several winters, such as in the example of the Ierapetra anticyclone in Fig. 10. The high frequency of "non-connecting" anticyclone MLD observed in our study then suggests that anticyclones in the eastern Mediterranean Sea are to be considered ultra-oligotrophic systems more frequently than previously thought. Temporal evolution of such "non-connecting" events with biogeochemical instruments such as BGC-Argo would be interesting to follow this analysis.

6 Conclusions

In this paper, we were able to analyse, thanks to a combination of satellite observations and numerous in situ data, several time series that finely describe the evolution of the winter mixed layer in the core of Mediterranean anticyclones. We even succeeded in following, for the same long-lived anticyclone, the evolution of its MLD over 2 consecutive years. This allowed us to quantify extreme anomalies induced by mesoscale eddies in the mixed layer, which would have been smoothed in a standard composite analysis. Indeed, we observed that the winter mixed layer can go down to 380 m in the core of Levantine Basin anticyclones, while the surrounding background MLD does not go deeper than 80 m or 100 m.

We also observed a time lag of several weeks and sometimes of up to 2 months in the spring restratification between the core of these deep anticyclones and the background sea, revealing that MLD temporal evolution is not uniform. Indeed, when the later restratifies due to the rising temperature of the atmosphere, the core of these mesoscale anticyclones, which are warmer, continues to deepen and to cool. This time lag induces very strong spatial heterogeneities of the MLD in the eastern Mediterranean Sea during the early spring, with observed maximal MLD ranging from 50 to 330 m.

We showed that this localized deepening of the MLD is controlled by the vertical structure of these eddies. When the surface mixing layer connects with the subsurface core of pre-existing anticyclones, a rapid deepening of the surface mixed layer is observed. Conversely, when the surface mixed layer does not connect with the subsurface core, a double-core eddy is formed. Connection or not with pre-existing subsurface cores proves to be more relevant to a description of MLD deepening than other eddy parameters such as SSH amplitude or size. MLD anomalies were observed to linearly increase with restratification delay but increased roughly 2 to 3 times faster for "connecting" MLD than for the "non-connecting" one.

These extreme MLD deepenings in anticyclone cores reveal complex and rich interaction between the surface and subsurface of the eddies. Connection between the mixed layer and subsurface anomalies provides a way to propagate heat at depth while mixing in winter, the consequences of which remain to be investigated. These winter deepenings inside anticyclones could also play a role in sustaining the extremely long-lived anticyclone in the eastern Mediterranean. MLD anomalies in cyclonic eddies remain to be investigated, and an open question would be to know if a restratification delay could also be observed in cyclones.

Appendix A: In situ profile-checking methodology

In both CORA-DT (Szekely et al., 2019b) and Copernicus-NRT (Copernicus, 2021) datasets, vertical profiles data coming from XBT, CTD, glider and profiling floats are collected by selecting files with respective data type codes XB, CT, GL and PF. When a profile from 2000 to 2019 was available in both DT and NRT mode, it was retrieved from the CORA-DT dataset, which performs more quality checks (Szekely et al., 2019a). Selection was done with the following steps, separately for temperature and salinity, and when available, "ADJUSTED" properties were collected:

- Position and date quality control (QC) flags equal to 1, 2 or 5 and position not on land.
- Select the first valid value (QC = 1,2 or 5) above 50 m, the last valid value below 400 m, and at least 40 measurements between 50 and 400 m.
- Temperature data below 12 °C or above 35 °C are discarded, and salinity data below 30 PSU or above 42 PSU are discarded. These parameters are specific to the Mediterranean Sea.
- When both temperature and salinity are available, density is computed using the TEOS-10 equation (McDougall et al., 2013) from the Python package `gsw` (https://teos-10.github.io/GSW-Python/, last access: 21 February 2023).
- Profiles are linearly interpolated on the same vertical grid, with 5 m grid steps from 5 to 300 m depth and 10 m grid steps from 300 to 2000 m. The maximal gap allowed is 20 m, and profiles with gaps are discarded.
- Profiles with temperature jumps higher than +6 °C or −2 °C (positive upwards) between two grid points are discarded, as they are assumed to be unrealistic. This is required particularly to filter out noisy XBT profiles.
- After these steps, only profiles with more than 40 data on the interpolated grid between 50 and 400 m are kept.

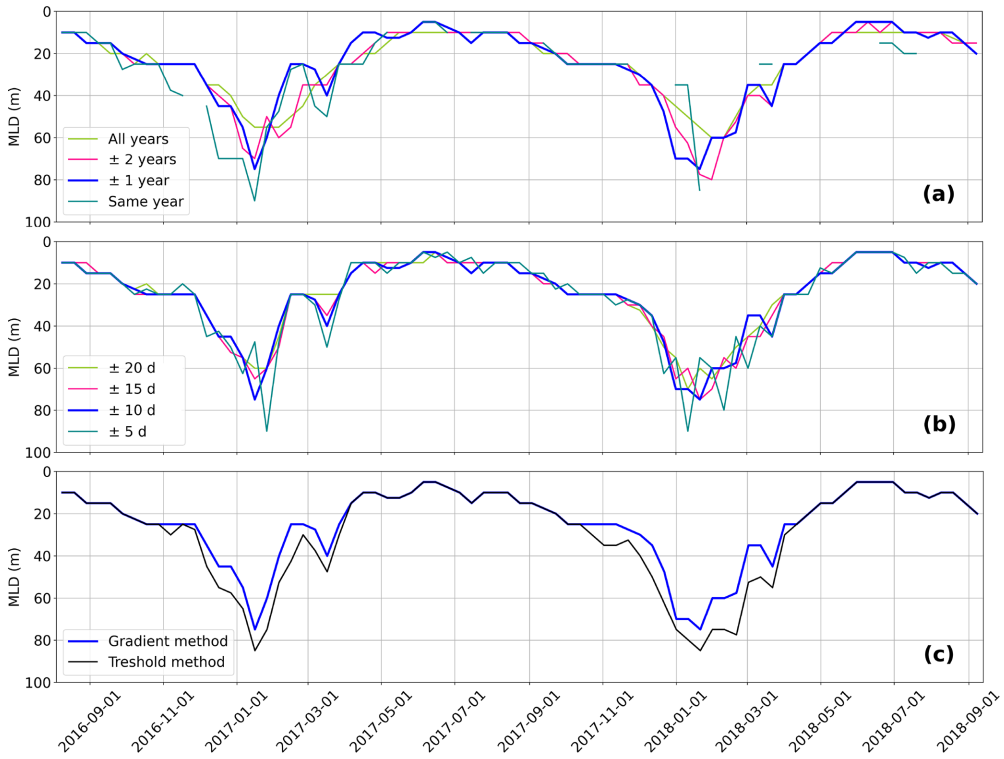

Figure A1. Sensitivity of the background MLD on the different parameters for events IER1–2 (see Table 1 and Fig. 10a): **(a)** Δy (year interval) and **(b)** Δday (day interval). **(c)** Sensitivity to the MLD computation method. The background MLD method used throughout this study is Δday $= 10$ d, $\Delta y = 1$ year and the gradient method (common navy blue line on panels **a–c**).

Data availability. CORA DT profiles (Szekely et al., 2019b) are freely available online on the Copernicus Marine Service (CMEMS, https://marine.copernicus.eu/, last access: 28 February 2023) under product name INSITU_GLO_TS_REP_OBSERVATIONS_013_001_b. Copernicus NRT profiles (Copernicus, 2021) are freely available on CMEMS under product name INSITU_GLO_NRT_OBSERVATIONS_013_030. DYNED-Atlas eddy altimetric detections and contours from 2000 to 2019 are available at https://doi.org/10.14768/2019130201.2 (Stegner and Le Vu, 2019). AVISO SSHNRT day + 6 1/8° data (Pujol, 2021) are freely available on CMEMS under product name SEALEVEL_EUR_PHY_L4_NRT_OBSERVATIONS_008_060 AMEDA eddy-tracking algorithm is open source and available at https://doi.org/10.5281/zenodo.7673442 (Le Vu, 2023). The complete used in-situ dataset colocalized with eddy detections (Barboni et al., 2023) is available at SEANOE and through the link: https://doi.org/10.17882/93077.

Author contributions. AB and SCC built the methodology, performed the data analysis and investigation, wrote the paper, and contributed equally to this work. AS supervised and validated the study and did funding acquisition. BLV processed and produced eddy detections. FD provided in situ data in cooperation with SHOM cruises.

Competing interests. The contact author has declared that none of the authors has any competing interests.

Disclaimer. Publisher's note: Copernicus Publications remains neutral with regard to jurisdictional claims in published maps and institutional affiliations.

Acknowledgements. The authors gratefully acknowledge the French Naval Hydrologic and Oceanographic Service (SHOM) and the crew of the RV *L'Atalante* (Ifremer) for their contribution to the PERLE1 campaign, the crew of the RV *Pourquoi Pas?* (Ifremer) for their contribution to the PERLE2 campaign, and the crew of the BHO *Beautemps-Beaupré* (SHOM) for their contribution to the opportunity Arvor deployments in the Mersa Matruh eddy in February 2021. The Argo data were collected and made freely available by the International Argo Programme and the national programmes that contribute to it (http://argo.jcommops.org/, last access: 21 February 2023). We would also like to thank Arthur Capet and an anonymous referee, as their contributions and comments improved the article.

Financial support. The PERLE programme has received funding from the European FEDER Fund under project 1166-39417. The PROTEVS programme was funded by the Direction Générale de l'Armement. Most Argo floats presented in this study were funded by the NAOS (funded by the Agence Nationale de la Recherche – ANR – in the framework of the French programme "Equipement d'Avenir", grant no. ANR J11R107-F) and MISTRALS-MERMEX (CNRS, INSU) programmes. The DYNED-Atlas project was part of the ANRAstrid project (grant no. ANR-15-ASMA-0003-01), CNES, and SHOM (contract no. 18CP01).

Review statement. This paper was edited by Aida Alvera-Azcárate and reviewed by Arthur Capet and one anonymous referee.

References

Amores, A., Jordà, G., and Monserrat, S.: Ocean eddies in the Mediterranean Sea from satellite altimetry: Sensitivity to satellite track location, Front. Mar. Sci., 6, p. 703, 2019.

Arai, M. and Yamagata, T.: Asymmetric evolution of eddies in rotating shallow water, Chaos: An Interdisciplinary, J. Nonlinear Sci., 4, 163–175, 1994.

Aroucha, L. C., Veleda, D., Lopes, F. S., Tyaquiçã, P., Lefèvre, N., and Araujo, M.: Intra- and Inter-Annual Variability of North Brazil Current Rings Using Angular Momentum Eddy Detection and Tracking Algorithm: Observations From 1993 to 2016, J. Geophys. Res.-Ocean., 125, e2019JC015921, https://doi.org/10.1029/2019JC015921, 2020.

Assassi, C., Morel, Y., Vandermeirsch, F., Chaigneau, A., Pegliasco, C., Morrow, R., Colas, F., Fleury, S., Carton, X., Klein, P., and Cambra, R.: An index to distinguish surface-and subsurface-intensified vortices from surface observations, J. Phys. Oceanogr., 46, 2529–2552, 2016.

Ayouche, A., De Marez, C., Morvan, M., L'Hegaret, P., Carton, X., Le Vu, B., and Stegner, A.: Structure and dynamics of the Ras al Hadd oceanic dipole in the Arabian Sea, in: Oceans, Vol. 2, 105–125, MDPI, https://doi.org/10.3390/oceans2010007, 2021.

Barboni, A., Lazar, A., Stegner, A., and Moschos, E.: Lagrangian eddy tracking reveals the Eratosthenes anticyclonic attractor in the eastern Levantine Basin, Ocean Sci., 17, 1231–1250, https://doi.org/10.5194/os-17-1231-2021, 2021.

Barboni, A., Stegner, A., Le Vu, B., and Dumas, F.: 2000–2021 In situ profiles colocalized with AMEDA eddy detections from 1/8 AVISO altimetry in the Mediterranean sea, SEANOE [data set], https://doi.org/10.17882/93077, 2023.

Belkin, I., Foppert, A., Rossby, T., Fontana, S., and Kincaid, C.: A Double-Thermostad Warm-Core Ring of the Gulf Stream, J. Phys. Oceanogr., 50, 489–507, https://doi.org/10.1175/JPO-D-18-0275.1, 2020.

Bevington, P. R., Robinson, D. K., Blair, J. M., Mallinckrodt, A. J., and McKay, S.: Data reduction and error analysis for the physical sciences, Comput. Phys., 7, 415–416, 1993.

Boccaletti, G., Ferrari, R., and Fox-Kemper, B.: Mixed layer instabilities and restratification, J. Phys. Oceanogr., 37, 2228–2250, 2007.

Bosse, A., Fer, I., Lilly, J. M., and Søiland, H.: Dynamical controls on the longevity of a non-linear vortex: The case of the Lofoten Basin Eddy, Sci. Rep., 9, 1–13, 2019.

Brenner, S.: Long-term evolution and dynamics of a persistent warm core eddy in the Eastern Mediterranean Sea, Deep-Sea Res. Pt. II, 40, 1193–1206, 1993.

Budillon, G., Gasparini, G., and Schroeder, K.: Persistence of an eddy signature in the central Tyrrhenian basin, Deep-Sea Res. Pt. II, 56, 713–724, 2009.

Chelton, D. B., Schlax, M. G., and Samelson, R. M.: Global observations of nonlinear mesoscale eddies, Prog. Oceanogr., 91, 167–216, 2011.

Chen, Y., Speich, S., and Laxenaire, R.: Formation and Transport of the South Atlantic Subtropical Mode Water in Eddy-Permitting Observations, J. Geophys. Res.-Ocean., 127, e2021JC017767, https://doi.org/10.1029/2021JC017767, 2022.

Copernicus: Global Ocean-In-Situ Near-Real-Time Observations, Copernicus Marine In Situ Tac Data Management [data set], https://doi.org/10.48670/moi-00036, 2021.

D'Asaro, E. A.: The energy flux from the wind to near-inertial motions in the surface mixed layer, J. Phys. Oceanogr., 15, 1043–1059, 1985.

de Boyer Montégut, C., Madec, G., Fischer, A. S., Lazar, A., and Iudicone, D.: Mixed layer depth over the global ocean: An examination of profile data and a profile-based climatology, J. Geophys. Res.-Ocean., 109, C12, https://doi.org/10.1029/2004JC002378, 2004.

de Marez, C., Le Corre, M., and Gula, J.: The influence of merger and convection on an anticyclonic eddy trapped in a bowl, Ocean Model., 167, 101874, https://doi.org/10.1016/j.ocemod.2021.101874, 2021.

Dong, S., Sprintall, J., Gille, S. T., and Talley, L.: Southern Ocean mixed-layer depth from Argo float profiles, J. Geophys. Res.-Ocean., 113, C6, https://doi.org/10.1029/2006JC004051, 2008.

D'Ortenzio, F. and Ribera d'Alcalà, M.: On the trophic regimes of the Mediterranean Sea: a satellite analysis, Biogeosciences, 6, 139–148, https://doi.org/10.5194/bg-6-139-2009, 2009.

D'Ortenzio, F., Iudicone, D., de Boyer Montégut, C., Testor, P., Antoine, D., Marullo, S., Santoleri, R., and Madec, G.: Seasonal variability of the mixed layer depth in the Mediterranean Sea as derived from in situ profiles, Geophys. Res. Lett., 32, 12, https://doi.org/10.1029/2005GL022463, 2005.

D'Ortenzio, F., Taillandier, V., Claustre, H., Coppola, L., Conan, P., Dumas, F., Durrieu du Madron, X., Fourrier, M., Gogou, A., Karageorgis, A., Lefevre, D., Leymarie, E., Oviedo, A., Pavlidou, A., Poteau, A., Poulain, P. M., Prieur, L., Psarra, S., Puyo-Pay, M., Ribera d'Alcalà, M., Schmechtig, C., Terrats, L., Velaoras, D., Wagener, T., and Wimart-Rousseau, C.: BGC-Argo Floats Observe Nitrate Injection and Spring Phytoplankton Increase in the Surface Layer of Levantine Sea (Eastern Mediterranean), Geophys. Res. Lett., 48, e2020GL091649, https://doi.org/10.1029/2020GL091649, 2021.

Dufois, F., Hardman-Mountford, N. J., Greenwood, J., Richardson, A. J., Feng, M., and Matear, R. J.: Anticyclonic eddies are more productive than cyclonic eddies in subtropical gyres because of winter mixing, Sci. Adv., 2, e1600282, https://doi.org/10.1126/sciadv.1600282, 2016.

Dugan, J., Mied, R., Mignerey, P., and Schuetz, A.: Compact, intrathermocline eddies in the Sargasso Sea, J. Geophys. Res.-Ocean., 87, 385–393, 1982.

Fox-Kemper, B., Ferrari, R., and Hallberg, R.: Parameterization of mixed layer eddies, Part I: Theory and diagnosis, J. Phys. Oceanogr., 38, 1145–1165, 2008.

Frenger, I., Gruber, N., Knutti, R., and Münnich, M.: Imprint of Southern Ocean eddies on winds, clouds and rainfall, Nat. Geosci., 6, 608–612, 2013.

Garreau, P., Dumas, F., Louazel, S., Stegner, A., and Le Vu, B.: High-Resolution Observations and Tracking of a Dual-Core Anticyclonic Eddy in the Algerian Basin, J. Geophys. Res.-Ocean., 123, 9320–9339, 2018.

Gaube, P., Chelton, D. B., Samelson, R. M., Schlax, M. G., and O'Neill, L. W.: Satellite observations of mesoscale eddy-induced Ekman pumping, J. Phys. Oceanogr., 45, 104–132, 2015.

Gaube, P., J. McGillicuddy Jr., D., and Moulin, A. J.: Mesoscale eddies modulate mixed layer depth globally, Geophys. Res. Lett., 46, 1505–1512, 2019.

Graves, L. P., McWilliams, J. C., and Montgomery, M. T.: Vortex evolution due to straining: A mechanism for dominance of strong, interior anticyclones, Geophys. Astrophys. Fluid Dynam., 100, 151–183, 2006.

Hamad, N., Millot, C., and Taupier-Letage, I.: The surface circulation in the eastern basin of the Mediterranean Sea, Sci. Mar., 70, 457–503, 2006.

Hausmann, U. and Czaja, A.: The observed signature of mesoscale eddies in sea surface temperature and the associated heat transport, Deep-Sea Res. Pt. I, 70, 60–72, 2012.

Hausmann, U., McGillicuddy Jr., D. J., and Marshall, J.: Observed mesoscale eddy signatures in Southern Ocean surface mixed-layer depth, J. Geophys. Res.-Ocean., 122, 617–635, 2017.

Hayes, D., Zodiatis, G., Konnaris, G., Hannides, A., Solovyov, D., and Testor, P.: Glider transects in the Levantine Sea: Characteristics of the warm core Cyprus eddy, in: OCEANS 2011 IEEE-Spain, 1–9, IEEE, https://doi.org/10.1109/Oceans-Spain.2011.6003393, 2011.

He, Q., Zhan, H., Cai, S., He, Y., Huang, G., and Zhan, W.: A new assessment of mesoscale eddies in the South China Sea: Surface features, three-dimensional structures, and thermohaline transports, J. Geophys. Res.-Ocean., 123, 4906–4929, 2018.

Holte, J. and Talley, L.: A new algorithm for finding mixed layer depths with applications to Argo data and Subantarctic Mode Water formation, J. Atmos. Ocean. Technol., 26, 1920–1939, 2009.

Holte, J., Talley, L. D., Gilson, J., and Roemmich, D.: An Argo mixed layer climatology and database, Geophys. Res. Lett., 44, 5618–5626, 2017.

Houpert, L., Testor, P., De Madron, X. D., Somot, S., D'ortenzio, F., Estournel, C., and Lavigne, H.: Seasonal cycle of the mixed layer, the seasonal thermocline and the upper-ocean heat storage rate in the Mediterranean Sea derived from observations, Prog. Oceanogr., 132, 333–352, 2015.

Ioannou, A., Stegner, A., Le Vu, B., Taupier-Letage, I., and Speich, S.: Dynamical evolution of intense Ierapetra eddies on a 22 year long period, J. Geophys. Res.-Ocean., 122, 9276–9298, 2017.

Ioannou, A., Stegner, A., Tuel, A., LeVu, B., Dumas, F., and Speich, S.: Cyclostrophic corrections of AVISO/DUACS surface velocities and its application to mesoscale eddies in the Mediterranean Sea, J. Geophys. Res.-Ocean., 124, 8913–8932, 2019.

Ioannou, A., Stegner, A., Dumas, F., and Le Vu, B.: Three-dimensional evolution of mesoscale anticyclones in the lee of Crete, Front. Mar. Sci., 7, 609156, https://doi.org/10.3389/fmars.2020.609156, 2020.

Ivanov, V. and Korablev, A.: Formation and regeneration of intrapycnocline lense in the Norwegian Sea, Russ. Meteor. Hydrol., 9, 62–69, 1995.

Köhl, A.: Generation and stability of a quasi-permanent vortex in the Lofoten Basin, J. Phys. Oceanogr., 37, 2637–2651, 2007.

Krom, M., Brenner, S., Kress, N., Neori, A., and Gordon, L.: Nutrient dynamics and new production in a warm-core eddy from the Eastern Mediterranean Sea, Deep-Sea Res. Pt. A, 39, 467–480, 1992.

Kunze, E.: Near-inertial wave propagation in geostrophic shear, J. Phys. Oceanogr., 15, 544–565, 1985.

Kurkin, A., Kurkina, O., Rybin, A., and Talipova, T.: Comparative analysis of the first baroclinic Rossby radius in the Baltic, Black, Okhotsk, and Mediterranean seas, Russ. J. Earth Sci., 20, 8, https://doi.org/10.2205/2020ES000737, 2020.

Lacour, L., Briggs, N., Claustre, H., Ardyna, M., and Dall'Olmo, G.: The intraseasonal dynamics of the mixed layer pump in the subpolar North Atlantic Ocean: A Biogeochemical-Argo float approach, Global Biogeochem. Cy., 33, 266–281, 2019.

Large, W. and Yeager, S.: On the observed trends and changes in global sea surface temperature and air–sea heat fluxes (1984–2006), J. Clim., 25, 6123–6135, 2012.

Lascaratos, A. and Tsantilas, S.: Study of the seasonal circle of the Ierapetra gyra, using satellite imager, in: Proc. Hell. Symp. Oceanogr. Fish, Vol. 1, 165–168, 1997.

Lavigne, H., d'Ortenzio, F., Migon, C., Claustre, H., Testor, P., d'Alcalã, M. R., Lavezza, R., Houpert, L., and Prieur, L.: Enhancing the comprehension of mixed layer depth control on the Mediterranean phytoplankton phenology, J. Geophys. Res.-Ocean., 118, 3416–3430, 2013.

Legg, S. and McWilliams, J. C.: Convective modifications of a geostrophic eddy field, J. Phys. Oceanogr., 31, 874–891, 2001.

Legg, S., McWilliams, J., and Gao, J.: Localization of deep ocean convection by a mesoscale eddy, J. Phys. Oceanogr., 28, 944–970, 1998.

Le Traon, P. Y.: From satellite altimetry to Argo and operational oceanography: three revolutions in oceanography, Ocean Sci., 9, 901–915, https://doi.org/10.5194/os-9-901-2013, 2013.

Le Vu, B.: briaclevu/AMEDA: AMEDA v2.2 (v2.2), Zenodo [code], https://doi.org/10.5281/zenodo.7673442, 2023.

Le Vu, B., Stegner, A., and Arsouze, T.: Angular Momentum Eddy Detection and tracking Algorithm (AMEDA) and its application to coastal eddy formation, J. Atmos. Ocean. Technol., 35, 739–762, 2018.

Lévy, M., Ferrari, R., Franks, P. J., Martin, A. P., and Rivière, P.: Bringing physics to life at the submesoscale, Geophys. Res. Lett., 39, https://doi.org/10.1029/2012GL052756, 2012.

Lilly, J. M., Rhines, P. B., Schott, F., Lavender, K., Lazier, J., Send, U., and D'Asaro, E.: Observations of the Labrador Sea eddy field, Prog. Oceanogr., 59, 75–176, 2003.

Liu, F., Zhou, H., Huang, W., and Wen, B.: Submesoscale Eddies Observation Using High-Frequency Radars: A Case Study in the Northern South China Sea, IEEE J. Ocean. Eng., 46, 624–633, 2020.

L'Hévéder, B., Li, L., Sevault, F., and Somot, S.: Interannual variability of deep convection in the Northwestern Mediterranean simulated with a coupled AORCM, Clim. Dynam., 41, 937–960, 2013.

McDougall, T. J., Feistel, R., and Pawlowicz, R.: Thermodynamics of seawater, in: International Geophysics, Vol. 103, 141–158, Academic Press, 2013.

Meunier, T., Pallás-Sanz, E., Tenreiro, M., Portela, E., Ochoa, J., Ruiz-Angulo, A., and Cusí, S.: The vertical structure of a Loop Current Eddy, J. Geophys. Res.-Ocean., 123, 6070–6090, 2018.

Millot, C. and Taupier-Letage, I.: Circulation in the Mediterranean Sea, in: The Mediterranean Sea, edited by: Saliot, A., Handbook of Environmental Chemistry, Vol. 5, Springer, Berlin, Heidelberg, https://doi.org/10.1007/b107143, 2005.

Mkhinini, N., Coimbra, A. L. S., Stegner, A., Arsouze, T., Taupier-Letage, I., and Béranger, K.: Long-lived mesoscale eddies in the eastern Mediterranean Sea: Analysis of 20 years of AVISO geostrophic velocities, J. Geophys. Res.-Ocean., 119, 8603–8626, 2014.

Moschos, E., Barboni, A., and Stegner, A.: Why do inverse eddy surface temperature anomalies emerge? The case of the Mediterranean Sea, Remote Sens., 14, 3807, https://doi.org/10.3390/rs14153807, 2022.

Moutin, T. and Prieur, L.: Influence of anticyclonic eddies on the Biogeochemistry from the Oligotrophic to the Ultraoligotrophic Mediterranean (BOUM cruise), Biogeosciences, 9, 3827–3855, https://doi.org/10.5194/bg-9-3827-2012, 2012.

Nilsson, C. and Cresswell, G.: The formation and evolution of East Australian Current warm-core eddies, Prog. Oceanogr., 9, 133–183, 1980.

Nof, D. and Dewar, W.: Alignment of lenses: Laboratory and numerical experiments, Deep-Sea Res. Pt. I, 41, 1207–1229, 1994.

Ozer, T., Gertman, I., Kress, N., Silverman, J., and Herut, B.: Interannual thermohaline (1979–2014) and nutrient (2002–2014) dynamics in the Levantine surface and intermediate water masses, SE Mediterranean Sea, Glob. Planet. Change, 151, 60–67, 2017.

Parras-Berrocal, I. M., Vazquez, R., Cabos, W., Sein, D., Mañanes, R., Perez-Sanz, J., and Izquierdo, A.: The climate change signal in the Mediterranean Sea in a regionally coupled atmosphere–ocean model, Ocean Sci., 16, 743–765, https://doi.org/10.5194/os-16-743-2020, 2020.

Pastor, F., Valiente, J. A., and Khodayar, S.: A warming Mediterranean: 38 years of increasing sea surface temperature, Remote Sens., 12, 2687, https://doi.org/10.3390/rs12172687, 2020.

Pegliasco, C., Delepoulle, A., Mason, E., Morrow, R., Faugère, Y., and Dibarboure, G.: META3.1exp: a new global mesoscale eddy trajectory atlas derived from altimetry, Earth Syst. Sci. Data, 14, 1087–1107, https://doi.org/10.5194/essd-14-1087-2022, 2022.

Pettenuzzo, D., Large, W., and Pinardi, N.: On the corrections of ERA-40 surface flux products consistent with the Mediterranean heat and water budgets and the connection between basin surface total heat flux and NAO, J. Geophys. Res.-Ocean., 115, C6, https://doi.org/10.1029/2009JC005631, 2010.

Pujol, M.-I.: Europeans Seas gridded L4 Sea Surface Height and derived variables NRT, Copernicus Marine In Situ Tac Data Management [data set], https://doi.org/10.48670/moi-00142, 2021.

Smith, W. H. and Sandwell, D. T.: Global sea floor topography from satellite altimetry and ship depth soundings, Science, 277, 1956–1962, 1997.

Somot, S., Sevault, F., and Déqué, M.: Transient climate change scenario simulation of the Mediterranean Sea for the twenty-first century using a high-resolution ocean circulation model, Clim. Dynam., 27, 851–879, 2006.

Stegner, A. and Le Vu, B.: Atlas of 3D Eddies in the Mediterranean Sea from 2000 to 2017, ESPRI/IPSL, https://doi.org/10.14768/2019130201.2, 2019.

Stegner, A., Le Vu, B., Dumas, F., Ghannami, M. A., Nicolle, A., Durand, C., and Faugere, Y.: Cyclone-Anticyclone Asymmetry of Eddy Detection on Gridded Altimetry Product in the Mediter-

ranean Sea, J. Geophys. Res.-Ocean., 126, e2021JC017475, https://doi.org//10.1029/2021JC017475, 2021.

Stern, M. E.: Interaction of a uniform wind stress with a geostrophic vortex, in: Deep Sea Research and Oceanographic Abstracts, Vol. 12, 355–367, Elsevier, https://doi.org/10.1016/0011-7471(65)90007-0, 1965.

Szekely, T., Gourrion, J., Pouliquen, S., and Reverdin, G.: The CORA 5.2 dataset for global in situ temperature and salinity measurements: data description and validation, Ocean Sci., 15, 1601–1614, https://doi.org/10.5194/os-15-1601-2019, 2019a.

Szekely, T., Gourrion, J., Pouliquen, S., Reverdin, G., and Merceur, F.: CORA, Coriolis Ocean Dataset for Reanalysis, SEANOE [data set], https://doi.org/10.17882/46219, 2019b.

Taillandier, V., D'ortenzio, F., Prieur, L., Conan, P., Coppola, L., Cornec, M., Dumas, F., Durrieu de Madron, X., Fach, B., Fourrier, M., Gentil, M., Hayes, D., Husrevoglu, S., Legoff, H., Le Ster, L., Örek, H., Ozer, T., Poulain, P. M., Pujo-Pay, M., Ribera d'Alcalà, M., Salihoglu, B., Testor, P., Velaoras, D., Wagener, T., and Wimart-Rousseau, C.: Sources of the Levantine Intermediate Water in winter 2019, J. Geophys. Res.-Ocean., 127, e2021JC017506, https://doi.org/10.1029/2021JC017506, 2022.

Takahashi, T., Sutherland, S. C., Wanninkhof, R., Sweeney, C., Feely, R. A., Chipman, D. W., Hales, B., Friederich, G., Chavez, F., Sabine, C., Watson, A., Bakker, D. C. E., Schuster, U., Metzl, N., Yoshikawa-Inoue, H., Ishii, M., Midorikawa, T., Nojiri, Y., Körtzinger, A., Steinhoff, T., Hoppema, M., Olafsson, J., Arnarson, T. S., Tilbrook, B., Johannessen, T., Olsen, A., Bellerby, R., Wong, C. S., Delille, B., Bates, N. R., and de Baar, H. J. W.: Climatological mean and decadal change in surface ocean pCO_2, and net sea–air CO_2 flux over the global oceans, Deep-Sea Res. Pt. II, 56, 554–577, 2009.

Taupier-Letage, I., Millot, C., Fuda, J., Rougier, G., Gerin, R., Poulain, P., Pennel, R., Beranger, K., Emelinaov, M., Font, J., Ben Ismail, S., and Sammari, C.: The surface circulation in the eastern basin oh the Mediterranean and the impact of the mesoscale eddies, Rapp. Comm. Int. Mer. Medit., 39, 189, 2010.

Theocharis, A., Georgopoulos, D., Lascaratos, A., and Nittis, K.: Water masses and circulation in the central region of the Eastern Mediterranean: Eastern Ionian, South Aegean and Northwest Levantine, 1986–1987, Deep-sea Res. Pt. II, 40, 1121–1142, 1993.

Trodahl, M., Isachsen, P. E., Lilly, J. M., Nilsson, J., and Kristensen, N. M.: The regeneration of the Lofoten Vortex through vertical alignment, J. Phys. Oceanogr., 50, 2689–2711, 2020.

Villas Bôas, A., Sato, O., Chaigneau, A., and Castelão, G.: The signature of mesoscale eddies on the air-sea turbulent heat fluxes in the South Atlantic Ocean, Geophys. Res. Lett., 42, 1856–1862, 2015.

Williams, R. G.: Modification of ocean eddies by air-sea interaction, J. Geophys. Res.-Ocean., 93, 15523–15533, 1988.

Wimart-Rousseau, C., Wagener, T., Álvarez, M., Moutin, T., Fourrier, M., Coppola, L., Niclas-Chirurgien, L., Raimbault, P., D'Ortenzio, F., Durrieu de Madron, X., Taillandier, V., Dumas, F., Conan, P., Pujo-Pay, M., and Lefèvre, D.: Seasonal and Interannual Variability of the CO_2 System in the Eastern Mediterranean Sea: A Case Study in the North Western Levantine Basin, Front. Mar. Sci., 8, 649246, https://doi.org/10.3389/fmars.2021.649246, 2021.

Chapter 5

Anticyclone evolution in numerical simulation

Temporal evolution of mesoscale eddies in the Mediterranean Sea can be accurately observed using eddy Lagrangian tracking and collocation methods (Sect.2). In both surface through remote-sensing SST (Moschos et al., 2022) and in the subsurface on the mixed layer (Barboni et al., 2023a) it revealed a marked seasonal cycle. This mesoscale seasonal evolution in a Lagrangian point of view has not been studied so far in ocean models, whether they are idealized, regional or operational. We then aim to retrieve eddy SST evolution and MLD anomalies in models, and investigate what are the key parameters needed to have an accurate anticyclone temporal evolution. In particular we aim to test the eddy vertical mixing modulation proposed by Moschos et al. (2022) and its link with NIW trapping due to negative relative vorticity (Kunze, 1985). This idealized numerical study included below was submitted to *Journal of Advanced in Modeling Earth Systems*.

Additional investigations of the numerical set-up are detailed later. Stratification stability towards atmospheric forcing is assessed in Sect.5.2.1, and initial mesoscale anticyclone stability in Sect.5.2.2. A last further investigation further includes an experiment with eddy current feedback on the wind stress (Sect.5.3).

5.1 Barboni et al. (2023b). How atmospheric forcing frequency, horizontal and vertical grid resolutions impact mesoscale eddy evolution in a numerical model. *submitted to JAMES.*

How atmospheric forcing frequency, horizontal and vertical grid resolutions impact mesoscale eddy evolution in a numerical model

Alexandre Barboni [1,2,3], Alexandre Stegner [1], Franck Dumas [2,3], Xavier Carton [3]

[1]Laboratoire de Météorologie Dynamique/IPSL, Ecole Polytechnique, Institut Polytechnique de Paris, ENS, Université PSL, Sorbonne Université, CNRS, 91128 Palaiseau, France
[2]Service Hydrographique et Océanographique de la Marine, 29200 Brest, France
[3]Laboratoire d'Océanographie Physique et Spatiale, UBO, CNRS, IRD, Ifremer, 29280 Plouzané, France

Key Points:

- Enhanced mixing in anticyclones explain inverse eddy SST signature
- Near-inertial waves mixing is sensitive to vertical resolution
- Mixed layer anomaly is mainly driven by SST retroaction on air-sea fluxes

Corresponding author: Alexandre Barboni, alexandre.barboni@laposte.net

Abstract

Seasonal evolution of both surface signature and subsurface structure of a Mediterranean mesoscale anticyclones is assessed using the CROCO high-resolution numerical model with realistic background stratification and fluxes. In good agreement with remote-sensing and in-situ observations, our numerical simulations capture the seasonal cycle of the anomalies induced by the anticyclone, both in the sea surface temperature (SST) and in the mixed layer depth (MLD). The eddy signature on the SST shifts from warm-core in winter to cold-core in summer, while the MLD deepens significantly in the core of the anticyclone in late winter. Our sensitivity analysis shows that the eddy SST anomaly can be accurately reproduced only if the vertical resolution is high enough ($\sim 4m$ in near surface) and if the atmospheric forcing contains high-frequency. In summer with this configuration, the vertical mixing parameterized by the $k-\epsilon$ closure scheme is three times higher inside the eddy than outside the eddy, and leads to an anticyclonic cold core SST anomaly. This differential mixing is explained by near-inertial waves, triggered by the high-frequency atmospheric forcing. Near-inertial waves propagate more energy inside the eddy because of the lower effective Coriolis parameter in the anticyclone core. On the other hand, eddy MLD anomaly appears more sensitive to horizontal resolution, and requires SST retroaction on air-sea fluxes. These results detail the need of high frequency forcing, high vertical and horizontal resolutions to accurately reproduce the evolution of a mesoscale eddy.

Plain Language Summary

Mesoscale eddies are turbulent structures present in every regions of the world ocean, and accounting for a significant part of its kinetic energy budget. These structures can be tracked in time and recently revealed a seasonal cycle from in situ data. An anticyclone (clockwise rotating eddy in the northern hemisphere) is observed in the Mediterranean to be predominantly warm at the surface and to deepen the mixed layer in winter, but shifts to a cold-core summer signature. This seasonal signal is not yet understood and studied in ocean models. In this study we assess the realism of an anticyclone seasonal evolution in high resolution numerical simulations. Eddy surface temperature seasonal shift is retrieved and is linked to an increased mixing at the eddy core spontaneously appearing at high vertical resolution (vertical grid size smaller than 4m) in the presence of high frequency atmospheric forcing. This increased mixed is due to the preferred propagation of near-inertial waves in the anticyclone due to its negative relative vorticity. Eddy-induced mixed layer depth anomalies also appear to be triggered by sea surface temperature retroaction on air-sea fluxes. These results suggest that present-day operational ocean forecasting models are too coarse to accurately retrieve mesoscale evolution.

1 Introduction

Mesoscale eddies are ubiquitous turbulent structures in the oceans, in thermal wind balance with a signature in density : positive density anomaly for an anticyclone, respectively negative for a cyclone. Eddies statistical descriptions really began with the availability of eddy automated detections based on gridded altimetry products (Doglioli et al., 2007; Chaigneau et al., 2009; Nencioli et al., 2010; Chelton, Schlax, & Samelson, 2011; Mason et al., 2014; Le Vu et al., 2018; Laxenaire et al., 2018). The first quantitative studies were done in a composite approach : many daily snapshots detections are colocated with eddy contours and gathered into a single annual mean eddy signature (Hausmann & Czaja, 2012; Everett et al., 2012). This approach combined with remote-sensing measurements provides an extensive view of eddies in various regions of the global ocean, with SST, sea surface salinity (Trott et al., 2019), chlorophyll (Chelton, Gaube, et al., 2011) and also meteorological variables (Frenger et al., 2013). Composite approach also

allowed to reveal a modulation of air-sea fluxes at the eddy scale : in the Agulhas retroflexion region, (Villas Bôas et al., 2015) showed the total heat flux to the atmosphere to be enhanced over very strong and warm anticyclones. Similarly for the eddy vertical structure, gathering Argo profiles as a function of normalized distance to the eddy center, eddies were found to influence the mixed layer depth (MLD) (Sun et al., 2017; Gaube et al., 2019). Anticyclones have deeper MLD in their core, cyclones shallower MLD, with larger mixed layer anomalies in winter. Eddies were also observed to incorporate a significant seasonal cycle in their radius variations (Zhai et al., 2008) and their SST signature (Sun et al., 2019; Y. Liu et al., 2021). Anticyclones (respectively cyclones) usually identified as warm in surface, actually shift to cold (warm) signatures in summer in several regions of the world ocean (Sun et al., 2019; Moschos et al., 2022). This phenomenon is then referred to as 'inverse' SST signatures. (Moschos et al., 2022) showed that these 'inverse' signatures actually become predominant in summer in the Mediterranean Sea, a seasonal shift yet not properly understood.

The composite approach is nonetheless ill-suited to study eddy temporal variability due to the stacking of numerous observations in time. Recently Lagrangian approaches were developed to study eddies enabling to better track their temporal variability (Pessini et al., 2018; Laxenaire et al., 2020; Barboni et al., 2021). Using a Lagrangian approach, Moschos et al. (2022) showed that the same individual anticyclones shift from a warm winter SST anomaly to a cold one in summer (and conversely for cyclone). With the additional Argo floats trapped in anticyclones, they further noticed that anticyclonic density anomaly remains warmer at depth while becoming colder in surface, leading to a smoother density gradient. Hence the hypothesis that this seasonal shift could be explained by a modulation of the vertical mixing by mesoscale eddies, anticyclones (cyclones) likely enhancing (decreasing) mixing in surface. Recent observations in the Mediterranean Sea of inside-anticyclone properties temporal evolution further revealed eddy mixed layer anomalies to be much larger than the composite approach mean value, reaching sometimes 300m (Barboni, Coadou-Chaventon, et al., 2023). MLD anomalies evolution was also shown to have evolution much faster than the month, with delayed restratification inside anticyclones. Mechanisms driving these MLD anomalies are also unexplained, but Barboni, Coadou-Chaventon, et al. (2023) found it to be impacted by interactions with the anticyclone vertical structure.

An eddy modulation of vertical mixing was recently investigated to be linked with a modulation of near-inertial waves (NIW) propagation. NIW can not propagate at frequencies lower than the inertial frequency f due to Earth rotation (Garrett & Munk, 1972). However in the presence of a balanced flow, anticyclones (cyclones) with negative (positive) relative vorticity ζ locally shift this cut-off to an effective inertial frequency $f_e = f + \zeta/2$ (Kunze, 1985). Sub-inertial waves ($\omega \lesssim f$) can then remained trapped in anticyclones and supra-inertial waves ($\omega \gtrsim f$) can be expelled from cyclones. Consequently, NIW propagate more inside anticyclones, what was experimentally (D'Asaro, 1995) and numerically (Danioux et al., 2008, 2015; Asselin & Young, 2020) proven. This NIW trapping potential partly explains the interest in anticyclones rather than in cyclones, the other reason likely being that anticyclones are more stable in time (Arai & Yamagata, 1994; Graves et al., 2006), in particular for large structures (Perret et al., 2006), then more easily detected and trapping more often profilers (thus easing field campaigns). Several recent observations (Martínez-Marrero et al., 2019; Fernández-Castro et al., 2020) showed that mixing at depth is enhanced below anticyclones due to this more energetic NIW propagation. On the other hand numerical studies assumed extremely simplified set-up with constant wind (Danioux et al., 2008) or an idealized wind burst (Asselin & Young, 2020). They also looked at NIW propagation in an eddying field at short time scales, then without significant evolution of the eddies and stratification. Eddy-NIW interaction on longer time scales - eddy evolving time scales like months - in a varying stratification due to seasonal cycle has never been assessed so far. In particular the effect of

this differential NIW propagation on eddies remains unknown and a gap remains to link wave propagation and enhanced mixing.

Some recent studies started to assess eddy temporal evolution in high resolution regional models. In the Mediterranean Sea, Escudier et al. (2016) compared eddy size, drift and lifetime compared to eddies in altimetric observations. Mason et al. (2019) investigated these variables in assimilated operational models and additionally looked at MLD anomalies, but both were in a composite approach and did not look at eddy SST variations. More recently Stegner et al. (2021) performed an observation system simulation experiment on a 1/60°simulation of the Mediterranean sea and found great bias on size and strength for small eddy detections, but did not look at SST variations. Using the same simulation, an interesting method was developed by Ioannou et al. (2021), investigating differences in both trajectories, size and stratification of the Ierapetra anticyclonic eddy, but restricted to this particular case.

Eddy SST anomalies seasonal shift and mixed layer depth anomalies remain poorly investigated so far in ocean models. If NIW propagation and eddy vertical structure are considered, grid resolution - both horizontal and vertical - and atmospheric forcing are likely key aspects to take into account. Air-sea fluxes and near-inertia-gravity waves involve much shorter temporal and spatial scales, not reproduced even in eddy-permitting models at present stage. We then aim to assess the realism of an anticyclone seasonal signal, in both surface and mixed layer, using an idealized but high-resolution simulation and investigating driving physical processes. The goal is to assess the realism of the eddy temporal evolution compared to similar observations, in particular the retrieval of the surface signature seasonal cycle. In a first part we conduct a sensitivity analysis on horizontal grid cell. In a second part we study the sensitivity to atmospheric forcing frequency. Last, the effect of SST retroaction on air-sea fluxes is discussed.

2 Methods

2.1 Model set-up

Idealized numerical experiments are performed using the Coastal and Regional Ocean Community (CROCO) model. CROCO is based on the Regional Ocean Modeling System (ROMS) kernel (Shchepetkin & McWilliams, 2005). It uses a time splitting method between the fast barotropic mode and the slow baroclinic ones. Advection schemes are UP3 for horizontal and Akima-Splines for the vertical. Trying to conciliate realistic and idealized approach, we use double periodic conditions in a realistic stratification and on long timescale. The atmospheric forcing has realistic temporal variations but is spatially homogeneous. The only active tracer used is temperature. As a consequence, a linear state equation links density ρ and temperature T, with thermal expansion $T_c = 0.28 kg.m^{-3}.K^{-1}$ and linear approximation close to $T_0 = 25$°C and $\rho_0 = 1026 kg.m^{-3}$:

$$\rho = \rho_0 + T_c(T - T_0) \tag{1}$$

Discarding salinity effects is justified by the very weak salinity seasonal cycle in the Mediterranean Sea. The heat flux seasonal cycle is roughly $\pm 150\, W.m^{-2}$ (Pettenuzzo et al., 2010), whereas salinity fluxes are mostly driven by the evaporation minus precipitation balance, with a mean of roughly $10^3 mm/y$, a seasonal cycle maximal amplitude of $\Delta F = 4 \times 10^2 mm/y$ and river input being negligible (Mariotti, 2010). Considering a haline contraction coefficient of $S_c = 0.78 kg.m^{-3}.PSU^{-1}$, a ΔF freshwater input would have a seasonal equivalent effect on buoyancy $Q_{eq} = \rho_0 c_p \frac{S_c}{T_c} S_0 \Delta F \approx 5\, W.m^{-2}$, indeed almost two orders of magnitude lower than Q_{tot}.

Grid

Simulation domain is double periodic, on the f-plane, with a flat bottom $H_{bot} = 3000m$. Horizontal extent is 200km in both directions, with horizontal resolution ranging between 4km and 500m, with 25 to 150 vertical levels. Coriolis parameter is $f = 9.0\times10^{-5}s^{-1}$. CROCO uses a σ terrain-following coordinate, the N vertical levels being modulated in time between bottom and sea surface height η. Constant depth level z_0 are stretched over thickness h_c with surface coefficient θ_s :

$$z = \eta + (\eta + H_{bot})z_0 \tag{2}$$

$$z_0 = \frac{h_c\sigma + H_{bot}C_s(\sigma)}{h_c + H_{bot}} \quad \text{with} \quad C_s(\sigma) = \frac{1 - cosh\left(\theta_s \frac{\sigma - N}{N}\right)}{cosh(\theta_s) - 1} \tag{3}$$

With $N = 100$ levels, $h_c = 400m$ and $\theta_s = 8$, vertical grid step dz is then $3.5m$ in the upper $200m$. $200m$ being the vertical scale of the thermocline, it ensures a maximal resolution in the upper ocean where seasonal variations occur (Houpert et al., 2015). This configuration has then a higher vertical resolution than previous similar studies ($N = 32$, $h_c = 250m$ and $\theta_s = 6.5$ for Escudier et al. (2016)) or operational models (Juza et al., 2016).

Turbulent closure

Mixing is parameterized through $k-\epsilon$ closure scheme (Rodi, 1987) using the generic length scale approach (Umlauf & Burchard, 2003). Turbulent kinetic energy k dissipates with rate ϵ and stability function c_v into an effective viscosity ν (respectively c_T and κ for diffusivity). No additional explicit mixing is added.

$$\nu = \frac{c_v k^2}{\epsilon} \quad \text{and} \quad \kappa = \frac{c_T k^2}{\epsilon} \tag{4}$$

A minimal k input is parameterized. Given that the minimal dissipation rate ϵ is set to $10^{-12}W.kg^{-1}$, the minimal k has to be set to $10^{-9}m^2.s^{-2}$ in order to retrieve a minimal diffusivity of $10^{-6}m^2.s^{-1}$ with a stability function of order unity. This diffusivity value is close to kinematic viscosity and thermal diffusivity for water (respectively 1×10^{-6} and $1\times10^{-7}\,m^2.s^{-1}$). This issue was also discussed by Perfect et al. (2020).

2.2 Background stratification and initial mesoscale anticyclone

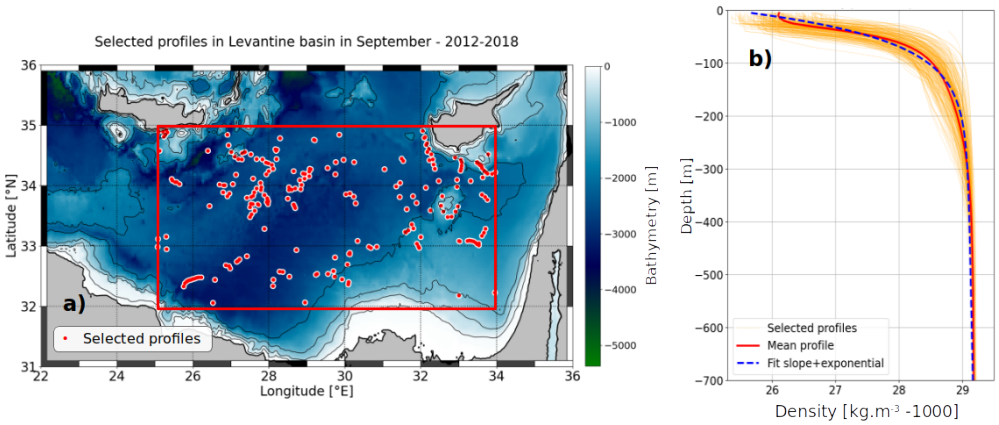

Figure 1. (a) Map showing the region of high long-lived anticyclones occurrence in the Levantine basin. The atmospheric fields used as input are averaged over the area delimited by the red frame. Red dots are the cast position of 242 selected in situ profiles identified as outside-eddy. Bathymetry is ETOPO1 data (Smith & Sandwell, 1997) with 0, 500, 1000 and 1500m isobaths. (b) Selected density profiles (orange thin lines), mean profile (red thick line) and fitted profile using Eq.5 (blue dashed).

A realistic background stratification is set from a climatological database gathering in situ data from Copernicus Marine Environment Monitoring Service (Barboni, Stegner, et al., 2023). A region of interest is considered at the center of the Levantine Basin (25 to 34 °E and 32 to 35 °N, shown in Fig.1a). For background stratification we used only profiles in the region of interest, detected as outside-eddy using the DYNED eddy atlas dataset (see Barboni, Coadou-Chaventon, et al. (2023) for details), from 2012 to 2018 and for each year in September. Considering these criteria, 242 profiles are averaged into a mean stratification $\rho_b(z)$ fitted over the first 1000m with a linear slope S added to an upper ocean thermocline with exponential shape and vertical scale Z_T (Eq.5, see Fig.1b). September is chosen as the end of summer when the thermocline is marked and stratification gradient the strongest, allowing a better fit with exponential slope.

$$\rho_b(z) = \rho_1 + (\rho_s - \rho_1) exp\left(-\frac{z}{Z_T}\right) + Sz \tag{5}$$

Regression fit gave $\rho_1 = 1029.03 kg.m^{-3}$, $\rho_s = 1025.3 kg.m^{-3}$, $Z_T = 55m$, $S = 1.8 \times 10^{-4} kg.m^{-4}$. Corresponding baroclinic deformation radius R_d is approximately $11km$. An initial density anomaly σ in geostrophic equilibrium is added to the background stratification. $\sigma(r, z)$ is azimuthally symmetric and has a Gaussian shape in the vertical direction and pseudo-Gaussian in the radial one, with radius R_{max} and vertical extent H :

$$\sigma(r,z) = \sigma_0 \frac{z}{H} exp\left(-\frac{1}{\alpha}\left(\frac{r}{R_{max}}\right)^{\alpha}\right) exp\left(-\frac{1}{2}\left(\frac{z}{H}\right)^2\right) \quad \text{with} \quad \sigma_0 = \frac{\rho_0 f V_{max} R_{max} e^{1/\alpha}}{gH} \tag{6}$$

The initial maximal speed radius R_{max} is 25 km, slightly more than twice the deformation radius but still smaller than the large long-lived Eastern Mediterranean anticyclones (Barboni, Coadou-Chaventon, et al., 2023), giving a Burger number ($Bu = R_d^2/R_{max}^2$) close to 0.2. Maximal speed is initially set to $V_{max} = 0.4\,m.s^{-1}$ giving a Rossby number ($Ro = V_{max}/R_{max}f$) of 0.16, but later decays around 0.1. $Ro = 0.1$ is a standard value in the Mediterranean Sea (Ioannou et al., 2019). H is set to $100m$ on the same order as thermocline extent Z_T, and shape parameter $\alpha = 1.6$ ensures barotropic stability (Carton et al., 1989; Stegner & Dritschel, 2000). Cyclogeostrophic correction is added following Penven et al. (2014).

2.3 Atmospheric heat forcing

ERA5 reanalysis input is used for atmospheric forcing. Fields are available with a 1 hour temporal resolution and 1/4°horizontal resolution (Hersbach et al., 2020). Retrieved variables are surface short wave Q_{SW}^{surf}, downward long wave flux $Q_{LW}^{\downarrow}$, sea level pressure P_{SL}, h_{2m} and T_{2m} relative humidity and temperature at 2m above surface, and last u and v 10m neutral zonal and meridional wind components. To focus on the temporal variability, these time series are spatially averaged over the Levantine basin (Fig.1a). Air-sea fluxes are then computed with the Coupled Ocean–Atmosphere Response Experiment (COARE) 3.0 parametrization (Fairall et al., 2003), with improved accuracy for large wind speeds ($> 10m.s^{-1}$) encountered in high frequency forcing. Net heat flux Q_{tot} is defined as the sum of surface short wave, long wave (upward $Q_{LW}^{\uparrow}$ and downward $Q_{LW}^{\downarrow}$ components), latent (Q_{Lat}) and sensible (Q_{Sen}) fluxes, convention positive fluxes downwards :

$$Q_{tot} = Q_{SW}^{surf} + Q_{LW}^{\uparrow} + Q_{LW}^{\downarrow} + Q_{Lat} + Q_{Sen} \tag{7}$$

$Q_{tot} - Q_{SW}^{surf}$ is applied directly at the surface, while short wave heat flux $Q_{SW}(z)$ is distributed on the vertical following Paulson and Simpson (1977) transparency model with Jerlov water type I , consistent with very clear Mediterranean waters ($R = 0.58$, $\zeta_1 = 0.35m$, $\zeta_2 = 23m$):

$$Q_{SW}(z) = Q_{SW}^{surf}\left(Rexp\left(-\frac{z}{\zeta_1}\right) + (1-R)exp\left(-\frac{z}{\zeta_2}\right)\right) \tag{8}$$

Upward long-wave heat flux $Q_{LW}^{\uparrow}$ computes the ocean SST (T_s) thermal loss using Stefan-Boltzmann black body law, with emissivity $\epsilon_{sb} = 98.5\%$ and $\sigma_{sb} = 5.6697\times 10^{-8}\,W.m^{-2}.K^{-4}$:

$$Q_{LW}^{\uparrow} = -\epsilon_{sb}\sigma_{sb}T_s^4 \tag{9}$$

Latent heat flux Q_{Lat} and sensible heat flux Q_{Sen} also involves a direct SST retroaction:

$$Q_{Lat} = -\rho_a L_E C_E |V|(q_s - q_a) \quad ; \quad Q_{Sen} = -\rho_a c_p C_S |V|(T_s - T_{2m}) \tag{10}$$

With ρ_a air density, c_p air thermal capacity, L_E evaporation enthalpy, $|V|$ 10m wind speed. q_s and q_a are specific humidity for ocean and atmosphere at 2m respectively. q_s is saturated at T_s and P_{SL} : $q_s = 0.98 \times 0.622 \times P_{sat}(T_s)/P_{SL}$. Factor 0.98 accounts for water vapor reduction caused by salinity (Sverdrup et al., 1942). q_a is related to saturated water pressure P_{sat} : $q_a = 0.622 h_{2m} P_{sat}(T_{2m})/P_{SL}$. Last, wind stress is computed from u and v) :

$$\tau_x = \frac{\rho_a}{\rho_0} C_D |u| u \quad \text{and} \quad \tau_y = \frac{\rho_a}{\rho_0} C_D |v| v \tag{11}$$

In equations 10-11, C_E, C_S and C_D are corresponding transfer coefficients considering the stability of the atmospheric boundary layer based on the Monin-Obukhov similarity theory. They are all on the order of 1×10^{-3} (Fairall et al., 2003).

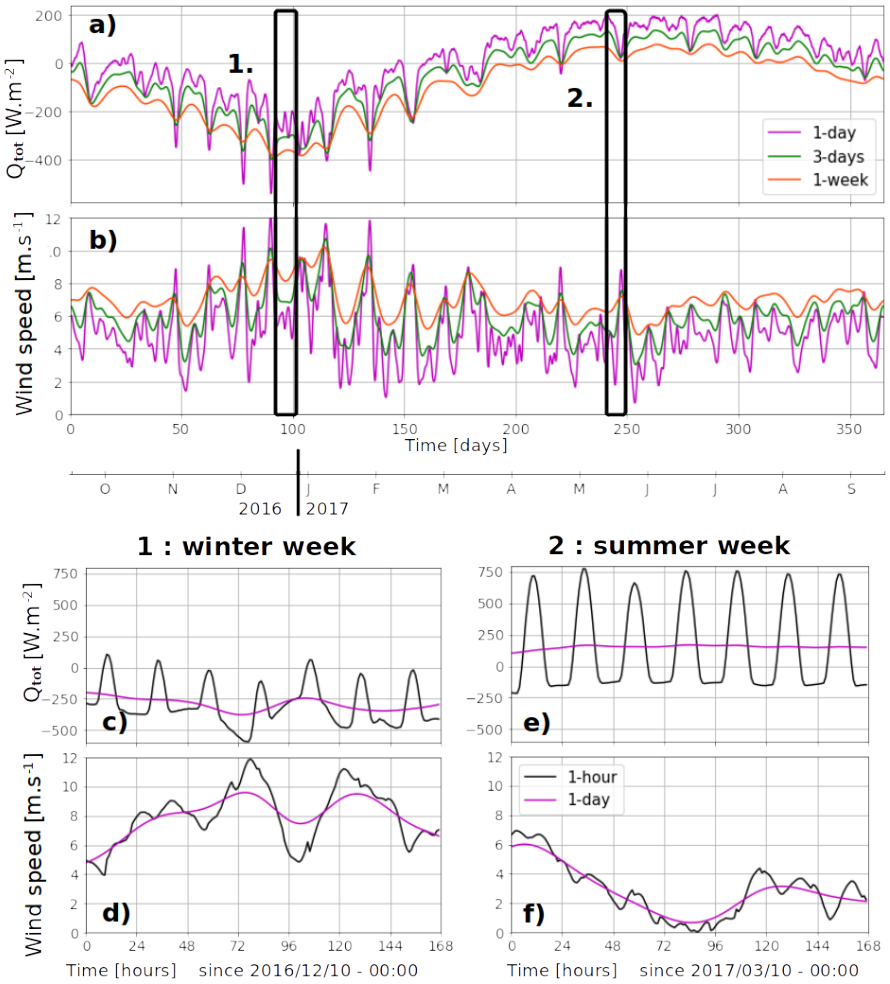

Figure 2. Net heat flux and wind speed from ERA5, for the 4 input time series, shown separately as diurnal cycle gives larger variations. (a) Net heat flux and (b) corrected wind speed (see Eq.12) for the 1-day (magenta line), 3-day (green) and 1-week (orange) time series over one year. To enhance readability, 3-day and 1-week net heat fluxes are lowered by 20 and 40 $W.m^{-2}$ respectively, and 3-day and 1-week wind speeds are heightened by 1 and 2$m.s^{-1}$ respectively. (c) 1-hour (black) and 1-day (magenta) net heat flux (respectively (d) for wind speed) in a winter week of 2016. (e) and (f) : same as (c) and (d) in a summer 2017 week.

To study the impact of temporal variability, four forcing inputs with different temporal scales are tested : 1-hour, 1-day, 3-day and 1-week. The 1-hour forcing is the original ERA5 time series, the three later ones are Gaussian smoothing of the 1-hour time

series with window size (two standard deviations) of 1, 3 and 7 days respectively, shown in Fig.2. One year of forcing from 15 September 2016 to 15 September 2017 runs cyclically for 2 years as forcing input, with mean wind speed magnitude $V_{rms} = 5.0 m.s^{-1}$. 10m neutral wind from ERA5 is used for wind stress in Eq.11. To keep the same wind speed magnitude with varying wind frequency, smoothed time series for zonal and meridional winds ($[u]$ and $[v]$) have to be re-scaled. The correction factor λ being $\gtrsim 1.1$ for 1-day time series, and $1.1 < \lambda < 2$ for 3-day and 1-week :

$$\tilde{u} = \lambda[u]\,;\, \tilde{v} = \lambda[v] \quad \text{with} \quad \lambda = \frac{[\sqrt{u^2+v^2}]}{\sqrt{[u]^2+[v]^2}} \tag{12}$$

The same year is kept to avoid disturbance with interannual variations, which are strong for heat fluxes over the Mediterranean Sea (Mariotti, 2010; Pettenuzzo et al., 2010), but no significant variations were observed when selecting another year.

Forcing without surface temperature retroaction

A comparison experiment is run without SST retroaction on ocean-atmosphere fluxes. In this configuration, the net heat flux Q_{tot} from ERA5 directly forces the upper ocean layer, the short wave part $Q_{SW}(z)$ being still distributed on the vertical (Eq.8). Momentum fluxes are computed from Eq.11 with constant drag coefficient $C_D = 1.6{\times}10^{-3}$. The net heat flux Q_{tot} time series in ERA5 has daily amplitudes around $\pm 150 W.m^{-2}$ and an annual average of $-3.0\, W.m^{-2}$, consistent with the net evaporation of the Mediterranean Sea (Mariotti, 2010). Q_{tot} is then corrected by linearly decreasing the negative values to achieve a zero annual average, avoiding a drift of the mean stratification.

2.4 Eddy tracking indicators

Eddy shape, radius and intensity

Eddy detections are provided through the Angular Momentum Eddy Detection and Tracking Algorithm (AMEDA). AMEDA is a mixed velocity-altimetry approach, its relies on using primarily streamlines from a velocity field and identifying possible eddy centers computed as maxima of local normalized angular momentum (Le Vu et al., 2018). It was successfully used in several regions of the world ocean in altimetric data (Aroucha et al., 2020; Ayouche et al., 2021; Barboni et al., 2021), high frequency radar data (F. Liu et al., 2020) or numerical simulations (de Marez et al., 2021). In each eddy single observation (one eddy observed one day), AMEDA gives a center (which position is noted $\mathbf{X}_e$ hereafter), a maximal rotation speed V_{max} and two contours. The 'maximal speed' contour is the enclosed streamline with maximal speed (i.e. in the geostrophic approximation, with maximal SSH gradient) ; it is assumed to be the limit of the eddy core region where water parcels are trapped. The 'end' contour is the outermost closed SSH contour surrounding the eddy center and the maximal speed contour ; it is assumed to be the area of the eddy footprint, larger than just its core but still influenced by the eddy shear (Le Vu et al., 2018). The observed maximal speed radius R_{max} is defined as the radius of the circle having an area equal to the maximal speed contour. Eddy detection in real interpolated SSH observations leads to imperfections. It typically smooths gradients and then reduces observed geostrophic velocities (Amores et al., 2018; Stegner et al., 2021). To mimic those imperfections in the numerical simulations, AMEDA detections are performed on the 48h-averaged SSH field at model grid resolution, or interpolated at 2km if grid resolution is smaller.

Eddy SST signature δT, heat flux δQ, differential mixing ratio ξ and mixed layer anomaly

The anticyclone-induced SST signature δT is defined as the difference of SST between the eddy core SST_{in} and its periphery SST_{peri}. Adapting Moschos et al. (2022), SST_{in} is the average of the area centered on $\mathbf{X}_e(t)$ with radius $2/3R_{max}(t)$; SST_{peri} is the average on an annular area centered on $\mathbf{X}_e$ with radius between $2/3R_{max}(t)$ and $2R_{max}(t)$. Positive (negative) δT then indicates a warm-core (cold-core) signature. Similarly the induced signature on total net heat flux is defined as δQ, with positive δQ for increased warming at the eddy core. Thermal heat flux feedback (THFF) is then defined as the linear regression of δQ as a function of δT over the second year of simulation (from 365 to 730 days, see Sect.3.3).

Differential mixing between the eddy core and outside-eddy are measured through the index ξ. Temperature vertical diffusivity κ computed by $k-\epsilon$ mixing closure from instantaneous history record is spatially averaged in the eddy core (κ^{AE}) and outside-eddy (κ^{Out}). The eddy core region corresponds here to the area around the eddy center with radius $2/3R_{max}(t)$. The outside-eddy region is defined as the area outside any 'end' contours detected by the tracking algorithm. Diffusivity spanning several orders of magnitude, differential mixing ξ is then evaluated as a vertical average of the ratio of these two quantities, typically using a depth $h = 20m$ to focus on the upper layers stratified in summer :

$$\xi = \frac{1}{h}\int_{-h}^{surf} \frac{\kappa^{AE}}{\kappa^{Out}} dz \tag{13}$$

Summer eddy SST signature magnitude $\overline{\delta T}$ is defined as the 30th δT percentile over the summer, and its spread as the difference between the 30th and the 10th percentiles (see results in Table 1). Similarly $\overline{\xi}$ is defined as the median of the ξ distribution over the summer, and its spread as the difference between the median and the 30th percentile. First and second summers are defined as 230 to 340 days and 590 to 700 days respectively, corresponding to the May to August period when a significant number of warm-core anticyclones are observed (Moschos et al., 2022).

Last, the MLD anomaly ΔMLD is defined as the maximal difference reached between the MLD outside- and inside-eddy, with a 1-day Gaussian smoothing to remove peaks. In the following numerical experiments running for 2 years, the first winter is considered as a transient period not retained for analysis. ΔMLD is then computed only for the second winter, defined as 450 to 590 days, corresponding to the December to April period, when maximal MLD are reached in the Mediterranean Sea (Houpert et al., 2015).

3 Idealized simulations compared to observations

The temporal evolution of mesoscale eddies in the Levantine basin can be retrieved for several anticyclones where Argo floats remained trapped several months, as extensively studied in Barboni, Coadou-Chaventon, et al. (2023). A marked seasonal signal is detected in both SST and vertical structure. An example is shown in Fig.3 with a Ierapetra anticyclone, a strong recurrent anticyclonic structure formed each year in the lee of Crete island (Ioannou et al., 2020). In the example shown below, δT index has a marked oscillation between a winter warm core and summer cold core. The weekly smoothed signature can be measured to about $\delta T \approx +0.7°C$ in both winters 2016-2017 and 2017-2018, and about $-0.3°C$ in summer 2017 (about $-0.2°C$ in summer 2018). The vertical structure could also be measured thanks to large Argo deployments (Fig.3h) ; due to errors in the salinity sensors, density in 2018 is estimated from temperature applying a linear regression using 2017 data. One can also notice the seasonal variations of the anticyclone maximal speed, with two maxima in late winter. This is consistent with

kinetic energy inverse cascade maximal peak from submesoscale to mesoscale in kinetic energy distributions (Zhai et al., 2008; Steinberg et al., 2022), but it is still noticeable to have the same phenomenon tracking a single individual structure. In this study the physical processes driving these observed seasonal variations are studied with numerical experiments, investigating sensitivity to horizontal and vertical resolutions, forcing frequency and SST retroaction on air-sea fluxes. Simulations are summarized in Table 1, the reference considered being 1km resolution with 1-hour forcing, 100 vertical levels with SST retroaction (run 1K100-1H in Table 1 below).

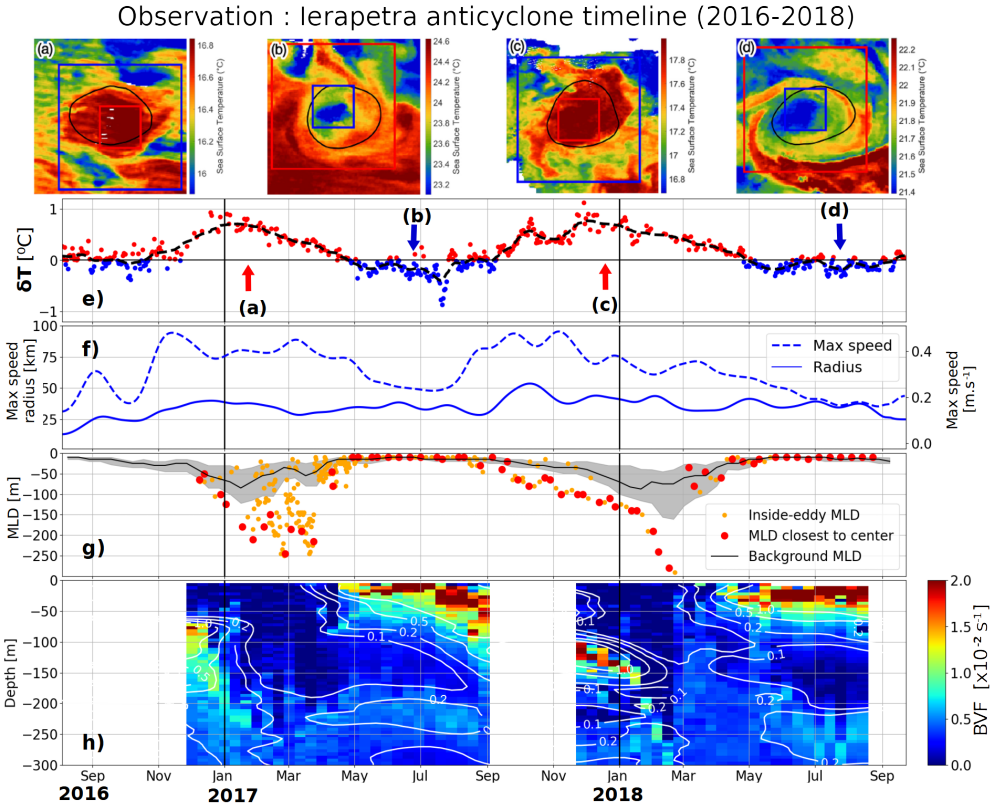

Figure 3. Temporal evolution of the Ierapetra anticyclone formed South-East of Crete in late summer 2016. Upper panels are high-resolution SST snapshots in (a) January 2017, (b) June 2017, (c) December 2017 and (d) July 2018, the maximal speed contour (see Sect.2.4) is in black line. (e) Eddy SST anomaly δT, cold-core in blue and warm-core in red, with black dashed line showing the 5 days smoothed evolution. (f) Maximal speed V_{max} (dashed blue) and radius R_{max} (continuous blue) with 10 days smoothing. (g) MLD evolution inside the the anticyclone (dots, with red ones highlighting the closest to center), with outside-eddy background MLD in continuous black line (spread as 20-80 percentiles interval shown in gray shades). (h) Brunt-Vaisala frequency (BVF) Hovmöller diagram, with selected 0.001, 0.002, 0.01 and 0.01 s^{-1} stratification contours (using slight 2D smoothing for the contours only).

Table 1. Summary table of CROCO numerical experiments. Runs start in September of the atmospheric forcing time series. Thermal heat flux feedback (THFF), eddy SST anomaly index $\overline{\delta T}$ and differential mixing ratio $\overline{\xi}$ are defined in Sect.2.4, and $\overline{\xi}$ is computed over the upper 20m. Subscripts ($\overline{\xi}_1$,$\overline{\xi}_2$) refers to first and second summers defined as 230 to 340 days and 590 to 700 days respectively. ΔMLD refers only to the second winter defined as 450 to 590 days (see shades in Fig.4d-h).

Name	**Vertical levels (minimal dz in meters)**	**dx** (km)	**Freq**	**SST retroaction**	**THFF** ($W.m^{-2}.K^{-1}$)	$\overline{\delta T}_1$ (°C)	$\overline{\delta T}_2$ (°C)	$\overline{\xi}_1$	$\overline{\xi}_2$	**ΔMLD** (m)
1K100-1H	100 (3.5)	1	1-hour	Yes	-41.5 ± 1.3	-0.20 ± 0.10	-0.18 ± 0.04	3.05 ± 0.70	2.81 ± 0.74	51
2K50-1H	50 (7)	2	1-hour	Yes	-40.7 ± 1.0	-0.12 ± 0.14	-0.11 ± 0.06	1.54 ± 0.31	1.34 ± 0.22	63
4K25-1H	25 (15)	4	1-hour	Yes	-34.3 ± 1.8	0.01 ± 0.14	0.02 ± 0.10	1.10 ± 0.12	1.00 ± 0.12	48
05K150-1H	150 (2.5)	0.5	1-hour	Yes	-42.2 ± 33.9	-0.16 ± 0.10	-0.19 ± 0.06	2.58 ± 0.58	2.71 ± 0.45	91
1K40-1H	40 (9)	1	1-hour	Yes	-44.4 ± 2.4	-0.00 ± 0.10	-0.04 ± 0.02	1.22 ± 0.15	1.46 ± 0.19	10
2K80-1H	80 (4.5)	2	1-hour	Yes	-44.2 ± 1.3	-0.18 ± 0.15	-0.13 ± 0.07	2.73 ± 0.72	2.95 ± 1.24	60
1K100-1D	100 (3.5)	1	1-day	Yes	-42.1 ± 0.8	-0.21 ± 0.20	-0.31 ± 0.06	2.99 ± 0.44	3.34 ± 1.23	57
1K100-3D	100 (3.5)	1	3-day	Yes	-44.7 ± 1.0	-0.12 ± 0.14	-0.09 ± 0.03	1.41 ± 0.28	0.99 ± 0.09	70
1K100-1W	100 (3.5)	1	1-week	Yes	-41.0 ± 0.4	-0.05 ± 0.05	-0.03 ± 0.01	1.25 ± 0.14	1.02 ± 0.01	94
1K100-1H-NoSST	100 (3.5)	1	1-hour	No	-	-0.41 ± 0.16	-0.51 ± 0.00	2.60 ± 0.46	2.47 ± 0.25	18

3.1 Horizontal and vertical resolution sensitivity

The numerical simulation at 4km resolution and 25 vertical levels (run 4K25-1H in Table 1) reveals several discrepancies with real observations. A horizontal resolution of 4km is close to operational oceanography models in the Mediterranean Sea (Juza et al., 2016). At the surface, despite seasonal variations of the eddy SST signatures (Fig.4a-c) and in the δT index (Fig.4f), summer 'inverse' signatures are not retrieved, with no cold-core anticyclone. An erosion of the eddy strength is also noticeable, with V_{max}decreasing from $0.4m.s^{-1}$ to $0.15m.s^{-1}$ in 2 years, while its radius remains constant ($\approx 25km$, Fig. 4e). At depth, the mixed layer anomaly is significant, on the order of 50m (Fig.4g). Some bursts of differential mixing are observed in late winter from December to March when mixed layer instabilities and restratification processes can occur, with ξ reaching a few times values higher than 2 (Fig. 4h). However no differential mixing is retrieved in summer. In the eddy interior, the winter MLD cooling forms a homogeneous layer between 100 and 150m (Fig. 4i). These winter waters formed by convection do not accurately reproduce the homogeneous subsurface anticyclone cores, separated by persistent density jump or sharp temperature gradient (see continuous stratified layer in Fig.3h around 200m depth or other examples in Fig.4-5 from Barboni, Coadou-Chaventon, et al. (2023)). The inability to reproduce this mesoscale subsurface lens is not surprising given the low vertical resolution, the vertical steps being on the order of $20m$ at $100m$ depth.

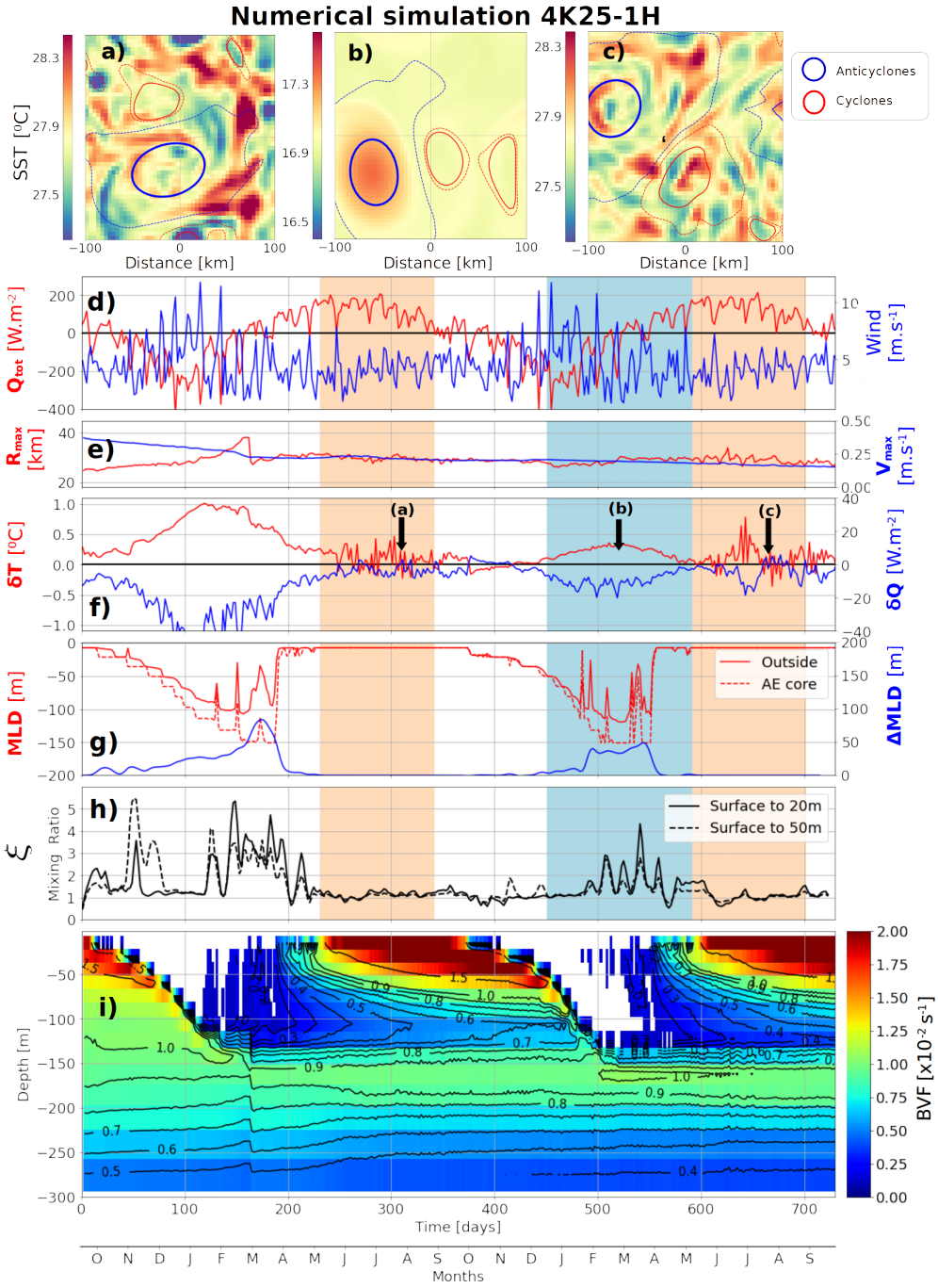

Figure 4. Simulation 4K25-1H from Table 1. (a) SST snapshot in the first summer, (b) in the second winter, (c) in the second summer, contours are AMEDA eddy detetions. The initial anticyclone is highlighted by a thicker line. (d) Net heat flux (red) and wind speed (blue). (e) R_{max} (red) and V_{max} (blue) from AMEDA. (f) SST anomaly index δT (red) and heat flux anomaly δQ (blue). (g) Mixed layer inside-eddy (dashed red) and outside-eddy (continuous red), mixed layer anomaly is in continuous blue. (h) Differential mixing ratio ξ defined in Eq.13 with $h = 20m$ (solid) and $h = 50m$ (dashed line). (i) Inside-eddy stratification evolution shown with Brunt-Vaisala frequency (scale factor 100) ; contours are overlaid with $0.001s^{-1}$ intervals and negative values are blanked. On panels d-h, summer periods are indicated by light red shades, winter by a light blue shade.

The same numerical set-up with a finer resolution (run 1K100-1H in Table 1) shows a net contrast with the previous coarser simulation. This simulation has a 1km horizontal grid size and 100 levels with same stretching parameters giving vertical grid steps close to 3m in the upper 200m. A summer 'inverse' eddy surface temperature is clearly retrieved with 1-hour frequency heat and momentum forcing. In this configuration, a clear anticyclonic cold-core SST signature is observed in summer (Fig.5a), switching back to a winter warm-core SST the next winter (Fig.5b) and appearing again in the second summer (Fig.5c). This anticyclone surface seasonal oscillation can clearly be tracked by δT (Fig.5f). $\overline{\delta T}$ reached about $-0.2°C$ in the both summers (see Table 1) with spikes of $\delta T \approx -0.5°C$ and maximal value around $+0.4°C$ in winter. Considering anticyclonic cold-core signatures statistics in the Mediterranean Sea (Moschos et al., 2022) in particular their Fig.5b) $\delta T \approx -0.2°C$ is a low but standard value, anticyclone SST anomalies typically not being colder than $-0.5°C$. This cold-core summer signature goes along with a mixing increase in the upper layers at the eddy core, measured by a diffusivity in summer more than twice stronger inside the eddy core than outside. Sensibility of the ξ indicator is shown on Fig.5h, with ξ averaged over the upper 20m or 50m, the first case leading to ξ values higher than 4 in summer despite some variability. This enhanced mixing seems to be confined in the upper layers, as ξ decreases to approximately 1 as soon as the mixed layer deepens, but it increases again to similar values during the second summer.

At depth, after the first transient winter, the maximal mixed layer anomaly reaches about 50m (Fig.5g), very close to the value of the simulation at 4km resolution. However the vertical structure is better reproduced at 1km, and in particular between 100 and 150m deep the $5\times10^{-3}s^{-1}$ stratification isoline closes in December, 4 months later than in the 4km simulation (in August, see Fig.4i). This means that homogeneous waters formed at depth in the first winter restratify more slowly. Eddy decay in time is also slower on maximal speed : after 2 years the anticyclone velocity is about $0.3m.s^{-1}$ with 1km resolution compared to $0.15m.s^{-1}$ with 4km (Fig.4e). Sharp density gradients are smoothed in a coarser simulation, leading to unrealistic temporal evolution of the anticyclones vertical structure. Surface (SST) or depth-integrated (maximal geostrophic speed) measurements are then not accurately reproduced at a spatial resolution of 4km.

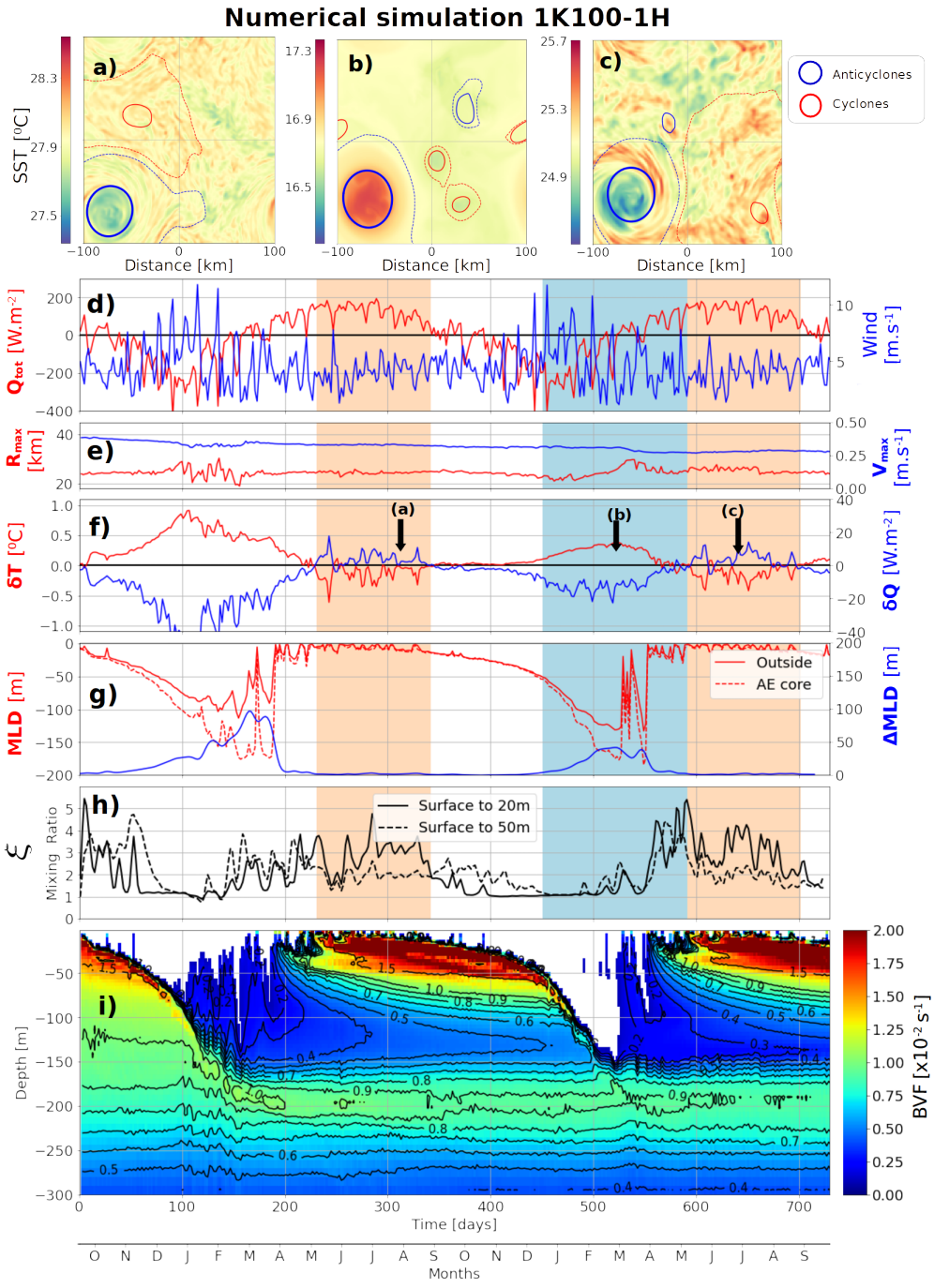

Figure 5. Simulation 1K100-1H from Table1. Same as in Fig.4 but with a 1km horizontal resolution.

An experimental series with the same numerical set-up is performed, increasing horizontal resolution from 4km to 500m and also vertical resolution, listed in Table 1. In runs 05K150-1H, 1K100-1H, 2K50-1H and 4K25-1H, horizontal to vertical resolutions ratio is kept similar to the ratio of Brunt-Vaisala frequency over Coriolis parameter, about

1000/3 (vertical grid step is then about 3m near surface in run 1K100-1H). In runs 2K80-1H horizontal resolution (2km) is coarser but vertical grid step smaller (about 4.5m in the upper layers), while in run 1K40-1H horizontal resolution (1km) is refined but vertical grid step larger (about 9m in the upper layers). Comparison of SST signatures and differential mixing (Fig.6c) reveals that summer anticyclonic cold-core signature $\overline{\delta T}$ and differential mixing $\overline{\xi}$ both continuously increase when decreasing the vertical grid cell. Summer eddy SST inversions are also consistently correlated with an increased mixing. In addition a convergence behavior is observed for more than 80 vertical levels to $\overline{\xi} \approx 3$, as no further mixing is obtained increasing the resolution to 150 levels. On the other hand very similar δT are retrieved in winter at all resolution, with a maximum around $+0.4°C$ (Fig.6a) and similar THFF suggesting that winter thermal loss is less affected by grid resolution. THFF slightly decreases for lower horizontal resolution, likely due to smoothing effect of strong SST patterns.

Significant differential mixing in run 2K80-1H with only 2km horizontal resolution but refined vertical grid implies that explicit resolution of vertical gradients are at stake, which is expected to resolve near-inertial waves. 2km horizontal resolution with a baroclinic first deformation radius around 11km entails that deformation radius is only partly resolved, as noticed in other numerical studies (Marchesiello et al., 2011; Soufflet et al., 2016). This further highlights the key role of vertical resolution in accurately resolving eddy SST anomalies.

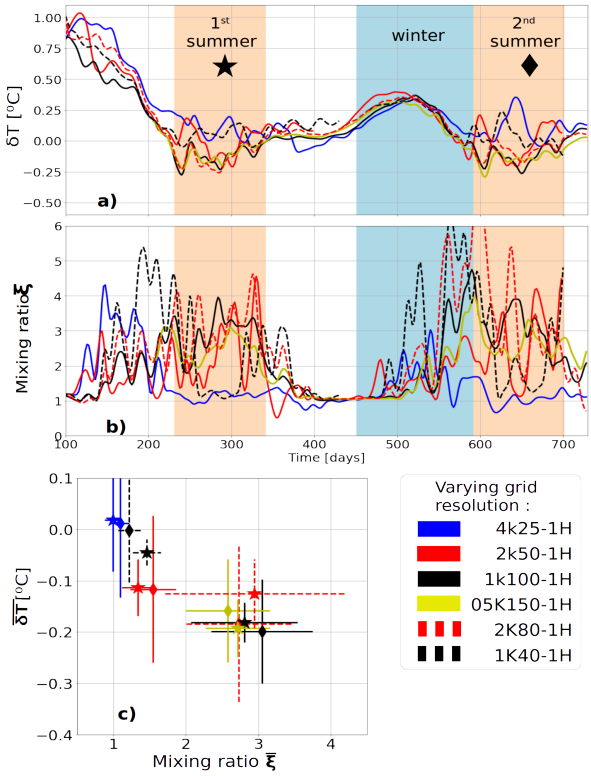

Figure 6. (a) δT and (b) ξ time series for experiments 1K100-1H, 2K50-1H, 4K25-1H, 05K150-1H listed in Table 1 with SST retroaction on air-sea fluxes and varying horizontal resolution frequency. 2-days Gaussian smoothing is applied and summer periods are shaded in light red, winter in light blue. Due to computer memory issues, the first transient winter at 500m resolution was not recorded. (c) Summer-averaged eddy-induced SST anomalies ($\overline{\delta T}$) and mixing ratio ($\overline{\xi}$), with stars for the first summer and diamonds for the second one. Errorbars are ξ spread (30^{th} percentile) over the same period.

For the eddy-induced mixed layer anomaly, similar values are obtained from 4km to 1km horizontal resolution ($\Delta MLD \approx 50m$), but a larger $\Delta MLD = 91m$ is retrieved at 500m resolution. This effect could be due to the partial resolution of sub-mesoscale processes such as mixed layer instabilities (Boccaletti et al., 2007; Capet et al., 2008). Maximal background mixed layer deepens when resolution gets finer down to 1km resolution (see Fig.4g and 5g), in consistence with previous experiments (Couvelard et al., 2015). At 500m resolution, a closer look at the MLD evolution inside- and outside-eddy shows that the outside-eddy MLD restratified earlier in run 05K150-1H (in March) than in run 1K100-1H (in April) due to restratification beginning at submesoscale with mixed layer instabilities (Fig.7b). But in both cases inside-eddy MLD reached the same depth (about $190m$, see Fig.7e-f). This suggests that maximal mixed layer inside-eddy indeed reached a maximum driven by air-sea cooling, while restratification outside-eddy occurred too late in run 1K100-1H because vertical buoyancy fluxes are too weak (Capet et al., 2008). Compared to Mediterranean MLD climatology, a restratification in April is indeed quite late (Houpert et al., 2015).

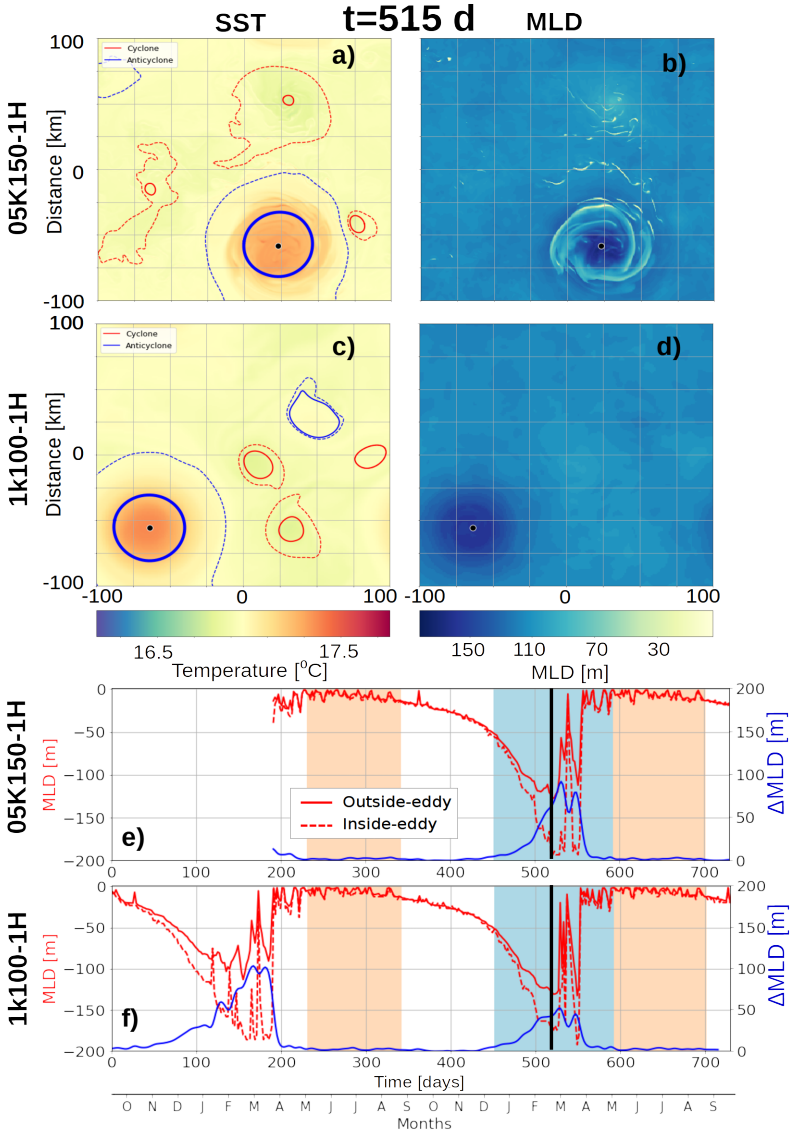

Figure 7. (a) SST with anticyclones and cyclones as in Fig.4 (the initial anticyclone has thicker contour) for the 05K150-1H simulation. (b) MLD in 05K150-1H. (c) and (d) : same as (a) and (b) but for the 1K100-1H simulation. (e) MLD time series inside-anticyclone (dashed red), outside-eddy (continous red) and ΔMLD (blue) for the 05K150-1H simulation, a black line indicates the time step shown in panels (a)-(d). Due to memory issues, the first transient winter was not recorded. (f) Same as (e) in 1K100-1H simulation.

Mixing patterns over the vertical in the high resolution simulations are also consistent with observations. Anticyclones were recently observed to enhance mixing at depth through the propagation of trapped near-inertial internal waves in their core. In studies from Martínez-Marrero et al. (2019) and Fernández-Castro et al. (2020), in situ measurements revealed lower dissipation rate ϵ in anticyclonic homogeneous core than in the neighboring background, and enhanced ϵ below at depth. In our numerical experiments, both diffusivity κ (Fig.8c) and dissipation rate ϵ (Fig.8e for run 1K100-1H) match this

feature, with enhanced mixing in summer below the anticyclone, up to one order of magnitude larger from 200 to 300m depth. The anticyclone subsurface core revealed by thick isopycnal displacement on Fig.8e, also shows locally reduced ϵ between 100 and 200m. Fig.8e is then a striking reproduction of dissipation rate section obtained by Fernández-Castro et al. (2020) (see in particular their Fig.5f). However those in situ measurements could not compare outside- and inside-eddy mixing close to the surface, because the value range for ϵ would be too large with surface processes a lot more powerful than deep ocean ones. Numerical simulation enables to reveal that anticyclones also enhance mixing in near surface, with higher ϵ and κ just above the homogeneous core, in the upper 50 meters. The differential mixing ratio ξ previously shown in anticyclone time series then accurately measures a surface-enhanced mixing.

The seasonal cycle of eddy SST signature is then effectively reproduced at 1km horizontal resolution, close to observed value for the example shown above (Fig.3e). eddy SST seasonal shift correlates with increased mixing at the anticyclone core, in consistence with Moschos et al. (2022) hypothesis. This differential mixing is absent at low vertical resolution. But it appears through $k-\epsilon$ mixing parametrization and converges with a sufficiently high number of vertical levels, with vertical grid step smaller equal or smaller than 4m in near surface.

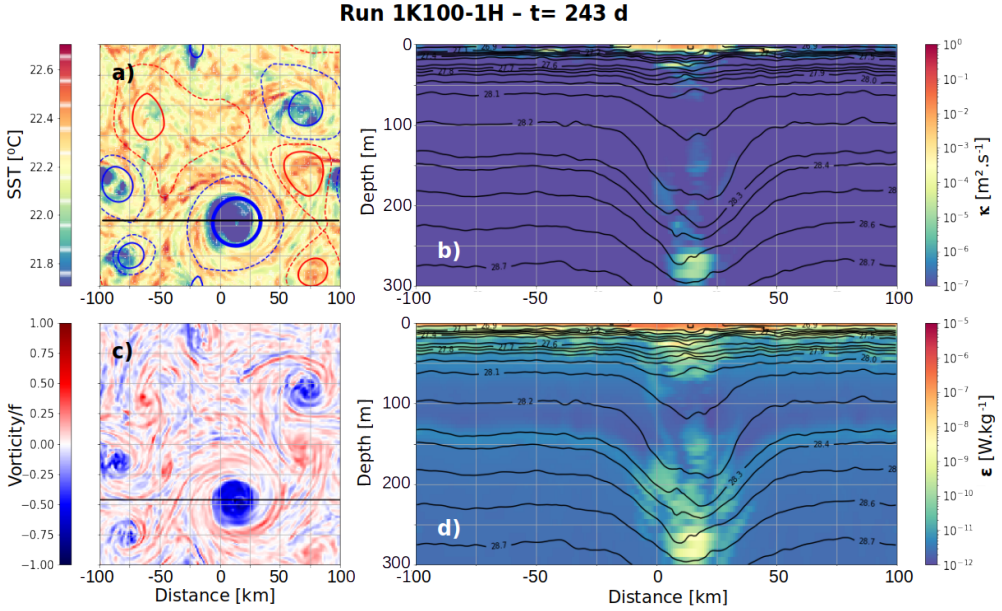

Figure 8. Snapshot at $t = 243\,d$ for the 1K100-1H simulation (see Fig.5). (a) SST and (c) surface vorticity normalized by f with eddy detections as in Fig.4 (initial anticyclone has a thicker contour). (b) κ and (d) ϵ vertical sections along black lines in panels (a)-(c) in the upper 300m with logarithmic color scales ; in both case the colorbar lower bound is the minimal possible value (see Sect.2.1). Isopycnals are added in black lines.

3.2 Forcing frequency sensitivity

Sensitivity of the eddy SST signature δT and differential mixing ξ to temporal resolution of the forcing is investigated by progressively removing high frequencies from the atmospheric inputs. These experiences are summarized as 1K100-1D to 1K100-1W in Table 1, using 1-day, 3-day and 1-week atmospheric time series respectively. δT and dif-

ferential mixing ξ time series for these experiments are shown in Fig.9a-b. Significantly cold SST signatures ($\overline{\delta T} \lesssim -0.2°C$) are obtained together with strong mixing ratio ($\overline{\xi} \approx 3$) for 1-hour and 1-day frequency, but no significant differential mixing is retrieved ($1 < \overline{\xi} < 1.5$) for all lower forcing frequencies (Fig.9c). This threshold behavior is a strong result and shows that spontaneous appearance of differential mixing is driven by small scale and high frequency features. With a Coriolis parameter $f = 9.0 \times 10^{-5} s^{-1} = 1.24 cpd$ (*count per day*), the inertial period is about 19h, the 1-day forcing can then partly trigger near-inertial waves.

The relationship between $\overline{\delta T}$ and $\overline{\xi}$ is however less clear than for the resolution sensitivity analysis (Fig.6). No differential mixing is observed for forcing frequencies lower than 1 day, but summer cold-core signatures are still found ($-0.12 < \overline{\delta T} < -0.03°C$, see Table1), even for the 1-week forcing. δT time series clearly show for all frequencies a marked seasonal signal (Fig.9a). In particular a significant warm winter signature is always observed, with stable maximal value at $\delta T \approx +0.4°C$. In the same context a surprising result is the summer averaged $\overline{\delta T}$ being colder on average at 1-day than 1-hour forcing, despite similar differential mixing. Temporal evolution of eddy SST anomalies reveals this effect to be caused by a larger oscillation of the eddy surface signature (Fig.9a) about $\pm 0.2°C$, hence larger errorbars at 1-day on Fig.9c. This suggests that other mechanisms not triggered by high frequency winds also contribute to the eddy SST seasonal cycle. If no differential vertical mixing is observed but if seasonal variations of the anticyclone SST (and hence surface density) is found, one can only hypothesize the role of lateral exchanges. Despite some tries, we were unsuccessful in quantifying eddy lateral exchanges following a varying $R_{max}(t)$ contour. No particular asymmetric wave modes was observed on SST snapshots, discarding the hypothesis of vortex Rossby waves (Guinn & Schubert, 1993; Montgomery & Kallenbach, 1997).

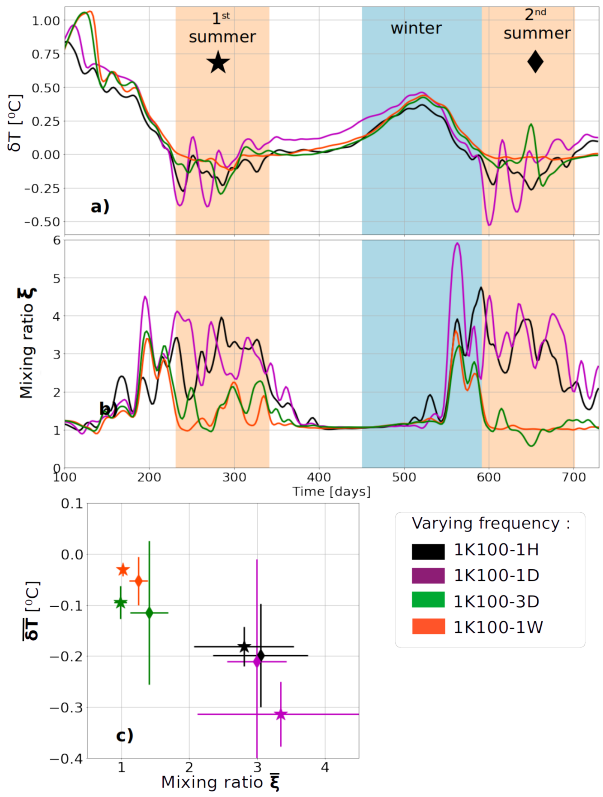

Figure 9. (a) δT and (b) ξ time series for experiments 1K100-1H, 1K100-1D, 1K100-3D and 1K100-1W listed in Table 1 with SST retroaction on air-sea fluxes and varying forcing frequency. Gaussian smoothing with 1-day standard deviation is applied, summer periods are shaded in light red, winter in light blue. (c) Summer-averaged eddy-induced SST anomalies ($\overline{\delta T}$) and mixing ratio ($\overline{\xi}$), with stars for the first summer and diamonds for the second one.

Near-inertial internal waves are investigated using Fourier transforms on vertical speed anomalies in run 1K100-1H. We focus on a single vertical level at 20m in near-surface where the enhanced mixing occurs (see Fig.8c). Transforms are computed only in the second summer (590 to 700 simulated days) with a 1-hour sampling frequency. Following Babiano et al. (1987), inside-eddy spectrum is performed keeping only the eddy core area (around the eddy center with radius $2/3R_{max}(t)$) and the remaining area is set to 0 before performing the Fourier transform. Similarly outside-eddy spectrum is performed blanking all value inside any eddy contours. The results clearly show a differential effect inside-eddy vertical kinetic energy density revealing a second powerful peak at the effective inertial frequency $f_e = f + \zeta/2 \approx 1.0cpd$, lower than the inertia frequency (Fig.10a). Outside-eddy spectrum (Fig.10b) shows only one peak at the inertial frequency, and internal waves cannot propagate at lower frequencies due to the f-cut-off (Garrett & Munk, 1972). Normalizing by the investigated area, total vertical kinetic energy per unit surface is indeed higher inside the anticyclone ($4.19\times10^{-14}m^2.s^{-2}/m^2$) than outside-eddy ($1.64\times10^{-14}m^2.s^{-2}/m^2$) due to these powerful sub-inertial internal waves. Further investigation confirmed that sub-inertial waves are absent inside-eddy with the 1-week forcing (Fig.13). An assumption of this method is however to assume that both inside- and outside-eddy areas roughly keep the same area, which is verified. This result is consistent with (Kunze, 1985) theory and recent numerical works (Danioux et al., 2015; As-

selin & Young, 2020) sub-inertial waves ($\omega \lesssim f$) can be trapped in the anticyclone due to the locally lower absolute vorticity, and enhance mixing while breaking as proposed by Fernández-Castro et al. (2020).

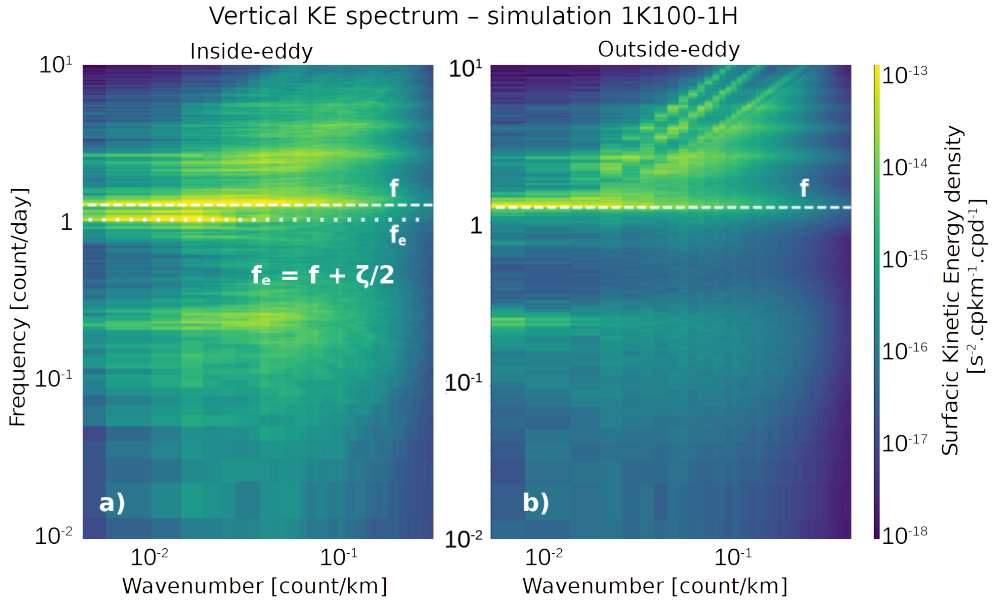

Figure 10. (a) Inside-eddy and (b) outside-eddy vertical kinetic energy density spectrum at 20m depth. For comparison, spectrum are normalized by the area of interest. Analysis performed on simulation 1K100-1H with 1-hour sampling. Normal (respectively effective) inertial frequencies $f = 1.24cpd$ ($f_e \approx 1.0cpd$) are highlighted by a white dashed (dotted) line.

3.3 Air-sea fluxes sensitivity

Sensitivity of the anticyclone temporal evolution to air-sea fluxes components is further investigated. A $1km$ resolution simulation experiment is run similarly as the 1K100-1H simulation without applying SST retroaction on air-sea fluxes (see Sect.2.3, run 1K100-1H-NoSST in Table 1). Although quite unrealistic, this experiment enables to check if the eddy SST anomaly seasonal shift and differential mixing observed in previous simulations are triggered by air-sea fluxes retroaction. Time series for SST reveals that eddy SST anomalies seasonal oscillation is retrieved without SST retroaction (Fig.11a-c), and summer cold-core signatures are even stronger : $\overline{deltaT} \approx -0.5°C$ for both summers (Fig.11f). Simultaneously, differential mixing reaches $\xi \approx 3$, approximately the same value as run 1K100-1H (Fig.11h). This confirms that differential eddy mixing triggering the eddy SST variations is not linked to air-sea fluxes retroaction. However this feedback can modulate and dampen the δT seasonal cycle leading to reduced anomalies.

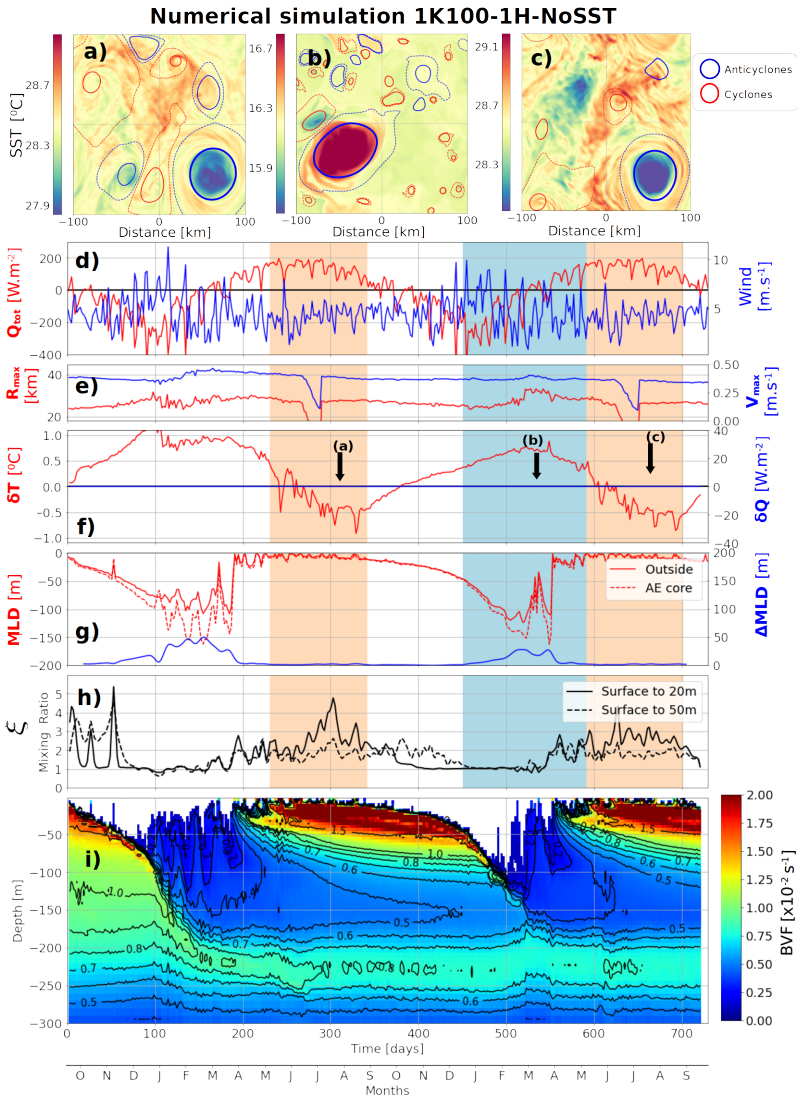

Figure 11. Simulation 1K100-1H-NoSST from Table 1. Same as in Fig.4 but without SST retroaction on air-sea fluxes. Discontinuities in R_{max} and V_{max} in panel (e) are due to the anti-cyclone crossing twice the grid borders.

SST retroaction acting as a negative feedback on SST anomalies can be analytically expected as linear. The derivative of each heat component with respect to T_s is indeed approximately constant (T_s being in Kelvin in Eq.14). Transfer coefficients C_E and C_S are indeed much more dependent on wind speed than on temperature, varying roughly about 0.2 with a T_s change of $1K$. The most sensitive case is a low air-sea temperature difference with weak wind, in which the boundary layer can switch from stable to unstable conditions (see for instance Fig.A1b from Pettenuzzo et al. (2010)). Assuming C_E and C_S are roughly constant with respect to temperature one gets :

$$\frac{\partial Q^{\uparrow}_{LW}}{\partial T_s} = -4\epsilon_{sb}\sigma_{sb}T_s^3 \approx -6\,W.m^{-2}.K^{-1} \tag{14}$$

529

$$\frac{\partial Q_{Lat}}{\partial T_s} \approx -\frac{\rho_a L_E C_E |V| 0.610}{P_{SL}} \frac{dP_{sat}}{dT_s} \approx -30\, W.m^{-2}.K^{-1} \tag{15}$$

$$\frac{\partial Q_{Sen}}{\partial T_s} = -\rho_a c_p C_S |V| \approx -10\, W.m^{-2}.K^{-1} \tag{16}$$

530 These estimations are in agreement with recent statistical observations from Aguedjou
531 et al. (2023) who found contributions about $-25\, W.m^{-2}.K^{-1}$ and $-8\, W.m^{-2}.K^{-1}$ for
532 latent and sensible heat fluxes respectively in the Tropical Atlantic Ocean. Altogether
533 a thermal feedback on the order of $\frac{\partial Q_{tot}}{\partial T_s} \approx -45 W.m^{-2}.K^{-1}$ is then expected, mostly
534 driven by latent heat flux. THFF in Table 1 is computed only on the whole simulated
535 year (from 365 to 730 days) and a value of $\approx -40\, W.m^{-2}.K^{-1}$ is retrieved with a sim-
536 ple SST retroaction, in consistence with Eq.14 to 16. This value is relatively constant
537 in our simulations, slightly decreasing for coarser resolution and lower forcing frequen-
538 cies (see Table 1). $\partial C_E/\partial T_s$ and $\partial C_S/\partial T_s$ being also positive, taking this into account
539 in Eq.15 would lead to a even higher THFF estimate. THFF for the 1K100-1H simula-
540 tion, defined here as δQ as a function of δT is shown in Fig.12. The obtained thermal
541 feedback is consistent with previous estimates in coupled climate model : Ma et al. (2016)
542 found a higher THFF ranging between 40 and $56 W.m^{-2}.K^{-1}$ but in the specific area
543 of very warm eddies of the Kuroshio extension region. Moreton et al. (2021) found THFF
544 ranging between 35 and $45\, W.m^{-2}.K^{-1}$ over mesoscale eddies. They however used a com-
545 posite approach in a model coupled with atmosphere and maximal oceanic resolution of
546 $1/12°$, for effective radius about $40km$. A coupled atmosphere layer is expected to fur-
547 ther dampen the total THFF, taking into account other feedbacks than SST, in partic-
548 ular evaporation. Humidity is expected to increase over warm eddy, consequently decreas-
549 ing the latent heat flux driving evaporation, whereas we applied a uniform h_{2m} field. Sim-
550 ilar THFF in our simulations compared to coupled ocean-atmosphere models suggests
551 that our results would not change significantly with more complex heat flux retroaction.

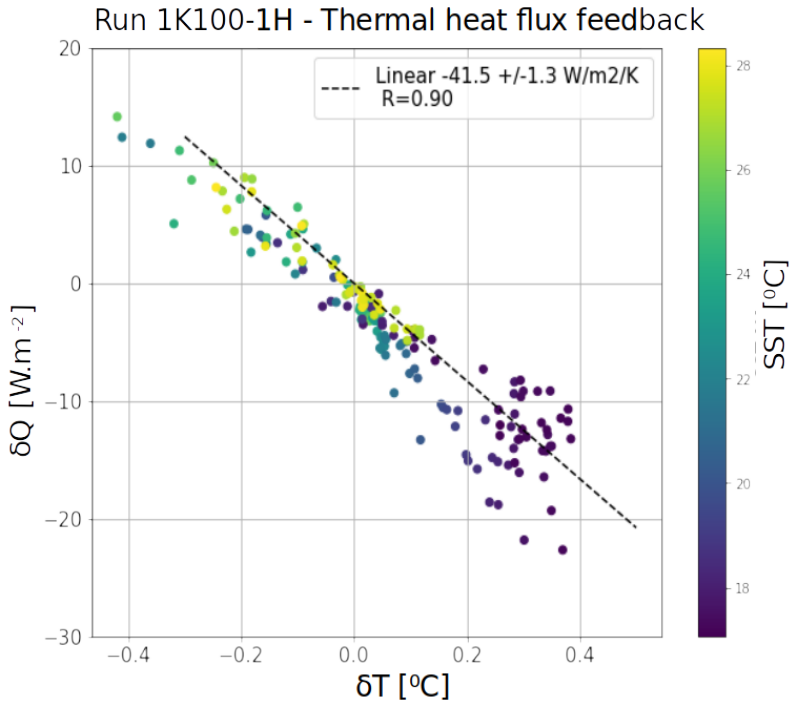

Figure 12. Thermal heat flux feedback in run 1K100-1H on the 2^{nd} simulated year, with linear regression as dashed black line, δQ and δT are from Fig.5f. Regression coefficient and parameters are indicated in the legend.

Without SST retroaction on air-sea fluxes, the most important difference from run 1K100-1H is the MLD anomaly variations. Outside-eddy, mixed layer evolution is very similar in runs 1K100-1H and 1K100-1H-NoSST reaching about $120m$ at its winter maximum, but the eddy MLD anomaly is about 5 times smaller ($\Delta MLD = 18m$, see Fig.11h). With no THFF, the MLD deepens at the same rate outside- and inside-eddy. Winter MLD deepening can be computed estimating the thermal loss ΔT, assuming a linear thermal linear stratification $\partial_z T$:

$$MLD = \frac{\Delta T}{\partial_z T} \tag{17}$$

The thermal loss is the integration of the heat flux over winter duration D. Assuming stratification is at first order the same outside- and inside-eddy, MLD anomaly would then be driven only by heat flux lateral gradients :

$$\Delta MLD = \frac{D}{\rho_0 c_p \partial_z T} \delta Q \tag{18}$$

In the 1K100-1H run with SST retroaction on air-sea fluxes, δQ is positive in winter reaching about $+15 W.m^{-2}$ over 4 months. This leads to an estimate $\Delta MLD \approx 20m$. This is the estimated contribution on eddy MLD anomaly from THFF alone, but $\Delta MLD = 18m$ is still retrieved in run 1K100-1H-NoSST. It shows that difference between inside- and outside-eddy stratification also contribute to MLD anomaly in the absence of THFF. Assuming that $\partial_z T$ is roughly the same inside- and outside-eddy is valid in the upper

layers where stratification is mostly the seasonal thermocline. At depth lower than 100m however, the anticyclone constitutes a more homogenized layer and this assumption should not hold. MLD is then expected to deepen faster inside-eddy even with no SST retroaction. An example in observations is shown in Fig.3g : the inside-eddy MLD connects in February 2018 with the layer homogenized the previous winter and reaching quickly about 300m. Such mixed layer deepening acceleration is partly retrieved in run 1K100-1H around 500 days, when the mixed layer reaches the subsurface homogenized layer formed in the first winter (Fig.5g). To sum up, ΔMLD is about 2 to 3 times smaller in run 1K100-1H-NoSST than in run 1K100-1H. This gives an estimate of the relative contribution of THFF and stratification difference on MLD anomalies.

In all simulations ΔMLD is anyway still relatively weak compared to the 200 to 300m MLD anomalies observed in Mediterranean anticyclones (Barboni, Coadou-Chaventon, et al., 2023). Two main hypotheses can be proposed, the first being that some interannual variability is needed. The second hypothesis is that layers homogenized by winter MLD progressively restratify at depth in summer due to numerical diffusion (stratification isolines progressively closing, Fig. 5i). MLD in the following winter will then have to break this artificial stratification. This second hypothesis entails that the vertical grid is not enough refined yet to correctly preserve homogenized layers from one winter to another. The comparison between runs 1K100-1H and 1K100-1H-NoSST shows that SST retroaction on air-sea fluxes is necessary to obtained eddy MLD anomalies, but quantitative description deserves further research and ΔMLD is not only driven by fluxes gradients at the eddy scale.

Conclusions

Idealized numerical experiments at high horizontal resolution and high frequency atmospheric forcing are able to qualitatively and quantitatively retrieve SST signature seasonal cycle for a mesoscale anticyclone. Starting from a surface intensified mesoscale anticyclone at $Ro \approx 0.16$, seasonal oscillations of the eddy SST anomalies are recovered with a 1km horizontal resolution, 100 vertical levels, hourly atmospheric forcing and SST retroaction on air-sea fluxes. Retrieved eddy anomalies are a warm winter SST feature at $\delta T \approx +0.5°C$ and a cold summer SST at $\delta T \approx -0.2°C$, in consistence with observations. The shift from warm winter SST signature to summer cold one is explained by an increased vertical mixing in the anticyclone upper layers. This differential mixing is due to higher NIW energy propagation well captured through the $\kappa - \epsilon$ mixing parametrization.

A sensitivity analysis reveals that this differential mixing depends on the grid vertical resolution. Model diffusivity near the surface is then consistently 3 times higher in summer inside-eddy than outside for vertical grid step about 4m or less in near surface. On the other hand horizontal resolution appears less critical to accurately resolve eddy differential mixing. Sensitivity to the forcing frequency is investigated by progressively removing high frequencies from the atmospheric input fields. A threshold behavior is observed when forcing frequency is lower than a day, then differential mixing dramatically vanishes with no significant summer cold-core anticyclonic SST. With high frequency forcing, vertical kinetic energy indeed reveals a second powerful peak only inside the anticyclone in near-surface, corresponding to internal waves at the effective inertial frequency. Such an analysis suggests a significant impact of the eddy vorticity as cut-off frequency in allowing or not the selective NIW propagation. Weaker eddy SST seasonal oscillations are also retrieved in the absence of high frequently forcing and consequently without differential mixing (3-day and 1-week experiments). This highlights that other contributions might participate to these eddy SST signatures, in particular lateral exchanges. A new question for future research opened by this eddy-modulated mixing is how it depends on the eddy vorticity and size.

SST retroaction on air-sea fluxes is not found to be responsible of eddy SST signatures seasonal shift, as the seasonal oscillation is retrieved with and without air-sea fluxes parametrization. However this retroaction is logically found to dampen the SST anomalies, and then reduces eddy anomalies magnitude in both summer and winter. The average thermal heat flux feedback of our mesoscale anticyclone is approximately $40 W.m^{-2}.K^{-1}$, in consistence with analytical derivation and previous studies.

Significant eddy-induced mixed layer anomaly $\Delta MLD \approx 50m$ are found at 1km horizontal resolution, only in the presence of SST retroaction on fluxes. Linear MLD anomaly analysis suggests that the thermal feedback is only responsible for about half of the MLD anomaly. Further analysis should then investigate how SST retroaction impacts inside-eddy stratification. MLD anomalies do not completely converge at 1km as larger anomalies are obtained with a 500m resolution due to restratification beginning outside-eddy driven by submesoscale instabilities, despite similar maximal mixed-layer at the anticyclone core. No restratification delay is clearly observed, but it could occur at even higher horizontal resolution inside the anticyclone because the balanced density gradients inhibits mixed layer instabilities there. This hypothesis is consistent with observations (Barboni, Coadou-Chaventon, et al., 2023) but would deserve more investigation in the future. This result is also important as the mixed layer is a significant driver of atmospheric and biogeochemical exchanges, and the explicit resolution of submesoscale processes might be needed to accurately reproduce their interaction with eddies (Capet et al., 2008; Lévy et al., 2018).

This is the first time that sub-inertial waves concentration in anticyclones is linked in a numerical study to an increased mixing in near surface, spontaneously retrieved through the $k-\epsilon$ mixing closure. Mixing modulation by eddies suggests a strong scale interactions between sub-inertial internal waves ($\omega \lesssim f$) and the mesoscale ($\omega \ll f$). Differential mixing triggered by high frequency winds is an important result highlighting the need of both fine vertical resolution and atmospheric forcing at sufficiently high frequency to correctly reproduce mesoscale eddies evolution. At present stage, global operational models do not have the resolution to capture these phenomena. According to this study vertical grid step about 4m in the upper thermocline would then be necessary to accurately reproduce mesoscale temporal evolution, or parameterize a differential mixing ratio $\xi \approx 3$ in near surface.

Open Research Section

In-situ profiles collocated ed with mesoscale eddies database is available at `https://doi.org/10.17882/93077`. AMEDA eddy tracking algorithm is open source and available at `https://github.com/briaclevu/AMEDA`. ERA5 atmospheric reanalysis are publicly available at `https://doi.org/10.24381/cds.adbb2d47`. The CROCO code is publicly available at `https://www.croco-ocean.org/`.

Acknowledgments

Authors gratefully acknowledge *Ifremer* and *Service Hydrographique et Océanographique de la Marine* for their use of the *Datarmor* computing facility. Authors acknowledge Evangelos Moschos (*Amphitrite*) for the reuse of his figures as snapshots in Fig.3a-d. Authors also acknowledge fruitful discussions with Clément Vic (*Ifremer*), in particular the comparison with observations in Fig.8 and 10, and the two anonymous reviewers whose comments greatly helped improving the present manuscript.

References

Aguedjou, H. M. A., Chaigneau, A., Dadou, I., Morel, Y., Baloïtcha, E., & Da-Allada, C. Y. (2023). Imprint of mesoscale eddies on air-sea interaction in the

tropical atlantic ocean. *Remote Sensing*, *15*(12), 3087.

Amores, A., Jordà, G., Arsouze, T., & Le Sommer, J. (2018). Up to what extent can we characterize ocean eddies using present-day gridded altimetric products? *Journal of Geophysical Research: Oceans*, *123*(10), 7220–7236.

Arai, M., & Yamagata, T. (1994). Asymmetric evolution of eddies in rotating shallow water. *Chaos: An Interdisciplinary Journal of Nonlinear Science*, *4*(2), 163–175.

Aroucha, L. C., Veleda, D., Lopes, F. S., Tyaquiçã, P., Lefèvre, N., & Araujo, M. (2020). Intra- and inter-annual variability of north brazil current rings using angular momentum eddy detection and tracking algorithm: Observations from 1993 to 2016. *Journal of Geophysical Research: Oceans*, *125*(12), e2019JC015921. doi: 10.1029/2019JC015921

Asselin, O., & Young, W. R. (2020). Penetration of wind-generated near-inertial waves into a turbulent ocean. *Journal of Physical Oceanography*, *50*(6), 1699–1716.

Ayouche, A., De Marez, C., Morvan, M., L'hegaret, P., Carton, X., Le Vu, B., & Stegner, A. (2021). Structure and dynamics of the ras al hadd oceanic dipole in the arabian sea. In *Oceans* (Vol. 2, pp. 105–125).

Babiano, A., Basdevant, C., Legras, B., & Sadourny, R. (1987). Vorticity and passive-scalar dynamics in two-dimensional turbulence. *Journal of Fluid Mechanics*, *183*, 379–397.

Barboni, A., Coadou-Chaventon, S., Stegner, A., Le Vu, B., & Dumas, F. (2023). How subsurface and double-core anticyclones intensify the winter mixed-layer deepening in the mediterranean sea. *Ocean Science*, *19*(2), 229–250.

Barboni, A., Lazar, A., Stegner, A., & Moschos, E. (2021). Lagrangian eddy tracking reveals the eratosthenes anticyclonic attractor in the eastern levantine basin. *Ocean Science*, *17*(5), 1231–1250.

Barboni, A., Stegner, A., Le Vu, B., & Dumas, F. (2023). *2000-2021 in situ profiles colocalized with ameda eddy detections from 1/8 aviso altimetry in the mediterranean sea.* SEANOE.

Boccaletti, G., Ferrari, R., & Fox-Kemper, B. (2007). Mixed layer instabilities and restratification. *Journal of Physical Oceanography*, *37*(9), 2228–2250.

Capet, X., Mcwilliams, J. C., Molemaker, M. J., & Shchepetkin, A. F. (2008). Mesoscale to submesoscale transition in the california current system. part i: Flow structure, eddy flux, and observational tests. *Journal of physical oceanography*, *38*(1), 29–43.

Carton, X., Flierl, G., & Polvani, L. (1989). The generation of tripoles from unstable axisymmetric isolated vortex structures. *EPL (Europhysics Letters)*, *9*(4), 339.

Chaigneau, A., Eldin, G., & Dewitte, B. (2009). Eddy activity in the four major upwelling systems from satellite altimetry (1992–2007). *Progress in Oceanography*, *83*(1-4), 117–123.

Chelton, D. B., Gaube, P., Schlax, M. G., Early, J. J., & Samelson, R. M. (2011). The influence of nonlinear mesoscale eddies on near-surface oceanic chlorophyll. *Science*, *334*(6054), 328–332.

Chelton, D. B., Schlax, M. G., & Samelson, R. M. (2011). Global observations of nonlinear mesoscale eddies. *Progress in oceanography*, *91*(2), 167–216.

Couvelard, X., Dumas, F., Garnier, V., Ponte, A., Talandier, C., & Treguier, A.-M. (2015). Mixed layer formation and restratification in presence of mesoscale and submesoscale turbulence. *Ocean Modelling*, *96*, 243–253.

Danioux, E., Klein, P., & Rivière, P. (2008). Propagation of wind energy into the deep ocean through a fully turbulent mesoscale eddy field. *Journal of Physical Oceanography*, *38*(10), 2224–2241.

Danioux, E., Vanneste, J., & Bühler, O. (2015). On the concentration of near-inertial waves in anticyclones. *Journal of Fluid Mechanics*, *773*, R2.

D'Asaro, E. A. (1995). Upper-ocean inertial currents forced by a strong storm. part iii: Interaction of inertial currents and mesoscale eddies. *Journal of physical oceanography*, *25*(11), 2953–2958.

de Marez, C., Le Corre, M., & Gula, J. (2021). The influence of merger and convection on an anticyclonic eddy trapped in a bowl. *Ocean Modelling*, *167*, 101874.

Doglioli, A., Blanke, B., Speich, S., & Lapeyre, G. (2007). Tracking coherent structures in a regional ocean model with wavelet analysis: Application to cape basin eddies. *Journal of Geophysical Research: Oceans*, *112*(C5).

Escudier, R., Renault, L., Pascual, A., Brasseur, P., Chelton, D., & Beuvier, J. (2016). Eddy properties in the western mediterranean sea from satellite altimetry and a numerical simulation. *Journal of Geophysical Research: Oceans*, *121*(6), 3990–4006.

Everett, J., Baird, M., Oke, P., & Suthers, I. (2012). An avenue of eddies: Quantifying the biophysical properties of mesoscale eddies in the tasman sea. *Geophysical Research Letters*, *39*(16).

Fairall, C. W., Bradley, E. F., Hare, J., Grachev, A. A., & Edson, J. B. (2003). Bulk parameterization of air–sea fluxes: Updates and verification for the coare algorithm. *Journal of climate*, *16*(4), 571–591.

Fernández-Castro, B., Evans, D. G., Frajka-Williams, E., Vic, C., & Naveira-Garabato, A. C. (2020). Breaking of internal waves and turbulent dissipation in an anticyclonic mode water eddy. *Journal of Physical Oceanography*, *50*(7), 1893–1914.

Frenger, I., Gruber, N., Knutti, R., & Münnich, M. (2013). Imprint of southern ocean eddies on winds, clouds and rainfall. *Nature geoscience*, *6*(8), 608–612.

Garrett, C., & Munk, W. (1972). Space-time scales of internal waves. *Geophysical Fluid Dynamics*, *3*(3), 225–264.

Gaube, P., J. McGillicuddy Jr, D., & Moulin, A. J. (2019). Mesoscale eddies modulate mixed layer depth globally. *Geophysical Research Letters*, *46*(3), 1505–1512.

Graves, L. P., McWilliams, J. C., & Montgomery, M. T. (2006). Vortex evolution due to straining: A mechanism for dominance of strong, interior anticyclones. *Geophysical and Astrophysical Fluid Dynamics*, *100*(3), 151–183.

Guinn, T. A., & Schubert, W. H. (1993). Hurricane spiral bands. *Journal of the atmospheric sciences*, *50*(20), 3380–3403.

Hausmann, U., & Czaja, A. (2012). The observed signature of mesoscale eddies in sea surface temperature and the associated heat transport. *Deep Sea Research Part I: Oceanographic Research Papers*, *70*, 60–72.

Hersbach, H., Bell, B., Berrisford, P., Hirahara, S., Horányi, A., Muñoz-Sabater, J., ... others (2020). The era5 global reanalysis. *Quarterly Journal of the Royal Meteorological Society*, *146*(730), 1999–2049.

Houpert, L., Testor, P., De Madron, X. D., Somot, S., D'ortenzio, F., Estournel, C., & Lavigne, H. (2015). Seasonal cycle of the mixed layer, the seasonal thermocline and the upper-ocean heat storage rate in the mediterranean sea derived from observations. *Progress in Oceanography*, *132*, 333–352.

Ioannou, A., Stegner, A., Dubos, T., Le Vu, B., & Speich, S. (2020). Generation and intensification of mesoscale anticyclones by orographic wind jets: The case of ierapetra eddies forced by the etesians. *Journal of Geophysical Research: Oceans*, *125*(8), e2019JC015810.

Ioannou, A., Stegner, A., & Dumas, F. (2021). Three-dimensional evolution of mesoscale anticyclones in the lee of crete. *Frontiers in Marine Science*.

Ioannou, A., Stegner, A., Tuel, A., LeVu, B., Dumas, F., & Speich, S. (2019). Cyclostrophic corrections of aviso/duacs surface velocities and its application to mesoscale eddies in the mediterranean sea. *Journal of Geophysical Research: Oceans*, *124*(12), 8913–8932.

Juza, M., Mourre, B., Renault, L., Gómara, S., Sebastián, K., Lora, S., ... others (2016). Socib operational ocean forecasting system and multi-platform validation in the western mediterranean sea. *Journal of Operational Oceanography*, *9*(sup1), s155–s166.

Kunze, E. (1985). Near-inertial wave propagation in geostrophic shear. *Journal of Physical Oceanography*, *15*(5), 544–565.

Laxenaire, R., Speich, S., Blanke, B., Chaigneau, A., Pegliasco, C., & Stegner, A. (2018). Anticyclonic eddies connecting the western boundaries of indian and atlantic oceans. *Journal of Geophysical Research: Oceans*, *123*(11), 7651–7677.

Laxenaire, R., Speich, S., & Stegner, A. (2020). Agulhas ring heat content and transport in the south atlantic estimated by combining satellite altimetry and argo profiling floats data. *Journal of Geophysical Research: Oceans*, *125*(9), e2019JC015511.

Le Vu, B., Stegner, A., & Arsouze, T. (2018). Angular momentum eddy detection and tracking algorithm (ameda) and its application to coastal eddy formation. *Journal of Atmospheric and Oceanic Technology*, *35*(4), 739–762.

Lévy, M., Franks, P. J., & Smith, K. S. (2018). The role of submesoscale currents in structuring marine ecosystems. *Nature communications*, *9*(1), 4758.

Liu, F., Zhou, H., Huang, W., & Wen, B. (2020). Submesoscale eddies observation using high-frequency radars: A case study in the northern south china sea. *IEEE Journal of Oceanic Engineering*, *46*(2), 624–633.

Liu, Y., Zheng, Q., & Li, X. (2021). Characteristics of global ocean abnormal mesoscale eddies derived from the fusion of sea surface height and temperature data by deep learning. *Geophysical Research Letters*, *48*(17), e2021GL094772.

Ma, X., Jing, Z., Chang, P., Liu, X., Montuoro, R., Small, R. J., ... others (2016). Western boundary currents regulated by interaction between ocean eddies and the atmosphere. *Nature*, *535*(7613), 533–537.

Marchesiello, P., Capet, X., Menkes, C., & Kennan, S. C. (2011). Submesoscale dynamics in tropical instability waves. *Ocean Modelling*, *39*(1-2), 31–46.

Mariotti, A. (2010). Recent changes in the mediterranean water cycle: a pathway toward long-term regional hydroclimatic change? *Journal of Climate*, *23*(6), 1513–1525.

Martínez-Marrero, A., Barceló-Llull, B., Pallàs-Sanz, E., Aguiar-González, B., Gordo, C., Grisolía, D., ... Arístegui, J. (2019). Near-inertial wave trapping near the base of an anticyclonic mesoscale eddy under normal atmospheric conditions. *Journal of Geophysical Research: Oceans*, *124*(11), 8455–8467.

Mason, E., Pascual, A., & McWilliams, J. C. (2014). A new sea surface height–based code for oceanic mesoscale eddy tracking. *Journal of Atmospheric and Oceanic Technology*, *31*(5), 1181–1188.

Mason, E., Ruiz, S., Bourdalle-Badie, R., Reffray, G., García-Sotillo, M., & Pascual, A. (2019). New insight into 3-d mesoscale eddy properties from cmems operational models in the western mediterranean. *Ocean Science*, *15*(4), 1111–1131.

Montgomery, M. T., & Kallenbach, R. J. (1997). A theory for vortex rossby-waves and its application to spiral bands and intensity changes in hurricanes. *Quarterly Journal of the Royal Meteorological Society*, *123*(538), 435–465.

Moreton, S., Ferreira, D., Roberts, M., & Hewitt, H. (2021). Air-sea turbulent heat flux feedback over mesoscale eddies. *Geophysical Research Letters*, *48*(20), e2021GL095407.

Moschos, E., Barboni, A., & Stegner, A. (2022). Why do inverse eddy surface temperature anomalies emerge? the case of the mediterranean sea. *Remote Sensing*, *14*(15), 3807.

Nencioli, F., Dong, C., Dickey, T., Washburn, L., & McWilliams, J. C. (2010). A vector geometry–based eddy detection algorithm and its application to a high-resolution numerical model product and high-frequency radar surface

velocities in the southern california bight. *Journal of atmospheric and oceanic technology*, *27*(3), 564–579.

Paulson, C. A., & Simpson, J. J. (1977). Irradiance measurements in the upper ocean. *Journal of Physical Oceanography*, *7*(6), 952–956.

Penven, P., Halo, I., Pous, S., & Marié, L. (2014). Cyclogeostrophic balance in the mozambique channel. *Journal of Geophysical Research: Oceans*, *119*(2), 1054–1067.

Perfect, B., Kumar, N., & Riley, J. (2020). Energetics of seamount wakes. part i: Energy exchange. *Journal of Physical Oceanography*, *50*(5), 1365–1382.

Perret, G., Stegner, A., Farge, M., & Pichon, T. (2006). Cyclone-anticyclone asymmetry of large-scale wakes in the laboratory. *Physics of Fluids*, *18*(3).

Pessini, F., Olita, A., Cotroneo, Y., & Perilli, A. (2018). Mesoscale eddies in the algerian basin: do they differ as a function of their formation site? *Ocean Science*, *14*(4), 669–688.

Pettenuzzo, D., Large, W., & Pinardi, N. (2010). On the corrections of era-40 surface flux products consistent with the mediterranean heat and water budgets and the connection between basin surface total heat flux and nao. *Journal of Geophysical Research: Oceans*, *115*(C6).

Rodi, W. (1987). Examples of calculation methods for flow and mixing in stratified fluids. *Journal of Geophysical Research: Oceans*, *92*(C5), 5305–5328. doi: 10.1029/JC092iC05p05305

Shchepetkin, A. F., & McWilliams, J. C. (2005). The regional oceanic modeling system (roms): a split-explicit, free-surface, topography-following-coordinate oceanic model. *Ocean modelling*, *9*(4), 347–404.

Smith, W. H., & Sandwell, D. T. (1997). Global sea floor topography from satellite altimetry and ship depth soundings. *Science*, *277*(5334), 1956–1962.

Soufflet, Y., Marchesiello, P., Lemarié, F., Jouanno, J., Capet, X., Debreu, L., & Benshila, R. (2016). On effective resolution in ocean models. *Ocean Modelling*, *98*, 36–50.

Stegner, A., & Dritschel, D. (2000). A numerical investigation of the stability of isolated shallow water vortices. *Journal of Physical Oceanography*, *30*(10), 2562–2573.

Stegner, A., Le Vu, B., Dumas, F., Ghannami, M. A., Nicolle, A., Durand, C., & Faugere, Y. (2021). Cyclone-anticyclone asymmetry of eddy detection on gridded altimetry product in the mediterranean sea. *Journal of Geophysical Research: Oceans*, *126*(9), e2021JC017475.

Steinberg, J. M., Cole, S. T., Drushka, K., & Abernathey, R. P. (2022). Seasonality of the mesoscale inverse cascade as inferred from global scale-dependent eddy energy observations. *Journal of Physical Oceanography*, *52*(8), 1677–1691.

Sun, W., Dong, C., Tan, W., & He, Y. (2019). Statistical characteristics of cyclonic warm-core eddies and anticyclonic cold-core eddies in the north pacific based on remote sensing data. *Remote Sensing*, *11*(2), 208.

Sun, W., Dong, C., Wang, R., Liu, Y., & Yu, K. (2017). Vertical structure anomalies of oceanic eddies in the kuroshio extension region. *Journal of Geophysical Research: Oceans*, *122*(2), 1476–1496.

Sverdrup, H. U., Johnson, M. W., Fleming, R. H., et al. (1942). *The oceans: Their physics, chemistry, and general biology* (Vol. 1087) (No. 8). Prentice-Hall New York.

Trott, C. B., Subrahmanyam, B., Chaigneau, A., & Roman-Stork, H. L. (2019). Eddy-induced temperature and salinity variability in the arabian sea. *Geophysical Research Letters*, *46*(5), 2734–2742.

Umlauf, L., & Burchard, H. (2003). A generic length-scale equation for geophysical turbulence models. *Journal of Marine Research*, *61*(2), 235–265.

Villas Bôas, A., Sato, O., Chaigneau, A., & Castelão, G. (2015). The signature of mesoscale eddies on the air-sea turbulent heat fluxes in the south atlantic

ocean. *Geophysical Research Letters*, *42*(6), 1856–1862.
Zhai, X., Greatbatch, R. J., & Kohlmann, J.-D. (2008). On the seasonal variability of eddy kinetic energy in the gulf stream region. *Geophysical Research Letters*, *35*(24).

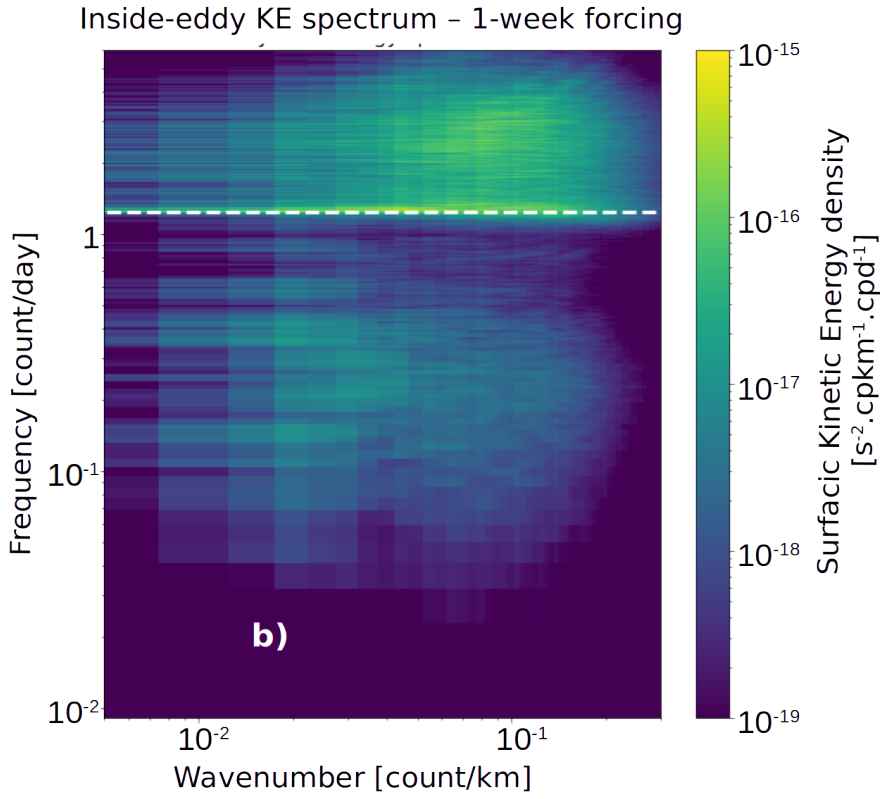

Figure 13. Inside-eddy vertical kinetic energy density spectrum at 20m depth in run 1K100-1W. For computational cost constraints, sampling is performed every 2 hours, then y-axis is slightly changed compared to Fig.10a, and colorbar is adapted. White dashed line shows inertial frequency.

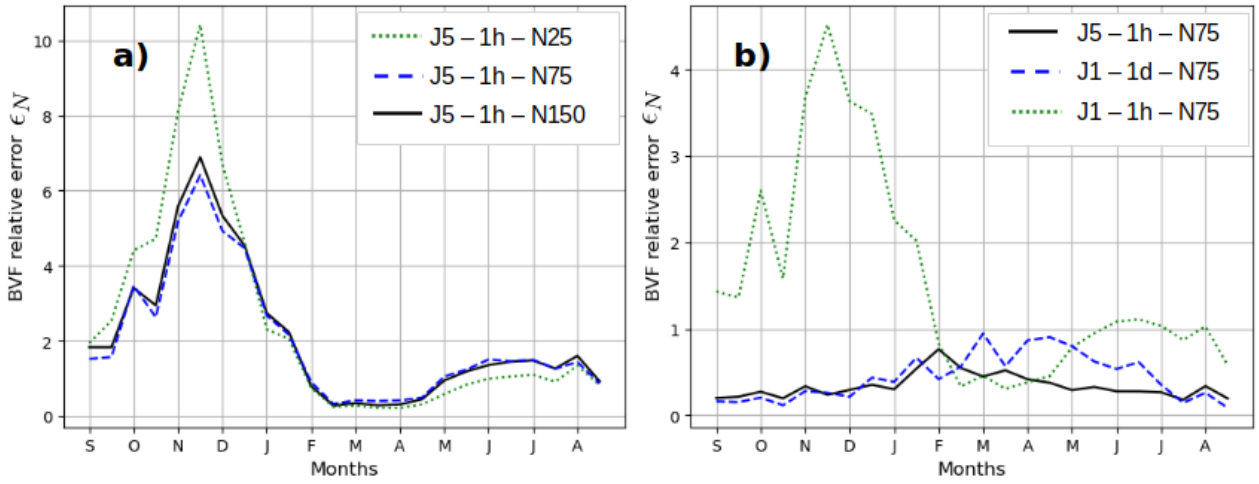

Figure 5.1: Stratification error testing sensitivity to (a) vertical resolution, ranging from 25 to 150 streched levels, and (b) water transparency with Jerlov water types 1 ($J1$, high transparency) to 5 ($J5$, low transparency) and 1-hour (1h) versus 1-day (1d) fluxes inputs.

5.2 Stability analysis

5.2.1 Stratification stability

The accurate reproduction of the ocean stratification seasonal cycle is important to simulate the eddy by comparison. Stability of the background stratification presented in the above study ($R_d \approx 11km$) under ERA5 atmospheric forcing is assessed by running stratification experiments without significant eddy. A small (40km x 40km) grid with 2km horizontal resolution with varying vertical resolution is forced by the ERA5 atmospheric time series for 3 years. An initial kinetic energy input is given by a small anticyclone ($V_{max} = 0.2m.s^{-1}$, $R_{max} = 10km$, $H = 40m$, $\alpha = 2$, cf Eq.5.2). This eddy is assumed to be smaller than the effective resolution of the AVISO product in the Mediterranean Sea (Stegner et al., 2021). Such set-up allows to see the 3D effects of mixing due to eddies in addition to $\kappa - \epsilon$ parameterized vertical mixing. Simulated stratification $N_{simu}(z)$ is compared to observed stratification $N_{obs}(z)$ on the third simulated year. $N_{obs}(z)$ and its spread $\sigma_{obs}(z)$, is computed using outside-eddy profile (see Sect.2.3) available per 15 days time steps in the Levantine Basin (see map in Barboni et al. (2023b), Fig.1a). An integrated stratification error ϵ_N is computed, from surface to $h = 150m$, setting a minimum stratification uncertainty to $1.0 \times 10^{-4} s^{-1}$:

$$\epsilon_N = \frac{1}{h} \int_h^{surf} \frac{(N_{simu}(z) - N_{obs}(z))^2}{\sigma_{obs}(z)^2} dz \tag{5.1}$$

An error in simulated stratification is then less important when a higher variability is observed, which is the case at the surface. Stratification error is evaluated for different forcing and vertical resolution set-ups on Fig.5.1. On Fig.5.1a, the same forcing with 1h atmospheric flux and no short wave solar flux penetration is applied on a varying vertical resolution: the number of vertical levels ranges from 25 to 150 with unchanged stretching parameters ($\theta_s = 8; h_c = 400m$). It reveals that stratification is not very sensitive to vertical resolution throughout the year, maximal ϵ_N decreasing from 11 with 25 levels to 7 with 150 levels. No significant improvement is noticed with more than 75 levels. On Fig.5.1b, atmospheric forcing is applied differently on the same vertical grid with 75 levels, with 1-hour or 1-day inputs (see Barboni et al. (2023b) Sect.2.3), and by increasing the penetration depth of solar short wave radiation. Water transparency has an exponential decay on 2 wavelengths (proportion of short wave heat flux on the first wavelength in parentheses) which extent is set using Jerlov water types with Paulson and Simpson (1977) parameters: 7.9m/1.4m (78%) for Jerlov water type 5 (opaque) to 23m/0.35m (58%) for Jerlov water type 1 (very clear). Stratification happens to be very sensitive to water transparency, and is in the range of observation uncertainty for Jerlov type 1, in consistence with very clear waters of the Levantine Basin. Once the correct transparency is set, there is a slight increase to give fluxes with 1-hour inputs instead of 1-day.

Following this sensitivity analysis, our reference simulation in Barboni et al. (2023b) at 1km resolution has 100 vertical levels using hourly inputs with Jerlov type 1 transparency. Figure 5.2 shows the corresponding

simulated stratification (black lines on Fig.5.2a-d) compared with observations (red line with spread) at four different times of the third simulated year. Figure 5.2e shows the corresponding heat and wind fluxes time series. Figure 5.2f (respectively 5.2g) are Hövmoller diagrams for density (stratification) and MLD over three years. All these vertical properties are well reproduced from one year to another without significant drift.

5.2.2 Anticyclone stability analysis

Our numerical work uses an idealized anticyclonic mesoscale density anomaly with Gaussian shape in the vertical direction and pseudo-Gaussian in the radial one with shape parameter α. It is reminded below with radius R_max and vertical extent H, and further illustrated in Fig.5.3a-b:

$$\sigma(r,z) = \sigma_0 \frac{z}{H} exp\left(-\frac{1}{\alpha}\left(\frac{r}{R_max}\right)^{\alpha}\right) exp\left(-\frac{1}{2}\left(\frac{z}{H}\right)^2\right) \quad \text{with} \quad \sigma_0 = \frac{\rho_0 f V_max R_max e^{1/\alpha}}{gH} \tag{5.2}$$

Following Carton et al. (1989) and Stegner and Dritschel (2000), the shape parameter α turns out to be a crucial parameters to keep eddy as a stable monopole. However previous studies were either 2D (Carton et al., 1989; Stegner and Dritschel, 2000) or 3D (Smyth and McWilliams, 1998) but always assumed a barotropic eddy. Stability was studied for a baroclinic eddy by Yim et al. (2019) but with a Gaussian-Gaussian eddy, i.e. with $\alpha = 2$, and with linear stratification. In the horizontally non-Gaussian case, no analytical solution can be found due to the impossibility to radially integrate the thermal wind equation with $exp\left(-\frac{1}{\alpha}\frac{r^\alpha}{R^\alpha_{max}}\right)$ when α is not equal to 2, and no numerical study was neither performed so far.

Stability analysis is then performed as a reference to ensure the absence of growing perturbation without atmospheric forcing, in particular the fastest barotropic mode 2 (large scale) instabilities (Stegner and Dritschel, 2000). A reference simulation is run for 3 years at 4km resolution with initial anticyclonic density anomaly from Eq.5.2, perturbed by small radial perturbations accounting for about 10% of the initial kinetic energy. Figure 5.3c shows the evolution of azimuthal modes (for initial parameters $\alpha = 1.8$ and $H = 40m$) as a function of time, ensuring no slow instabilities are growing. A more detailed analysis on eddy stability is worth additional investigation, notably sensibility to the eddy characteristic vertical scale H. We only report here that baroclinic instabilities were not triggered and static equilibrium of the initial profile is reached when the vertical extent is on the order of the thermocline depth ($H \sim Z_T$).

5.3 Current feedback and Ekman pumping

An obvious limit in Barboni et al. (2023b) is the unexplored sensitivity of air-sea fluxes to ocean currents and not only SST. Eddy swirling velocities provide a differential current feedback on the wind stress applied on the ocean surface, giving a local wind stress curl and then an eddy-induced Ekman pumping (Gaube et al., 2015). McGillicuddy (2015) proposed this mechanism to explain the formation of mode-water eddies, in particular subsurface anticyclones with isopycnals doming in the upper layers. Schütte et al. (2016) interestingly observed mode-water anticyclones as being persistently cold-core in SST, whereas normal surface-intensified anticyclones are warm in the Northeastern tropical Atlantic. A recent study from Ni et al. (2023) also explored this mechanism and proposed it as the main driver of cold-core anticyclone and warm-core cyclone formation.

The same numerical set-up as in Barboni et al. (2023b) is run at 1km horizontal resolution with 100 vertical levels and 1-hour atmospheric forcing. Current feedback (CBF) is implemented as in Renault et al. (2016a) in an additional wind stress term $\vec{\tau}'$, with $\vec{U_o}$ ocean surface velocity and $|U_A|$ 10m wind speed:

$$\vec{\tau}' = s_\tau \vec{U_o} \quad \text{with} \quad s_\tau = -2.20 \times 10^{-3} N.m^{-4}.s^2 |U_A| \tag{5.3}$$

Similar temporal tracking as in Barboni et al. (2023b) with δT and ξ indicators recovers again eddy SST anomaly seasonal variations. But the cold-core SST signature extents after the summer until early winter (from $t = 200$ to about $500d$) without marked winter warm signature again (Fig.5.4c). Consequently, eddy SST anomaly is almost continuously cold. Significant differential mixing is also recovered with $\xi > 2$ in early summer, roughly from $t = 200d$ to $350d$. But in late summer until early winter ξ gets below one which means weaker mixing inside-eddy, roughly from $t = 350d$ to $t = 500d$. At the same time MLD starts deepening with buoyancy loss, and unlike previous experiment ΔMLD is negative (shallower MLD inside-eddy) until MLD

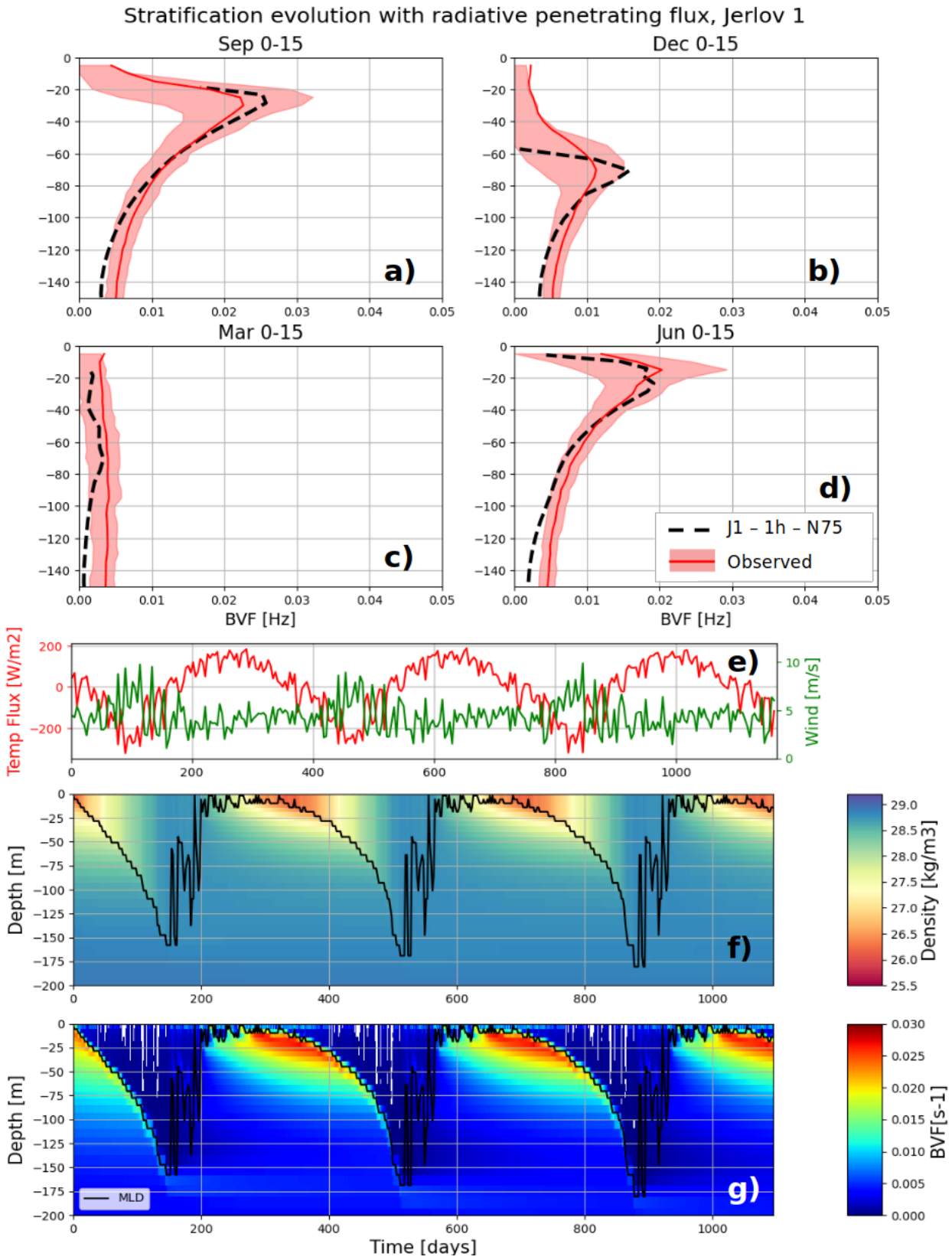

Figure 5.2: Testing stratification in a (40km x 40km) 3D simulation 75 vertical levels with water transparency type Jerlov 1 and 1-hour ERA5 fluxes. (a-d) Simulated stratification $N(z)$ at four different time of the third simulated year. (e) Fluxes time series for heat (red line) and wind (cyan) fluxes; data are shown per day to enhance readability. Corresponding Hövmoller diagram for (f) density and (g) stratification.

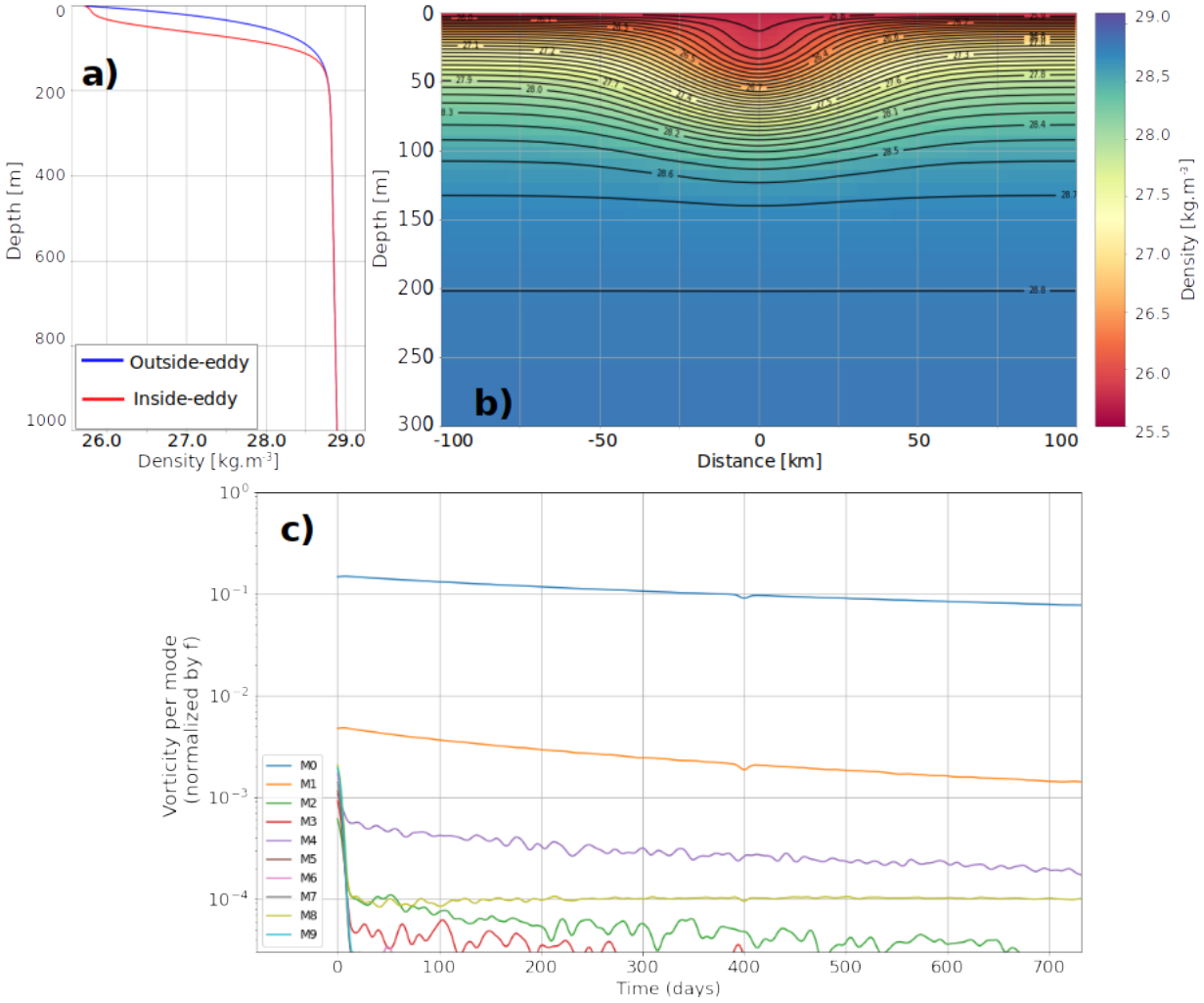

Figure 5.3: (a) Initial vertical density profile in the background (red line, see Eq.5 in Barboni et al. (2023b)) and at the anticyclone core (blue line, Eq.6 in Barboni et al. (2023b)); (b) section of the initial density field; (c) evolution of vorticity azimuthal modes m, with a small initial radial disturbance. $m = 0$ is the axisymmetric vortex rotation decreasing over time due to diffusivity. $m = 1$ does not decrease fast because of the mismatch between grid cell to define the vortex center.

reaches about 80m (Fig.5.4d). Another significant difference is the stronger eddy decay from $V_{max} \approx 0.4$ to $\approx 0.1 m.s^{-1}$ in 2 years, consistent with CFB acting as energy sink at the mesoscale (Renault et al., 2016a).

A density and vorticity section helps to understand this counter-intuitive situation in fall when SST is kept colder inside-eddy while there is less vertical mixing, shown in Fig.5.5 at $t = 420d$. MLD and SST map (Fig.5.5b-c) confirm respectively the shallower MLD inside-eddy with consistent cold SST anomaly despite the total heat flux being negative for about 2 months. Vertical section reveals the anticyclonic vorticity core to be actually in subsurface, between about 50 to 150m (Fig.5.5d). It is capped by seasonal thermocline progressively removed with winter cooling, but isopycnals are domed above the core which is consequently in subsurface. Doming produces isopycnals outcropping, then positive density and hence negative temperature anomaly above the anticyclone. MLD above the anticyclone is also logically shallower because isopycnals are moved upwards. This behavior could be expected to persist as long as the MLD is under Ekman pumping influence, which would mean until the Ekman layer is shallower than the MLD.

Persistence of anticyclonic cold-core SST anomalies until winter is not uncommon. Moschos et al. (2022) gave an example in their Figure A2: an Eratosthenes anticyclone staying cold-core in surface from May 2017 to January 2018, then warm-core again from February to May 2018, then cold-core again until December 2018. Shallower MLD in anticyclone in autumn are also observed in long-lived anticyclone. Figure 5.6 shows the evolution of another Eratosthenes anticyclone in the Levantine Basin from 2012, with δT index and MLD computed as in Barboni et al. (2023a). δT is computed on the same Ultra-High resolution (1/120°) SST product (Nardelli et al., 2013), which since the study from Moschos et al. (2022) was extended from 2008 onward. Profiles in early winter (Fig.5.6e) clearly shows domed isopycnals above the lighter anticyclonic subsurface anomaly. In the upper layers the density anomaly is positive (denser) with shallower MLD coinciding with $\delta T \approx -0.1°C$. The later subsurface evolution is reported in Barboni et al. (2023a) as event ERA1.

Numerical simulation retrieving a persistent anticyclonic cold-core SST signature then seems in agreement with observations for subsurface eddies. This result suggests a transition between 2 mechanisms contributing to eddy SST cold anomalies. At spring restratification it seems that enhanced mixing inside anticyclone smooths temperature gradient, then producing cold-core signatures. Later in fall, MLD starts to deepen, then letting space for isopycnals doming above the anticyclone core. In this configuration current feedback above the anticyclonic negative vorticity produces an upward Ekman pumping, outcropping isopycnals as visible on section in Fig.5.5d, as argued by Ni et al. (2023). This isopycnal doming mechanism is to be compared with the index proposed by Schütte et al. (2016) and Assassi et al. (2016) using SST signature as an index to distinguish surface- and subsurface-intensified mesoscale anticyclones (the latter case being defined as a negative density anomaly below a positive one). They proposed cold-core anticyclone to occur above subsurface anticyclone because of isopycnal doming, as opposed to the eddy-modulated vertical mixing hypothesis (Moschos et al., 2022). Assassi's criterion however only applies in a stratified ocean without mixed layer (hence without atmospheric interaction). They also considered a static vision without investigating temporal variations. Our simulation results suggest that both vertical mixing modulation and Ekman pumping mechanisms are efficient in producing cold-cor anticyclones but at different time of the summer. Cold-core signature could appear first through enhanced-mixing inside anticyclones, an could be continued because of isopycnal doming. Ni et al. (2023) also showed the Ekman pumping mechanism to be likely efficient, but their study uses idealized but unrealistic constant heat and wind stress fluxes over several months in a linear stratification. Our findings of this section shows that Ekman pumping is indeed efficient but does not explain the timing of SST inverse signatures. More importantly, it suggests that the subsurface or mode-water anticyclone distinction criteria from Schütte et al. (2016) and Assassi et al. (2016) - positive SLA with negative SST - could be improved by not looking at the occurrence of the cold-core SST signature, but rather at its persistence in time, and also by implying mixed layer interaction. Other mechanisms were proposed to contribute to these eddy SST anomalies, in particular lateral advection which is discussed later in Sect.6.1.

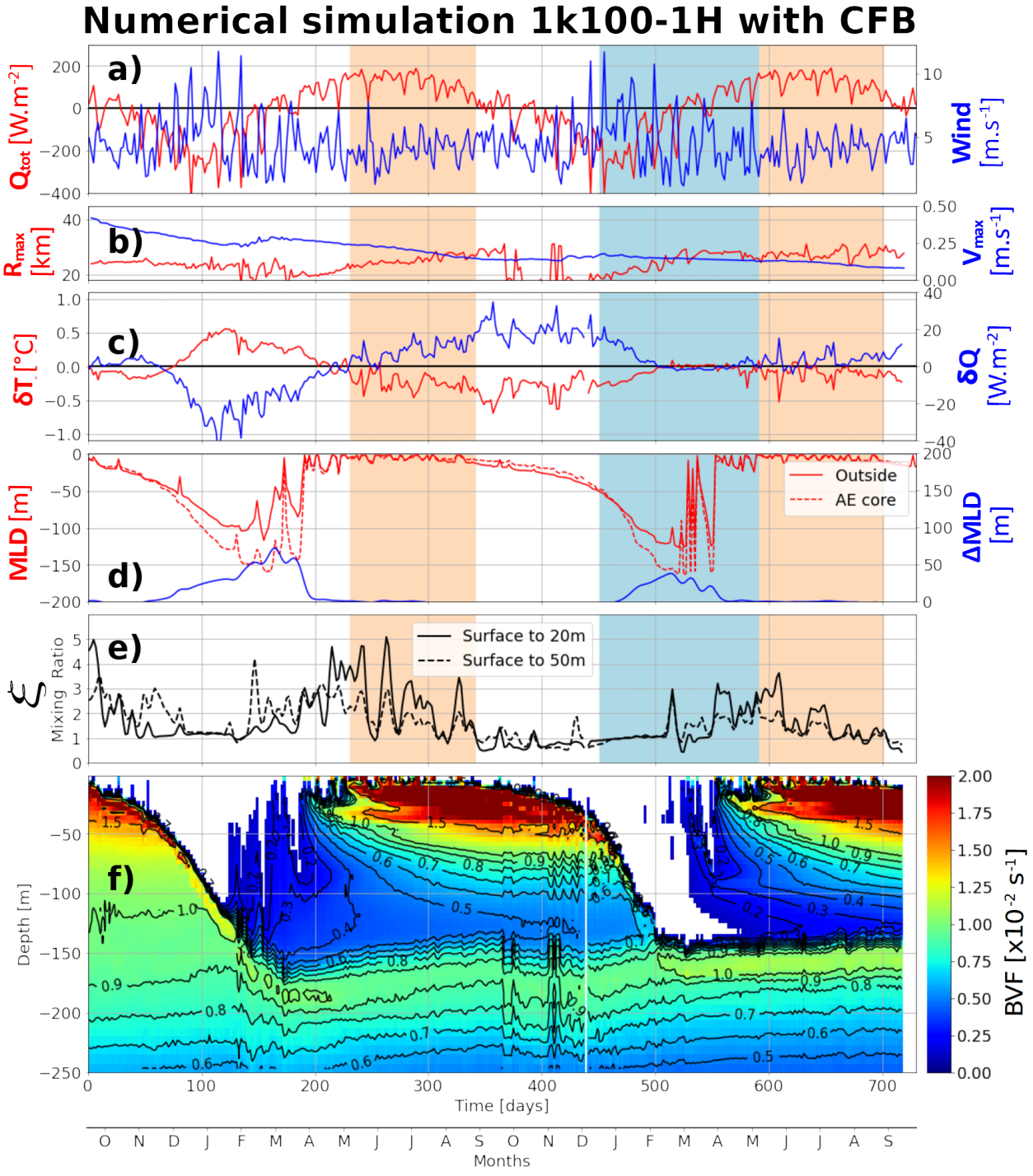

Figure 5.4: Same as run 1K100-1H in Barboni et al. (2023b) but with current feedback (CFB). (a) Heat flux (red) and wind speed (blue) time series. (b) R_{max} (red) and V_{max} (blue) time series. (c) SST δT anomaly (red) and heat flux δQ (blue) anomaly. (d) Inside-eddy MLD (dashed red), background MLD (continuous red) and MLD anomaly (blue) time series. 2-day smoothing is applied for MLD anomaly. (e) Differential mixing ratio ξ. (f) Inside-eddy Brunt-Vaisala frequency time series (scale factor 100). δT, δQ, ξ, summer and winter time periods (orange and blue shades) are defined as in Barboni et al. (2023b).

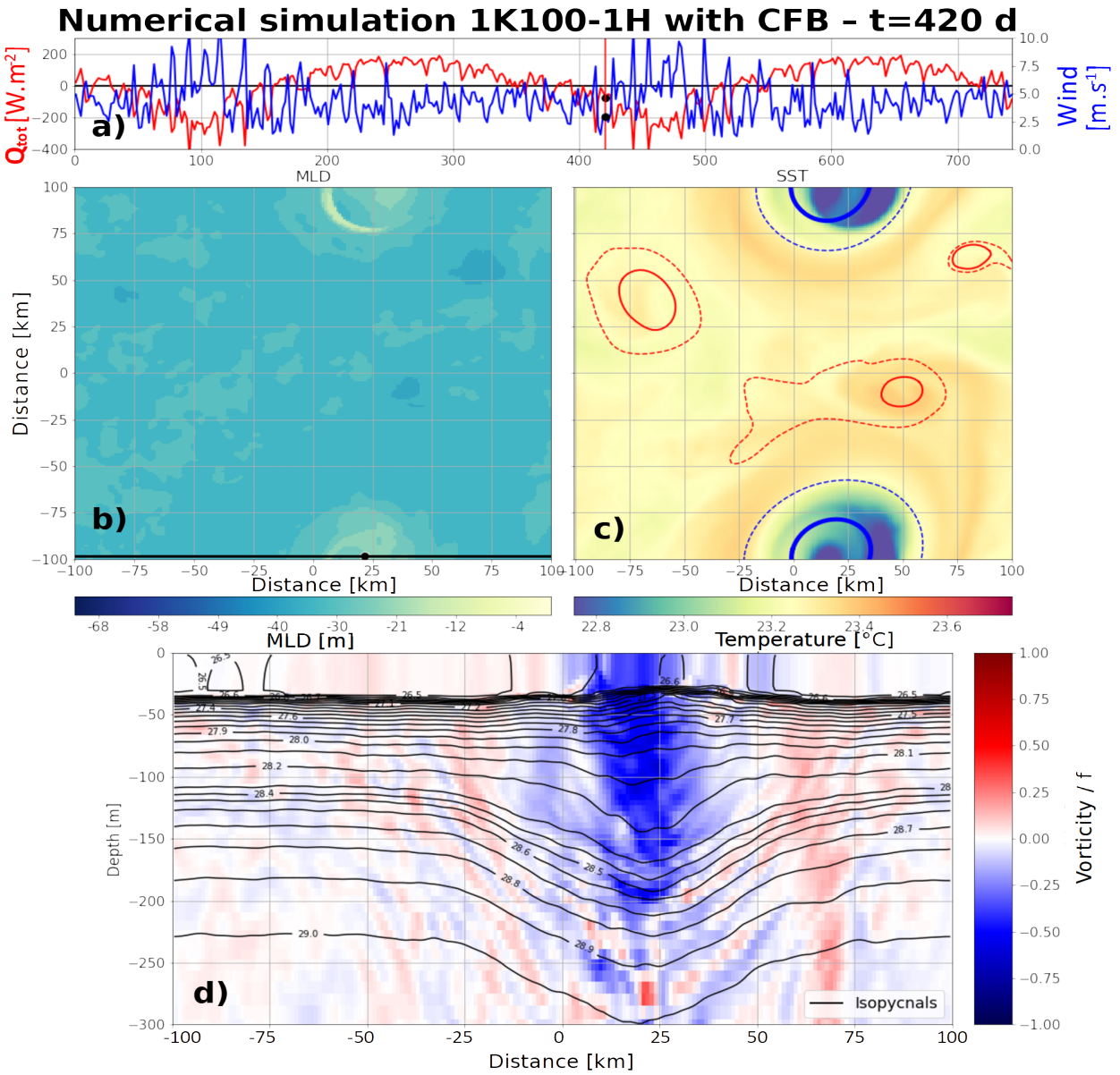

Figure 5.5: Same as run 1K100-1H in Barboni et al. (2023b) but with CFB, at $t = 420d$. (a) Heat flux (red) and wind speed (blue) time series, with a red line indicating time moment of the section. (b) MLD and (c) SST maps, with cyclones detections in red and anticyclones in blue (initial anticyclone with a thicker line). (d) Vorticity section normalized by f, with isopycnals in black lines. A black thick line in panel (b) indicates the section location.

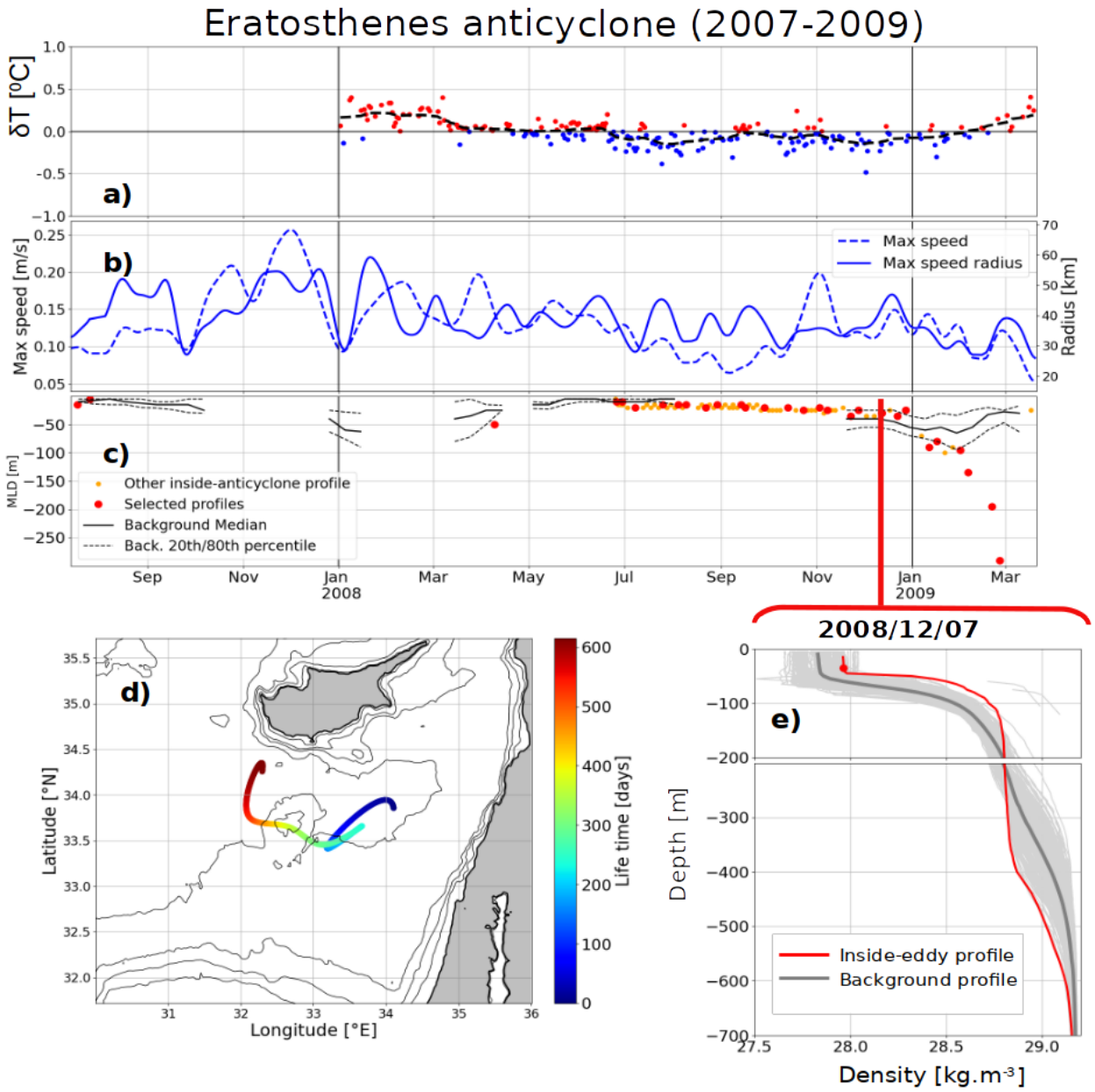

Figure 5.6: (a) δT index as in Moschos et al. (2022). (b) Maximal speed (dashed blue) and maximal speed radius (continuous blue). (c) MLD inside anticyclone (red dots) with background MLD (continuous black line) and spread (dashed black lines) as in Barboni et al. (2023a). (d) Map showing Eratosthenes anticyclone drift along its lifetime. (e) Density profiles in winter, inside-eddy is in red (its MLD is highlighted by a red dot), background profiles as thin gray lines and mean background in black line.

Chapter 6

Discussion

In addition to eddy-modulated vertical mixing (Moschos et al., 2022) and eddy-induced Ekman pumping (McGillicuddy, 2015; Ni et al., 2023), eddy lateral exchanges (in various forms) were also proposed to explain eddy inverse SST signatures (Yasuda et al., 2000; Sun et al., 2022). A fourth mechanism was proposed by He et al. (2020) in the case of strong freshwater flux creating a salt barrier layer, then possibly driving negative mixed layer anomalies in anticyclones and cold-core signatures. All theses processes are summarized in Fig.6.1. Eddy-modulated mixing and Ekman pumping were addressed in the above chapter, and we aim here to discuss the two remaining processes. Also note that influence of differential heat flux alone was also investigated through SST retroaction in the above chapter. Not yet introduced, the effect of interannual variability is also discussed. As our work focused mostly on anticyclone, some comments on cyclone evolution are presented in a last section.

6.1 Advective terms to explain inverse SST signatures

Horizontal watermasses exchanges were also proposed as a possible mechanism to explain eddy inverse SST signatures, in particular near boundary currents. Indeed watermasses with distinct density and temperature close to each other because of topography (straits, boundary currents) or upwelling can interact and change eddy properties. Lateral exchanges are suggested by the observational evidence of abundant inverse signatures close to ocean basin boundaries. Earlier study from Chaigneau et al. (2011) already measured composite anticyclonic eddy to be warm at depth but cold in surface for anticyclones detached from the Peru-Chile upwelling system. Ni et al. (2021) measured high occurrence in the Northwestern Pacific and in the Hudson Bay. Similar results were obtained in numerical simulations by (Sun et al., 2022) and in the South China Sea by (Sun et al., 2021) where most inverse signatures are concentrated near the Luzon Strait where warm Kuroshio intrusions are possible.

A first category of lateral exchanges is the vertical alignment theory. Some cold-core anticyclones were observed earlier in the Northwestern Pacific near the Bussol Strait, but these eddies were anticyclones directly formed from a cold and fresh low-vorticity water input from the Okhotsk Sea. These "Bussol" eddies are then a different type of cold-core anticyclones because their core is already cold in subsurface, with negative density anomaly driven by salinity (Yasuda et al., 2000; Rabinovich et al., 2002). They do not present this characteristic temperature anomaly inversion between a warmer core and a colder surface (as in the Ierapetra eddy in Fig.9 from Moschos et al. (2022)). Yasuda et al. (2000) also observed modification of a warm and salty anticyclone detached from the Kuroshio, drifted northwards at the Bussol Strait and influenced by cold and fresh Okhotsk waters in surface, but not leading to cold surface signature and warmer subsurface core. In their observed 1995 Bussol anticyclone, both watermasses seems to coexist at similar depth. Yasuda et al. (2000) interestingly also noticed a seasonality in cold-core "Bussol" anticyclones growth, but this is more likely due to a seasonal variation of the Okhotsk Sea cold and fresh outflow. Itoh and Yasuda (2010b) conducted more investigation and found that cold-core Bussol eddies could get vertically aligned with warm Kuroshio rings. Due to the density difference, the cold and fresh core tends to be deeper than the warm and saline one, leading to double core anticyclones formation as warmer in surface. No anticyclone formation as cold in surface with a warmer subsurface core was reported so far from this mechanism. But cold-core anticyclones detached from boundary currents are also observed in the Beaufort gyres and could experience

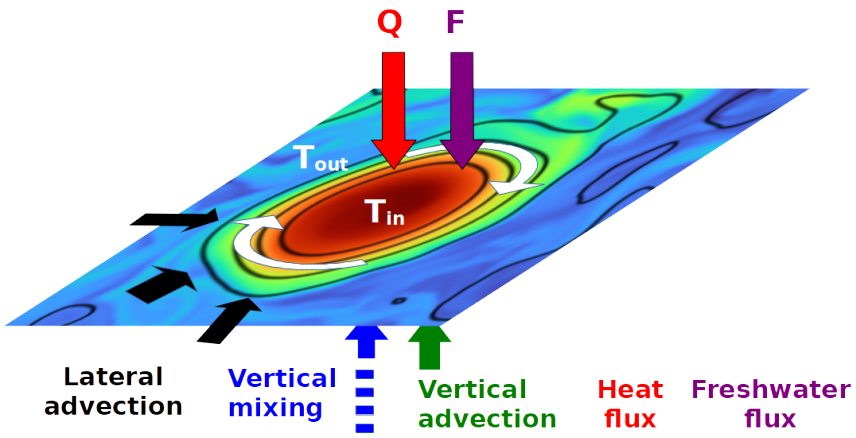

Differential processes driving T_{in}-T_{out}	Vertical alignment, Boundaries instabilities	Near-inertial waves trapping	Ekman pumping	SST retroaction on air-fluxes and salt barrier layer
Reference study	Yasuda et al. (2000), Itoh et Yasuda (2010), Sun et al. (2022)	Moschos et al. (2022)	McGillicuddy et al.(2015), Ni et al. (2023)	He et al. (2020)

Figure 6.1: Summary of various proposed mechanisms to explain eddy-induced inverse SST signatures.

similar interactions (Pickart et al., 2005). This mechanism could then partly explain the high occurrence of inverse eddy SST anomalies at high latitudes (Ni et al., 2021), where density is much more affected by salinity gradients.

A second lateral exchange mechanism is proposed by Sun et al. (2021) at the Luzon Strait. Warm filaments sheared from Kuroshio intrusions can wind over an already existing warm core anticyclone, but still cooler than tropical waters advected by the Kuroshio. Their study only used numerical simulations and deserve observational confirmation. But in many regions anticyclones coexist with a nearby warm current from which filaments can be expelled (e.g. anticyclones in the Levantine Basin shown in Fig.1.1c, reproduced from Hamad et al. (2006)). This mechanism is then more likely to happen at global scale than vertical alignment of cold-fresh and warm-saline cores.

Lateral advection terms in simulation were investigated in Ni et al. (2023) but in extremely idealized cases where eddies conserve their circular shape. This is not the case at all with realistic heat fluxes and wind stress generating strong submesoscale instabilities, as shown in our seasonal evolution study in Sect.5.1. The contour chosen to study eddy evolution in our numerical study is the AMEDA contour based on 48h average SSH map. Such method allows comparison with remote-sensing eddy observations, but does not allow to quantify lateral exchanges with varying eddy boundaries. As already discussed in the introduction, the non-linear hydrological definition we chose based on a SSH contour is not perfect when considering water transport issues (Beron-Vera et al., 2013). A better definition for eddy boundaries is then needed, and promising methods are coherent Lagrangian boundaries (Haller, 2005) or eddy boundaries based on Ertel potential vorticity contours (Hoskins, 1974), the latter being likely more easy to implement.

6.2 Interannual variability

The Mediterranean Sea has a marked seasonal cycle in both heat and freshwater fluxes, discussed in Sect.1.5 and presented on Fig.1.5. The interannual variability is however also significant, on atmospheric fluxes (Mariotti, 2010) but also physical properties (Ozer et al., 2017) with long-term warming and higher evaporation trends. We built our background method to minize bias due to interannual variability by selecting only closer

years ($\Delta year = \pm 1$) in our reference background, as discussed in Sect.2.5 (see Fig.2.10 for heat and salt anomalies, Fig.A1 in Barboni et al. (2023a) for MLD). This enabled us to focus on the drivers of the seasonal variability, but the difference from one year to another was not really addressed. We showed that maximal winter MLD in anticyclones greatly depends on its vertical profile, whether the current winter MLD connects and mixes the density anomaly at depth or not. As already discussed in Sect.5.2 in Barboni et al. (2023a), this MLD interannual variability is likely driven by winter heat loss variability. Heat fluxes time series in the Mediterranean Sea indeed showed that most of the interannual variability comes in winter, basin-wide and monthly averages reaching for some winters $Q_{tot} \approx -250\, W.m^{-2}$ and barely reaching $Q_{tot} \approx -150\, W.m^{-2}$ for other winters (Pettenuzzo et al., 2010). The proposed mechanism for a double-core anticyclone would be that a second winter is less cold than the first one, as schematically depicted in Fig.6.2a ($|Q_1| > |Q_2|$). If on the opposite the second winter is colder than the first one, the maximal winter mixed layer will only get deeper but no double-core anticyclone is formed (Fig.6.2b with $|Q_1| < |Q_2|$). Also note that in Fig.6.2, the first winter forms a mode-water core from an originally anticyclonic stratified density anomaly. But in practice, and as shown in our MLD study (Sect4), subsurface density anomaly are still homogenized even before the first winter (homogenized being defined as $|\partial_z T| < 2.5 \times 10^{-3} °C.m^{-1}$). Hence our concept of "connecting"/"non-connecting" winter can be applied even on the first winter of an eddy lifetime (e.g. IER1 event in Fig.10 from Barboni et al. (2023a)). Further development of our MLD evolution study could then look at the correlation with winter heat loss variability. Would the proposed mechanism in Fig.6.2 be confirmed, it could have important consequence on anticyclone vertical structure and biological productivity in a warming climate. Winters are indeed projected to be warmer in the Mediterranean Sea, even with limited anthropogenic CO_2 production (Giorgi and Lionello, 2008). As already discussed in Sect.5.2 in Barboni et al. (2023a), warmer winters could then lead to more often double-core anticyclone formation, then limiting the nutrient input for phytoplankton bloom at the eddy center.

Another question is the signature in SST of these mixed layer deepening events and whether they sign differently between "connecting" or "non-connecting" events. The mixed layer temperature signature was shown in Fig.9 in Barboni et al. (2023a), however this was for two "non-connecting" MLD events, and correlation with remote-sensing SST was not attempted. An interesting link to try is to test whether stratification removal by heat loss can be monitored from SST. Indeed it is buoyancy flux which drives isopycnals outcropping and hence SST variations, as sketched in Fig.6.2. This is not true in the general case outside-eddy because it neglects lateral fluxes from submesoscale instabilities. However continuous winter mixed layer deepening inside anticyclone is observed in Barboni et al. (2023a) and in high resolution numerical simulation the anticyclone core appeared to be shielded from submesoscale instabilities (Fig.7 in Barboni et al. (2023b)). Lateral exchanges could then be assumed as negligible compared to winter heat loss at the eddy core. This suggests new possibilities to unveil mesoscale eddy subsurface evolution tracking only SST variation at its center.

Interannual variability is also a limit of the numerical study in Sect.5.1, where the same heat and wind time series from September 2015 to September 2016 runs cyclically as input atmospheric forcing. Choosing 2014-2015 instead of 2015-2016 as forcing time series did not change the results, but this should be checked numerically in a more systematic way. It should also be noted that eddy MLD anomalies are not retrieved in our numerical simulations with the same magnitude as in observations. this might be caused to inaccurate background MLD due to unresolved mixed layer instabilities outside-eddy (see Sect.3.1 in Barboni et al. (2023b)).

SST signature Interannual variability is also a limit of the eddy-induced SST anomaly study in Sect.3, because at that time the Ultra-High resolution SST product was only available from 2016 to 2018. Now that it is available from 2008 onward, this limit could also be checked. in their global study with deep learning approach, Liu et al. (2021) very interestingly observed a significant decrease for both warm-core cyclones and cold-core anticyclones, with a linear trend for global fraction at $-0.26\%.y^{-1}$ (respectively $-0.27\%.y^{-1}$) from 1996 to 2015. In absolute number they observed both an increase of normal signatures and a decrease in inverse one, with no convincing mechanism. If this strong interannual trend is a climate change signal, then it is likely to be also recovered in the Mediterranean Sea where surface temperature is warming fast, in particular in the Levantine Basin (Pastor et al., 2020). A possible explanation would be that if SST is warmer while heat accumulates only at slower rate at depth, surface stratification is stronger. Stronger stratification reduces the efficiency of differential effects (vertical mixing modulation and Ekman pumping),

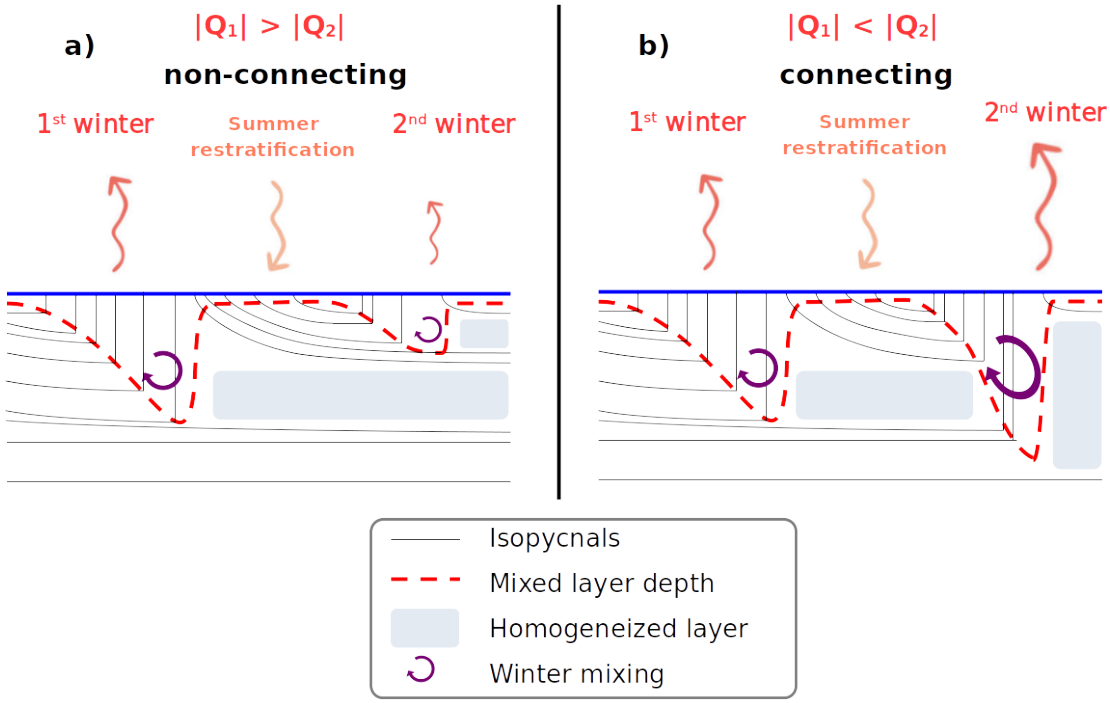

Figure 6.2: Proposed mechanism to explain different anticyclone MLD anomalies from interannual flux variability. (a) A second winter is less cold than the first, MLD then does not deepen as much and forms a second mode water core. A double-core anticyclone is formed with new summer restratification. (b) The second winter is colder than the first one, then the whole anticyclone core is mixed and no double-core anticyclone is formed.

then decreasing the appearance of inverse SST anomalies. Last, looking at inverse SST signatures interannual variability with wind could be a way to determine the main driving mechanism. Eddy vertical mixing modulation should indeed be more sensitive wind spectral content for NIW generation, whereas eddy Ekman pumping should be more sensitive to wind speed average.

6.3 Coupled atmospheric response

In all physical mechanisms listed so far and presented in Fig.6.1, we mostly consider the eddy response to an atmospheric forcing, assumed constant, except for thermal heat flux feedback (Barboni et al., 2023b) and possibly freshwater fluxes (He et al., 2020). We then took the opposite viewpoint from numerous studies investigating the atmospheric response to an heterogeneous ocean, for SST (O'Neill et al., 2005; Frenger et al., 2013) and wind stress (Chelton et al., 2004). Considering a full atmospheric retroaction entails different mechanisms, gathered here in two main part: the effect of surface currents on boundary layer stability - referred to as thermal current feedback - and surface waves current interactions with mesoscale eddies.

6.3.1 Thermal current feedback

An atmospheric retroaction not discussed in this study is the crossed effect of ocean currents on turbulent heat fluxes, and of SST on wind stress, from which observational evidences are numerous (Chelton et al., 2004; Frenger et al., 2013). In our set-up SST and velocity sensitivities of C_D (drag), C_S (sensible heat) and C_E (latent heat) exchange coefficients were assumed to be very weak compared to the linear thermal heat flux feedback (Eq.13-15 in Barboni et al. (2023b)) and wind stress. If eddy SST anomaly has a large impact on marine atmospheric boundary layer stability, one can expect this thermal current feedback to increase the total thermal heat flux feedback, and hence only further dampen eddy SST anomalies and reduce δT seasonal cycle. As discussed in Sect.3.3 from Barboni et al. (2023b), this is due to $\partial C_E/\partial_{T_s}$ being positive. The eddy-averaged thermal feedback being already on the order of what is found in ocean simulations coupled with atmosphere, this effect seems at second order. Thermal feedback on wind stress however could have more

influence. As detailed in Gaube et al. (2015), SST anomaly will drive a differential wind stress at the eddy scale, hence wind stress curl and Ekman pumping dipole. But this effect is also diagnosed by Gaube et al. (2015) as secondary. All these atmospheric processes could be further investigated with a new atmospheric boundary layer module developed for CROCO (Lemarié et al., 2021).

6.3.2 Eddy interactions with surface waves

At the ocean interface between atmosphere and ocean mixed layer, there are surface waves, greatly impacting air-sea fluxes through the surface roughness, taken into account via the Charnock parameter. In COARE parametrization, the wave height is assumed to response directly to the 10m wind speed (Fairall et al., 2003). Yet several recent observational works (Romero et al., 2017) and numerical simulations (Ardhuin et al., 2017) showed a significant modulation of wave height by ocean currents, thermal fronts and mesoscale eddy field. Ongoing research on numerical simulations coupling ocean currents, surface waves and atmospheric boundary layers are promising for a better representation of submesoscale processes in models. But the implications of these wave-eddy interaction for mesoscale evolution are yet unknown. In an idealized study comparable to our eddy-modulated vertical mixing (Sect.5.1), Marechal and de Marez (2021) investigated the impact of an individual cyclone on a surface wave field with three different frequencies. In addition to the already known wave rays refraction effect and wavelength modulation (Mapp et al., 1985), they showed that the eddy branch following (opposing) wave direction resulted in elongated (shortened) wave period and decreased (increased) wave height. All these processes contribute to decrease (enhance) surface slope, hence weaker (stronger) heat and momentum fluxes in the following (opposing) part of the eddy. The effect should then have a bipolar shape, acting as a corrective dampening of the monopolar heat flux feedback and Ekman pumping, in a similar way to the SST-induced Ekman pumping described by Gaube et al. (2015). But this theory should be further developed and numerically assessed in numerical simulations on mesoscale evolution timescales.

6.4 Salinity and freshwater fluxes

Freshwater fluxes were assumed in our study to be negligible compared to heat fluxes in the buoyancy forcing at the seasonal scale in the Mediterranean Sea (see Sect.1.5). This neglects in particular the role of river plumes, assumed to be also negligible following Mariotti et al. (2002). The role of salinity on the anticyclone density anomaly is however far from being null, as anticyclonic structure across the Mediterranean basin have negative buoyancy anomalies strengthened by fresher core in the Western Basin (Garreau et al., 2018; Budillon et al., 2009) but reduced by a saltier core in the Levantine Basin (Hayes et al., 2011), which was also measured by the BOUM cruise (Moutin and Prieur, 2012). When freshwater fluxes also starts to be non negligible on buoyancy, some studies showed that the average behavior in terms of MLD anomalies can be different than heat fluxes, as shown in the Bengal Bay by He et al. (2020), unveiling another complexity.

Salinity then needs to be added to have a more realistic buoyancy forcing. It also offers another hypothesis to explain the shift from "non-connecting" winter MLD to "connecting" ones, different from scheme in Fig.6.2. Despite similar heat loss in consecutive winter, the advection of fresher water at the anticyclone core could increase the stratification barrier for winter convection, resulting in a "non-connecting" mixed layer. This hypothesis could be considered as likely as our long-lived anticyclones see frequent mergings from smaller structures detached from the Libyo-Egyptian current near the coast (Barboni et al., 2021), with modified Atlantic waters slightly fresher (Millot and Taupier-Letage, 2005). This was investigated in various "non-connecting" events reported in Barboni et al. (2023a), however no strong stratification barrier due to salt was recorded. Even in the Tyrrhenian Sea, where salt accounts for a significant part of the anticyclone density anomaly, this was not observed. An example in Fig.6.3 shows the temperature, salt and density profiles at the mixed layer deepening maximum in the Central Tyrrhenian anticyclone included in our study (Barboni et al., 2023a) as event TYR2. The residual stratification barrier is indeed driven by warm ($+1.5°C$) rather than fresh ($+0PSU$) anomaly. The case of Algerian anticyclones was not investigated in our study, however an Algerian eddy with a fresher shallower core was surveyed by Garreau et al. (2018), revealing a marked density difference due to salinity. This salinity variability might be specific to Algerian eddies because they are fed by detachment of fresher Atlantic waters along the Algerian coast. It could explain why no larger anticyclonic MLD anomalies are observed in this region (see Fig.4.1b). Salinity fluxes variability impacting Mediterranean eddies is worth additional investigation. But salinity fluxes in the Mediterranean Sea are for an unknown part driven by lateral exchanges with filaments and eddies from the coastal current, mak-

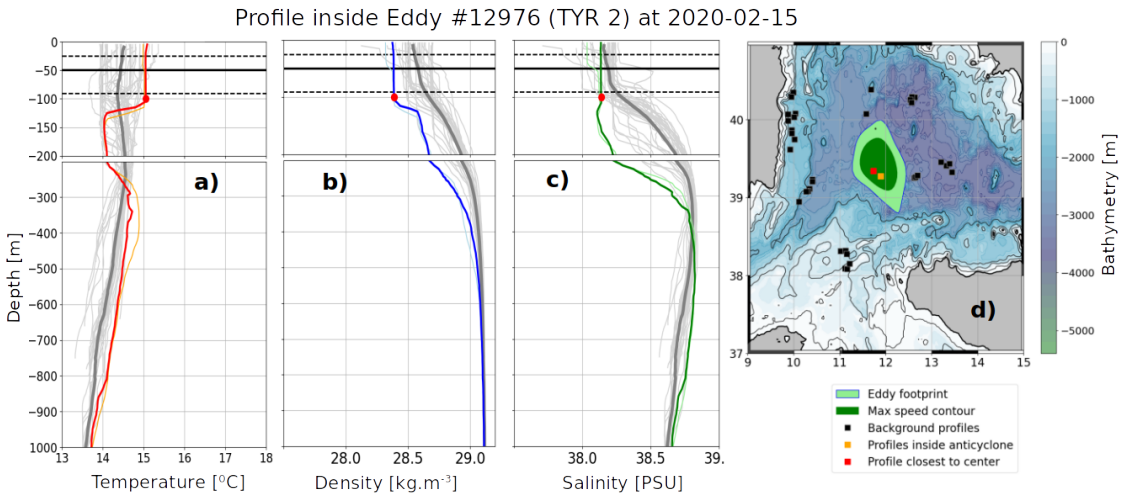

Figure 6.3: (a) Temperature, (b) density and (c) salt profiles collocated inside anticyclone in event TYR2 at the moment of maximal MLD anomaly (see Table 1 in Barboni et al. (2023a)). Colored line is the profile inside-eddy closest to eddy center, thin gray lines are profiles constituting the background and thick gray lines is the average background. Red dot is inside-eddy MLD, black continuous line is background MLD and spread in dashed black line. (d) Bathymetric map showing the eddy footprint, inside-eddy and background profiles.

ing it very difficult to constrain if one wants to remain in an idealized perspective as in Barboni et al. (2023b).

An insight into Arabian Sea eddies

Due to the small deformation radius in the Mediterranean Sea and the overall small salinity range compared to tropical seas, it is not possible to measure eddy Sea Surface Salinity (SSS) anomaly. Available remote-sensing SSS products are indeed at best at a 1/4°resolution resolution (Boutin et al., 2018). In the Arabian Sea, the deformation radius spans between roughly 200km at 5°N and 100km at 25°N. The Arabian Sea offers a very different range of processes compared to the Mediterranean Sea. β-drift is significant and faster near the Equator, about $4km.d^{-1}$, leading to an overall westwards drift of mesoscale eddies. Most eddies on the Omani coast are then at lot older than eddies on the eastern boundary. The monsoon regime, with strong Southwest winds in summer and Northeast winds in winter (Bruce, 1983), leads to a reversal of the mean surface circulation from anticyclonic in summer to cyclonic in winter (Shetye et al., 1994). Summer monsoon also gives strong Western boundary upwelling off the Somali coast (Schott and Quadfasel, 1982) and the seasonal formation the large anticyclonic Great Whirl (Vic et al., 2014). Strong low salinity input comes from the Bay of Bengal current, forming large anticyclonic eddy near the Lakshadweep islands drifting westwards (Ernst et al., 2022). Last, there is seasonally a strong atmospheric freshwater flux zonal gradient between the large precipitation over the Indian subcontinent and the dry Arabia. Eddy SST, SSS and MLD variability was so far only assessed by a composite approach (Trott et al., 2019). We then aim to investigate the variability of eddy SST and SSS anomalies in the Arabian context, from a Lagrangian viewpoint. This project is ongoing with a Physical Oceanography master student from University of Western Brittany, Florian Barge. Some analyses are shown here as examples of different eddy behavior with different physical processes as the Mediterranean Sea.

We were able to compute eddy-induced SST and SSS anomalies in the Arabian Sea from 2010 to 2015. Thanks to a project with CLS, an AVISO product at 1/8°resolution was produced from 2000 to 2015, together with an equivalent version of the DYNED Atlas with AMEDA eddy detections. This dataset was already used to investigate the vertical structure of eddies in the Arabian Sea (de Marez et al., 2019). Applying the δT method from Moschos et al. (2022), we computed an SST anomaly index using the daily ODYSSEA SST with 0.1°resolution (Piolle et al., 2010). An SSS anomaly index is computed using SMOS L3 SSS version 5 gridded at 1/4 °with 4-days output Gaussian smoothed over 9 days (Boutin et al., 2018). Effective spatial resolution is about 45km and standard error when compared to ship data is 0.2 PSU. A threshold for eddy observations of 4cm was applied on eddy sea level elevation (SSH maxima between the eddy center and the outermost closed SSH contour) to discard weak detections with unreliable SSH contours. 4cm is up to three

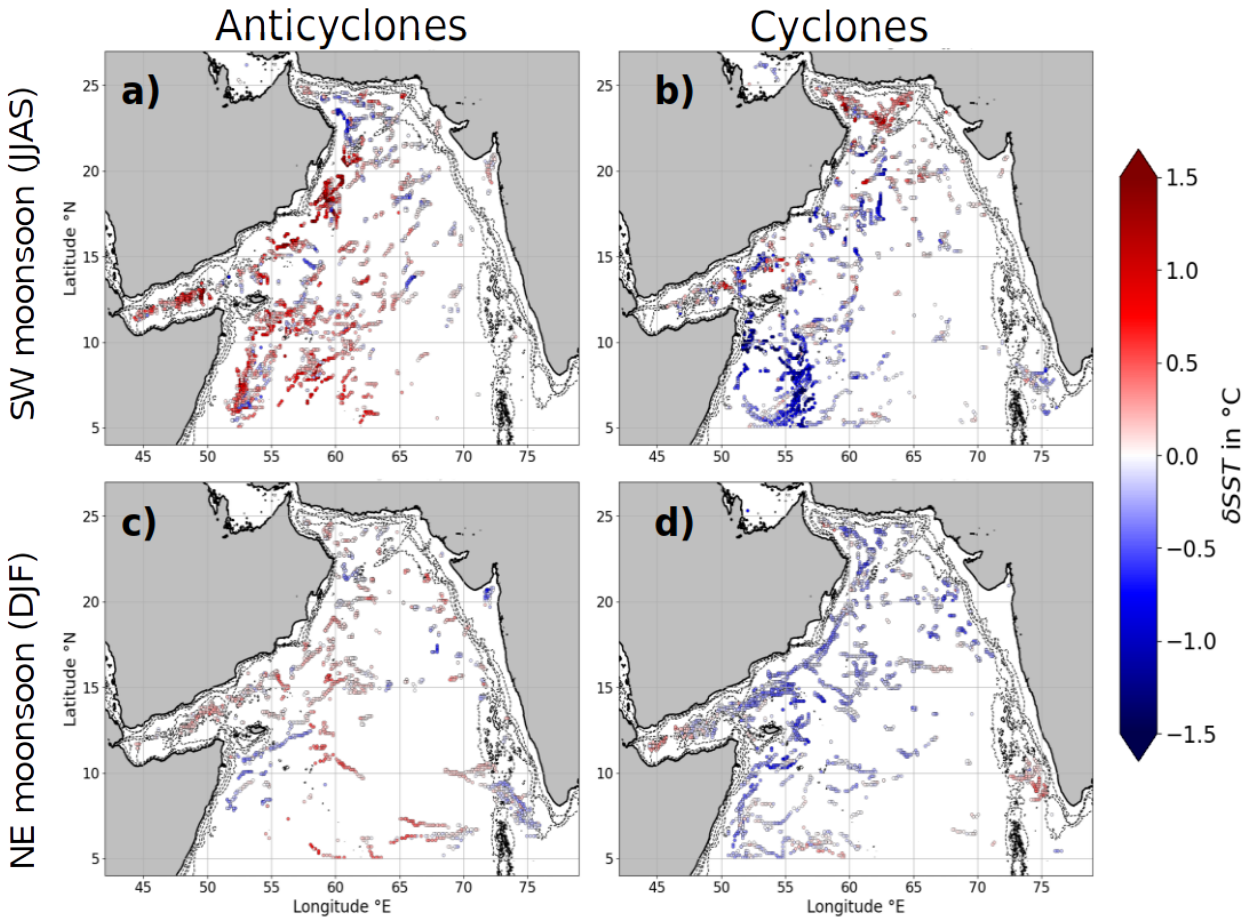

Figure 6.4: Eddy SST anomaly in the Arabian Sea from ODYSSEA SST. (a) Anticyclones and (b) cyclones in the Southwestern monsoon (January to September). (c) Anticyclones and (d) cyclones in the Northeastern monsoon (December to February). Figures are from Florian Barge.

times the usual SSH mapping error (Pujol et al., 2016). This dataset ensures SSS and SST coverage from October 2010 to December 2015, but could be even improved with more recent SSS data (SMOS L3 version 7) or OSTIA SST at 0.05°resolution (Donlon et al., 2012).

The variability of SST and SSS anomalies is shown here in Fig.6.4 and 6.5 respectively. For δT, the most important feature is the strong zonal gradient between weak signatures on the eastern side and marked ones on the western side. The eddy heterogeneous repartition can also be noted, many eddy detections in the Central Arabian Sea being removed due to our 4cm threshold. Very warm anticyclones $\delta T > 1°C$ and very cold cyclones $\delta T < -1°C$ are found in summer only along the Omani coast, with no inverse signatures, except further North than 21°N. During the winter monsoon, anticyclones are overall also warm and cyclones cold but with weaker signatures $|\delta T| < 1°C$. But few cold-core anticyclones near the Somali coast are observed and both warm-core cyclones and cold-core anticyclones near the Lakshadweep archipelago. For δSSS, the picture is very different with fresher anticyclones and saltier cyclones in the Southwestern part of the Arabian sea, in particular during the summer monsoon. The SSS anomaly is however extremely strong near the Indian coast during the winter monsoon with $|\delta SSS| > 1PSU$. Eddy SSS anomaly are more variable in the Northern Arabian Sea. Simply with statistics, this shows us that eddy seasonal surface anomalies are driven by different water properties.

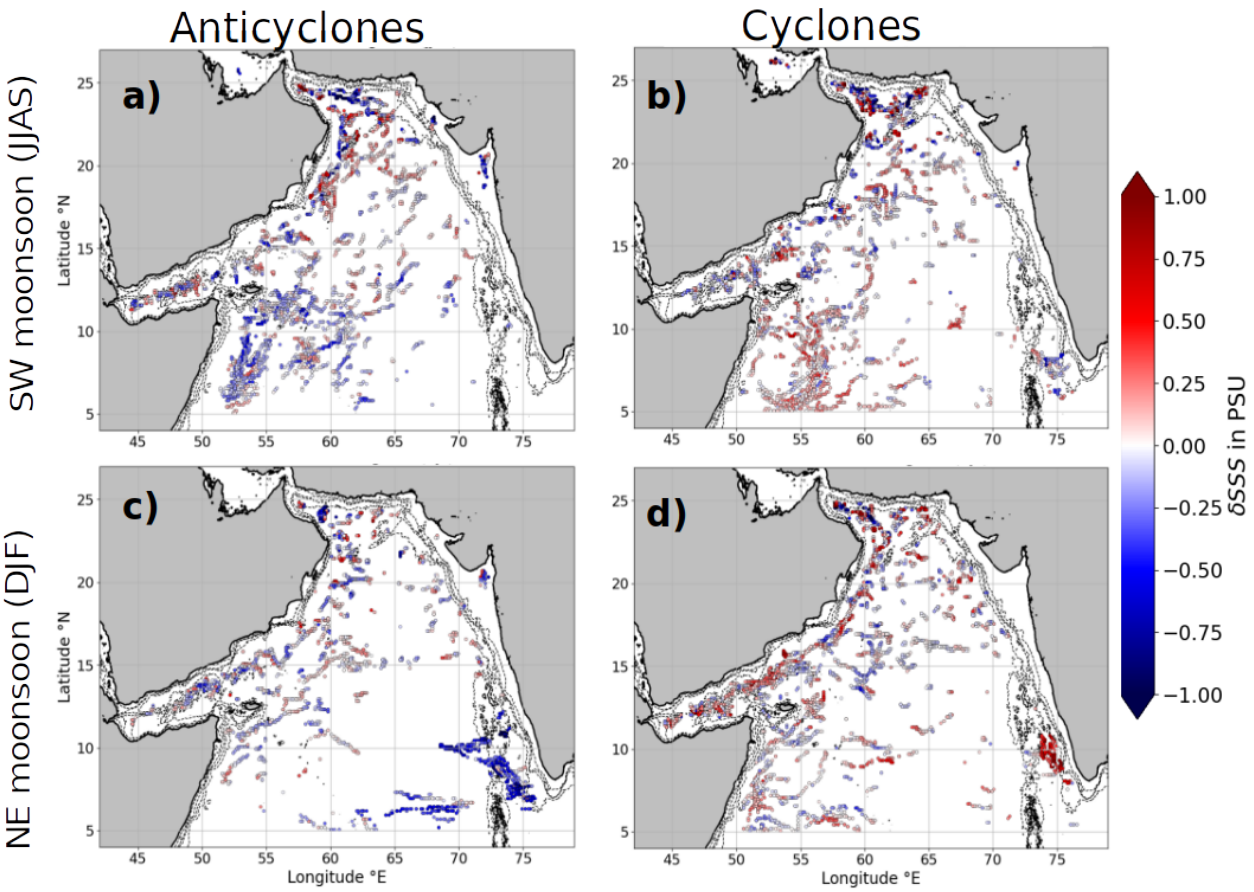

Figure 6.5: Same as Fig.6.4 but for SMOS SSS. Figures are from Florian Barge.

6.5 About cyclones

6.5.1 Cyclonic SST anomaly

Eddy SST evolution with a realistic atmospheric forcing was focused in our study (Sect.5.1) on an anticyclonic case. However in remote-sensing SST, cyclones have very similar trend of predominant warm-core signatures from May to July (Fig.6 in Moschos et al. (2022)). Despite local slight variations, no cyclone-anticyclone asymmetry was detected in global studies (Sun et al., 2019; Ni et al., 2021). The same numerical set-up could be used to determine if inverse SST signature also appear for cyclones in high-resolution numerical simulation.

Considering NIIW waves propagation, the linear theory from Kunze (1985) predict waves being expelled from cyclones. But it is however not straightforward that this eddy-waves interaction would result linearly in a decreased mixing as proposed by Moschos et al. (2022). Observational (D'Asaro, 1995; Fernández-Castro et al., 2020) and numerical studies (Asselin and Young, 2020) mostly focused on NIIW concentration in anticyclones. Then even if the mixing parametrization computes a decreased mixing in cyclone as a consequence of higher effective Coriolis frequency, comparison with observation will remain an issue.

The main alternative mechanism to explain eddy SST inverse signatures is Ekman pumping, and is symmetric between cyclone and anticyclones in theory (McGillicuddy, 2015; Gaube et al., 2015). Interaction between a subsurface cyclone should result in an isopycnal thinning at depth and then surface isopycnals deflected downwards with downwelling (McGillicuddy, 2015; Ni et al., 2023). However isopycnals outcropping with Ekman pumping in anticyclones automatically brings colder waters upwards. But in cyclones the isopycnals deflection could be less efficient because it requires surface heat flux to warm up waters. Ni et al. (2023) recovered a slight cyclone-anticyclone asymmetry in SST anomalies with anticyclonic anomaly stronger than cyclonic one despite identical heat flux and symmetric velocity field. The isopycnal thinning in the cyclone core might also have a different dynamical impact than on an anticyclone.

Interestingly, if no asymmetry is observed with remote-sensing, several studies which used vertical profiles to collocate eddy SST with subsurface signatures noticed that anticyclones can be very often subsurface-intensified but with cold SST signatures. Chaigneau et al. (2011) observed this for the mean anticyclone signature, Schütte et al. (2016) observed this as a separate mode-waters anticyclone eddy category. But geometrically, no equivalent of mode water cyclone can be defined, strong heat loss with isopycnals outcropping in cyclones ending in deep convection (Legg and Marshall, 1998). Submesoscale coherent vortices however can be observed (de Marez et al., 2020), but their are not formed from atmospheric interactions. This lack of mode water eddy cyclonic counterpart suggests that if Ekman pumping is an efficient mechanism, this does not apply for cyclones.

Last, another clear source of cyclone-anticyclone asymmetrical evolution is that cyclones tend to be smaller, typically smaller than the deformation radius to be stable (Arai and Yamagata, 1994; Stegner et al., 2021). This translates in much shorter lifetimes, few cyclones living longer than a year in the Mediterranean Sea (see Fig.2.4), but this is likely also biased by less reliable cyclonic detections and hence structures being more difficult to track. But a strong consequence for our topic is that in smaller structures, ratio of lateral compared to vertical exchanges is more important. Lateral advective terms at the eddy boundary can then be less negligible for cyclones than for anticyclone. This hypothesis is strengthened by the tendency for cyclones to be more sensible to external shear (Graves et al., 2006).

As detailed above, a paradox of eddy inverse SST signatures is then that despite being symmetrically observed between cyclones and anticyclones, no explanatory mechanism is asserted to be symmetric. Investigating cyclones SST signatures is then an interesting way to unveil the determining driving processes for inverse SST anomalies.

6.5.2 Winter mixed layer anomaly in cyclones

Barboni et al. (2023a) focused on long-lived anticyclone MLD, but a similar analysis is still lacking for cyclones evolution, and several questions remain. First of all, is the MLD indeed shallower inside long-lived cyclones than outside-eddy? This issue was addressed so far only through composites by Sun et al. (2017) and Gaube et al. (2019) (see also point-wise map in Fig.4.1). And secondly, does a similar MLD stratification

delay or advance occurs in mesoscale cyclones? As explained in Sect.1.5, cyclones are often smaller than the effective resolution of altimetry product and consequently cyclone observations are less reliable (Stegner et al., 2021). The availability of long time series of Argo floats trapped inside cyclones enabling comparison to Fig.4 or 5 in Sect.4 is then not possible.

If no subsurface time series are available, Fig.4.1a previously presented offers a first point-wise vision of cyclone MLD anomalies. MLD anomalies computed as difference from the outside-eddy background are simply shown as colored dots were the profile was cast. Only profiles identified inside the maximal speed radius of a cyclone at $\pm$ 2 days (as in section 2.3) are shown, only from January to March.This method allows to show MLD anomalies without composites but also without temporal variability. Despite more noise for cyclones, shallower MLD is the dominant signal. Some discrepancies occur in larger cyclonic Ligurian, Adriatic and Rhodes gyres with extremely deep MLD anomalies. This signal is very likely due to deep or intermediate winter convection in these regions due to stratification preconditioning because of the cyclonic circulation. The difference between a gyre (larger than R_d, bounded by topography) and a mesoscale eddy (scaling with R_d) needs to be taken into account to improve this analysis, but cyclonic eddies seems to have indeed shallower MLD on the order of several dozens of meters. As expected cyclonic MLD anomalies are not as large upwards as anticyclonic ones downwards because MLD can not be shallower than the sea surface, and we recover here another aspect of cyclone-anticyclone asymmetry. Numerical simulations will be of great help to test MLD and eddy-induced SST signatures in cyclones.

Chapter 7

Conclusions and perspectives

In this study, we investigated mesoscale eddy surface and subsurface evolution. We adopted a non-linear hydrological definition: an eddy is defined as a density anomaly in thermal wind balance at scale close to or larger than the baroclinic deformation radius, and slowly drifting compared to Rossby wave phase speed. This definition ensures a compromise between hydrological and geometrical realities of an eddy. It can be easily adapted to altimetry remote-sensing to detect and track eddies in time through the AMEDA algorithm, following eddies in a Lagrangian approach. Eddy tracks in the Mediterranean Sea using 1/8 °AVISO altimetry are gathered in the DYNED Atlas. A collocation method between in situ measurements and SSH-based eddy contours was developed to accurately classify inside- and outside-eddy data. A reference outside-eddy background allows to accurately measure the eddy-induced anomalies.

Application of Lagrangian tracking collocated with sea surface temperature data revealed a marked seasonal signal in eddy surface signatures. Anticyclones are predominantly warm in surface in winter, but shift to predominantly cold in early summer with mixed layer restratification. Conversely cyclones are generally cold in winter but warm in summer. This could be observed through SST signatures statistics but also tracking individual structure. Collocated Argo profile inside-eddy also revealed these "inverse" SST signature to occur only in near-surface, in the upper 50m. Anticyclone cores then remain warmer at depth, and it is only the upper temperature gradient of summer restratification which is less pronounced. From these observations, a driving mechanism in proposed based on eddy-modulated vertical mixing, anticyclones (cyclone) being assumed to enhance (decrease) mixing in near-surface due to near-inertial waves modulation by the geostrophic eddy field. This mechanism was numerically proven in an idealized anticyclone submitted to realistic atmospheric forcing. Summer cold-core signature is recovered in similar way for two years, together with an mixing enhanced by a factor 3 in the upper layers of an anticyclone. Removing high frequency content from forcing input confirmed the importance of high frequency forcing. Differential mixing vanishes when the inertial frequency is not triggered anymore. Sensitivity to grid cell resolution also showed that the differential mixing and eddy SST signature variations are greatly diminished when resolution is coarser than and 3m in the vertical. Thermal heat flux feedback driven by eddy SST anomaly appears on the opposite to dampen the eddy SST variations. Among other driving mechanisms proposed in the literature, eddy-induced Ekman pumping also appears to control SST variations. It creates an isopycnals doming responsible for summer cold-core SST anomaly lasting until early winter above a subsurface anticyclone. The eddy vertical mixing modulation and Ekman pumping both seem to match qualitatively observations. Further investigation should then focus on examining quantitative agreement of observed inverse SST anomalies, eddy vertical structures and atmospheric forcing. In particular future work could be dedicated to SST anomalies sensibility to eddy strength, size and cyclone-anticyclone asymmetry. Both phenomenon are interesting in suggesting a way to deduce information on eddy vertical structures from its SST signature temporal remanence.

Below the surface, vertical evolution of collocated profiles inside long-lived Mediterranean anticyclones revealed a different mixed layer evolution compared to outside-eddy background. Winter mixed layer deepening is prolonged by one to two months, letting time for warm surface temperature in the anticyclone to cool down. Fluxes differences between the eddy and the exterior seem at stake and would need further investigation. Winter mixed layer in anticyclones can connect or not with a preexisting subsurface anomaly. In the first case, this leads to extreme MLD down to 350m; in the latter case, a double-core anticyclone is formed during spring restratification. Such mechanisms show the possibility of complex interaction between air-sea fluxes and subsurface density anomaly, and also suggest a pathway for mode waters inside anticyclone in the

formation of multi-layer eddies. This mechanism is interesting in suggesting a more frequent way to form double-core anticyclone than the vertical alignment process often spotlighted in the literature. What drives the shift from a "connecting" winter to a "non-connecting" one would need further investigation. Their different consequences on the anticyclone fate, energy budget, and in a later step its biogeochemistry influence are also at stake. The segmentation between these two different MLD evolution patterns is however thought to be linked with winter heat loss variability. Variability of salinity fluxes, more difficult to estimate, could also be a differential mechanism to increase and reduce buoyancy loss, and deserves additional investigation. The relationship between differential mixed layer deepening with SST variations remains to be clarify, but it provides a promising clue for anticyclone vertical structure estimation with remote-sensing. MLD anomalies and restratification delay are not recovered yet in simulation, but our numerical results show an important role of submesoscale. Mixed layer anomalies could trigger an earlier restratification outside-eddy, letting mixed deepen further inside anticyclones. This interesting mechanism also suggests a sensitivity to horizontal grid resolution.

These results show that far from being only unperturbed structures modulating heat fluxes and wind stress, eddies also response to this atmospheric forcing on longer seasonal timescale. There is then a significant impact of air-sea heat and momentum fluxes on mesoscale eddies, in both surface signature and at depth on their density anomalies. Fluxes modulation by eddies involve various physical processes investigated in this study, among which thermal heat flux feedback, mixed layer restratification, vertical mixing, near-inertial waves focalisation and Ekman pumping. Other mechanisms were proposed deserve further investigation, such as lateral exchanges, then likely requiring an eddy definition more accurate for water transport. Salinity fluxes was not discussed in our study and could be an important mechanism in modulating the seasonal density variations. It appears that eddy surface signature evolution strongly couples air-sea fluxes with the eddy density anomaly through the mixed layer, in both summer and winter. This suggests several path for research to retrieve information on the ocean interior using remote-sensing measurements. Recent research efforts in coupled simulations with surface waves and atmospheric boundary layers are also promising to describe more accurately eddy retroactions with atmosphere. An interesting outcome of these various interactions is that mesoscale eddies not only integrate atmospheric fluxes variations - typically seasons - but also act on forcing derivatives - typically after a wind blow - with near-inertial waves trapping. The implication for more accurate eddy resolution in numerical simulations entails to consider eddies as evolving entities instead of Eulerian statistics, but also to resolve a very wide range of spatial and temporal scales, from near-inertial periods to seasons.

Bibliography

Amitai, Y., Lehahn, Y., Lazar, A., and Heifetz, E.: Surface circulation of the eastern Mediterranean Levantine basin: Insights from analyzing 14 years of satellite altimetry data, Journal of Geophysical Research: Oceans, 115, 2010.

Amores, A., Jordà, G., Arsouze, T., and Le Sommer, J.: Up to what extent can we characterize ocean eddies using present-day gridded altimetric products?, Journal of Geophysical Research: Oceans, 123, 7220–7236, 2018.

Arai, M. and Yamagata, T.: Asymmetric evolution of eddies in rotating shallow water, Chaos: An Interdisciplinary Journal of Nonlinear Science, 4, 163–175, 1994.

Ardhuin, F., Gille, S. T., Menemenlis, D., Rocha, C. B., Rascle, N., Chapron, B., Gula, J., and Molemaker, J.: Small-scale open ocean currents have large effects on wind wave heights, Journal of Geophysical Research: Oceans, 122, 4500–4517, 2017.

Argo Steering Team: On the design and Implementation of Argo-an initial plan for the global array of profiling floats. International CLIVAR Project Office Report, 21, 32, GODAE Report, 5, 32, 1998.

Aroucha, L. C., Veleda, D., Lopes, F. S., Tyaquiçã, P., Lefèvre, N., and Araujo, M.: Intra- and Inter-Annual Variability of North Brazil Current Rings Using Angular Momentum Eddy Detection and Tracking Algorithm: Observations From 1993 to 2016, Journal of Geophysical Research: Oceans, 125, e2019JC015 921, https://doi.org/10.1029/2019JC015921, 2020.

Artale, V., Astraldi, M., Buffoni, G., and Gasparini, G.: Seasonal variability of gyre-scale circulation in the northern Tyrrhenian Sea, Journal of Geophysical Research: Oceans, 99, 14 127–14 137, 1994.

Assassi, C., Morel, Y., Vandermeirsch, F., Chaigneau, A., Pegliasco, C., Morrow, R., Colas, F., Fleury, S., Carton, X., Klein, P., et al.: An index to distinguish surface-and subsurface-intensified vortices from surface observations, Journal of Physical Oceanography, 46, 2529–2552, 2016.

Asselin, O. and Young, W. R.: Penetration of wind-generated near-inertial waves into a turbulent ocean, Journal of Physical Oceanography, 50, 1699–1716, 2020.

Ayoub, N., Le Traon, P.-Y., and De Mey, P.: A description of the Mediterranean surface variable circulation from combined ERS-1 and TOPEX/POSEIDON altimetric data, Journal of Marine Systems, 18, 3–40, 1998.

Ayouche, A., De Marez, C., Morvan, M., L'hegaret, P., Carton, X., Le Vu, B., and Stegner, A.: Structure and dynamics of the Ras al Hadd oceanic dipole in the Arabian Sea, in: Oceans, vol. 2, pp. 105–125, MDPI, 2021.

Barboni, A., Lazar, A., Stegner, A., and Moschos, E.: Lagrangian eddy tracking reveals the Eratosthenes anticyclonic attractor in the eastern Levantine Basin, Ocean Science, 17, 1231–1250, 2021.

Barboni, A., Coadou-Chaventon, S., Stegner, A., Le Vu, B., and Dumas, F.: How subsurface and double-core anticyclones intensify the winter mixed-layer deepening in the Mediterranean Sea, Ocean Science, 19, 229–250, 2023a.

Barboni, A., Stegner, A., Dumas, F., and Carton, X.: How high frequency atmospheric forcing impacts mesoscale eddy surface signature and vertical structure, submitted to Journal of Advanced Modeling Earth Systems, 2023b.

Barboni, A., Stegner, A., Le Vu, B., and Dumas, F.: [Dataset] 2000-2021 In situ profiles colocalized with AMEDA eddy detections from 1/8 AVISO altimetry in the Mediterranean sea, 2023c.

Barton, E. D., Basterretxea, G., Flament, P., Mitchelson-Jacob, E. G., Jones, B., Arîstegui, J., and Herrera, F.: Lee region of gran canaria, Journal of Geophysical Research: Oceans, 105, 17 173–17 193, 2000.

Beron-Vera, F. J., Wang, Y., Olascoaga, M. J., Goni, G. J., and Haller, G.: Objective detection of oceanic eddies and the Agulhas leakage, Journal of Physical Oceanography, 43, 1426–1438, 2013.

Bosse, A., Fer, I., Lilly, J. M., and Søiland, H.: Dynamical controls on the longevity of a non-linear vortex: The case of the Lofoten Basin Eddy, Scientific reports, 9, 1–13, 2019.

Boutin, J., Vergely, J.-L., Marchand, S., d'Amico, F., Hasson, A., Kolodziejczyk, N., Reul, N., Reverdin, G., and Vialard, J.: New SMOS Sea Surface Salinity with reduced systematic errors and improved variability, Remote Sensing of Environment, 214, 115–134, 2018.

Braby, L., Backeberg, B., Krug, M., and Reason, C.: Quantifying the impact of wind-current feedback on mesoscale variability in forced simulation experiments of the Agulhas Current using an eddy-tracking algorithm, Journal of Geophysical Research: Oceans, 125, e2019JC015 365, 2020.

Brekhovskikh, L., Fedorov, K., Fomin, L., Koshlyakov, M., and Yampolsky, A.: Large-scale multi-buoy experiment in the tropical Atlantic, in: Deep Sea Research and Oceanographic Abstracts, vol. 18, pp. 1189–1206, Elsevier, 1971.

Brenner, S.: Long-term evolution and dynamics of a persistent warm core eddy in the Eastern Mediterranean Sea, Deep Sea Research Part II: Topical Studies in Oceanography, 40, 1193–1206, 1993.

Bruce, J.: The wind field in the western Indian Ocean and the related ocean circulation, Monthly weather review, 111, 1442–1452, 1983.

Budillon, G., Gasparini, G., and Schroeder, K.: Persistence of an eddy signature in the central Tyrrhenian basin, Deep Sea Research Part II: Topical Studies in Oceanography, 56, 713–724, 2009.

Caldeira, R. and Marchesiello, P.: Ocean response to wind sheltering in the Southern California Bight, Geophysical Research Letters, 29, 13–1, 2002.

Caldeira, R. M., Stegner, A., Couvelard, X., Araújo, I. B., Testor, P., and Lorenzo, A.: Evolution of an oceanic anticyclone in the lee of Madeira Island: In situ and remote sensing survey, Journal of Geophysical Research: Oceans, 119, 1195–1216, 2014.

Carton, X., Flierl, G., and Polvani, L.: The generation of tripoles from unstable axisymmetric isolated vortex structures, EPL (Europhysics Letters), 9, 339, 1989.

Castelão, G. and Johns, W.: Sea surface structure of North Brazil Current rings derived from shipboard and moored acoustic Doppler current profiler observations, Journal of Geophysical Research: Oceans, 116, 2011.

Castelao, R. M.: Mesoscale eddies in the South Atlantic Bight and the Gulf Stream recirculation region: vertical structure, Journal of Geophysical Research: Oceans, 119, 2048–2065, 2014.

Chaigneau, A. and Pizarro, O.: Eddy characteristics in the eastern South Pacific, Journal of Geophysical Research: Oceans, 110, 2005.

Chaigneau, A., Gizolme, A., and Grados, C.: Mesoscale eddies off Peru in altimeter records: Identification algorithms and eddy spatio-temporal patterns, Progress in Oceanography, 79, 106–119, 2008.

Chaigneau, A., Eldin, G., and Dewitte, B.: Eddy activity in the four major upwelling systems from satellite altimetry (1992–2007), Progress in Oceanography, 83, 117–123, 2009.

Chaigneau, A., Le Texier, M., Eldin, G., Grados, C., and Pizarro, O.: Vertical structure of mesoscale eddies in the eastern South Pacific Ocean: A composite analysis from altimetry and Argo profiling floats, Journal of Geophysical Research: Oceans, 116, 2011.

Chelton, D. B., DeSzoeke, R. A., Schlax, M. G., El Naggar, K., and Siwertz, N.: Geographical variability of the first baroclinic Rossby radius of deformation, Journal of Physical Oceanography, 28, 433–460, 1998.

Chelton, D. B., Schlax, M. G., Freilich, M. H., and Milliff, R. F.: Satellite measurements reveal persistent small-scale features in ocean winds, science, 303, 978–983, 2004.

Chelton, D. B., Schlax, M. G., Samelson, R. M., and de Szoeke, R. A.: Global observations of large oceanic eddies, Geophysical Research Letters, 34, 2007.

Chelton, D. B., Gaube, P., Schlax, M. G., Early, J. J., and Samelson, R. M.: The influence of nonlinear mesoscale eddies on near-surface oceanic chlorophyll, Science, 334, 328–332, 2011a.

Chelton, D. B., Schlax, M. G., and Samelson, R. M.: Global observations of nonlinear mesoscale eddies, Progress in oceanography, 91, 167–216, 2011b.

Church, P. E.: Surface temperatures of the Gulf Stream and its bordering waters, Geographical Review, 22, 286–293, 1932.

Ciuffardi, T., Napolitano, E., Iacono, R., Reseghetti, F., Raiteri, G., and Bordone, A.: Analysis of surface circulation structures along a frequently repeated XBT transect crossing the Ligurian and Tyrrhenian Seas, Ocean Dynamics, 66, 767–783, 2016.

Copernicus: [Dataset] Copernicus Marine In Situ Tac Data Management Team : Global Ocean- In-Situ Near-Real-Time Observations, https://doi.org/10.48670/moi-00036, 2021.

Coppola, L., Raimbault, P., Mortier, L., and Testor, P.: Monitoring the environment in the northwestern Mediterranean Sea, Eos, Transactions American Geophysical Union, 100, 2019.

Courtier, P., Freydier, C., Geleyn, J., Rabier, F., and Rochas, M.: The ARPEGE project at METEO-FRANCE, Proc ECMWF Workshop, 9-13 Sept 1991. Numerical methods in atmospheric modelling, 2, 193–231, 1991.

Cushman-Roisin, B., Tang, B., and Chassignet, E. P.: Westward motion of mesoscale eddies, Journal of Physical Oceanography, 20, 758–768, 1990.

D'Asaro, E. A.: Upper-ocean inertial currents forced by a strong storm. Part III: Interaction of inertial currents and mesoscale eddies, Journal of physical oceanography, 25, 2953–2958, 1995.

de Boyer Montégut, C., Madec, G., Fischer, A. S., Lazar, A., and Iudicone, D.: Mixed layer depth over the global ocean: An examination of profile data and a profile-based climatology, Journal of Geophysical Research: Oceans, 109, 2004.

de Marez, C., l'Hégaret, P., Morvan, M., and Carton, X.: On the 3D structure of eddies in the Arabian Sea, Deep Sea Research Part I: Oceanographic Research Papers, 150, 103 057, 2019.

de Marez, C., Carton, X., Corréard, S., l'Hégaret, P., and Morvan, M.: Observations of a deep submesoscale cyclonic vortex in the Arabian Sea, Geophysical Research Letters, 47, e2020GL087 881, 2020.

de Marez, C., Le Corre, M., and Gula, J.: The influence of merger and convection on an anticyclonic eddy trapped in a bowl, Ocean Modelling, 167, 101 874, 2021.

Delahoyde, F. and Hyland, G.: Python implementation of the Gibbs SeaWater (GSW) Oceanographic Toolbox of TEOS-10, 2017.

Delcroix, T., Chaigneau, A., Soviadan, D., Boutin, J., and Pegliasco, C.: Eddy-induced salinity changes in the tropical Pacific, Journal of Geophysical Research: Oceans, 124, 374–389, 2019.

Dewar, W. K. and Flierl, G. R.: Some effects of the wind on rings, Journal of physical oceanography, 17, 1653–1667, 1987.

Dibarboure, G., Pujol, M.-I., Briol, F., Traon, P. L., Larnicol, G., Picot, N., Mertz, F., and Ablain, M.: Jason-2 in DUACS: Updated system description, first tandem results and impact on processing and products, Marine Geodesy, 34, 214–241, 2011.

Doglioli, A., Blanke, B., Speich, S., and Lapeyre, G.: Tracking coherent structures in a regional ocean model with wavelet analysis: Application to Cape Basin eddies, Journal of Geophysical Research: Oceans, 112, 2007.

Dong, C., McWilliams, J. C., and Shchepetkin, A. F.: Island wakes in deep water, Journal of Physical Oceanography, 37, 962–981, 2007.

Donlon, C. J., Martin, M., Stark, J., Roberts-Jones, J., Fiedler, E., and Wimmer, W.: The operational sea surface temperature and sea ice analysis (OSTIA) system, Remote Sensing of Environment, 116, 140–158, 2012.

d'Ortenzio, F., Iudicone, D., de Boyer Montegut, C., Testor, P., Antoine, D., Marullo, S., Santoleri, R., and Madec, G.: Seasonal variability of the mixed layer depth in the Mediterranean Sea as derived from in situ profiles, Geophysical Research Letters, 32, 2005a.

d'Ortenzio, F., Iudicone, D., de Boyer Montégut, C., Testor, P., Antoine, D., Marullo, S., Santoleri, R., and Madec, G.: Seasonal variability of the mixed layer depth in the Mediterranean Sea as derived from in situ profiles, Geophysical Research Letters, 32, 2005b.

Dufois, F., Hardman-Mountford, N. J., Greenwood, J., Richardson, A. J., Feng, M., and Matear, R. J.: Anticyclonic eddies are more productive than cyclonic eddies in subtropical gyres because of winter mixing, Science advances, 2, e1600 282, 2016.

Duo, Z., Wang, W., and Wang, H.: Oceanic mesoscale eddy detection method based on deep learning, Remote Sensing, 11, 1921, 2019.

d'Ovidio, F., Isern-Fontanet, J., López, C., Hernández-García, E., and García-Ladona, E.: Comparison between Eulerian diagnostics and finite-size Lyapunov exponents computed from altimetry in the Algerian basin, Deep Sea Research Part I: Oceanographic Research Papers, 56, 15–31, 2009.

Ernst, P. A., Subrahmanyam, B., and Trott, C. B.: Lakshadweep high propagation and impacts on the Somali Current and eddies during the southwest monsoon, Journal of Geophysical Research: Oceans, 127, e2021JC018 089, 2022.

Everett, J., Baird, M., Oke, P., and Suthers, I.: An avenue of eddies: Quantifying the biophysical properties of mesoscale eddies in the Tasman Sea, Geophysical Research Letters, 39, 2012.

Faghmous, J. H., Frenger, I., Yao, Y., Warmka, R., Lindell, A., and Kumar, V.: A daily global mesoscale ocean eddy dataset from satellite altimetry, Scientific data, 2, 1–16, 2015.

Fairall, C. W., Bradley, E. F., Hare, J., Grachev, A. A., and Edson, J. B.: Bulk parameterization of air–sea fluxes: Updates and verification for the COARE algorithm, Journal of climate, 16, 571–591, 2003.

Fang, F. and Morrow, R.: Evolution, movement and decay of warm-core Leeuwin Current eddies, Deep Sea Research Part II: Topical Studies in Oceanography, 50, 2245–2261, 2003.

Fernández-Castro, B., Evans, D. G., Frajka-Williams, E., Vic, C., and Naveira-Garabato, A. C.: Breaking of internal waves and turbulent dissipation in an anticyclonic mode water eddy, Journal of Physical Oceanography, 50, 1893–1914, 2020.

Flierl, G. R.: Particle motions in large-amplitude wave fields, Geophysical & Astrophysical Fluid Dynamics, 18, 39–74, 1981.

Franz, K., Roscher, R., Milioto, A., Wenzel, S., and Kusche, J.: Ocean eddy identification and tracking using neural networks, in: Igarss 2018-2018 IEEE international geoscience and remote sensing symposium, pp. 6887–6890, IEEE, 2018.

Frenger, I., Gruber, N., Knutti, R., and Münnich, M.: Imprint of Southern Ocean eddies on winds, clouds and rainfall, Nature geoscience, 6, 608–612, 2013.

Fuglister, F. C. and Worthington, L.: Some results of a multiple ship survey of the Gulf Stream, Tellus, 3, 1–14, 1951.

Gačić, M., Civitarese, G., Miserocchi, S., Cardin, V., Crise, A., and Mauri, E.: The open-ocean convection in the Southern Adriatic: a controlling mechanism of the spring phytoplankton bloom, Continental shelf research, 22, 1897–1908, 2002.

Garreau, P., Dumas, F., Louazel, S., Stegner, A., and Le Vu, B.: High-Resolution Observations and Tracking of a Dual-Core Anticyclonic Eddy in the Algerian Basin, Journal of Geophysical Research: Oceans, 123, 9320–9339, 2018.

Gaube, P., McGillicuddy, D. J., Chelton, D. B., Behrenfeld, M. J., and Strutton, P. G.: Regional variations in the influence of mesoscale eddies on near-surface chlorophyll, Journal of Geophysical Research: Oceans, 119, 8195–8220, 2014.

Gaube, P., Chelton, D. B., Samelson, R. M., Schlax, M. G., and O'Neill, L. W.: Satellite observations of mesoscale eddy-induced Ekman pumping, Journal of Physical Oceanography, 45, 104–132, 2015.

Gaube, P., J. McGillicuddy, D., and Moulin, A. J.: Mesoscale eddies modulate mixed layer depth globally, Geophysical Research Letters, 46, 1505–1512, 2019.

Giorgi, F. and Lionello, P.: Climate change projections for the Mediterranean region, Global and planetary change, 63, 90–104, 2008.

Graves, L. P., McWilliams, J. C., and Montgomery, M. T.: Vortex evolution due to straining: A mechanism for dominance of strong, interior anticyclones, Geophysical and Astrophysical Fluid Dynamics, 100, 151–183, 2006.

Griffa, A., Lumpkin, R., and Veneziani, M.: Cyclonic and anticyclonic motion in the upper ocean, Geophysical Research Letters, 35, 2008.

Grignon, L., Smeed, D., Bryden, H., and Schroeder, K.: Importance of the variability of hydrographic preconditioning for deep convection in the Gulf of Lion, NW Mediterranean, Ocean Science, 6, 573–586, 2010.

Haller, G.: An objective definition of a vortex, Journal of fluid mechanics, 525, 1–26, 2005.

Haller, G. and Beron-Vera, F. J.: Geodesic theory of transport barriers in two-dimensional flows, Physica D: Nonlinear Phenomena, 241, 1680–1702, 2012.

Halo, I., Backeberg, B., Penven, P., Ansorge, I., Reason, C., and Ullgren, J.: Eddy properties in the Mozambique Channel: A comparison between observations and two numerical ocean circulation models, Deep Sea Research Part II: Topical Studies in Oceanography, 100, 38–53, 2014.

Hamad, N., Millot, C., and Taupier-Letage, I.: The surface circulation in the eastern basin of the Mediterranean Sea, Scientia Marina, 70, 457–503, 2006.

Hausmann, U. and Czaja, A.: The observed signature of mesoscale eddies in sea surface temperature and the associated heat transport, Deep Sea Research Part I: Oceanographic Research Papers, 70, 60–72, 2012.

Hayes, D., Zodiatis, G., Konnaris, G., Hannides, A., Solovyov, D., and Testor, P.: Glider transects in the Levantine Sea: Characteristics of the warm core Cyprus eddy, in: OCEANS 2011 IEEE-Spain, pp. 1–9, IEEE, 2011.

He, Q., Zhan, H., and Cai, S.: Anticyclonic eddies enhance the winter barrier layer and surface cooling in the Bay of Bengal, Journal of Geophysical Research: Oceans, 125, e2020JC016 524, 2020.

Horton, C., Kerling, J., Athey, G., Schmitz, J., and Clifford, M.: Airborne expendable bathythermograph surveys of the eastern Mediterranean, Journal of Geophysical Research: Oceans, 99, 9891–9905, 1994.

Hoskins, B.: The role of potential vorticity in symmetric stability and instability, Quarterly Journal of the Royal Meteorological Society, 100, 480–482, 1974.

Houpert, L., Testor, P., De Madron, X. D., Somot, S., D'ortenzio, F., Estournel, C., and Lavigne, H.: Seasonal cycle of the mixed layer, the seasonal thermocline and the upper-ocean heat storage rate in the Mediterranean Sea derived from observations, Progress in Oceanography, 132, 333–352, 2015.

Ioannou, A., Stegner, A., Le Vu, B., Taupier-Letage, I., and Speich, S.: Dynamical evolution of intense Ierapetra eddies on a 22 year long period, Journal of Geophysical Research: Oceans, 122, 9276–9298, 2017.

Ioannou, A., Stegner, A., Tuel, A., LeVu, B., Dumas, F., and Speich, S.: Cyclostrophic corrections of AVISO/DUACS surface velocities and its application to mesoscale eddies in the Mediterranean Sea, Journal of Geophysical Research: Oceans, 124, 8913–8932, 2019.

Ioannou, A., Stegner, A., Dubos, T., Le Vu, B., and Speich, S.: Generation and intensification of mesoscale anticyclones by orographic wind jets: The case of Ierapetra eddies forced by the Etesians, Journal of Geophysical Research: Oceans, 125, e2019JC015 810, 2020a.

Ioannou, A., Stegner, A., Dumas, F., and Le Vu, B.: Three-dimensional evolution of mesoscale anticyclones in the lee of Crete, Frontiers in Marine Science, p. 1019, 2020b.

Isern-Fontanet, J., García-Ladona, E., and Font, J.: Identification of marine eddies from altimetric maps, Journal of Atmospheric and Oceanic Technology, 20, 772–778, 2003.

Isern-Fontanet, J., García-Ladona, E., and Font, J.: Vortices of the Mediterranean Sea: An altimetric perspective, Journal of physical oceanography, 36, 87–103, 2006.

Itoh, S. and Yasuda, I.: Characteristics of mesoscale eddies in the Kuroshio–Oyashio Extension region detected from the distribution of the sea surface height anomaly, Journal of Physical Oceanography, 40, 1018–1034, 2010a.

Itoh, S. and Yasuda, I.: Water mass structure of warm and cold anticyclonic eddies in the western boundary region of the subarctic North Pacific, Journal of Physical Oceanography, 40, 2624–2642, 2010b.

Iudicone, D., Santoleri, R., Marullo, S., and Gerosa, P.: Sea level variability and surface eddy statistics in the Mediterranean Sea from TOPEX/POSEIDON data, Journal of Geophysical Research: Oceans, 103, 2995–3011, 1998.

Jerlov, N.: 1968: Optical Oceanography, Amsterdam, London and New York: Elsevier Publishing Co.

Jordà, G., Von Schuckmann, K., Josey, S., Caniaux, G., García-Lafuente, J., Sammartino, S., Özsoy, E., Polcher, J., Notarstefano, G., Poulain, P.-M., et al.: The Mediterranean Sea heat and mass budgets: Estimates, uncertainties and perspectives, Progress in Oceanography, 156, 174–208, 2017.

Kersale, M., Petrenko, A., Doglioli, A. M., Dekeyser, I., and Nencioli, F.: Physical characteristics and dynamics of the coastal Latex09 Eddy derived from in situ data and numerical modeling, Journal of Geophysical Research: Oceans, 118, 399–409, 2013.

Killworth, P. D.: On the motion of isolated lenses on a beta-plane, Journal of Physical Oceanography, 13, 368–376, 1983.

Koshlyakov, M. and Belokopytov, V.: Mesoscale eddies in the open ocean: Review of experimental investigations, Physical Oceanography, 27, 559–572, 2020.

Kotroni, V., Lagouvardos, K., and Lalas, D.: The effect of the island of Crete on the Etesian winds over the Aegean Sea, Quarterly Journal of the Royal Meteorological Society, 127, 1917–1937, 2001.

Kunze, E.: Near-inertial wave propagation in geostrophic shear, Journal of Physical Oceanography, 15, 544–565, 1985.

Kurian, J., Colas, F., Capet, X., McWilliams, J. C., and Chelton, D. B.: Eddy properties in the California current system, Journal of Geophysical Research: Oceans, 116, 2011.

Larnicol, G., Ayoub, N., and Le Traon, P.-Y.: Major changes in Mediterranean Sea level variability from 7 years of TOPEX/Poseidon and ERS-1/2 data, Journal of Marine Systems, 33, 63–89, 2002.

Laxenaire, R., Speich, S., Blanke, B., Chaigneau, A., Pegliasco, C., and Stegner, A.: Anticyclonic eddies connecting the western boundaries of Indian and Atlantic Oceans, Journal of Geophysical Research: Oceans, 123, 7651–7677, 2018.

Laxenaire, R., Speich, S., and Stegner, A.: Evolution of the thermohaline structure of one Agulhas ring reconstructed from satellite altimetry and Argo floats, Journal of Geophysical Research: Oceans, 124, 8969–9003, 2019.

Laxenaire, R., Speich, S., and Stegner, A.: Agulhas ring heat content and transport in the South Atlantic estimated by combining satellite altimetry and Argo profiling floats data, Journal of Geophysical Research: Oceans, 125, e2019JC015 511, 2020.

Le Traon, P., Nadal, F., and Ducet, N.: An improved mapping method of multisatellite altimeter data, Journal of atmospheric and oceanic technology, 15, 522–534, 1998.

Le Vu, B., Stegner, A., and Arsouze, T.: Angular Momentum Eddy Detection and tracking Algorithm (AMEDA) and its application to coastal eddy formation, Journal of Atmospheric and Oceanic Technology, 35, 739–762, 2018.

Legg, S. and Marshall, J.: The influence of the ambient flow on the spreading of convected water masses, Journal of marine research, 56, 107–139, 1998.

Lemarié, F., Samson, G., Redelsperger, J.-L., Giordani, H., Brivoal, T., and Madec, G.: A simplified atmospheric boundary layer model for an improved representation of air–sea interactions in eddying oceanic models: implementation and first evaluation in NEMO (4.0), Geoscientific Model Development, 14, 543–572, 2021.

Lévy, M., Klein, P., and Treguier, A.-M.: Impact of sub-mesoscale physics on production and subduction of phytoplankton in an oligotrophic regime, Journal of marine research, 59, 535–565, 2001.

Lévy, M., Franks, P. J., and Smith, K. S.: The role of submesoscale currents in structuring marine ecosystems, Nature communications, 9, 4758, 2018.

Lguensat, R., Sun, M., Fablet, R., Tandeo, P., Mason, E., and Chen, G.: EddyNet: A deep neural network for pixel-wise classification of oceanic eddies, in: IGARSS 2018-2018 IEEE International Geoscience and Remote Sensing Symposium, pp. 1764–1767, IEEE, 2018.

Lilly, J. M. and Rhines, P. B.: Coherent eddies in the Labrador Sea observed from a mooring, Journal of Physical Oceanography, 32, 585–598, 2002.

Lilly, J. M., Rhines, P. B., Schott, F., Lavender, K., Lazier, J., Send, U., and D'Asaro, E.: Observations of the Labrador Sea eddy field, Progress in Oceanography, 59, 75–176, 2003.

Liu, F., Zhou, H., Huang, W., and Wen, B.: Submesoscale Eddies Observation Using High-Frequency Radars: A Case Study in the Northern South China Sea, IEEE Journal of Oceanic Engineering, 46, 624–633, 2020.

Liu, Y. and Li, X.: Impact of surface and subsurface-intensified eddies on sea surface temperature and chlorophyll *a* in the northern Indian Ocean utilizing deep learning, Ocean Science, 19, 1579–1593, https://doi.org/10.5194/os-19-1579-2023, 2023.

Liu, Y., Zheng, Q., and Li, X.: Characteristics of global ocean abnormal mesoscale eddies derived from the fusion of sea surface height and temperature data by deep learning, Geophysical Research Letters, 48, e2021GL094 772, 2021.

Lumpkin, R.: Global characteristics of coherent vortices from surface drifter trajectories, Journal of Geophysical Research: Oceans, 121, 1306–1321, 2016.

L'Hégaret, P., Lacour, L., Carton, X., Roullet, G., Baraille, R., and Corréard, S.: A seasonal dipolar eddy near Ras Al Hamra (Sea of Oman), Ocean Dynamics, 63, 633–659, 2013.

Malanotte-Rizzoli, P., Manca, B. B., d'Alcalà, M. R., Theocharis, A., Bergamasco, A., Bregant, D., Budillon, G., Civitarese, G., Georgopoulos, D., Michelato, A., et al.: A synthesis of the Ionian Sea hydrography, circulation and water mass pathways during POEM-Phase I, Progress in Oceanography, 39, 153–204, 1997.

Malanotte-Rizzoli, P., Manca, B. B., d'Alcala, M. R., Theocharis, A., Brenner, S., Budillon, G., and Ozsoy, E.: The Eastern Mediterranean in the 80s and in the 90s: the big transition in the intermediate and deep circulations, Dynamics of Atmospheres and Oceans, 29, 365–395, 1999.

Mapp, G. R., Welch, C. S., and Munday, J. C.: Wave refraction by warm core rings, Journal of Geophysical Research: Oceans, 90, 7153–7162, 1985.

Marechal, G. and de Marez, C.: Variability of wind wave field by realistic mesoscale and submesoscale eddy field, Ocean Sci. Discuss, 53, 1–18, 2021.

Margirier, F., Testor, P., Heslop, E., Mallil, K., Bosse, A., Houpert, L., Mortier, L., Bouin, M.-N., Coppola, L., D'ortenzio, F., et al.: Abrupt warming and salinification of intermediate waters interplays with decline of deep convection in the Northwestern Mediterranean Sea, Scientific Reports, 10, 20 923, 2020.

Mariotti, A.: Recent changes in the Mediterranean water cycle: a pathway toward long-term regional hydroclimatic change?, Journal of Climate, 23, 1513–1525, 2010.

Mariotti, A., Struglia, M. V., Zeng, N., and Lau, K.: The hydrological cycle in the Mediterranean region and implications for the water budget of the Mediterranean Sea, Journal of climate, 15, 1674–1690, 2002.

Mason, E., Pascual, A., and McWilliams, J. C.: A new sea surface height–based code for oceanic mesoscale eddy tracking, Journal of Atmospheric and Oceanic Technology, 31, 1181–1188, 2014.

Matteoda, A. M. and Glenn, S. M.: Observations of recurrent mesoscale eddies in the eastern Mediterranean, Journal of Geophysical Research: Oceans, 101, 20 687–20 709, 1996.

McCreary, J. P., Lee, H. S., and Enfield, D. B.: The response of the coastal ocean to strong offshore winds: With application to circulations in the Gulfs of Tehuantepec and Papagayo, Journal of Marine Research, 47, 81–109, 1989.

McDougall, T., Feistel, R., Millero, F., Jackett, D., Wright, D., King, B., Marion, G., Chen, C., Spitzer, P., and Seitz, S.: The international thermodynamic equation of seawater 2010 (TEOS-10): Calculation and use of thermodynamic properties, Global ship-based repeat hydrography manual, IOCCP report no, 14, 2009.

McDowell, S. E. and Rossby, H. T.: Mediterranean water: An intense mesoscale eddy off the Bahamas, Science, 202, 1085–1087, 1978.

McGillicuddy, D. J.: Formation of intrathermocline lenses by eddy–wind interaction, Journal of Physical Oceanography, 45, 606–612, 2015.

McGillicuddy, D. J., Johnson, R., Siegel, D., Michaels, A., Bates, N., and Knap, A.: Mesoscale variations of biogeochemical properties in the Sargasso Sea, Journal of Geophysical Research: Oceans, 104, 13 381–13 394, 1999.

McGillicuddy, D. J., Anderson, L. A., Bates, N. R., Bibby, T., Buesseler, K. O., Carlson, C. A., Davis, C. S., Ewart, C., Falkowski, P. G., Goldthwait, S. A., et al.: Eddy/wind interactions stimulate extraordinary mid-ocean plankton blooms, Science, 316, 1021–1026, 2007.

McWilliams, J. C.: A review of research on mesoscale ocean currents, Reviews of Geophysics, 17, 1548–1558, 1979.

McWilliams, J. C.: The emergence of isolated coherent vortices in turbulent flow, Journal of Fluid Mechanics, 146, 21–43, 1984.

McWilliams, J. C.: Submesoscale, coherent vortices in the ocean, Reviews of Geophysics, 23, 165–182, 1985.

MEDOC Group: Observation of formation of deep water in the Mediterranean Sea, 1969, Nature, 227, 1037–1040, 1970.

Menna, M., Poulain, P.-M., Zodiatis, G., and Gertman, I.: On the surface circulation of the Levantine subbasin derived from Lagrangian drifters and satellite altimetry data, Deep Sea Research Part I: Oceanographic Research Papers, 65, 46–58, 2012.

Meunier, T., Pallás-Sanz, E., Tenreiro, M., Portela, E., Ochoa, J., Ruiz-Angulo, A., and Cusí, S.: The vertical structure of a Loop Current Eddy, Journal of Geophysical Research: Oceans, 123, 6070–6090, 2018.

Millot, C.: Some features of the Algerian Current, Journal of Geophysical Research: Oceans, 90, 7169–7176, 1985.

Millot, C. and Gerin, R.: The Mid-Mediterranean Jet Artefact, Geophysical research letters, 37, 2010.

Millot, C. and Taupier-Letage, I.: Circulation in the Mediterranean sea, The Mediterranean Sea, pp. 29–66, 2005.

Mkhinini, N., Coimbra, A. L. S., Stegner, A., Arsouze, T., Taupier-Letage, I., and Béranger, K.: Long-lived mesoscale eddies in the eastern Mediterranean Sea: Analysis of 20 years of AVISO geostrophic velocities, Journal of Geophysical Research: Oceans, 119, 8603–8626, 2014.

MODE Group: The mid-ocean dynamics experiment, Deep Sea Research, 25, 859–910, 1978.

Moen, J.: Variability and mixing of the surface layer in the Tyrrhenian Sea: MILEX-80, Saclantcen report SR-75, 128, 1984.

Monin, A. S. and Zhikharev, G. M.: Ocean eddies, Soviet Physics Uspekhi, 33, 313, 1990.

Morrow, R., Birol, F., Griffin, D., and Sudre, J.: Divergent pathways of cyclonic and anti-cyclonic ocean eddies, Geophysical Research Letters, 31, 2004.

Moschos, E., Barboni, A., and Stegner, A.: Why do inverse eddy surface temperature anomalies emerge? The case of the Mediterranean Sea, Remote Sensing, 14, 3807, 2022.

Moschos, E., Kugusheva, A., Coste, P., and Stegner, A.: Computer Vision for Ocean Eddy Detection in Infrared Imagery, in: Proceedings of the IEEE/CVF Winter Conference on Applications of Computer Vision, pp. 6395–6404, 2023.

Moutin, T. and Prieur, L.: Influence of anticyclonic eddies on the Biogeochemistry from the Oligotrophic to the Ultraoligotrophic Mediterranean (BOUM cruise), Biogeosciences, 9, 3827–3855, 2012.

Nardelli, B. B., Tronconi, C., Pisano, A., and Santoleri, R.: High and Ultra-High resolution processing of satellite Sea Surface Temperature data over Southern European Seas in the framework of MyOcean project, Remote Sensing of Environment, 129, 1–16, 2013.

Nencioli, F., Dong, C., Dickey, T., Washburn, L., and McWilliams, J. C.: A vector geometry–based eddy detection algorithm and its application to a high-resolution numerical model product and high-frequency radar surface velocities in the Southern California Bight, Journal of atmospheric and oceanic technology, 27, 564–579, 2010.

Nencioli, F., Dall'Olmo, G., and Quartly, G. D.: Agulhas ring transport efficiency from combined satellite altimetry and Argo profiles, Journal of Geophysical Research: Oceans, 123, 5874–5888, 2018.

Ni, Q., Zhai, X., Jiang, X., and Chen, D.: Abundant cold anticyclonic eddies and warm cyclonic eddies in the global ocean, Journal of Physical Oceanography, 51, 2793–2806, 2021.

Ni, Q., Zhai, X., Yang, Z., and Chan, D.: Generation of Cold Anticyclonic Eddies and Warm Cyclonic Eddies in the Tropical Oceans, Journal of Physical Oceanography, 2023.

Nilsson, C. and Cresswell, G.: The formation and evolution of East Australian Current warm-core eddies, Progress in oceanography, 9, 133–183, 1980.

Nof, D.: On the β-induced movement of isolated baroclinic eddies, Journal of Physical Oceanography, 11, 1662–1672, 1981.

Okubo, A.: Horizontal dispersion of floatable particles in the vicinity of velocity singularities such as convergences, in: Deep sea research and oceanographic abstracts, vol. 17, pp. 445–454, Elsevier, 1970.

Ollitrault, M. and Rannou, J.-P.: ANDRO: An Argo-based deep displacement dataset, Journal of Atmospheric and Oceanic Technology, 30, 759–788, 2013.

Olson, D. B. and Evans, R. H.: Rings of the Agulhas current, Deep Sea Research Part A. Oceanographic Research Papers, 33, 27–42, 1986.

Ovchinnikov, I.: Circulation in surface and intermediate layers of Mediterranean, Oceanology-USSR, 6, 48–+, 1966.

Ozer, T., Gertman, I., Kress, N., Silverman, J., and Herut, B.: Interannual thermohaline (1979–2014) and nutrient (2002–2014) dynamics in the Levantine surface and intermediate water masses, SE Mediterranean Sea, Global and Planetary Change, 151, 60–67, 2017.

O'Neill, L. W., Chelton, D. B., Esbensen, S. K., and Wentz, F. J.: High-resolution satellite measurements of the atmospheric boundary layer response to SST variations along the Agulhas Return Current, Journal of Climate, 18, 2706–2723, 2005.

Park, J. J., Kim, K., King, B. A., and Riser, S. C.: An advanced method to estimate deep currents from profiling floats, Journal of Atmospheric and Oceanic Technology, 22, 1294–1304, 2005.

Pastor, F., Valiente, J. A., and Khodayar, S.: A warming Mediterranean: 38 years of increasing sea surface temperature, Remote sensing, 12, 2687, 2020.

Patzert, W. C.: Eddies in Hawaiian waters, vol. 69, Hawaii Institute of Geophysics, University of Hawaii Honolulu, Hawaii, 1969.

Paulson, C. A. and Simpson, J. J.: Irradiance measurements in the upper ocean, Journal of Physical Oceanography, 7, 952–956, 1977.

Pegliasco, C., Chaigneau, A., and Morrow, R.: Main eddy vertical structures observed in the four major Eastern Boundary Upwelling Systems, Journal of Geophysical Research: Oceans, 120, 6008–6033, 2015.

Pegliasco, C., Chaigneau, A., Morrow, R., and Dumas, F.: Detection and tracking of mesoscale eddies in the Mediterranean Sea: A comparison between the Sea Level Anomaly and the Absolute Dynamic Topography fields, Advances in Space Research, 68, 401–419, 2021.

Pegliasco, C., Delepoulle, A., Mason, E., Morrow, R., Faugère, Y., and Dibarboure, G.: META3. 1exp: a new global mesoscale eddy trajectory atlas derived from altimetry, Earth System Science Data, 14, 1087–1107, 2022.

Peixoto, J. P., De Almeida, M., Rosen, R. D., and Salstein, D. A.: Atmospheric moisture transport and the water balance of the Mediterranean Sea, Water Resources Research, 18, 83–90, 1982.

Penven, P., Echevin, V., Pasapera, J., Colas, F., and Tam, J.: Average circulation, seasonal cycle, and mesoscale dynamics of the Peru Current System: A modeling approach, Journal of Geophysical Research: Oceans, 110, 2005.

Penven, P., Halo, I., Pous, S., and Marié, L.: Cyclogeostrophic balance in the Mozambique Channel, Journal of Geophysical Research: Oceans, 119, 1054–1067, 2014.

Perret, G., Stegner, A., Farge, M., and Pichon, T.: Cyclone-anticyclone asymmetry of large-scale wakes in the laboratory, Physics of Fluids, 18, 2006.

Pessini, F., Olita, A., Cotroneo, Y., and Perilli, A.: Mesoscale eddies in the Algerian Basin: do they differ as a function of their formation site?, Ocean Science, 14, 669–688, 2018.

Petrenko, A. A., Doglioli, A. M., Nencioli, F., Kersalé, M., Hu, Z., and d'Ovidio, F.: A review of the LATEX project: mesoscale to submesoscale processes in a coastal environment, Ocean Dynamics, 67, 513–533, 2017.

Pettenuzzo, D., Large, W., and Pinardi, N.: On the corrections of ERA-40 surface flux products consistent with the Mediterranean heat and water budgets and the connection between basin surface total heat flux and NAO, Journal of Geophysical Research: Oceans, 115, 2010.

Philippe, M. and Harang, L.: Surface temperature fronts in the Mediterranean Sea from infrared satellite imagery, in: Elsevier Oceanography Series, vol. 34, pp. 91–128, Elsevier, 1982.

Pickart, R. S., Weingartner, T. J., Pratt, L. J., Zimmermann, S., and Torres, D. J.: Flow of winter-transformed Pacific water into the Western Arctic, Deep Sea Research Part II: Topical Studies in Oceanography, 52, 3175–3198, 2005.

Piolle, J.-F., Autret, E., Arino, O., Robinson, I. S., and Le Borgne, P.: Medspiration: toward the sustained delivery of satellite SST products and services over regional seas, in: ESA Living Planet Symposium, vol. 686, p. 361, 2010.

Pollard, R. T. and Regier, L. A.: Vorticity and vertical circulation at an ocean front, Journal of Physical Oceanography, 22, 609–625, 1992.

Poulain, P.-M. and Zambianchi, E.: Surface circulation in the central Mediterranean Sea as deduced from Lagrangian drifters in the 1990s, Continental Shelf Research, 27, 981–1001, 2007.

Puillat, I., Taupier-Letage, I., and Millot, C.: Algerian eddies lifetime can near 3 years, Journal of Marine Systems, 31, 245–259, 2002.

Pujol, M.-I.: [Dataset] European Seas gridded L4 Sea Surface Height and derived variables NRT, https://doi.org/10.48670/moi-00142, 2021.

Pujol, M.-I. and Larnicol, G.: Mediterranean sea eddy kinetic energy variability from 11 years of altimetric data, Journal of Marine Systems, 58, 121–142, 2005.

Pujol, M.-I., Faugère, Y., Taburet, G., Dupuy, S., Pelloquin, C., Ablain, M., and Picot, N.: DUACS DT2014: the new multi-mission altimeter data set reprocessed over 20 years, Ocean Science, 12, 1067–1090, 2016.

Rabinovich, A. B., Thomson, R. E., and Bograd, S. J.: Drifter observations of anticyclonic eddies near Bussol'Strait, the Kuril Islands, Journal of oceanography, 58, 661–671, 2002.

Raj, R., Johannessen, J., Eldevik, T., Nilsen, J. Ø., and Halo, I.: Quantifying mesoscale eddies in the Lofoten Basin, Journal of Geophysical Research: Oceans, 121, 4503–4521, 2016.

Renault, L., Molemaker, M. J., Gula, J., Masson, S., and McWilliams, J. C.: Control and stabilization of the Gulf Stream by oceanic current interaction with the atmosphere, Journal of Physical Oceanography, 46, 3439–3453, 2016a.

Renault, L., Molemaker, M. J., McWilliams, J. C., Shchepetkin, A. F., Lemarié, F., Chelton, D., Illig, S., and Hall, A.: Modulation of wind work by oceanic current interaction with the atmosphere, Journal of Physical Oceanography, 46, 1685–1704, 2016b.

Richardson, P., Price, J., Walsh, D., Armi, L., and Schröder, M.: Tracking three meddies with SOFAR floats, Journal of Physical Oceanography, 19, 371–383, 1989.

Richardson, P., Bower, A., and Zenk, W.: A census of Meddies tracked by floats, Progress in Oceanography, 45, 209–250, 2000.

Richardson, P. L.: Gulf Stream ring trajectories, Journal of Physical Oceanography, 10, 90–104, 1980.

Rio, M.-H., Mulet, S., and Picot, N.: Beyond GOCE for the ocean circulation estimate: Synergetic use of altimetry, gravimetry, and in situ data provides new insight into geostrophic and Ekman currents, Geophysical Research Letters, 41, 8918–8925, 2014.

Robinson, A., Golnaraghi, M., Leslie, W., Artegiani, A., Hecht, A., Lazzoni, E., Michelato, A., Sansone, E., Theocharis, A., and Ünlüata, Ü.: The eastern Mediterranean general circulation: features, structure and variability, Dynamics of Atmospheres and Oceans, 15, 215–240, 1991.

Robinson, A. R.: Overview and summary of eddy science, in: Eddies in marine science, pp. 3–15, Springer, 1983.

Robinson, A. R., Hecht, A., Pinardi, N., Bishop, J., Leslie, W. G., Rosentroub, Z., Mariano, A. J., and Brenner, S.: Small synoptic/mesoscale eddies and energetic variability of the eastern Levantine basin, Nature, 327, 131–134, 1987.

Roemmich, D. and Argo Steering Team: Argo: the challenge of continuing 10 years of progress, Oceanography, 22, 46–55, 2009.

Romero, L., Lenain, L., and Melville, W. K.: Observations of surface wave–current interaction, Journal of Physical Oceanography, 47, 615–632, 2017.

Rossby, C.: On displacements and intensity changes of atmospheric vortices, 1948.

Rudnick, D. L. and Ferrari, R.: Compensation of horizontal temperature and salinity gradients in the ocean mixed layer, Science, 283, 526–529, 1999.

Sadarjoen, I. A. and Post, F. H.: Detection, quantification, and tracking of vortices using streamline geometry, Computers & Graphics, 24, 333–341, 2000.

Schott, F. and Quadfasel, D. R.: Variability of the Somali Current system during the onset of the southwest monsoon, 1979, Journal of Physical Oceanography, 12, 1343–1357, 1982.

Schott, F., Leaman, K. D., and Zika, R. G.: Deep mixing in the Gulf of Lions, revisited, Geophysical research letters, 15, 800–803, 1988.

Schroeder, K., Gasparini, G., Tangherlini, M., and Astraldi, M.: Deep and intermediate water in the western Mediterranean under the influence of the Eastern Mediterranean Transient, Geophysical Research Letters, 33, 2006.

Schütte, F., Brandt, P., and Karstensen, J.: Occurrence and characteristics of mesoscale eddies in the tropical northeastern Atlantic Ocean, Ocean Science, 12, 663–685, 2016.

Send, U., Schott, F., Gaillard, F., and Desaubies, Y.: Observation of a deep convection regime with acoustic tomography, Journal of Geophysical Research: Oceans, 100, 6927–6941, 1995.

Shetye, S., Gouveia, A., and Shenoi, S.: Circulation and water masses of the Arabian Sea, Proceedings of the Indian Academy of Sciences-Earth and Planetary Sciences, 103, 107–123, 1994.

Siegel, D. A., McGillicuddy, D. J., and Fields, E. A.: Mesoscale eddies, satellite altimetry, and new production in the Sargasso Sea, Journal of Geophysical Research: Oceans, 104, 13 359–13 379, 1999.

Smith, W. H. and Sandwell, D. T.: Global sea floor topography from satellite altimetry and ship depth soundings, Science, 277, 1956–1962, 1997.

Smyth, W. and McWilliams, J.: Instability of an axisymmetric vortex in a stably stratified, rotating environment, Theoretical and Computational Fluid Dynamics, 11, 305–322, 1998.

Souza, J., de Boyer Montégut, C., and Le Traon, P.-Y.: Comparison between three implementations of automatic identification algorithms for the quantification and characterization of mesoscale eddies in the South Atlantic Ocean, Ocean Science, 7, 317–334, 2011.

Stammer, D.: Global characteristics of ocean variability estimated from regional TOPEX/POSEIDON altimeter measurements, Journal of Physical Oceanography, 27, 1743–1769, 1997.

Stegner, A. and Dritschel, D.: A numerical investigation of the stability of isolated shallow water vortices, Journal of Physical Oceanography, 30, 2562–2573, 2000.

Stegner, A., Le Vu, B., Pegliasco, C., Moschos, E., and Faugere, Y.: 3D structure of long-lived eddies in the Mediterranean sea: the DYNED-Atlas database, Rapport Commission internationale Mer Méditerranée, 42, 2019.

Stegner, A., Le Vu, B., and Pegliasco, C.: [Dataset] Atlas of 3D Eddies in the Mediterranean Sea from 2000 to 2019, https://doi.org/10.14768/2019130201.2, 2020.

Stegner, A., Le Vu, B., Dumas, F., Ghannami, M. A., Nicolle, A., Durand, C., and Faugere, Y.: Cyclone-Anticyclone Asymmetry of Eddy Detection on Gridded Altimetry Product in the Mediterranean Sea, Journal of Geophysical Research: Oceans, 126, e2021JC017 475, 2021.

Stern, M. E.: Interaction of a uniform wind stress with a geostrophic vortex, in: Deep Sea Research and Oceanographic Abstracts, vol. 12, pp. 355–367, Elsevier, 1965.

Stockman, V. B., Koshlyakov, M. N., Ozmidov, R. V., Fomin, L. M., and Yampolsky, A. D.: Long-term measurements of the physical field variability on oceanic polygons, as a new stage in the ocean research, in: Doklady Akademii Nauk, vol. 186, pp. 1070–1073, Russian Academy of Sciences, 1969.

Stommel, H.: The westward intensification of wind-driven ocean currents, Eos, Transactions American Geophysical Union, 29, 202–206, 1948.

Stramma, L., Weller, R. A., Czeschel, R., and Bigorre, S.: Eddies and an extreme water mass anomaly observed in the eastern south Pacific at the Stratus mooring, Journal of Geophysical Research: Oceans, 119, 1068–1083, 2014.

Sun, W., Dong, C., Wang, R., Liu, Y., and Yu, K.: Vertical structure anomalies of oceanic eddies in the Kuroshio Extension region, Journal of Geophysical Research: Oceans, 122, 1476–1496, 2017.

Sun, W., Dong, C., Tan, W., and He, Y.: Statistical characteristics of cyclonic warm-core eddies and anticyclonic cold-core eddies in the North Pacific based on remote sensing data, Remote Sensing, 11, 208, 2019.

Sun, W., Liu, Y., Chen, G., Tan, W., Lin, X., Guan, Y., and Dong, C.: Three-dimensional properties of mesoscale cyclonic warm-core and anticyclonic cold-core eddies in the South China Sea, Acta Oceanologica Sinica, 40, 17–29, 2021.

Sun, W., An, M., Liu, J., Liu, J., Yang, J., Tan, W., and Dong, C.: Comparative analysis of four types of mesoscale eddies in the Kuroshio-Oyashio extension region, Frontiers in Marine Science, 2022.

Sutyrin, G., Stegner, A., Taupier-Letage, I., and Teinturier, S.: Amplification of a surface-intensified eddy drift along a steep shelf in the Eastern Mediterranean Sea, Journal of physical oceanography, 39, 1729–1741, 2009.

Sybrandy, A. L.: The WOCE/TOGASVP Lagrangian drifter construction manual., WOCE Rep., 63, 58, 1991.

Szekely, T., Gourrion, J., Pouliquen, S., Reverdin, G., and Merceur, F.: [Dataset] CORA, coriolis ocean dataset for reanalysis, https://doi.org/10.17882/46219, 2019.

Theocharis, A., Georgopoulos, D., Lascaratos, A., and Nittis, K.: Water masses and circulation in the central region of the Eastern Mediterranean: Eastern Ionian, South Aegean and Northwest Levantine, 1986–1987, Deep sea research part II: topical studies in oceanography, 40, 1121–1142, 1993.

Tourbillon Group: The Tourbillon experiment: a study of a mesoscale eddy in the eastern North Atlantic, Deep Sea Research Part A. Oceanographic Research Papers, 30, 475–511, 1983.

Trott, C. B., Subrahmanyam, B., Chaigneau, A., and Roman-Stork, H. L.: Eddy-induced temperature and salinity variability in the Arabian Sea, Geophysical Research Letters, 46, 2734–2742, 2019.

Vallis, G. K.: Atmospheric and oceanic fluid dynamics, Cambridge University Press, 2006.

Vazquez-Cuervo, J., Font, J., and Martinez-Benjamin, J. J.: Observations on the circulation in the Alboran Sea using ERSI altimetry and sea surface temperature data, Journal of physical oceanography, 26, 1426–1439, 1996.

Veneziani, M., Griffa, A., Reynolds, A. M., and Mariano, A. J.: Oceanic turbulence and stochastic models from subsurface Lagrangian data for the Northwest Atlantic Ocean, Journal of physical oceanography, 34, 1884–1906, 2004.

Vic, C., Roullet, G., Carton, X., and Capet, X.: Mesoscale dynamics in the A rabian S ea and a focus on the G reat W hirl life cycle: A numerical investigation using ROMS, Journal of Geophysical Research: Oceans, 119, 6422–6443, 2014.

Villas Bôas, A., Sato, O., Chaigneau, A., and Castelão, G.: The signature of mesoscale eddies on the air-sea turbulent heat fluxes in the South Atlantic Ocean, Geophysical Research Letters, 42, 1856–1862, 2015.

Weiss, J.: The dynamics of enstrophy transfer in two-dimensional hydrodynamics, Physica D: Nonlinear Phenomena, 48, 273–294, 1991.

Wilkin, J. L. and Morrow, R. A.: Eddy kinetic energy and momentum flux in the Southern Ocean: Comparison of a global eddy-resolving model with altimeter, drifter, and current-meter data, Journal of Geophysical Research: Oceans, 99, 7903–7916, 1994.

Yasuda, I., Okuda, K., and Hirai, M.: Evolution of a Kuroshio warm-core ring—Variability of the hydrographic structure, Deep Sea Research Part A. Oceanographic Research Papers, 39, S131–S161, 1992.

Yasuda, I., Ito, S.-I., Shimizu, Y., Ichikawa, K., Ueda, K.-I., Honma, T., Uchiyama, M., Watanabe, K., Sunou, N., Tanaka, K., et al.: Cold-core anticyclonic eddies south of the Bussol'Strait in the northwestern subarctic Pacific, Journal of Physical Oceanography, 30, 1137–1157, 2000.

Yim, E., Stegner, A., and Billant, P.: Stability criterion for the centrifugal instability of surface intensified anticyclones, Journal of Physical Oceanography, 49, 827–849, 2019.

Zhang, Z., Tian, J., Qiu, B., Zhao, W., Chang, P., Wu, D., and Wan, X.: Observed 3D structure, generation, and dissipation of oceanic mesoscale eddies in the South China Sea, Scientific Reports, 6, 24 349, 2016.

Appendix A

Eddy-induced impact on climatology

Various background methods were discussed in Sect.2.4. The most important difference we aim to discuss here the difference between an "All-profiles" climatology (Chaigneau et al. (2011)'s method) and a "Without-eddy" climatology (Laxenaire et al. (2019)'s method, adapted to the Mediterranean Sea with $D_c = 150km$ in Barboni et al. (2021)). The preferred locations for mesoscale eddies shown in Fig.2.2 translate in a mean signature on the temperature and salinity climatological field. Persistent eddies at a given location can then not be considered as transient structures. These two methods were previously summarized in Fig.2.7, and are computed for the present discussion per (0.5°x 0.5°) bins. It should be noted that profiles collocated as "ambiguous" (see Sect.2.3) are also discarded from the Without-eddies climatology because they correspond to the eddy margins, with variations due to altimetric tracks interpolation, where the eddy can still influence physical properties. To reduce bias of interannual variability, bins with less than 4 years available are discarded throughout this analysis, still covering a very large part of the Mediterranean Sea (see Fig.2.5). We first assess the climatological impact for temperature and salinity, then later for mixed layer depth.

Temperature and salinity

Figure A.1 shows the difference between the two climatologies, defined as All-profiles minus Without-eddies, in temperature (Fig.A.1a-c) and salinity (b-d), at 200m (a-b) and 500m (c-d) depth, from 2010 to 2019. Following previous upper layer Mediterranean climatology from Houpert et al. (2015), 200m is inside the thermocline and then should be affected by mesoscale eddies. It is however below the mixed layer in any season (apart from convective regions: Gulf of Lion, Adriatic and Aegean seas and Rhodes gyres), thus preventing a bias from data temporal heterogeneity. 500m is on the other hand well below the thermocline and should be only affected by the deepest eddy modulation of isopycnals. This figure shows then the map of the physical bias induced by the eddies without seasonal bias.

In the Eastern Mediterranean the signal on temperature is strong, localized and deep, more particularly in the Levantine Basin. Strong temperature bias on the order of +0.5°C or higher accurately coincides with known recurrent anticyclonic structures: the Pelops eddy south-east of the Peloponnese peninsula (36°N ; 22°E), Ierapetra eddy south-west of Crete (34°N ; 26°E), Mersa-Matruh eddy north-west of the Nile delta (33°N ; 29°E) and Eratosthenes eddy south of Cyprus (33°N ; 33°E). More importantly this eddy bias is persistent at depth, where warmer temperatures are computed in the All-profiles climatology at the same locations even at 500m deep, which is consistent with the observed deep and warm temperature anomalies reported in previous studies (Ioannou et al., 2020b; Barboni et al., 2021). On salinity the eddy-induced bias seems quite low in the Eastern Mediterranean, with an exception south of Cyprus where the Eratosthenes eddy induces a bias about +0.2 PSU, already reported by Hayes et al. (2011). The southern part of the Ionian Sea in the gulf of Sidra exhibits another exception with warm but very fresh anomalies at 200m, about +0.2°C and -0.2 PSU. This could be due to eddies formed by instability of the coastal Lybian current fed by modified Atlantic waters (Millot and Taupier-Letage, 2005), however such values should be considered with caution given the low amount of data (see Fig.2.5) and the lack of studies in this region. One can still notice the sampling of an anticyclone in this region by Moutin and Prieur (2012), which indeed revealed a warm and fresh density anomaly in the upper 250m but warm and salty below, in agreement with Fig.A.1b-d.

In the Western Mediterranean, the eddy impact on climatology is on the opposite mostly non-existent at depth, slight on temperature but marked on salinity with negative values, reaching about +0.1°C and

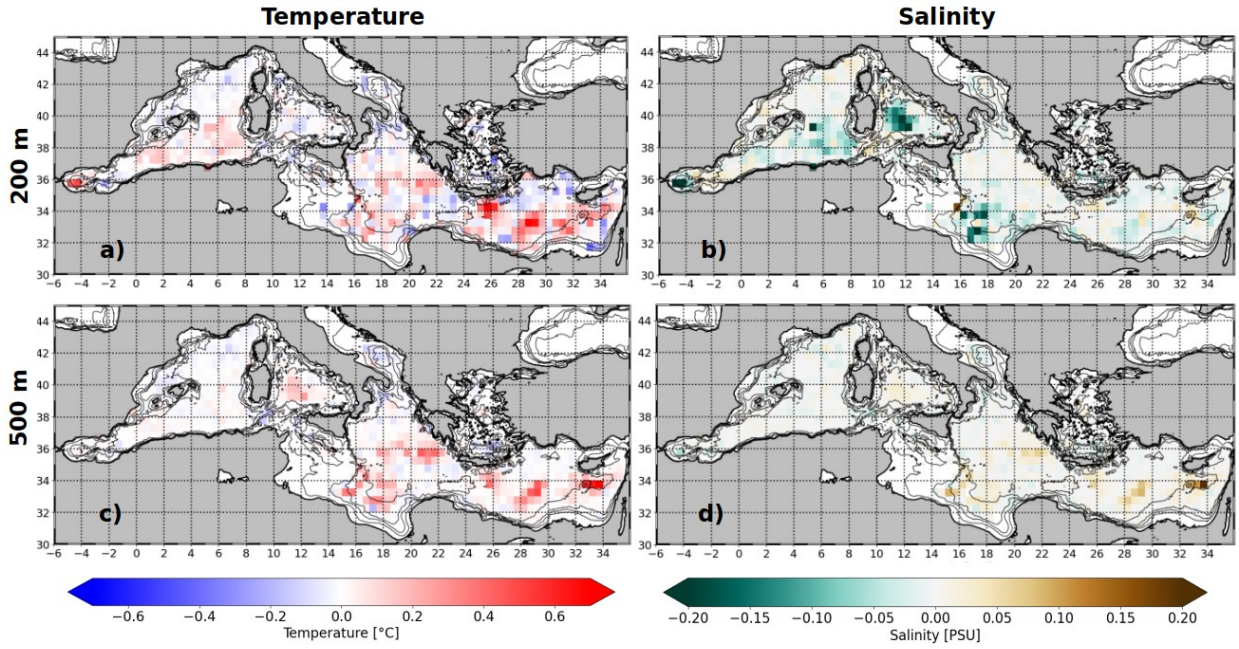

Figure A.1: Difference between the All-profiles and Without-eddies climatological approaches, showing the bias when not removing eddies from the climatology, on temperature (a,c) and salinity (b,d), at 200m (a,b) and 500m (c,d).

-0.2 PSU at 200m. In the Algerian basin there is bias of around +0.1°C and -0.1 PSU at 200m which can be explained by the influence of the warm and fresh Algerian anticyclones (Garreau et al., 2018) formed by instability of the coastal current (e.g, Millot (1985), already reporting eddy depths on the order of 200m). In the Tyrrhenian Sea the eddy signature is stronger on salinity with the influence of the Bonifacio and Central Tyrrhenian anticyclones. These anticyclones often exhibit warm anomalies in the upper 150m Ciuffardi et al. (2016) but fresher salinity anomalies up -0.2 to -0.3 PSU below 150m (Budillon et al., 2009), very consistent with Fig.A.1b (see also Fig.6.3).

At the regional Mediterranean scale, a strong eddy-induced bias can then exist when profiles inside eddies are not removed from the climatology. It is a direct impact of the eddy vertical structures, and more particularly anticyclones. It also follows the general trend of eddies in the Mediterranean Sea: eastwards, eddy anomalies tend to be warmer, switch from fresher to saltier and also tend to be deeper. This evolution can be seen at the scale of a single eddy campaign (Moutin and Prieur, 2012) or more statistically on collocated Argo profiles inside long-lived anticyclones (Stegner et al., 2019). Impact of cyclonic eddies does not seems to be significant, at least below 200m. This is not very surprising as cyclones tends to shoal isopycnals, then moving up deeper water, with less physical properties differences as gradients are at lot weaker at depth.

Mixed layer depth

Eddies also have a pronounced impact on MLD, as studied in Sect.4. We then aim to quantify the differences in term of climatological MLD between the All-profiles and Without-eddies climatologies. MLD median and spread is measured in the whole Mediterranean Sea and in three energetic eddying regions, the Algerian basin, Tyrrhenian Sea and Levantine Basin, highlighted in the map in Fig.A.2, then climatological differences are investigated in Fig.A.3. Two variables are considered: change in median MLD and MLD spread, with a temporal resolution of two weeks. As MLD distribution is skewed toward the bottom, the median is assumed more objective than the average. MLD standard deviation is also very high in the Mediterranean Sea, and often on the same order of magnitude than the MLD itself (Houpert et al., 2015). As a consequence defining the MLD spread by its standard deviation would be inaccurate, as the upper bound could then be above surface. We then consider MLD spread as the range between 20^{th} and 80^{th} MLD distribution percentile at each time step.

For most of the year, little deviation is observed between the All-profile and Without-eddy climatologies.

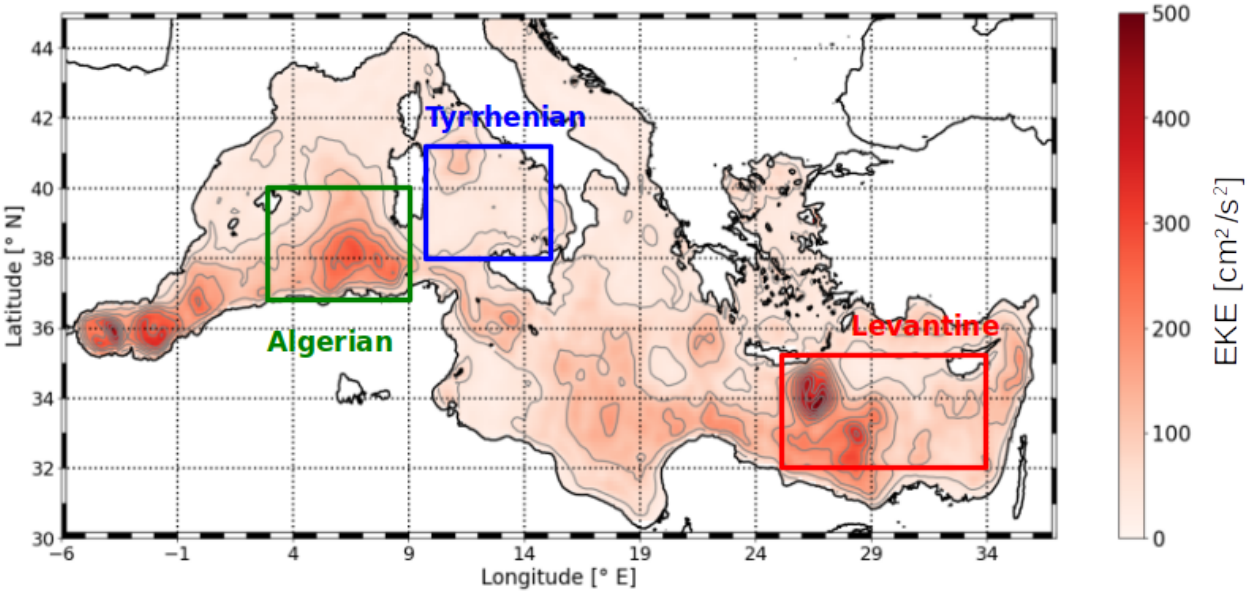

Figure A.2: Mean Eddy Kinetic Energy map of the Mediterranean Sea, showing the three eddying regions chosen to investigate climatological eddy impact on MLD.

MLD bias on the median (Fig.A.3, panels .1) is close to zero, MLD spread difference (Fig.A.3, panels .2) is very weak, and MLD distribution (Fig.A.3, panels .3) stay very close to each other. However in late winter, in February and March, significant differences are observed: in the Levantine region, the median MLD is 10 to 20m shallower, in the Tyrrhenian region it is about 10m shallower and in the Algerian region about 5m shallower. MLD spread is also significantly reduced, about 20 to 30% relative decrease in Levantine, Tyrrhenian and Algerian regions. In Levantine and Tyrrhenian regions, a significant decrease in MLD spread is also observed in late autumn, between October or November: MLD is about 20 less spread (up to 40% less spread in the Levantine region in October). This difference between both climatologies is not observed in autumn in the Algerian region, and not significantly at any time of the year when considering the Whole Mediterranean (Fig.A.3d). Some difference suggesting increased MLD spread in summer in the Without-eddy climatology are also recovered, but MLD being very shallow at this time, this is not significant. MLD distribution compared between the two climatologies revealed that despite having very little effect at the scale of the whole Mediterranean Basin, removing inside-eddy profiles from the climatology can locally slightly reduced the maximal winter MLD in eddying regions. Effect on MLD median is slight, but more interesting is the reduced MLD spread in those regions, revealing impact of eddy-induced anomalies. MLD spread remains however very high in winter (up to 100m in the Algerian and Tyrrhenian regions, up to 200m in the Levantine region). This suggests that MLD variability driven by mesoscale eddies is less important than other physical processes such as deep convection events or submesoscale instabilities. Using the Without-eddy MLD climatology instead of Houpert et al. (2015) will then mostly change spatial distribution of MLD deviations.

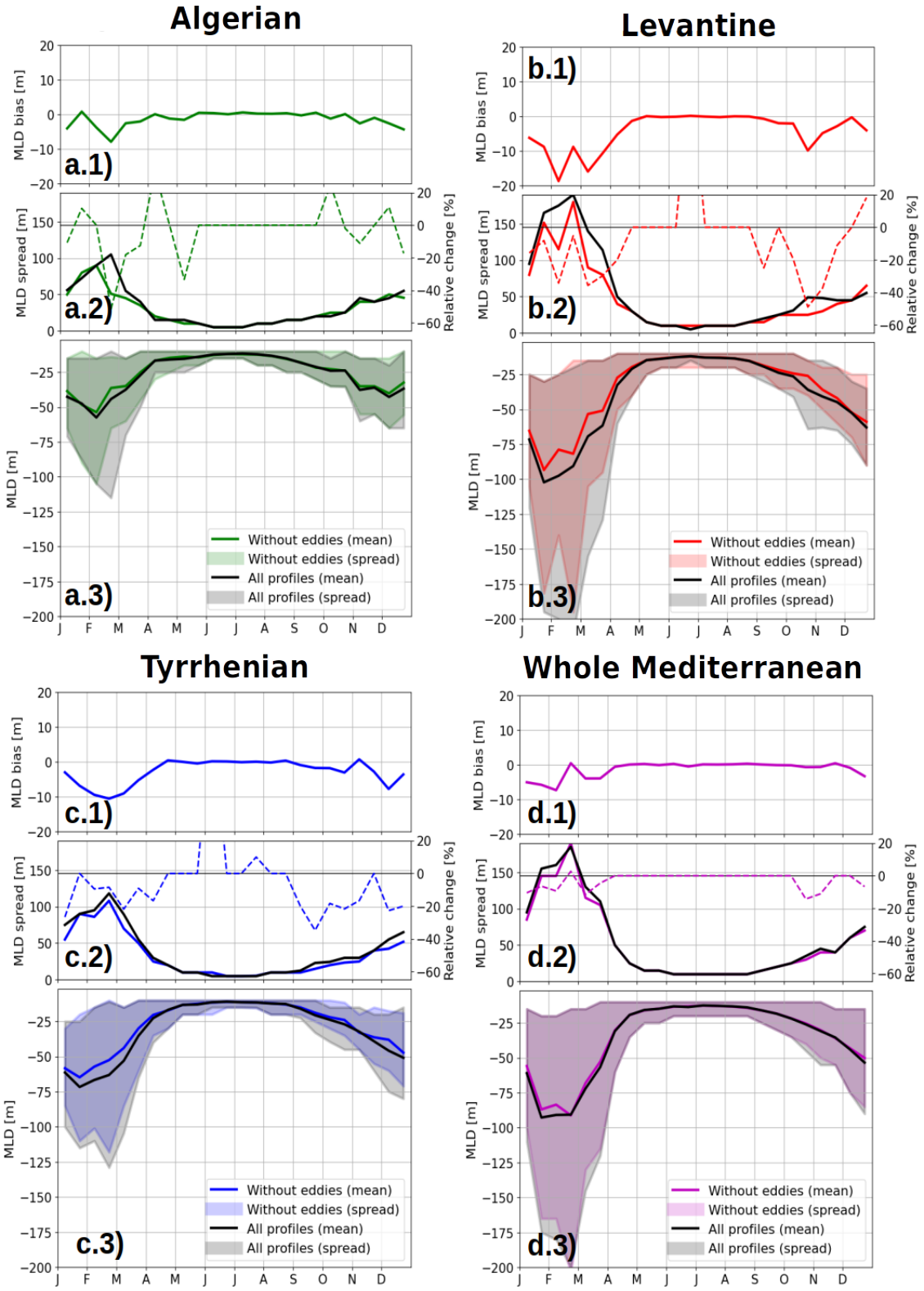

Figure A.3: MLD differences between the All-profiles and Without-eddy climatologies, for regions shown in Fig.A.2, and considering the whole basin (panel d). Subpanels .1: difference in median MLD. Subpanels .2: MLD spread in All-profiles (black continuous line) and in Without-eddy (colored continuous line) and relative difference (dashed line). Subpanels .3: MLD median (thick line) and spread (shades) in All-profiles (black) and in Without-eddy (color) climatologies.

Appendix B

Barboni et al. (2021), Lagrangian eddy tracking reveals the Eratosthenes anticyclonic attractor in the eastern Levantine Basin, *Ocean Science*

Ocean Sci., 17, 1231–1250, 2021
https://doi.org/10.5194/os-17-1231-2021

Ocean Science Open Access EGU

Lagrangian eddy tracking reveals the Eratosthenes anticyclonic attractor in the eastern Levantine Basin

Alexandre Barboni[1,2], **Ayah Lazar**[3], **Alexandre Stegner**[1], **and Evangelos Moschos**[1]

[1]Laboratoire de Météorologie Dynamique, Ecole Polytechnique, 91128 Palaiseau, France
[2]Département de Géosciences, Ecole Normale Supérieure de Paris, 75005 Paris, France
[3]Israel Oceanographic and Limnological Research, 31080 Haifa, Israel

Correspondence: Alexandre Barboni (alexandre.barboni@polytechnique.edu)

Received: 10 December 2020 – Discussion started: 11 January 2021
Revised: 11 June 2021 – Accepted: 17 June 2021 – Published: 15 September 2021

Abstract. Statistics of anticyclonic eddy activity and eddy trajectories in the Levantine Basin over the 2000–2018 period are analyzed using the DYNED-Atlas database, which links automated mesoscale eddy detection by the Angular Momentum Eddy Detection and Tracking Algorithm (AMEDA) algorithm to in situ oceanographic observations. This easternmost region of the Mediterranean Sea, delimited by the Levantine coast and Cyprus, has a complex eddying activity, which has not yet been fully characterized. In this paper, we use Lagrangian tracking to investigate the eddy fluxes and interactions between different subregions in this area. The anticyclonic structure above the Eratosthenes Seamount is identified as hosting an anticyclone attractor, constituted by a succession of long-lived anticyclones. It has a larger radius and is more persistent (staying in the same position for up to 4 years with successive merging events) than other eddies in this region. Quantification of anticyclone flux shows that anticyclones that drift towards the Eratosthenes Seamount are mainly formed along the Israeli coast or in a neighboring area west of the seamount. The southeastern Levantine area is isolated, with no anticyclone transfers to or from the western part of the basin, defining the effective attraction basin for the Eratosthenes anticyclone attractor. Colocalized in situ profiles inside eddies provide quantitative information on their subsurface physical anomaly signature, whose intensity can vary greatly with respect to the dynamical surface signature intensity. Despite interannual variability, the so-called Eratosthenes anticyclone attractor stores a larger amount of heat and salt than neighboring anticyclones, in a deeper subsurface anomaly that usually extends down to 500 m. This suggests that this attractor could concentrate heat and salt from this subbasin, which will impact the properties of intermediate water masses created there.

1 Introduction

The circulation in the eastern part of the Mediterranean Sea has not been investigated as extensively as the western part, and some aspects of its circulation are still the subject of scientific debate. Different pathways for the mean flow have been proposed with notable differences in the Gulf of Sidra and the Levantine Basin (LB) (Robinson et al., 1991; Hamad et al., 2006). Since the satellite sea surface temperature (SST) images in the 1990s, there has been overall agreement regarding the mean counterclockwise surface circulation in the eastern Mediterranean Basin, with the Atlantic waters (AWs) coming through the Strait of Sicily, following the Libyo-Egyptian coast, and then continuing along the Levantine and Turkish coasts (Hamad et al., 2006).

The Levantine Basin, defined as the part of the eastern Mediterranean, south of 37° N and east of 23° E (Hamad et al., 2006), appears to have a rather complex and turbulent circulation, particularly in its southeastern part, bound by the topography of Cyprus and the Egyptian and Levantine coasts. Extensive in situ oceanographic surveys have been performed in previous decades (Robinson et al., 1991; Brenner, 1993; Hayes et al., 2011); of note is the work of the Physical Oceanography of the Eastern Mediterranean (POEM) group, which detected some recurrent large long-lived (lasting longer than a year) anticyclonic structures in the 1980s: Ierapetra southeast of Crete and Marsa Matruh

offshore of Egypt above the Herodotus Trench, at approximately 33.2° N, 32.3° E (see scheme from Robinson et al., 1991). South of Cyprus, different authors proposed a multipole structure named "Shikmona", and they named the most active feature of this structure the "Cyprus eddy" (Brenner, 1993; Zodiatis et al., 2010). However, due to their limited time coverage, these studies had a static perspective. Zodiatis et al. (2010) probably presents the most advanced vision from this approach, displaying a hint of interannual variability. In the more recent hydrographic regionalization review of Ayata et al. (2018), the anticyclonic structure south of Cyprus is called the "Eratosthenes anticyclone", which is the name used hereafter.

In the 1990s, the development of satellite observation, initially undertaken using SST, already enabled the identification of some of these long-lived anticyclonic structures as accumulation areas for mesoscale eddies detached from the coast (Millot and Taupier-Letage, 2005; Hamad et al., 2006). Later altimetry products of sea surface height (SSH) such as Archiving, Validation, and Interpretation of Satellite Oceanographic Data (AVISO)/Copernicus Marine Environment Monitoring Service (CMEMS) with a grid resolution on the order of the deformation radius helped to investigate the unsteady dynamics of mesoscale structures in the region. Although not detected in instantaneous views, a constant and strong AW flux also exists in the center of the eastern basin in a turbulent Mid-Mediterranean Jet (MMJ) (Amitai et al., 2010). However, studies such as Amitai et al. (2010) used sea level anomalies fields (SLAs) and an Eulerian approach of turbulence instead of focusing on individual eddy behavior. Thus, eddy climatology in the LB remains unknown, and impact on water masses transport performed by such transient eddies has not yet been studied. Figure 1 presents the topography of the LB, overlaid with mean dynamic topography (MDT) from 2000 to 2018 retrieved from CMEMS at a $1/8°$ resolution. The Eratosthenes Seamount, whose summit is about 700 m deep at approximately 33.7° N, 32.7° E, appears to be a prominent topographic feature in the basin and indeed displays a mean anticyclonic circulation with a closed contour of higher MDT, coherent with recent campaigns sampling the Eratosthenes anticyclone (previously named the "Cyprus eddy") (Hayes et al., 2011; Moutin and Prieur, 2012). However, some differences from previous studies also appear, as this eddy is shifted westwards from its former reported location closer to the Levantine coast, at approximately 33.5° N, 33.5° E (Brenner, 1993; Amitai et al., 2010). Although there have been improvements in the SSH products since Amitai et al. (2010) (Taburet et al., 2019), this westward trend seems to be a physical displacement of the Eratosthenes anticyclone (Zodiatis et al., 2010).

Intense eddy activity in a basin with strong topographic constraints may lead to numerous eddy–eddy interactions, and highlights the need to take merging and splitting events between mesoscale structures into account. Initially, eddy automated detection and tracking algorithms were mostly based on SSH fields and did not detect such interactions (Chelton et al., 2011; Mason et al., 2014). Over the past decades, numerous algorithms have been further developed to take merging and splitting events into account, based on SSH (Matsuoka et al., 2016; Cui et al., 2019; Laxenaire et al., 2018) or a mixed velocity field–SSH approach (Yi et al., 2014; Le Vu et al., 2018).

The Angular Momentum Eddy Detection and Tracking Algorithm (AMEDA) developed by Le Vu et al. (2018) is used in this study. It detects eddy centers by computing the local normalized angular momentum (LNAM) introduced by Mkhinini et al. (2014) – as opposed to using the Okubo–Weiss parameter, as in Yi et al. (2014) – and computes the maximal tangential speed within the largest surrounding closed SSH contours to find eddy contours. Eddy observations at different time steps are gathered in tracks by minimizing a cost function, which considers the spatial proximity, as well as changes in eddy size and intensity. Merging and splitting events are next detected as the outcome of eddy interactions – when two eddies share a closed SSH contour with an averaged velocity higher than that for each eddy taken separately. The AMEDA algorithm has been used successfully in various case studies, notably in the Algerian Basin by Garreau et al. (2018) and in the Arabian Sea by de Marez et al. (2019). The detection of merging and splitting events enables one to reconstruct the eddy network, with mesoscale structures not being independent but often interacting with each other. Following this idea, Laxenaire et al. (2018) was able to show the connection between the Indian and Atlantic oceans through Agulhas rings crossing the Southern Atlantic. However, while several studies have developed algorithms to detect eddy interactions, we are not aware of any studies that have quantified or analyzed the additional information from merging and splitting events in terms of eddy behavior, apart from Laxenaire et al. (2018).

Nevertheless, satellite analysis alone cannot reveal the subsurface structure. Moutin and Prieur (2012), for instance, studied three anticyclones in the Mediterranean Sea with similar SLA signatures but discovered extremely different heat and salt integrated anomalies. In the LB, Gertman et al. (2010) discovered smaller-scale eddies detaching from the Israeli coast through SST and drifters data, and Hayes et al. (2011) discovered a huge salt anomaly in the Eratosthenes anticyclone despite a weak SSH signature. These studies show the importance of in situ observations in addition to satellite data, but they were campaign-specific instantaneous observations. Before eddy automated detection, Menna et al. (2012) conducted a statistical study of mesoscale interactions in the LB by adding in situ drifter velocities to SSH-derived velocities, but sampling was sparse and without vertical information. The large-scale deployment of autonomous drifters in the global ocean (such as the Argo or MEOP programs), as well as the centralization of collected data (such as CMEMS products), enables one to bridge the gap in the temporal scale between satellite and in situ data. Argo is a global

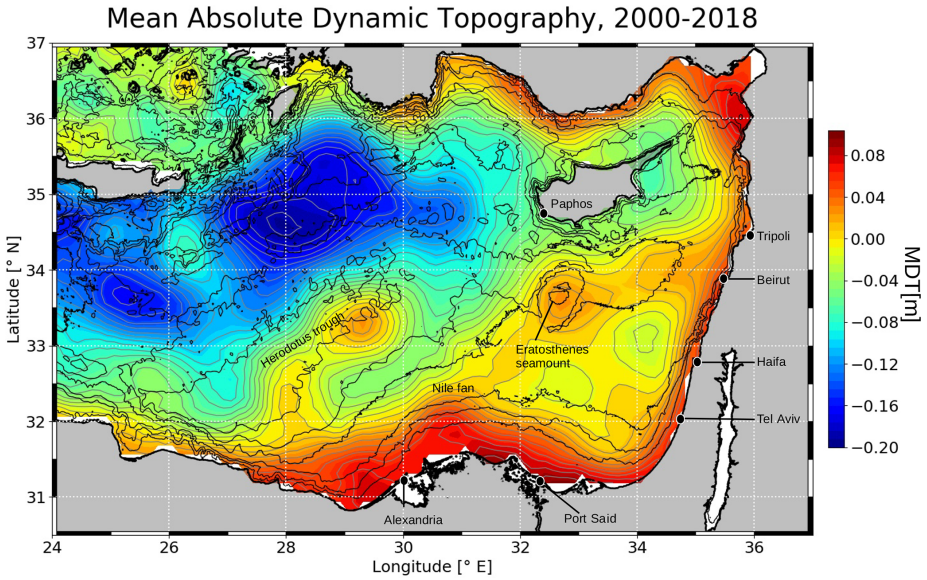

Figure 1. Mean dynamic topography (MDT) map of the LB and several toponyms used in this study. Thin black lines are the −100, −500, −1000, −1500, −2000 and −2500 m isobaths, and the thick black line is the 0 m isobath. Bathymetry is retrieved from GEBCO (2020). The same isobaths are shown on all maps.

array of more than 3000 floats measuring temperature and salinity down to 2000 m (ARGO, 2020). Using Argo data, Laxenaire et al. (2019) captured the subsurface evolution of one single Agulhas ring over 1.5 years in the South Atlantic with the conjunction of Argo profiles and SSH data. This demonstrates that long-lived anticyclones can transport warm water masses over very long distances isolated in their thick core. Recently, in the Algerian Basin, Pessini et al. (2018) attempted to link eddy observations to in situ measurements and to compute eddy regional statistics, although they utilized an algorithm that did account for merging and splitting events. Mason et al. (2019) also attempted to study the vertical eddy structure with regional variation in the Alboran Sea, although they used data from assimilated models. Thus far, no such regional characterization of eddy systematic detection has been attempted in the eastern Mediterranean.

This approach of both eddy tracking, detected by altimetry that takes merging and splitting events into account, and co-localization with in situ observations can be generalized into an eddy atlas. The DYNED-Atlas database combines over 19 years of subsurface observations from Argo floats of identified eddies, tracked in time and space by the AMEDA algorithm (DYNED-Atlas-Med, 2019). The DYNED-Atlas is the perfect tool for the study of eddy dynamics and the associated transport of water masses in their cores, as it combines eddy detection and physical properties. It has not been exploited in the LB yet, although Stegner et al. (2019) already demonstrated very deep subsurface eddy signatures in this area.

Using eddy contours, tracks and co-localized profiles from the DYNED-Atlas database, extended with available expendable bathythermograph (XBT) and conductivity–temperature–density (CTD) profiles to compensate for the sparsity of observations, this study will investigate additional information from Lagrangian anticyclone tracking and statistically significant drift patterns and structures in the south-eastern LB – east of 28° E and south of Cyprus. After introducing the datasets in Sect. 2, we present our methodology of a Lagrangian convergence framework and the regions studied in Sect. 3. Analysis of this method with DYNED-Atlas data is detailed in Sect. 4. Vertical structure oceanographic observations co-localized inside eddies are used to study the eddy vertical signatures (Sect. 5). Possible mechanisms at work and hydrographic effects are discussed in Sect. 6.

2 Data

2.1 Eddy contours, centers and tracks

The dynamical evolution of eddies and their individual tracks are retrieved from the DYNED-Atlas database (DYNED-Atlas-Med, 2019) for the 2000–2018 period. The DYNED-Atlas project, with eddy tracks and physical property signatures, is accessible online: https://www1.lmd.polytechnique.fr/dyned/ (last access: 18 August 2021). The dynamical characteristics of the eddies contained in the DYNED-Atlas database were computed by the AMEDA eddy detection algorithm (Le Vu et al., 2018) applied on daily surface velocity fields. The latter were derived from the absolute dynamic topography (ADT) maps produced by Salto/Duacs and distributed by the Copernicus Marine Environment Monitoring Service (CMEMS) with a spatial resolution of 1/8°,

which is on the order of the internal deformation radius in the Mediterranean Sea (10–12 km; Mkhinini et al., 2014). A cyclostrophic correction is applied on these geostrophic velocities to accurately quantify eddy dynamical properties (Ioannou et al., 2019). Unlike standard eddy detection and tracking algorithms, the main advantage of the AMEDA algorithm is that it detects the merging and the splitting events (Le Vu et al., 2018), which allows one to build a network of trajectories associated with each eddy. In other words, we can reconstruct the eddy's "genealogy".

2.2 Remote sensing measurements

To compute the MDT over the 2000–2018 period, we use the daily high-resolution (1/8°) AVISO ADT delayed-time product provided by CMEMS (SEALEVEL_MED_PHY_L4_REP_OBSERVATIONS_008_051). This altimetry gridded product is also used to locate the in situ CTD or glider measurements associated with the characteristic eddy contours in Sect. 5. Otherwise, to more precisely confirm the location of eddies and their size on specific days, we use the high-resolution (1/120°) merged-multisensor SST data representative of nighttime values provided by CMEMS (SST_MED_SST_L3S_NRT_OBSERVATIONS_010_012).

2.3 In situ oceanographic observations

About 34 406 Argo profiles are available from the DYNED-Atlas database in the whole Mediterranean Sea over this 19-year period. However, due to sparser campaigns, only 9384 were available in the LB, mostly after 2014. To complete these in situ measurements, we added 2311 CTD and 3860 XBT casts downloaded from the SeaDataNet portal (https://www.seadatanet.org/Data-Access, last access: 15 June 2020, data in unrestricted access) as well as 7020 additional profiles from the CORA (Coriolis Ocean database ReAnalysis) database, which is also available on the CMEMS catalogue: INSITU_GLO_TS_REP_OBSERVATIONS_013_001_b (https://resources.marine.copernicus.eu/?option=com_csw&view=details&product_id=INSITU_GLO_TS_REP_OBSERVATIONS_013_001_b, last access: 15 June 2020). Finally, glider measurements carried out in October 2018 by the Israel Oceanographic and Limnological Research (IOLR) in one transect offshore of Israel provided 370 profiles that were added to the database. The data sources listed above add up to 22 945 profiles from 2000 to 2018 in the LB. All of the hydrological profiles are then co-localized with detected eddies following the standard procedure used in the DYNED-Atlas database. Profiles are considered to be inside an eddy if they are inside its maximal speed contour.

3 Methodology

As opposed to previous studies that either considered eddy activity from "building-block" structures (Robinson et al., 1991) or eddy kinetic energy (EKE) fields derived from SLA compared to a MDT (Amitai et al., 2010), we follow eddies as daily, individual detections gathered in tracks. Eddies are not only active as individuals but also as a network of turbulent structures interacting with each other. Hence, the importance of taking merging and splitting events into account to reconstruct this network. This approach then aims to quantify eddy transfers between different subregions. This is similar to and greatly inspired by the previous work done by Laxenaire et al. (2018) for Agulhas rings in the South Atlantic.

3.1 Lagrangian convergence framework

Here, we define a framework to count eddy transfers imported to and exported from a study region, whose successive steps are shown in Fig. 2. The Eratosthenes Seamount region, studied as an example in Fig. 2, is bordered by a green line (coordinates in Table A1).

We consider importing eddies to be the eddies that are part of the family tree coming into a region. The order 0 eddies are defined as those converging directly to the region (the trajectories shown using blue lines in Fig. 2a). This order 0 label mainly encompasses eddies dying within the study region; however, some eddies can remain stationary for a very long period in the same area, later moving and dying in another place. In order to take the latter into account, the definition of an order 0 eddy is an eddy dying or spending more than half of its lifetime inside the perimeter of the study region. The sensitivity of this 50 % lifetime criterion is detailed in Fig. A1 in the Appendix, and this definition does not lead to inaccurately counting eddies that are just transiting the region as importing eddies. Indeed, eddies labeled as order 0 always disappear from the immediate vicinity when leaving the study region (see Fig. A2 for an example). Next, we label the eddies that merge with an order 0 eddy as order 1 (Fig. 2b, cyan lines). Recursively, we label the eddies that merge with an order 1 eddy as order 2 (not shown in Fig. 2 but displayed in Fig. 6a). Hereafter, we will discard orders higher than 2 from the discussion, as their quantity was found to be negligible.

In contrast, an exporting eddy flux moves some eddies outside of the region. We distinguish two categories of exporting eddies: (1) if two eddies undergo a splitting event and one of the split eddies spends more than half of its lifetime outside the region, it is considered an exporting split eddy; (2) if an order 0 eddy dies while merging with external eddies which themselves drift away from the region, this external eddy is considered an exporting merging eddy. Exporting split (yellow dashed lines) and merging (red dashed lines) eddies are shown in the example in Fig. 2c; however, none of the latter were detected for this particular region.

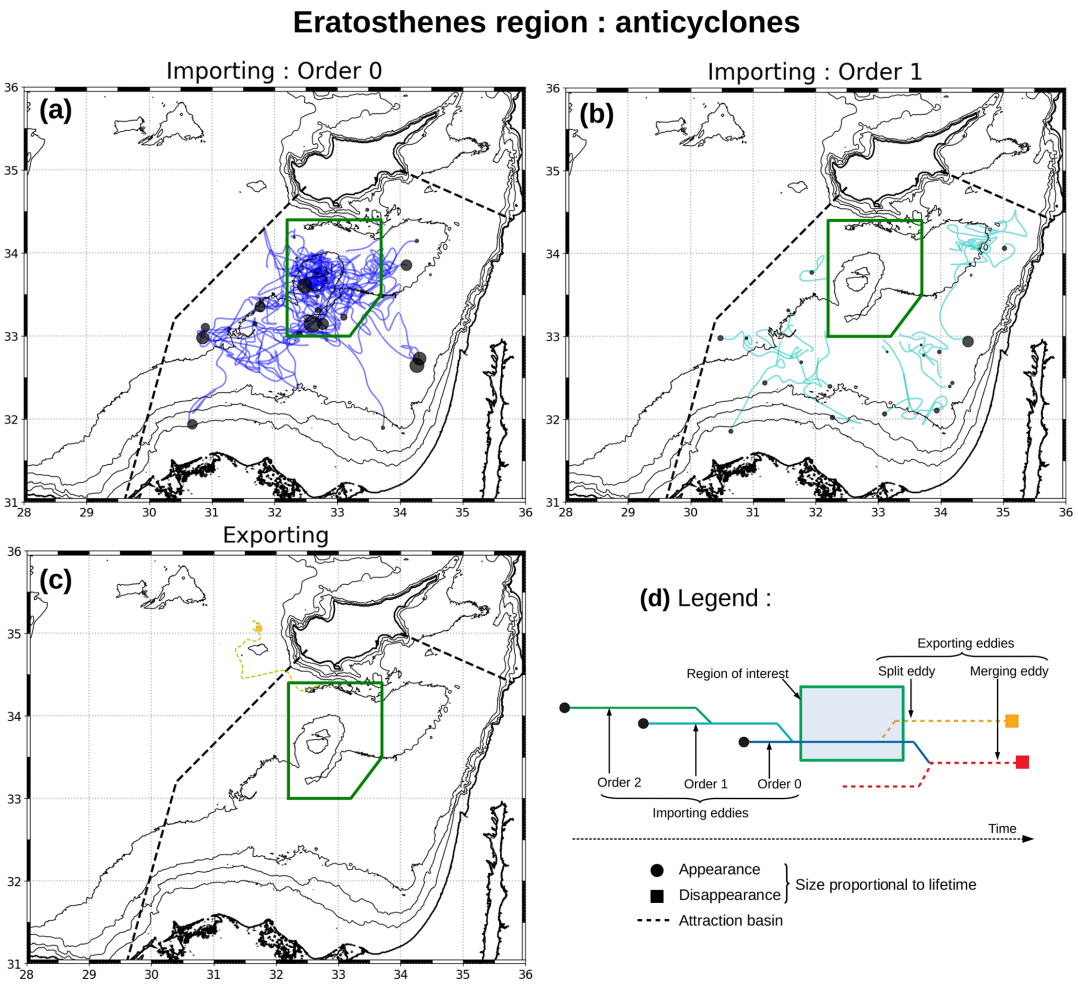

Figure 2. Lagrangian convergence framework applied to anticyclones in the Eratosthenes Seamount region and detailed in several steps: **(a)** order 0 – eddies converging directly; **(b)** order 1 – eddies merging with an order 0 eddy; **(c)** exporting split and merging eddies (no cases of the latter detected here). Locations of eddy appearance **(a, b)** and eddy disappearance (**c**) are shown using black dots and colored squares, respectively, the size of which is proportional to the eddy lifetime. **(d)** The black dashed line is the attraction basin introduced in Sect. 4.3.

It should be noted that, in this framework, the order 0 label prevails over other labels defined: if an eddy meets the criteria for both order 0 and order 1, it is labeled as order 0 only. Additionally, exporting (split and merging) eddies are labeled as such only if they are not already labeled as an importing eddy. It should also be noted that eddies labeled as order 0 can be born within or outside of the given region. Lastly, a label is relative to a region: an eddy spending more than half of its lifetime in a region but drifting and dying in another is labeled as importing order 0 for both regions (see the discussion about Table A2 in Sect. 4.2). In this framework and in the figures hereafter, importing eddies are plotted at their appearance location using black dots with sizes proportional to the eddy lifetime to show the origin of the water masses. Exporting split and merging eddies are plotted at their disappearance location as squares, also scaled according to their lifetime. Trajectories are smoothed through a (10 km × 10 km) window. The color chart is summarized in Fig. 2d and used throughout this study.

Finally, attractiveness of a region with respect to eddies – for a given polarity – is estimated in the "net eddy gain". This is the total number of importing eddies – the sum of orders 0–1–2 and possibly higher – minus the number of eddies already born in the region of interest. This gain is later shown in Table A2 and discussed in Sect. 4.2.

3.2 Definition of anticyclonic and cyclonic regions

To further study the exchanges between eddying structures in the southeastern part of the LB, eight regions of interest are considered and shown in the MDT in Fig. 3. These regions are defined as closely as possible to nonoverlapping rectangular shapes, tiling as much of the southeastern corner of the LB as possible (≈ 78 % of the attraction basin discussed in Sect. 4.3 is covered) and with a similar size (areas and co-

ordinates provided in Table A1 in the Appendix). Each box is defined to correspond to a structure in the MDT. Average cyclonic or anticyclonic activity can be inferred if it encompasses a depression or a hill in the MDT, respectively; hereafter, we refer to these regions as cyclonic (CY) or anticyclonic (AC) regions, respectively: Beirut (AC), Haifa (CY), Tel Aviv (AC), Port Said (CY), Herodotus (AC), Nile (AC) and Eratosthenes (AC, already shown in Fig. 2). Although not in our focus region, a comparison focused on the "Marsa Matruh" (AC) region is also carried out in Sect. 4.5. The eight distinct regions are presented on Fig. 3 with red or green solid borders denoting CY or AC regions, respectively. The attraction basin of the Eratosthenes region (see Sect. 4.3) is shown with a dashed line.

3.3 Eddy-induced physical property anomalies

The DYNED-Atlas database establishes a method to estimate the physical property anomalies induced by an eddy (DYNED-Atlas-Med, 2019). This method is followed in this study, only extending the database with profiles from sources other than Argo and using in situ temperature instead of potential temperature to match up with XBT profiles. Each oceanographic measurement is compared to the AMEDA observations. If it falls within the contour of an eddy on the same day that it is cast, the profile is co-localized with the eddy and then considered as sampling its physical properties. If it falls outside any eddy observation, it is considered an "outside-eddy" profile. Estimation of the eddy-induced physical property anomalies (temperature, salinity, density) is next done by comparison with a reference background. For each observation, a climatological background is then computed by averaging all outside-eddy profiles from 2000 to 2018, at a distance smaller than 150 km from the its cast position and in the same season (in any year, but within a ± 30 d period from the day of the cast). It is intended to be more statistically significant than estimates performed during a single campaign, usually through one profile inside an eddy and another one outside (e.g., Moutin and Prieur, 2012).

4 Lagrangian tracking results

4.1 Eddy activity from a Lagrangian framework

Figure 4 presents eddy occurrence and drift in the LB for anticyclones and cyclones, with the designated regions from Fig. 3. Time occurrence percentage (shown using color) is computed as the time spent inside the maximal speed contour of a detected eddy, whereas the drift (shown with arrows) is the mean speed of eddy centers passing through the pixel. The pixel size is $1/8^\circ \times 1/8^\circ$. Gaussian smoothing is performed using a 5 pixel $\times$ 5 pixel kernel size, and data from pixels crossed by less than five eddy centers are discarded. This picture can be seen as an eddy Lagrangian approach equivalent to the MDT shown in Figs. 1 and 3, adding new information. Firstly, the spatial distribution of cyclonic and anticyclonic eddies is extremely inhomogeneous: almost no anticyclones are present in the northern part of the LB. The prevalence of the Marsa Matruh and Eratosthenes structures as persistent anticyclones is confirmed, with coherent spots hosting anticyclones for more than 50 % of the 2000–2018 time period. Cyclones are present in the southeastern part of the LB, in particular in the Haifa region. All anticyclonic (cyclonic) regions have on average a higher presence of anticyclones (cyclones), confirming (through a Lagrangian approach) the regions defined in Sect. 3.2. The comparison with the Ierapetra eddies southeast of Crete in Fig. 4 highlights the difference between Lagrangian and Eulerian visions. The Ierapetra eddies show up very clearly in SLA maps and are the most intense eddies in the region (Amitai et al., 2010). However, as they do not have fixed stable position and can drift far away after their formation (Ioannou et al., 2017), they form a less concentrated spot in Fig. 4. The Lagrangian vision then shows more persistent, although maybe less intense, structures.

Additionally, Fig. 5 shows eddy lifetime statistics in the LB, with a comparison of the normalized cumulative eddy lifetime (i.e., the probability for an eddy to live longer than a given time period). In the Mediterranean Sea, the lifetime for cyclones is on average far shorter than for anticyclones, as already shown by Mkhinini et al. (2014). However, this disequilibrium is even more pronounced in the LB: the cyclones lifetime distribution is very similar to the rest of the Mediterranean, whereas anticyclones clearly tend to live longer. As an example, in absolute units of detected eddies, 105 anticyclones (out of 5770) compared with 70 cyclones (out of 7159) are found to live longer than 400 d in the whole Mediterranean, whereas in the LB, 39 anticyclones (out of 1210) compared with 17 cyclones (out of 1630) live longer than 400 d. The intense Ierapetra anticyclones have been shown to often live more than 3 years (Ioannou et al., 2017); however, as no more than one of these eddies is formed each year, they can not explain the trend of longer anticyclone lifetimes. These statistics suggest the existence of mechanisms prolonging anticyclone lifetimes in the LB. Hence, this study specifically focuses on anticyclones, whose longer lifetimes also lead them to capture water masses in their core for an extended period and have higher hydrologic impact.

4.2 Inter-region anticyclone transfers

The Lagrangian convergence framework detailed in Sect. 3.1 is applied to the seven regions of the southeastern LB (Eratosthenes, Beirut, Haifa, Tel Aviv, Port Said, Herodotus and Nile, with Marsa Matruh being studied later in Sect. 4.5) in Fig. 6, only considering anticyclones (statistics also shown in Table A2). The color code is the same as in Fig. 2 and Fig. 6h. For each panel in Fig. 6, all other regions are shown, with green (red) borders for AC (CY) regions. The region to which each panel title refers is outlined using a thicker line.

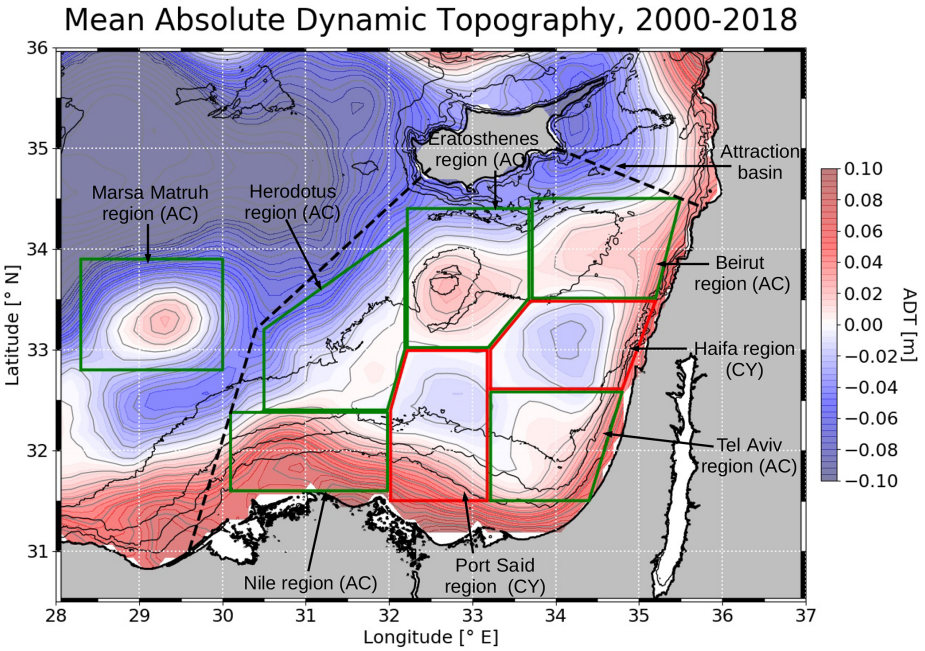

Figure 3. Mean dynamic topography (MDT) map of the southeastern LB labeled with borders and names of the study regions. Anticyclonic regions (AC) have a green border, cyclonic regions (CY) have a red border, and boxes are based on the coordinates indicated in the Appendix (Table A1). The black dashed line is the attraction basin introduced in Sect. 4.3.

For all AC regions (Fig. 6a, b, d, f, g), anticyclones trajectories form a rather concentrated bulk at the center of the region, whereas CY regions (Fig. 6c, e) only have a very sparse and random anticyclone occurrence. The mean dynamical activity from Sect. 3.2 is confirmed, as only AC regions host a preference spot for anticyclones, whereas CY regions tend to be avoided by anticyclones.

Important differences can, however, be noted between AC regions. In the Beirut region, anticyclones meander a lot but have few interactions (only two merging events and two splitting events in 19 years) and eddies have a moderate lifetime (126 d). In the Tel Aviv region, anticyclones are more short-lived (97 d on average), spend less time in the region with few meanders and four merging exports were recorded for the benefit of the Eratosthenes region; this characterizes the Tel Aviv region as an anticyclone formation region. Characterizing the Herodotus region is more difficult, as some eddies stem from the Nile region and some others eventually merge with Eratosthenes region long-lived anticyclones; thus, the Herodotus region seems to act as an anticyclone formation region (42 anticyclones born there) but also as a transitory region with respect to the Eratosthenes zone, with which it interacts a lot (eight merging exports). On the contrary, the Nile region is a strong and preferred anticyclonic spot, but eddies there interact very little with neighboring regions; the Nile region rather acts as a termination region for anticyclones formed to the west and following the Libyo-Egyptian coast.

Nonetheless, some anticyclones are formed inside CY regions, notably in the Haifa region. In this region anticyclones are generally short-lived (average lifetime of 94 d) and often disappear while being exported to the Eratosthenes region (six merging events recorded); the role of the Haifa region is then similar to the Tel Aviv region, acting as a region of anticyclone formation. The case of the Port Said region is more ambiguous, with no clear pattern being visible. Statistics in the Appendix (Table A2) seem to show that it attracts some anticyclones, but this can be due to the fact that some long-lived eddies of the Eratosthenes region sometimes venture approximately 100 km farther south. This ambiguity also shows the limits of this Lagrangian approach, as it is sensitive to a singular event for eddies with lifetimes longer than 3 years. As a comparison, Fig. A3 shows the same analysis as Fig. 6b for the Haifa region but studying cyclone transfers. Patterns for cyclones are less clear than for anticyclones, likely because cyclones have shorter lifetimes and are, thus, more numerous. However, it confirmed the Haifa region as a stable spot for cyclones.

4.3 Eratosthenes anticyclone attractor (EAA)

Figure 7 and Table A2 summarize anticyclone transfers in the southeastern LB. The attractiveness of each region is measured through the net eddy gain introduced in Sect. 3.1. The arrows in Fig. 7 indicate eddy transfers, with the thickness being proportional to the number of eddies transferred. The particular case of the Eratosthenes region shows a clear con-

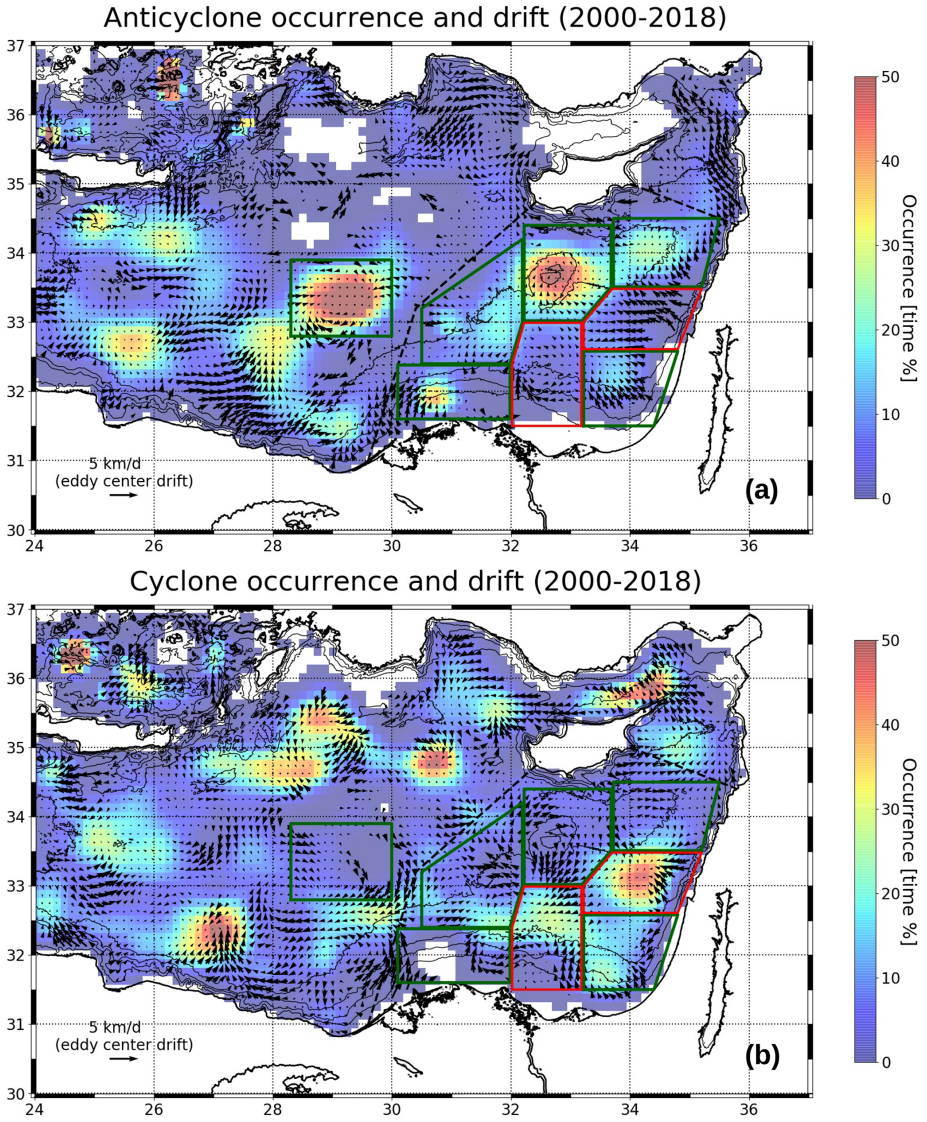

Figure 4. Eddy occurrence and drift in the LB for **(a)** anticyclones and **(b)** cyclones. The pixel size is $1/8° \times 1/8°$. Occurrence is shown as the time percentage that the pixel center spends inside maximal speed contours of eddies. Eddy drift is the mean Lagrangian drift of the eddy centers on pixels that more than five eddy centers passed; Gaussian smoothing is carried out with a 5×5 kernel size. The AC (CY) regions defined in Sect. 3.2 are drawn using a green (red) solid line, and the attraction basin defined in Sect. 4.3 is drawn using a black dashed line.

vergence with 44 importing anticyclones attracted, whereas only 14 were initially born in the region surrounding the Eratosthenes Seamount, from 2000 to 2018; this results in a net eddy gain of +30 and an approximate anticyclone flux of more than one merging per year. Instead of freely drifting westwards as expected from the β-drift (Chelton et al., 2011), anticyclone tracks shown in Fig. 2b (or alternatively Fig. 6a) reveal that eddies meander a lot over the high bathymetry, as shown by the density of blue tracks, seemingly trapped by the seamount. On the other hand, few exporting split eddies escape, and not a single exporting merging eddy is detected; these split eddies are even more short-lived, as shown by the small size of the disappearance square (Fig. 2c). This trend of a high net eddy gain along with few exporting eddies and the persistent anticyclonic activity in the Eratosthenes region (Fig. 4) allows for the identification of this region as hosting an anticyclonic attractor, which is hereafter referred to as the "Eratosthenes anticyclone attractor" (EAA).

Moreover, this observed convergence toward the Eratosthenes Seamount seems to be geographically bound, with the tracks in Fig. 2a–b showing that anticyclones come from as far as 300 km away but with a distinct westward limit, depicted by a black dashed line. This area of anticyclones converging to the EAA, although constrained by topography, covers a large part of the southeastern LB and is called the EAA attraction basin in this study (see Figs. 3, 4, 6 and 7). It

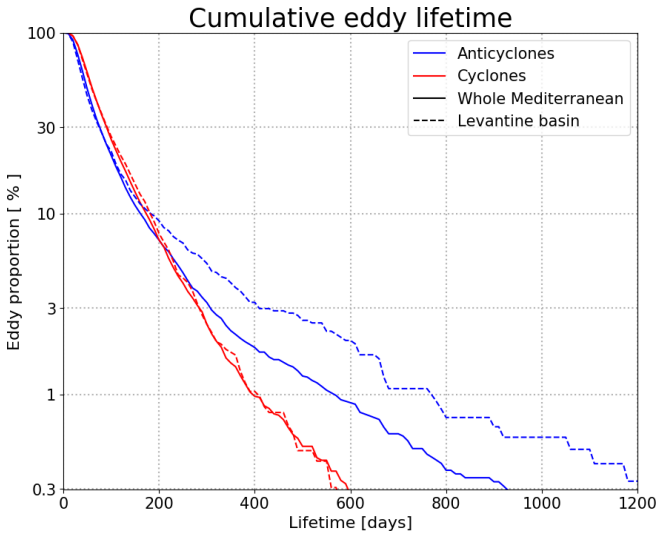

Figure 5. Cumulative eddy lifetime as a percentage on a logarithmic scale, separated for cyclones and anticyclones and for the LB and the whole Mediterranean Sea.

is defined as a straight line ranging from the Egyptian city of Alexandria (31.0° N, 29.6° E) to the Cypriot city of Paphos (34.8° N, 30.4° E) with a break angle at 33.2° N, 30.4° E and a second line closing it between the Greek cape on Cyprus island (35.0° N, 34.1° E) and the Lebanese city of Tripoli (34.4° N, 35.8° E).

Finally, Fig. 8 analyses the anticyclones constituting the EAA (i.e., order 0 importing anticyclones for the Eratosthenes region, shown using blue lines in Fig. 6a). The upper panel of Fig. 8 presents their time series, with the color indicating when the center is inside or outside of the region. An anticyclone is always present inside the region, with relay between long-lived eddies: each time an anticyclone inside the region dies, it is replaced by another, leading to only about 1 year out of 19 without an anticyclone over the Eratosthenes Seamount. Anticyclones in the Eratosthenes region also tend to be very different from their neighbors. Figure 8b classifies anticyclones in terms of mean maximal speed radius as a function of lifetime; each dot is an anticyclone labeled as order 0 for the seven regions studied in Fig. 6, with red color highlighting Eratosthenes anticyclones. The background is a density probability plot for all anticyclones in the LB – except Eratosthenes anticyclones to enhance comparison. The scatterplot presents an overall spread, with maximal density between 15 and 25 km, consistent with the limit of altimetric resolution (1/8°). However, long-lived Eratosthenes anticyclones form a clear cluster of eddies living longer than a year with a radius often greater than 40 km, outside the 90 % probability contour. Not all Eratosthenes anticyclones are encompassed in this category because the order 0 label also encompasses some short-lived eddies quickly merging, which unlikely have unusual characteristics – hence some of the red dots also being scattered. Eratosthenes anticyclones are the only eddies in the southeastern part of the LB that present such dynamical characteristics: apart from two outliers, this is the only region where the maximal speed radius can exceed 40 km, more than 3 times the internal deformation radius of approximately 10–12 km in the Mediterranean Sea (Mkhinini et al., 2014). This suggests the existence of different mechanisms acting on the eddy lifetime and radius.

4.4 Anticyclones detachments from the Levantine coast

In Sect. 4.3, the Eratosthenes attraction basin was identified, notably attracting anticyclones originally formed near the Levantine coast as seen in altimetric tracks (see Fig. 6a). However, altimetric eddy detections have important limitations stemming from the large spatiotemporal interpolation between satellite measurement tracks. This makes the resolution of altimetric maps (1/8° in the Mediterranean Sea) insufficient to adequately detect small-scale structures and introduces uncertainty in the detection, especially as the internal deformation radius is small (Le Vu et al., 2018). Nevertheless, other sources of satellite images such as SST contain visible eddy signatures on them (Moschos et al., 2020). On such images, we can observe filament exchanges between eddies as well as eddies moving too fast to be detected via altimetry, such as the eddies detaching from the Levantine coast. Gertman et al. (2010) spotted such a detachment in August 2009 by means of in situ data from drifting buoys. Here, we provide observational evidence from SST images of a similar event occurring on July 2016: a detached warm-core anticyclonic ring, part of a cyclone–anticyclone dipole, rapidly merged with another anticyclonic eddy that later subsequently merged with the Eratosthenes anticyclone. Figure 9 portrays this event through four daily SST image snapshots where the altimetric detection DYNED contours have been superimposed. An anticyclone not detected by surface altimetry with a particularly warm surface signature can be spotted on the right-hand side of Fig. 9a (17 July 2016). A cyclone with which it forms a dipole can be seen from the SST in its southeast corner and is also detected by the altimetry somewhat more southwards. In Fig. 9b, 5 d later (22 July 2016), this anticyclone has moved rapidly towards the DYNED anticyclone no. 10754, which was first detected offshore of Haifa on 10 February 2016. The track of DYNED anticyclone no. 10754 is depicted using a blue line. The warm-core detached anticyclone will eventually merge with it 6 d later (28 July 2016; Fig. 9c). A month later (2 September 2016; Fig. 9d), this anticyclone will eventually merge with the eddy on the Eratosthenes Seamount, having transferred the warm waters and the momentum of the detached warm-core eddy.

4.5 Marsa Matruh attractor

Eddy attraction to the other big anticyclonic structure of the region, called “Marsa Matruh”, can be studied in compari-

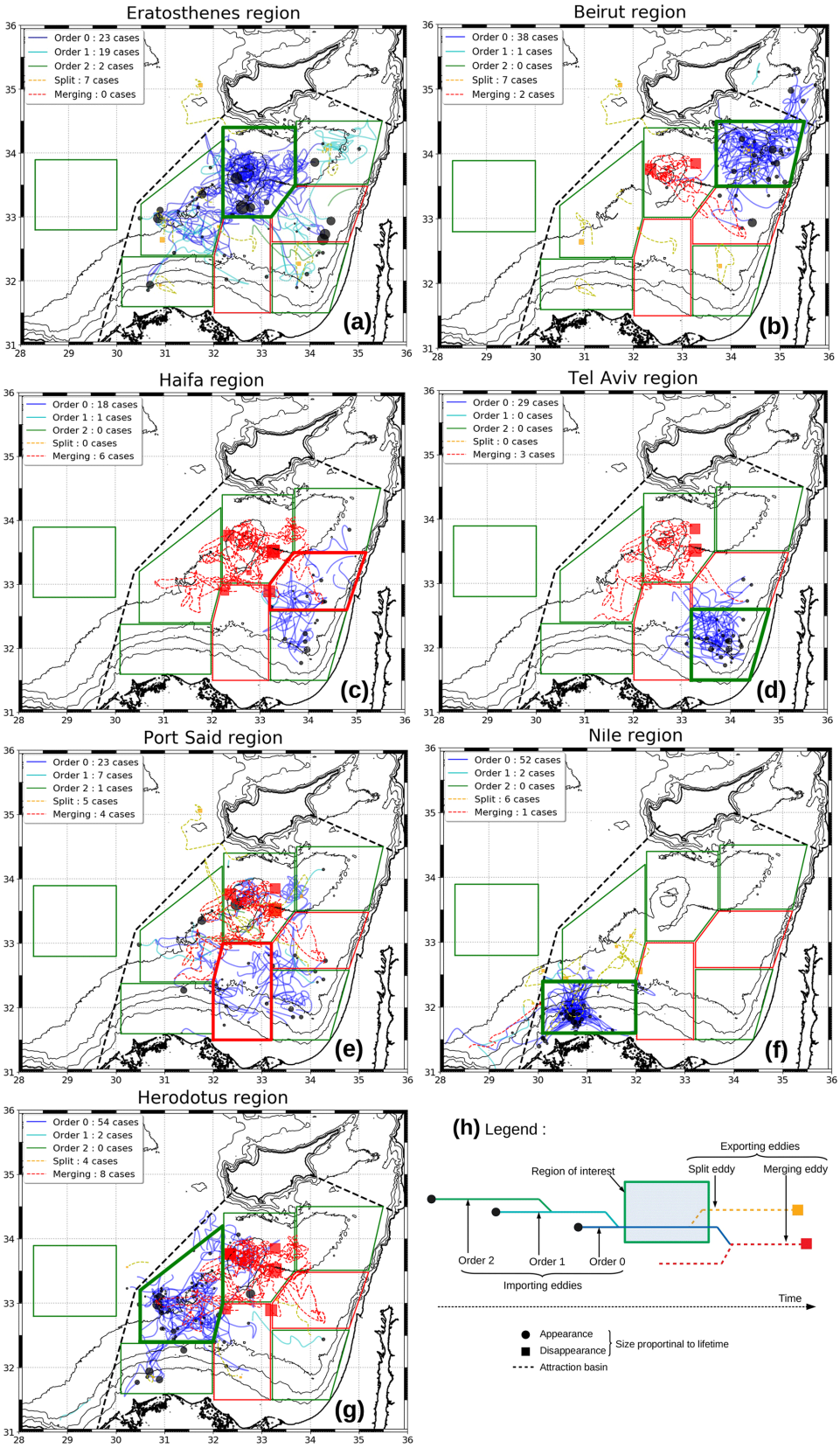

Figure 6. Eddy exchanges framework applied to the **(a)** Eratosthenes, **(b)** Beirut, **(c)** Haifa, **(d)** Tel Aviv, **(e)** Port Said, **(f)** Nile and **(g)** Herodotus regions. For each panel, all other regions are shown (green borders for AC regions, and red borders for CY regions); the thicker line indicates the study region. The color chart used is summarized in panel **(h)**. The Marsa Matruh region is studied later in Fig. 10.

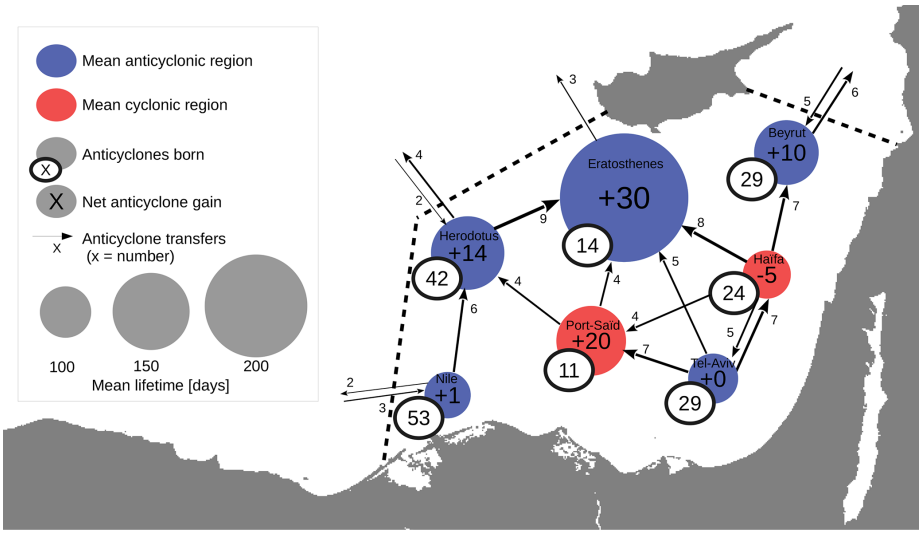

Figure 7. Scheme summarizing inter-region anticyclone transfers within the Eratosthenes anticyclone attractor (EAA) attraction basin (dashed line). Transfers encompass order 0–1–2 anticyclones. Within this basin, only transfers higher than or equal to 4 are represented by arrows (for legibility). All transfers across the basin border are shown. The arrow thickness is proportional to eddy transfers. Red circles represent CY regions, and blue circles represent AC regions; radii are proportional to the anticyclone mean lifetime in the region. More details are given in Table A2.

son to the Eratosthenes attractor. In Fig. 10, the Lagrangian framework defined in Sect. 3.1 is applied to this region. Firstly, it is notable that this structure clearly also acts as an attractor, with the total number of importing eddies (sum of orders 0–1–2) being a lot higher than order 0 alone and exporting eddies. In a similar fashion to the Eratosthenes region, which acts as a stranding place for anticyclones detached from the Levantine coast, a lot of the anticyclones that are detached from the Libyo-Egyptian coast (likely as instability of the Libyo-Egyptian current) end in the Marsa Matruh region, often through one merging event or more. In particular, a hotspot of anticyclone formation takes place in the Marsa Matruh gulf at approximately 31.5° N, 27.5° E, from which five anticyclones drifted towards the Marsa Matruh structure. No importing anticyclones come from the north, as expected given that almost no anticyclones occur in the Rhodes gyre (see Fig. 4a).

However, in contrast to the Eratosthenes attraction basin which is isolated with very few anticyclone exchanges outside, the Marsa Matruh anticyclone has no clear western boundaries. For instance, some merging export trajectories in red are present southwestwards, highlighting that some eddies escaped from this structure. On the contrary, one Ierapetra eddy did end through successive merging events into the Marsa Matruh area. This individual event seems to be isolated, as shown in Ioannou et al. (2017), Ierapetra eddies actually tend to go westwards, riding up the Libyo-Egyptian current, if they move away, in a similar way to the eddy behavior described by Sutyrin et al. (2009). More generally, the importance of higher-order anticyclones merging in successive steps to the Marsa Matruh anticyclone suggests that convergence is less straightforward and clear than for the EAA, likely because topographic constraints are less present.

5 Vertical structure of the Eratosthenes anticyclone attractor

The DYNED-Atlas co-localization and background method (see Sect. 3.3) is used to estimate the heat, salt and density anomalies associated with each eddy. For very persistent long-lived eddies, such as those constituting the EAA, this allows one to observe changes in the vertical structure and the evolution of the associated anomalies. Figure 11 shows the annual averaged vertical profiles of the Eratosthenes attractor, over all available profiles within each year and closer than 30 km to the eddy center, for different years during the 2000–2018 period. A histogram below indicates how many profiles are available for each year. This number varies a lot due to the inconstant frequency of oceanographic surveys, with the years from 2008 to 2011 being overrepresented because of extensive glider sections (Hayes et al., 2011) and several Argo floats being trapped for a very long time inside the anticyclone.

In the annual averaged vertical profiles in Fig. 11, the EAA anticyclones can be characterized by very deep anomalies, both in salt and temperature. For every year, the depth of maximal density anomaly is below 200 m, and it reaches 450 m some years. The magnitude of the anomalies can also be extremely marked, higher than +2.5 °C and +0.45 PSU in 2010. However, if annually averaged temperature anomalies always reach +1 °C at 200 m or below, Fig. 11 shows that

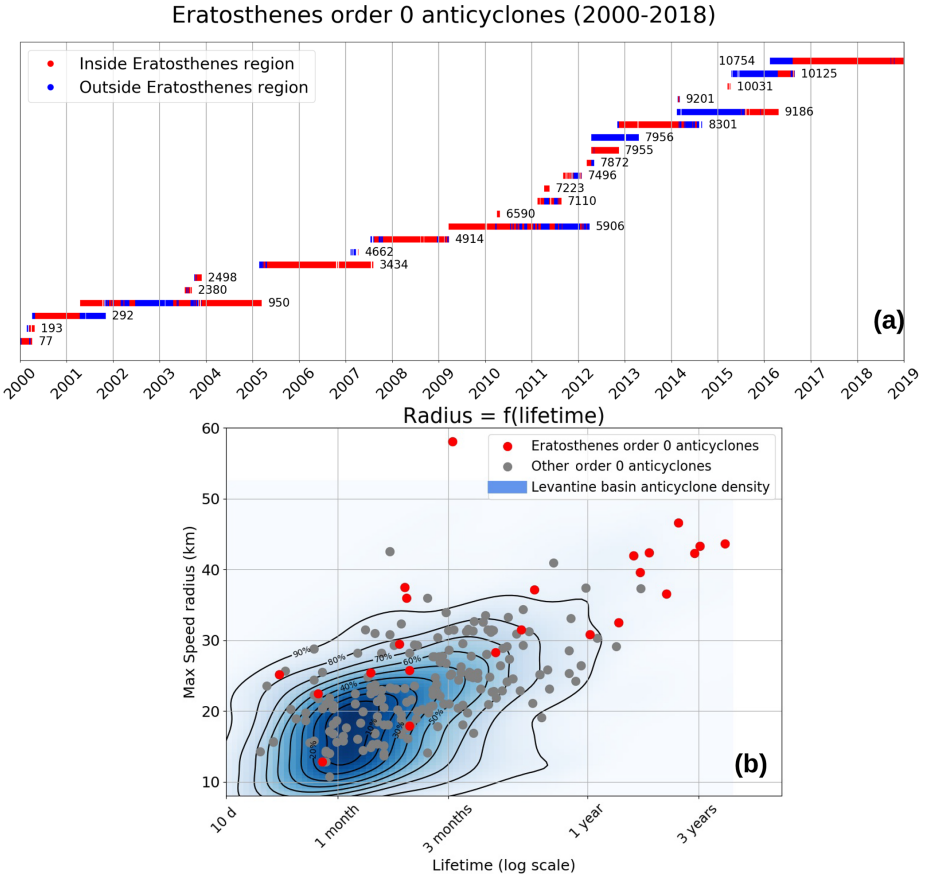

Figure 8. Details of the anticyclones constituting the EAA, detected as order 0 for the Eratosthenes region (tracks in Fig. 2a). **(a)** Time series with the eddy ID number from the DYNED database. The colored marker indicates when the eddy center is within (red) or outside of (blue) the region. **(b)** Scatterplot of the maximum speed radius as a function of lifetime, on a logarithmic scale, for order 0 anticyclones of the Eratosthenes region (red dots) and the other regions (gray dots); the blue shaded background is the density function for all LB anticyclones – except the Eratosthenes anticyclones – with contours each 10 % probability step.

there is a strong interannual variability in the vertical structures of these anticyclones. The year 2010 then appears as an extreme event, with the formation of a double-core structure visible on the density profile (Fig. 12c). This event was surveyed by gliders and described by Hayes et al. (2011); however, with longer time series, it can be seen that eddy-induced anomalies in 2009–2010 were extreme compared with the 19-year mean vertical structure.

In the BOUM campaign in 2008, Moutin and Prieur (2012) also compared the vertical structure of an Eratosthenes anticyclone with two other anticyclones in the Mediterranean Sea: a detached Algerian eddy and an anticyclone in the central Ionian Sea. Their comparison showed that the anticyclone constituting the EAA had the deepest potential density maximal anomaly (at 380 m compared with 160 m in the Algerian eddy) and that integrated anomalies were very warm and salty waters, with respective temperature and salinity anomalies of +2.35 °C and +0.388 PSU (+0.75 °C and −0.65 PSU in the Algerian eddy). Such values are consistent with observations in other years, as shown in Fig. 11b–c, although slightly higher.

The vertical structure of Eratosthenes anticyclones described above should be compared with physical properties of neighboring eddies in the LB. Figure 12 presents the comparison between a section representative of the Eratosthenes anticyclone, using data from the BOUM campaign in June 2008 (Moutin and Prieur, 2012), and an anticyclone section in the Tel Aviv region performed in October 2018 by a glider from IOLR. Next to each section is an ADT map representative of the SSH activity at that time (Fig 12b, d). The glider section lasts for 10 d, with 20 October 2018 being the median date; a magenta line indicates the glider track, and the position on the 20 October is shown with a magenta circle. The daily altimetric eddy contours are plotted on the ADT maps, with cyclones in red and anticyclones in blue, and a dot with a size proportional to the vortex Rossby number indicates the center. The upper panel of each section (Fig. 12a, c) marks the part of the cross section that is inside the maximal speed anticyclone contour using a blue

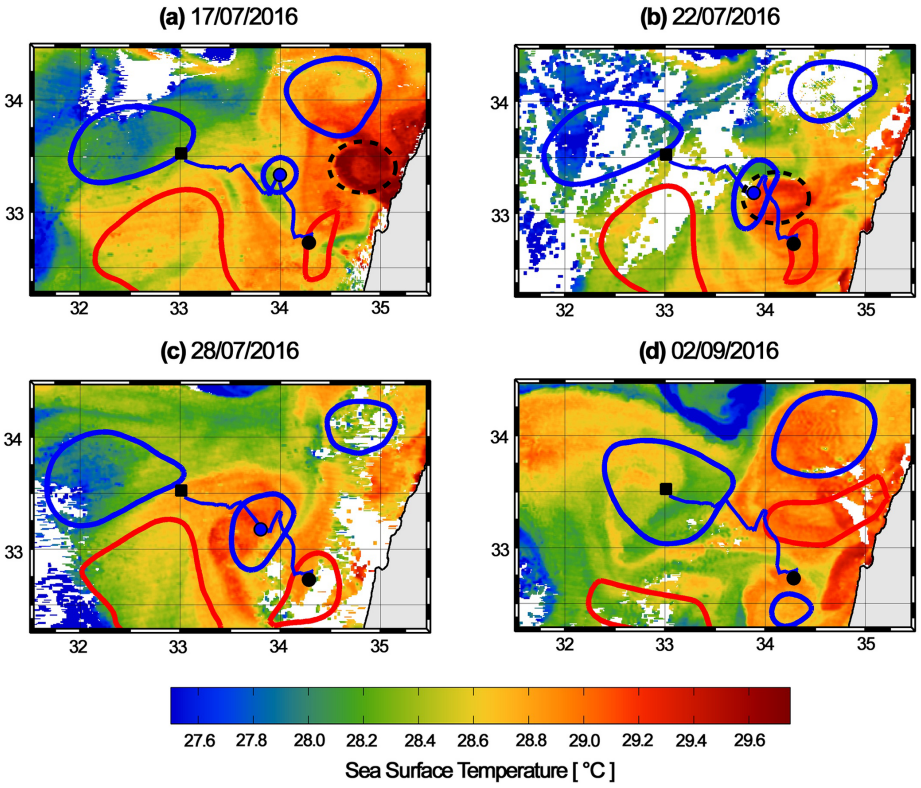

Figure 9. Daily snapshots of SST images showing a quickly moving warm-core anticyclone, part of a dipole that detaches from the Levantine coast and merges with a future Eratosthenes anticyclone. Superimposed DYNED contours are blue for anticyclones and red for cyclones. The track of the studied anticyclone is shown in blue line, its current center is shown using a blue circle, its initial detection on 10 February 2016 is shown using a black circle and its last detection on 2 September 2016 is shown using a black square. A blue line approximates the track of the warm-core anticyclone as seen in the SST sequence.

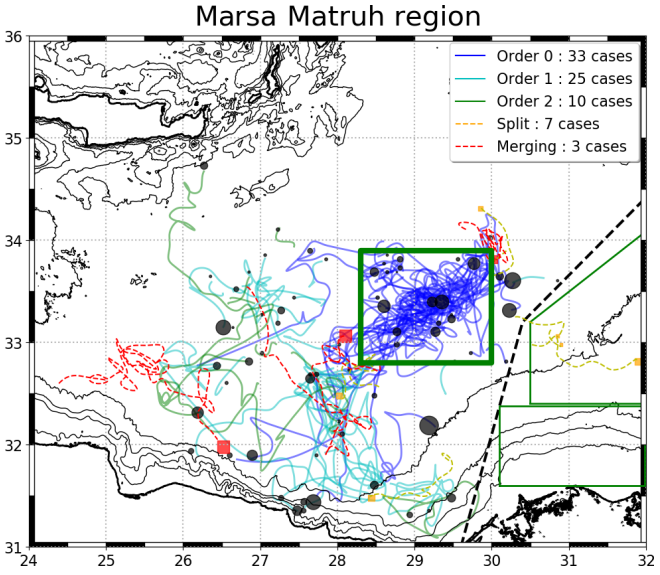

Figure 10. Convergence structure applied to the Marsa Matruh region, administered in the same way and using the same color code as in Fig. 6.

line. Thin black lines in the vertical sections are the absolute temperature isotherms, whereas color indicates the temperature anomaly relative to the climatological background; the isotherm intervals and the color bar range are the same in both sections for comparison purposes. An important difference is that Fig. 12a is an interpolation between the CTD measurements (indicated by black crosses), whereas Fig. 12b shows a glider track stacking in which each pixel corresponds to a measurement.

Although a 10-year period separates the two sections, it should first be noted that the local eddy activity is similar in both events and is very close to the mean circulation deduced from Fig. 1: anticyclones are found in Eratosthenes, Herodotus and Tel Aviv regions, whereas a cyclone is found in the Haifa region. Furthermore, as can be seen in the ADT maps, both sections crossed the anticyclones close to their respective center, allowing one to assume that the maximal anomaly was adequately sampled. Extensive glider sections were surveyed in the Eratosthenes region in 2009 and 2010, but as explained above, 2010 appears as an extreme year where comparison with neighboring eddies will be biased.

The anticyclone constituting the EAA surveyed in Fig. 12a is a long-lived anticyclone, referenced in the DYNED

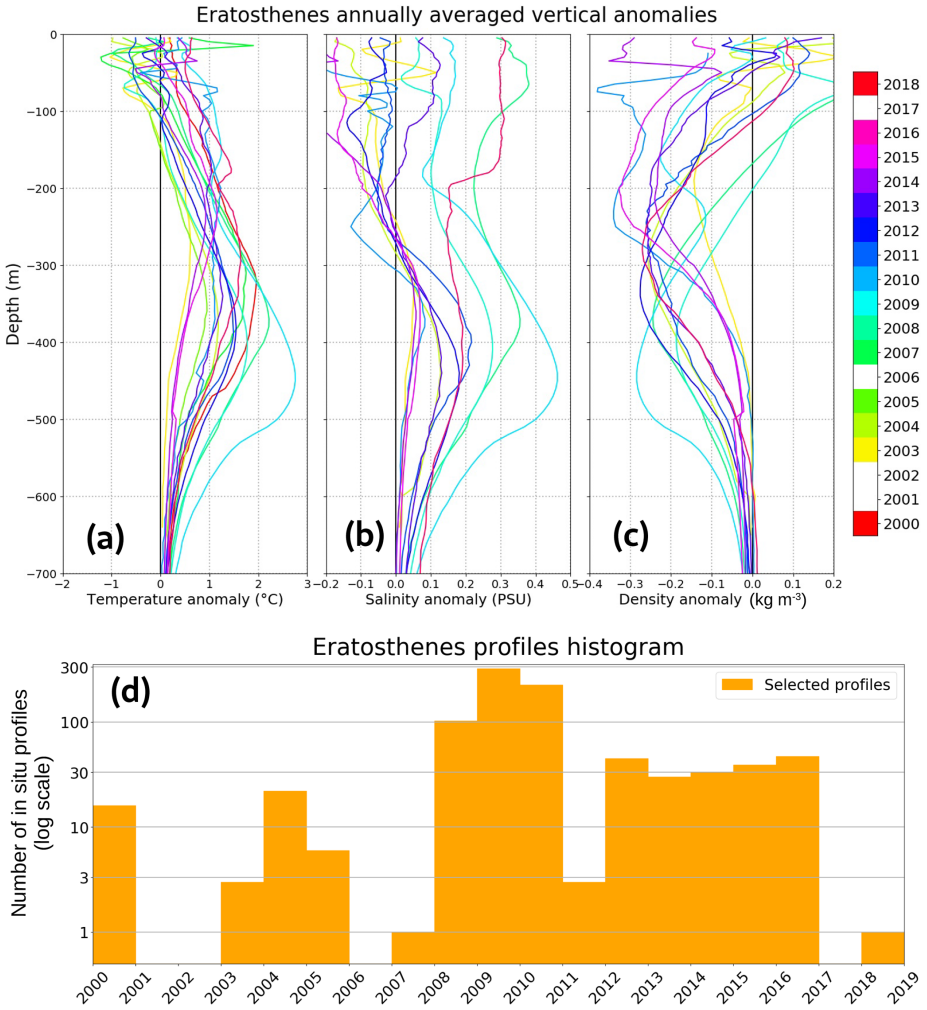

Figure 11. The annually averaged vertical profiles anomalies for **(a)** in situ temperature, **(b)** salinity and **(c)** density, inside Eratosthenes order 0 anticyclones. Profiles are selected if they are cast within 30 km of the eddy center, and their histogram is shown in panel **(d)** on a log scale. Years without any profiles are discarded from the color bar. Some years (e.g., 2005) only present a temperature profile, as only XBT casts were available.

database as no. 4914, born in the Beirut region before settling over the Eratosthenes Seamount for more than 6 months. The Tel Aviv eddy measured in Fig. 12c is a young anticyclone formed close to the shore in August 2018, as detected by AMEDA at approximately 32.0° N, 34.0° E and referenced as DYNED no. 12683. It drifted slowly offshore northwestwards before dying without merging at approximately 32.5° N, 33.0° E at the beginning of December 2018. It is, therefore, very similar to the anticyclones formed in the Tel Aviv region and drifting offshore, sometimes merging in the Eratosthenes region, in a similar way to the trajectories shown in Fig. 6c. In both events, the Tel Aviv anticyclone appears to be more intense in terms of Rossby number than the Eratosthenes anticyclone (as shown by a larger dot on the ADT maps), but the vertical structure shows that the Eratosthenes anticyclone, although weak in altimetric signature, hides a very deep and strong temperature anomaly: +2.35 °C at 380 m compared with +1.3 °C at the depth of the maximal density anomaly of 250 m in the Tel Aviv anticyclone. This comparison shows that anticyclones in the EAA can also be differentiated from neighboring eddies by a deeper subsurface anomaly, consistent with first observations by Stegner et al. (2019), who showed that the depth of the maximal density anomaly over the Eratosthenes Seamount (often below 300 m) is an almost unique specificity in the whole Mediterranean Sea.

6 Discussion

With only 3 years of SST data, Hamad et al. (2006) showed that along-shore current instabilities create eddies drifting offshore, and they identified the Eratosthenes Seamount as an anticyclone accumulation area (see their Fig. 16). In this study, with the hindsight of 19 years of eddy tracking, we

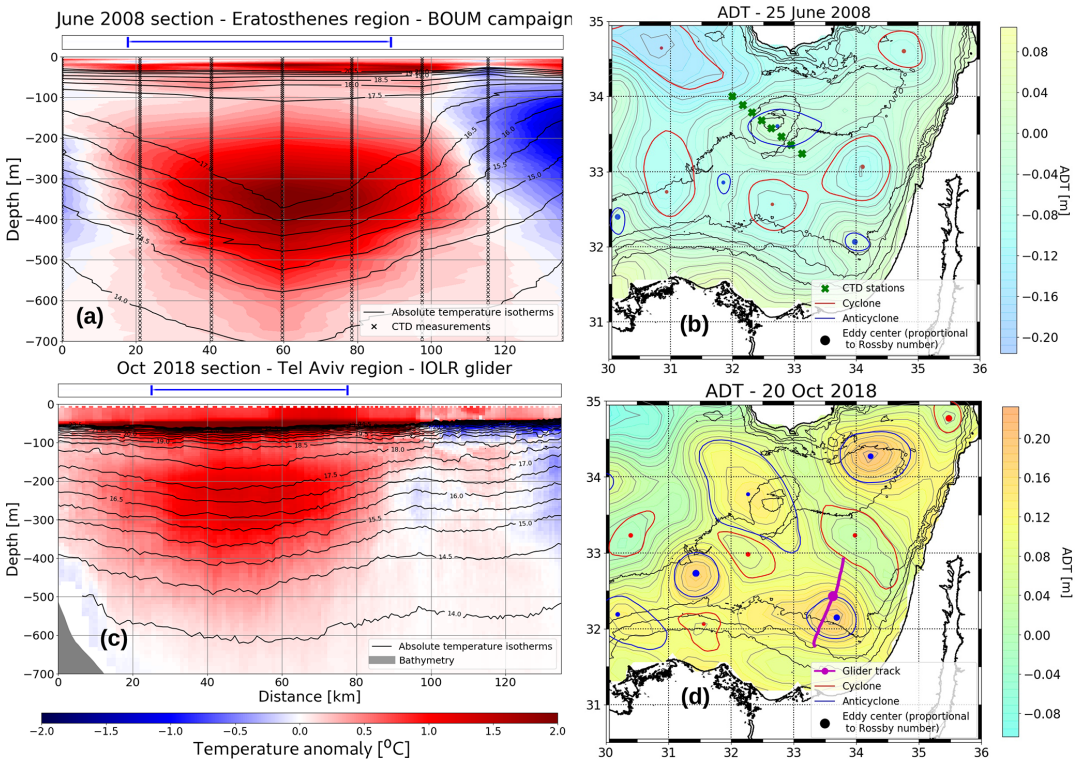

Figure 12. Comparison of anticyclone sections. The Eratosthenes (**a**) and Tel Aviv (**c**) region anticyclone sections in June 2008 and mid-October 2018, respectively. The left side is northwards, the horizontal axis (shared) is the distance along the section, black lines are the absolute temperature isotherms, the temperature anomaly is shown using the colored background and the blue cartridge above the panel outlines the limits of the eddy contours. Panels (**b**) and (**d**) show the respective ADT maps at the corresponding date of cast, presenting the neighboring eddy activity. Green crosses (a magenta line) show the CTD casts (the glider track). The eddy contours are maximal speed contours – blue denotes the anticyclones, red denotes cyclones and there is a Rossby number-scaled dot for their center.

add a quantification of the importing eddy flux and confirm what was previously inferred through a limited time period of data. We also observe that anticyclones are actually often formed offshore close to the seamount in the west, in the region referred to as "Herodotus" in this study.

Another important result of the eddy tracking performed here is the isolation of anticyclone dynamics from the rest of the LB: almost no anticyclones come from areas further west than the Herodotus region and, conversely, almost none escape this attraction basin (dashed black line on Figs. 3, 4, 6a–g and 7). It can be noted in Fig. 4a that the dashed line coincides with anticyclone drift divergence. This observation is not true for cyclones; however, as they do not have a thick core of homogeneous water and have significantly shorter lifetimes than anticyclones (see Fig. 5), they are assumed to contribute less to water mass transport. This western impermeable border could be linked to the presence of the Mid-Mediterranean Jet (MMJ). Zodiatis et al. (2010) suggested that this jet could be feeding the Eratosthenes anticyclonic structure. Nevertheless, the jet could also act as a barrier for anticyclones, explaining the absence of an anticyclone flux from the Marsa Matruh area into the Eratosthenes region (see Fig. 6a).

In older literature, Robinson et al. (1991) discussed the hypothesis of a northern path of Atlantic waters in the LB, isolating its southeastern part but grouping together the Marsa Matruh and Eratosthenes structures. This analysis was performed with a hydrographic vision using CTD stations. More recently, Ayata et al. (2018) carried out a review of the Mediterranean regionalization across eight studies using various parameters, mainly with a biological or hydrological focus. A remarkable result from this review is the very good agreement of these studies with respect to distinguishing a region of homogeneous properties in the southeastern LB, called "Levantine". The region proposed by the authors (see Fig. 4 in Ayata et al., 2018) matches very well with the borders of the EAA attraction basin delineated in this study, apart from the edge along the Egyptian and Levantine coasts. Thus, these results suggest a real hydrographic significance of the EAA attraction basin and a possible role of anticyclones in homogenizing water masses properties.

Additionally, given the importance of this area for intermediate water formation, the fate of water masses in the EAA core and its dissipation would be of great interest for extended research. Anticyclones coming from different formation areas regularly merge with the EAA, and the imported

water masses should, therefore, be transported. They likely feed its subsurface anomaly, which was shown to be deeper than surrounding structures (see Fig. 12), but the final destination of these waters is unknown. Erosion from its deep anomaly due to intense shear from topographic interaction with a seamount (Sutyrin et al., 2011) could provide a warm and salty water flux at depth, leading to the formation of intermediate water masses. Answering this very important question requires further simulation work as well as more in situ oceanographic data forming a consistent and continuous three-dimensional time series to accurately follow its evolution.

This study reveals the existence of the EAA from the analysis of eddy tracks, but questions remain regarding the mechanisms explaining this anticyclone convergence, whereas more classical westwards β-drift (Chelton et al., 2011) or current advection along the coast (Sutyrin et al., 2009) could be expected. There is controversy regarding whether the EAA effectively attracts other eddies or, conversely, if eddies detach from the coast and merge with a central and long-lived structure. In other words, does the EAA pull other anticyclones towards the seamount (in an active way) or is it acting as the stranding point of anticyclones advected by the mean flow (in a passive way)? SST images and detachments observed from the coast, shown in Fig. 9 in this study but previously observed in the literature by Hamad et al. (2006) and Gertman et al. (2010), suggest that the second option is likely happening. On the other hand, the high occurrence of eddy merging and splitting highlights the importance of eddy–eddy interactions in this basin. Further studies in this direction are needed to outline eddy dynamics, although the small internal deformation radius in the Mediterranean Sea of 10–12 km (Mkhinini et al., 2014) only allows one to accurately detect large mesoscale structures. Nevertheless, great improvements are possible via the application of eddy automatic detection at smaller scales than the mesoscale with the help of SST data (Moschos et al., 2020).

The presence of the EAA over a seamount obviously raises the question of topographic interactions. Two attractor structures are observed in the LB, over very different bathymetry: the Marsa Matruh attractor over the Herodotus Trench deeper than 2000 m and the EAA over the Eratosthenes Seamount whose summit is approximately 700 m deep. This similarity suggests that interactions with the seamount do not play a significant role in anticyclone convergence towards the EAA, and if significant, the presence of a seamount should actually destabilize anticyclone dynamics (Sutyrin et al., 2011). However, some differences between these structures (see Sect. 4.5), notably the more variable average position or attraction basin of Marsa Matruh, could be explained by topographic interactions.

Last but not least, the background used to estimate eddy vertical structure in Sect. 5 is considered a climatological reference at the same approximate location and time of the year (see Sect. 3.3). However, it is computed as a 2000–2018 average and could then be altered by events of strong interannual variability, reported in the LB by Ozer et al. (2017). Long-term evolution of the eddy-induced physical property signature deserves further work.

7 Conclusions

Using the DYNED-Atlas database of eddies in the Mediterranean Sea, a Lagrangian convergence method is defined, and its application to anticyclone tracking from 2000 to 2018 enables one to quantify anticyclone transfers between subregions of the southeastern LB. At the position of a known area of anticyclone accumulation, it reveals the existence of anticyclone convergence toward the Eratosthenes Seamount in a structure that we named the Eratosthenes anticyclone attractor. This attractor proves not to be a single fixed anticyclone but is rather constituted by a succession of long-lived anticyclones sharing dynamical characteristics, distinct from neighboring eddies: longer lifetime – more than 1 year and up to 4 years – and a maximal speed radius above 40 km – more than 3 times the internal deformation radius. Lagrangian eddy tracking also showed that the convergence towards the EAA is geographically bound to a clear attraction basin. Anticyclones drift towards the Eratosthenes Seamount after detaching from the current along the Levantine coast or being formed westward in the region that we named Herodotus. The formation of anticyclones with a short lifetime quickly merging with the EAA are spotted in the regions called Tel Aviv and Haifa. An effective barrier for anticyclones is then found between the Eratosthenes and Marsa Matruh regions. In situ vertical profiles are co-localized with eddies, and climatological backgrounds are computed using the DYNED-Atlas method, allowing one to estimate the eddy-induced physical property signatures. The anomalies induced by the anticyclones constituting the EAA are found to be extremely deep, with depths of maximal density anomaly always at or below 200 m, reaching 450 m in some years, but with pronounced interannual variability. Annual averages of the temperature anomaly are found to be always equal to or greater than $+1\,^{\circ}$C at 300 m, revealing a large heat storage capacity of the anticyclone.

Appendix A

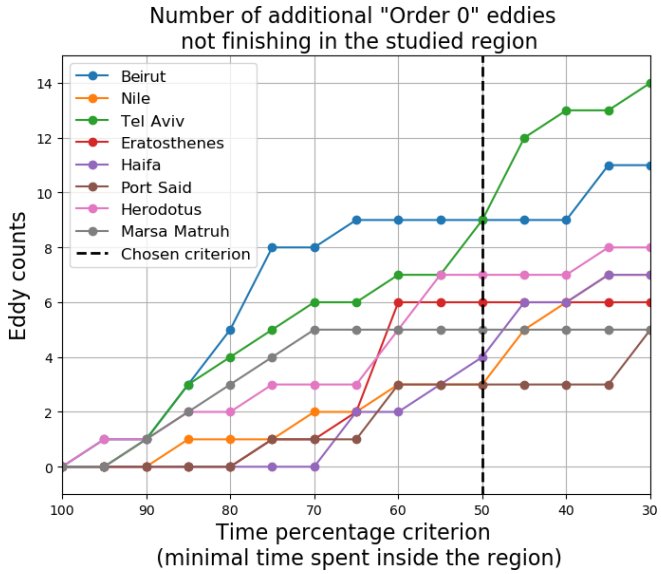

Figure A1. Sensitivity of the total number of order 0 anticyclones with the lifetime criterion, for four chosen regions: "100 %" means that order 0 anticyclones are strictly the ones dying in the study region; "30 %" means that order 0 are dying in the study region as well as anticyclones that spend 30 % of their lifetime within the borders of this region. A value of 50 % is chosen in this study (see Table A2).

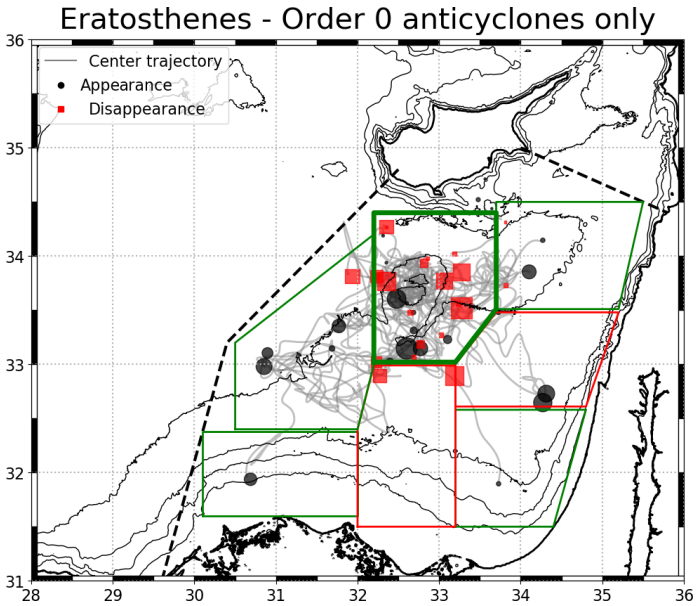

Figure A2. Appearance and disappearance locations for all order 0 anticyclones for the Eratosthenes region. Even if not all of them die within the region, they disappear very close to it.

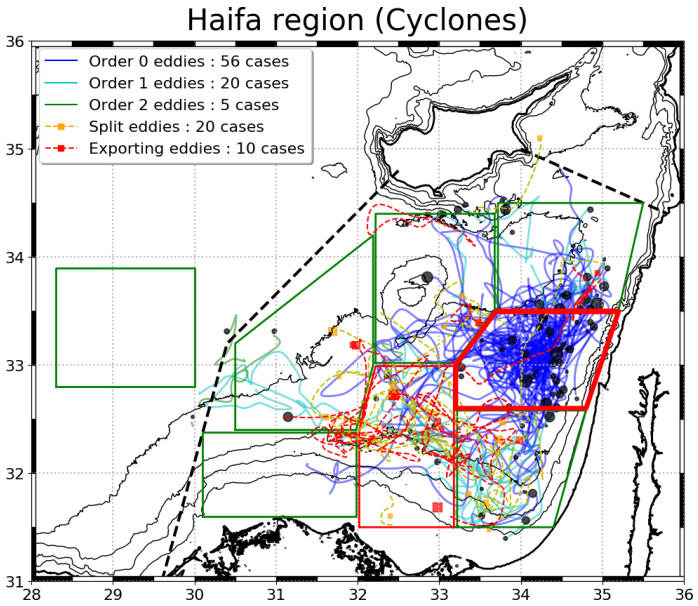

Figure A3. Cyclone transfers for Haifa region. Same as Fig. 6c but with the Lagrangian convergence framework applied to cyclones. Boxes and dashed line are the same as in Fig. 3.

Table A1. Regions studied in the LB, showing the coordinates and area. Corresponding boxes are shown in Fig. 3.

Region	Eratosthenes	Beirut	Haifa	Tel Aviv	Port Said	Herodotus	Nile	Marsa Matruh
Box coordinates (° N, ° E)	33.0, 32.2	33.5, 33.7	32.6, 33.2	31.5, 33.2	31.5, 32.0	32.4, 30.5	31.6, 30.1	32.8, 28.3
	33.0, 33.2	34.5, 33.7	32.6, 34.8	32.6, 33.2	32.4, 32.0	33.2, 30.5	32.4, 30.1	32.8, 30.0
	33.5, 33.7	34.5, 35.5	33.5, 35.2	32.6, 34.8	33.0, 32.2	34.2, 32.2	32.4, 32.0	33.9, 30.0
	34.4, 33.7	33.5, 35.2	33.5, 33.7	31.5, 34.4	33.0, 33.2	33.0, 32.2	31.6, 32.0	33.9, 28.3
	34.4, 32.2		33.0, 33.2		31.5, 33.2	32.4, 32.0		
Area ($\times 10^3$ km^2)	20.7	17.3	15.7	16.1	18.3	22.6	16.0	19.7

Table A2. Details of importing and exporting anticyclones for the seven regions of the southeastern LB identified in Sect. 3.2. Details are also shown in Fig. 6a–g, and the net anticyclone gain appears in Fig. 7.

Mean dynamical activity	Regions	Anticyclones born	Importing				Net anticyclone gain	Exporting	
			Order 0	Order 1	Order 2	Total		Split	Merging
AC region	Eratosthenes	14	23	19	2	44	30	7	0
	Beirut	29	38	1	0	39	10	2	2
	Tel Aviv	29	29	0	0	29	0	0	3
	Nile	53	52	2	0	54	1	6	1
	Herodotus	42	54	2	0	56	14	2	8
CY region	Haifa	24	18	1	0	19	−5	0	6
	Port Said	11	23	7	1	31	20	1	4

Data availability. The DYNED-Atlas database for 2000–2018 is freely available at https://doi.org/10.14768/2019130201.2 (Stegner and Briac, 2019). XBT and CTD casts used are freely available on the SeaDataNet portal (https://cdi.seadatanet.org/search, last access: 10 September 2021), by selecting data with unrestricted access in the LB (using the coordinates utilized in the present study which are available in the Supplement). The CORA database is available on the CMEMS catalogue: INSITU_GLO_TS_REP_OBSERVATIONS_013_001_b (https://doi.org/10.5194/os-9-1-2013, Cabanes et al., 2013). The IOLR glider data can be made available upon reasonable request from Ayah Lazar.

Supplement. The supplement related to this article is available online at: https://doi.org/10.5194/os-17-1231-2021-supplement.

Author contributions. AB carried out the main analysis and wrote the paper. AL supervised the study and provided the glider data. AS supervised the study. EM analyzed SST data and produced Fig. 9. All authors contributed to finalizing the paper.

Competing interests. The authors declare that they have no conflict of interest.

Disclaimer. Publisher's note: Copernicus Publications remains neutral with regard to jurisdictional claims in published maps and institutional affiliations.

Acknowledgements. The authors wish to thank the IOLR staff for help with glider operations. We are also grateful to the Agence National de la Recherche for financial support of the DYNED-Atlas project. Finally, the authors wish to acknowledge Briac Le Vu for fruitful discussions on AMEDA detections.

Financial support. This research has been supported by the Israel Science Foundation (grant no. 1666/18).

Review statement. This paper was edited by Anna Rubio and reviewed by two anonymous referees.

References

Amitai, Y., Lehahn, Y., Lazar, A., and Heifetz, E.: Surface circulation of the eastern Mediterranean Levantine basin: Insights from analyzing 14 years of satellite altimetry data, J. Geophys. Res.-Oceans, 115, C10058, https://doi.org/10.1029/2010JC006147, 2010.

ARGO: Argo float data and metadata from Global Data Assembly Centre, Argo GDAC, https://doi.org/10.17882/42182, 2020.

Ayata, S.-D., Irisson, J.-O., Aubert, A., Berline, L., Dutay, J.-C., Mayot, N., Nieblas, A.-E., d'Ortenzio, F., Palmiéri, J., Reygondeau, G., Rossi, V., and Guieu, C.: Regionalisation of the Mediterranean basin, a MERMEX synthesis, Prog. Oceanogr., 163, 7–20, 2018.

Brenner, S.: Long-term evolution and dynamics of a persistent warm core eddy in the Eastern Mediterranean Sea, Deep-Sea Res. Pt. II, 40, 1193–1206, 1993.

Cabanes, C., Grouazel, A., von Schuckmann, K., Hamon, M., Turpin, V., Coatanoan, C., Paris, F., Guinehut, S., Boone, C., Ferry, N., de Boyer Montégut, C., Carval, T., Reverdin, G., Pouliquen, S., and Le Traon, P.-Y.: The CORA dataset: validation and diagnostics of in-situ ocean temperature and salinity measurements, Ocean Sci., 9, 1–18, https://doi.org/10.5194/os-9-1-2013, 2013 (data available at: https://resources.marine.copernicus.eu/?option=com_csw&view=details&product_id=INSITU_GLO_TS_REP_OBSERVATIONS_013_001_b, last access: 10 September 2021).

Chelton, D. B., Schlax, M. G., and Samelson, R. M.: Global observations of nonlinear mesoscale eddies, Prog. Oceanogr., 91, 167–216, 2011.

Cui, W., Wang, W., Zhang, J., and Yang, J.: Multicore structures and the splitting and merging of eddies in global oceans from satellite altimeter data, Ocean Sci., 15, 413–430, https://doi.org/10.5194/os-15-413-2019, 2019.

de Marez, C., L'Hégaret, P., Morvan, M., and Carton, X.: On the 3D structure of eddies in the Arabian Sea, Deep-Sea Res. Pt. I, 150, 103057, https://doi.org/10.1016/j.dsr.2019.06.003, 2019.

DYNED-Atlas-Med (Stegner, A., Le Vu, B., Pegliasco, C., and Faugere, Y.): Dynamical Eddy Atlas of the Mediterranean-Sea 2000–2018, MISTRALS [data set], https://doi.org/10.14768/2019130201.2, 2019.

Garreau, P., Dumas, F., Louazel, S., Stegner, A., and Le Vu, B.: High-Resolution Observations and Tracking of a Dual-Core Anticyclonic Eddy in the Algerian Basin, J. Geophys. Res.-Oceans, 123, 9320–9339, 2018.

GEBCO: GEBCO Compilation Group, GEBCO 2020 Grid, https://doi.org/10.5285/a29c5465-b138-234d-e053-6c86abc040b9, 2020.

Gertman, I., Goldman, R., Rosentraub, Z., Ozer, T., Zodiatis, G., Hayes, D., and Poulain, P.: Generation of Shikmona anticyclonic eddy from an alongshore current, in: Rapp. Comm. int. Mer Medit. (CIESM Congress Proceedings), Vol. 39, p. 114, CIESM, Monaco, 2010.

Hamad, N., Millot, C., and Taupier-Letage, I.: The surface circulation in the eastern basin of the Mediterranean Sea, Sci. Mar., 70, 457–503, 2006.

Hayes, D., Zodiatis, G., Konnaris, G., Hannides, A., Solovyov, D., and Testor, P.: Glider transects in the Levantine Sea: Characteristics of the warm core Cyprus eddy, in: OCEANS 2011 IEEE-Spain, 1–9, IEEE, Santander, Spain, https://doi.org/10.1109/Oceans-Spain.2011.6003393, 2011.

Ioannou, A., Stegner, A., Le Vu, B., Taupier-Letage, I., and Speich, S.: Dynamical evolution of intense Ierapetra eddies on a 22 year long period, J. Geophys. Res.-Oceans, 122, 9276–9298, 2017.

Ioannou, A., Stegner, A., Tuel, A., Levu, B., Dumas, F., and Speich, S.: Cyclostrophic corrections of AVISO/DUACS surface velocities and its application to mesoscale eddies in the

Mediterranean Sea, J. Geophys. Res.-Oceans, 124, 8913–8932, https://doi.org/10.1029/2019JC015031, 2019.

Laxenaire, R., Speich, S., Blanke, B., Chaigneau, A., Pegliasco, C., and Stegner, A.: Anticyclonic eddies connecting the western boundaries of Indian and Atlantic Oceans, J. Geophys. Res.-Oceans, 123, 7651–7677, 2018.

Laxenaire, R., Speich, S., and Stegner, A.: Evolution of the Thermohaline Structure of One Agulhas Ring Reconstructed from Satellite Altimetry and Argo Floats, J. Geophys. Res.-Oceans, 124, 8969–9003, https://doi.org/10.1029/2018JC014426, 2019.

Le Vu, B., Stegner, A., and Arsouze, T.: Angular Momentum Eddy Detection and tracking Algorithm (AMEDA) and its application to coastal eddy formation, J. Atmos. Ocean. Tech., 35, 739–762, 2018.

Mason, E., Pascual, A., and McWilliams, J. C.: A new sea surface height–based code for oceanic mesoscale eddy tracking, J. Atmos. Ocean. Tech., 31, 1181–1188, 2014.

Mason, E., Ruiz, S., Bourdalle-Badie, R., Reffray, G., García-Sotillo, M., and Pascual, A.: New insight into 3-D mesoscale eddy properties from CMEMS operational models in the western Mediterranean, Ocean Sci., 15, 1111–1131, https://doi.org/10.5194/os-15-1111-2019, 2019.

Matsuoka, D., Araki, F., Inoue, Y., and Sasaki, H.: A new approach to ocean eddy detection, tracking, and event visualization–application to the northwest pacific ocean, Procedia Comput. Sci., 80, 1601–1611, 2016.

Menna, M., Poulain, P.-M., Zodiatis, G., and Gertman, I.: On the surface circulation of the Levantine sub-basin derived from Lagrangian drifters and satellite altimetry data, Deep-Sea Res. Pt. I, 65, 46–58, 2012.

Millot, C. and Taupier-Letage, I.: Circulation in the Mediterranean sea, in: The Mediterranean Sea, 29–66, Springer, Berlin, Heidelberg, 2005.

Mkhinini, N., Coimbra, A. L. S., Stegner, A., Arsouze, T., Taupier-Letage, I., and Béranger, K.: Long-lived mesoscale eddies in the eastern Mediterranean Sea: Analysis of 20 years of AVISO geostrophic velocities, J. Geophys. Res.-Oceans, 119, 8603–8626, 2014.

Moschos, E., Stegner, A., Schwander, O., and Gallinari, P.: Classification of Eddy Sea Surface Temperature Signatures under Cloud Coverage, IEEE J. Sel. Top. Appl., 13, 3437–3447, 2020.

Moutin, T. and Prieur, L.: Influence of anticyclonic eddies on the Biogeochemistry from the Oligotrophic to the Ultraoligotrophic Mediterranean (BOUM cruise), Biogeosciences, 9, 3827–3855, https://doi.org/10.5194/bg-9-3827-2012, 2012.

Ozer, T., Gertman, I., Kress, N., Silverman, J., and Herut, B.: Interannual thermohaline (1979–2014) and nutrient (2002–2014) dynamics in the Levantine surface and intermediate water masses, SE Mediterranean Sea, Global Planet. Change, 151, 60–67, 2017.

Pessini, F., Olita, A., Cotroneo, Y., and Perilli, A.: Mesoscale eddies in the Algerian Basin: do they differ as a function of their formation site?, Ocean Sci., 14, 669–688, https://doi.org/10.5194/os-14-669-2018, 2018.

Robinson, A., Golnaraghi, M., Leslie, W., Artegiani, A., Hecht, A., Lazzoni, E., Michelato, A., Sansone, E., Theocharis, A., and Ünlüata, Ü.: The eastern Mediterranean general circulation: features, structure and variability, Dynam. Atmos. Oceans, 15, 215–240, 1991.

Stegner, A. and Briac, L. V.: Atlas of 3D Eddies in the Mediterranean Sea from 2000 to 2017, ESPRI/IPSL [data set], https://doi.org/10.14768/2019130201.2, 2019.

Stegner, A., Le Vu, B., Pegliasco, C., Moschos, E., and Faugere, Y.: 3D structure of long-lived eddies in the Mediterranean sea: the DYNED-Atlas database, Rapp. Comm. Intern. Mer Meditter., 42, p. 74, 2019.

Sutyrin, G., Stegner, A., Taupier-Letage, I., and Teinturier, S.: Amplification of a surface-intensified eddy drift along a steep shelf in the Eastern Mediterranean Sea, J. Phys. Oceanogr., 39, 1729–1741, 2009.

Sutyrin, G., Herbette, S., and Carton, X.: Deformation and splitting of baroclinic eddies encountering a tall seamount, Geophys. Astro. Fluid, 105, 478–505, 2011.

Taburet, G., Sanchez-Roman, A., Ballarotta, M., Pujol, M.-I., Legeais, J.-F., Fournier, F., Faugere, Y., and Dibarboure, G.: DUACS DT2018: 25 years of reprocessed sea level altimetry products, Ocean Sci., 15, 1207–1224, https://doi.org/10.5194/os-15-1207-2019, 2019.

Yi, J., Du, Y., He, Z., and Zhou, C.: Enhancing the accuracy of automatic eddy detection and the capability of recognizing the multi-core structures from maps of sea level anomaly, Ocean Sci., 10, 39–48, https://doi.org/10.5194/os-10-39-2014, 2014.

Zodiatis, G., Hayes, D., Gertman, I., and Samuel-Rhodes, Y.: The Cyprus warm eddy and the Atlantic water during the CYBO cruises (1995–2009), Rapp. Comm. Intern. Mer Meditter., 39, p. 202, 2010.

Titre : Dynamique de surface et de subsurface de tourbillons sous l'influence du forçage atmosphérique : cas d'étude en mer Méditerranée

Mots clés : tourbillon, flux air-mer, méso-échelle, télédétection, stratification

Résumé : Les tourbillons méso-échelle sont des structures turbulentes omniprésentes dans l'océan. Les anticyclones tournent dans le sens horaire dans l'hémisphère Nord, et les cyclones dans le sens opposé. Ils interagissent avec la stratification de l'océan influencée par les flux air-mer. Nous étudions ici l'impact de ces flux sur leur évolution saisonnière et long terme, prenant le cas des tourbillons méditerranéens. Une méthode de suivi lagrangien ainsi qu'un état de référence hors-tourbillon sont définis, permettant de suivre les tourbillons par télédétection et dans les données in situ. Une oscillation saisonnière marquée est observée dans la température de surface des tourbillons. Les signatures de surface anticycloniques froides et cycloniques chaudes passent de très rares en hiver à prédominantes au début de l'été, une oscillation qui se retrouve pour une structure individuelle. En profondeur, les anticyclones approfondissent grandement la couche mélangée en hiver par rapport à l'extérieur, en interaction avec la structure en densité sous-jacente. Ils retardent également significativement la restratification de printemps dans leur cœur. Ces phénomènes peuvent être reproduits dans les simulations numériques. Le forçage atmosphérique haute fréquence génère des ondes quasi-inertielles qui se propagent davantage dans les anticyclones, renforçant ainsi le mélange vertical proche de la surface et expliquant les variations d'anomalie de température de surface. Les résultats présentés ici dévoilent une évolution complexe de la structure 3D des tourbillons en lien avec les flux atmosphériques. Ils montrent la nécessité de résoudre une vaste gamme d'échelles spatiales et temporelles pour reproduire correctement l'évolution des tourbillons dans des simulations numériques. Ces résultats ouvrent également des pistes intéressantes pour récupérer des informations sur leur structure 3D à partir de données de surface.

Title : Surface and subsurface evolution of mesoscale eddies under atmospheric forcing: case study in the Mediterranean Sea

Keywords : eddy, mesoscale, air-sea interactions, mesoscale, remote sensing, stratification

Abstract : Mesoscale eddies are turbulent structures present in every regions of the world ocean. Anticyclone are clockwise rotating structures in the North hemisphere, cyclones counter-clockwise ones. Eddies interact with ocean stratification impacted by air-sea fluxes. We study here their seasonal and long-term evolution, taking the case of Mediterranean eddies. We design a Lagrangian method allowing to track eddy signature in both remote-sensing and in situ data. In sea surface temperature a marked seasonal oscillation is observed. Anticyclonic cold-core and cyclonic warm-core shift from very rare in winter to predominant in early summer, a oscillation also retrieved tracking a single structure. At depth anticyclones are found to greatly deepen the winter mixed layer compared to outside eddy state, interacting with their subsurface density structure. They also significantly delay spring restratification in their core. Such behaviors can be retrieved in numerical simulations. High frequency forcing generate near-inertial waves propagating more in anticyclone, thus enhancing vertical mixing and explaining eddy surface temperature anomalies variations. The results presented here unveil a complex evolution of an eddy 3D structure linked with atmospheric fluxes. They show the need to resolve a wide range of both spatial and temporal scales to accurately reproduce eddies evolution in a numerical model. These results also open interesting further investigations to recover information about an eddy 3D structure based on surface remote-sensing data.

Institut Polytechnique de Paris
91120 Palaiseau, France